

Pyrene Excimer Formation: A Tool to Study Macromolecular Conformations in Solution

by

Sanjay Rajnikant Patel

A thesis

presented to the University of Waterloo

in fulfillment of the

thesis requirement for the degree of

Doctor of Philosophy

in

Chemistry

Waterloo, Ontario, Canada, 2024

© Sanjay Rajnikant Patel 2024

Examining Committee Membership

The following served on the Examining Committee for this thesis. The decision of the Examining Committee is by majority vote.

External Examiner

Dr. Ben Schuler

Professor, Department of Biochemistry
University of Zurich, Zurich, Switzerland

Supervisor

Dr. Jean Duhamel

Professor, Department of Chemistry
University of Waterloo, Waterloo, Canada

Internal Member #1

Dr. Scott Taylor

Professor, Department of Chemistry
University of Waterloo, Waterloo, Canada

Internal Member #2

Dr. Xiasong Wang

Professor, Department of Chemistry
University of Waterloo, Waterloo, Canada

Internal-External Member

Dr. Michael Tam

Professor, Department of Chemical Engineering
University of Waterloo, Waterloo, Canada

Author's Declaration

This thesis consists of material all of which I authored or co-authored: see Statement of Contribution included in the thesis. This is a true copy of the thesis, including any required final revisions, as accepted by my examiners. I understand that my thesis may be made electronically available to the public.

Statement of Contributions

Chapter 2: Patel, S.; Duhamel, J. Macromolecular Conformation of Low-Generation PAMAM Dendrimers Probed by Pyrene Excimer Formation. *Macromolecules* **2023**, *56*, 4012-4021. DOI: <https://doi.org/10.1021/acs.macromol.3c00418>

Chapter 3: Patel, S.; McNelles, S.; Adronov, A.; Duhamel, J. Intramacromolecular Conformational Changes in Low Generation PAMAM Dendrimers Probed by Pyrene Excimer Formation. *J. Phys. Chem. B.* **2023**, *127*, 8040-8048. DOI: <https://doi.org/10.1021/acs.jpcc.3c04053>

Abstract

The current view for fluorescence collisional quenching (FCQ) experiments is that no quantitative information can be retrieved from macromolecules containing more than a single dye-quencher pair attached at two specific positions on a macromolecule. This holds true for pyrene excimer formation (PEF), a well-established FCQ phenomenon, where an excimer is produced through the encounter between an excited and a ground-state pyrenyl labels attached onto a macromolecule. In contrast, recent studies suggest that the analysis of fluorescence decays acquired with macromolecules containing many pyrenyl labels with the model free analysis (MFA) and fluorescence blob model (FBM) yields quantitative information about the internal dynamics and local density of macromolecules in solution. The underlying physical principle enabling the MFA and FBM to probe macromolecules in this manner is based on the direct relationship existing between the average rate constant ($\langle k \rangle$) for PEF and the local concentration ($[Py]_{loc}$) of pyrenyl labels on the macromolecule. Yet, and despite its importance, no study has conclusively validated this relationship. This is due, in part, to the difficulty in determining $[Py]_{loc}$ for pyrene-labeled macromolecules (PyLM) and benchmarking this methodology against other experimental techniques. In the present thesis, this fundamental relationship was demonstrated with a series of polyamidoamine (PAMAM) dendrimers of generations GY ($=0, 1, \text{ or } 2$) that had been labeled with pyrene derivatives having different numbers X ($= 4, 8, \text{ or } 12$) of carbon atoms in the pyrenyl linker to yield the PyCX-PAMAM- GY samples. The fluorescence decays were acquired in N,N -dimethylformamide (DMF) and dimethylsulfoxide (DMSO) and analyzed with the MFA to retrieve $\langle k \rangle$, which was compared to $[Py]_{loc}$ obtained by assuming that the internal segments of the PyCX-PAMAM- GY samples linking the pyrenyl labels obeyed Gaussian statistics. The direct relationship found between $\langle k \rangle$ and $[Py]_{loc}$ for the PyCX-PAMAM- GY samples provided a

validation for this assumption and demonstrated that PEF can be employed to probe the conformation of macromolecules in solution.

Subsequently, PEF was applied to probe the conformational changes induced by protonating the internal tertiary amines of the PyCX-PAMAM-GY samples, showcasing PEF's ability to study these conformational changes intramolecularly, a feat difficult to achieve by traditional methods used for characterizing macromolecular conformations in solution.

Expanding beyond dendrimers, PEF was applied to study the conformation of larger macromolecules like poly(glutamic acid) (PGA) and polynorbornene (PNb) on different length scales by using 1-pyrenealkylamines with varied alkyl side chains. The fluorescence blob model (FBM) was applied to determine the number ($N_{\text{blob}}^{\text{exp}}$) of structural units within a *blob*, the volume probed by an excited pyrenyl label, taken as a measure of the local macromolecular density. Comparison of $N_{\text{blob}}^{\text{exp}}$ with $N_{\text{blob}}^{\text{MMO}}$ obtained through molecular mechanic optimizations (MMOs) validated PEF's ability to probe macromolecular conformations over different length scales. The conformation of the Py-PGA constructs was found to remain unchanged when probed with 1-pyrenealkylamines having different linker lengths reflecting a homogeneous conformation over different length scales. In contrast, the Py-PNb samples appeared helical and randomly coiled for the 1-pyrenealkylamines with a shorter and longer linker, respectively, highlighting the potential of PEF at probing complex macromolecules with heterogeneous conformation across various length scales.

In conclusion, this thesis further supports the applicability of PEF as a robust experimental technique for probing the conformations and internal dynamics of macromolecules in solution.

Acknowledgments

I would first like to thank Prof. Jean Duhamel for his constant guidance and providing the opportunity to work under his supervision over the span of my CHEM 494 research project, M. Sc., and Ph. D. research. I would also like to thank my committee members for their guidance and support over the years. Finally, I would also like to thank all past and current members of the Duhamel and Gauthier laboratories who have provided constant support and guidance over the course of my degree. I would like to further extend my gratitude to my family, who have always encouraged me throughout my academic career.

Table of Contents

Examining Committee Membership	ii
Author's Declaration.....	iii
Statement of Contributions	iv
Abstract	v
Acknowledgments.....	vii
List of Figures	xi
List of Tables	xvii
List of Abbreviations	xviii
List of Symbols	xx
Chapter 1: Introduction	1
1.1 Techniques Applied to Characterize Macromolecules	3
1.1.1 Microscopy-Based Techniques	3
1.1.2 Scattering-Based Experiments	7
1.1.3 Spectroscopy-Based Experiments.....	9
1.1.4 Current Limitations in the Characterization of Macromolecular Conformations	11
1.2 Fluorescence	12
1.2.2 Fluorescence Collisional Quenching (FCQ)	13
1.2.3 Pyrene	15
1.2.4 Fluorescence <i>Blob</i> Model (FBM).....	16
1.2.5 Model Free Analysis (MFA).....	17
1.2.6 Application of the Fluorescence <i>Blob</i> Model (FBM) and Model Free Analysis (MFA)	18
1.3 Macromolecules under Study.....	19
1.3.1 Dendrimers.....	19
1.3.2 Poly(glutamic acid) (PGA)	21
1.3.3 Polynorbornene	22
1.4 Research Objective and Thesis Outline	23
Chapter 2: Macromolecular Conformation of Low Generation PAMAM Dendrimers Probed by Pyrene Excimer Formation	26
2.1 ABSTRACT	27
2.2 INTRODUCTION.....	28
2.3 EXPERIMENTAL.....	30
2.3 RESULTS AND DISCUSSION	39
2.4 CONCLUSIONS	52
Chapter 3: Intra-Macromolecular Conformational Changes in Low Generation PAMAM Dendrimers Probed by Pyrene Excimer Formation	54
3.1 ABSTRACT	55
3.2 INTRODUCTION.....	56
3.3 EXPERIMENTAL.....	59
3.4 RESULTS AND DISCUSSION	63

3.5 CONCLUSIONS	78
Chapter 4: Extending the Range of Distances Used to Characterize the Conformation of Macromolecules by Pyrene Excimer Formation: Application to the Conformation of Poly(L-glutamic acid) in Dimethyl Sulfoxide.....	80
4.1 ABSTRACT	81
4.2 INTRODUCTION	82
4.3 EXPERIMENTAL	86
4.4 RESULTS AND DISCUSSION	93
4.5 CONCLUSIONS	106
Chapter 5: Pyrene Excimer Formation as a Tool for Probing Polymer Microstructure – Application to Poly(norbornene Acid).....	108
5.1 ABSTRACT	108
5.2 INTRODUCTION	110
5.3 EXPERIMENTAL	114
5.4 RESULTS AND DISCUSSION	118
5.5 CONCLUSIONS	135
Chapter 6: Concluding remarks & Future Works	136
6.1 Thesis Conclusion	137
6.2 Future Work	140
Letters of Copyright Permission.....	143
Permission for reproduction of Chapter 2	143
Permission for reproduction of Chapter 3	143
References.....	144
Chapter 1	144
Chapter 2	163
Chapter 3	167
Chapter 4	170
Chapter 5	178
Chapter 6	188
S2-References	189
S3-References	193
S4-References	193
Appendix: Supporting Information (SI).....	195
Appendix A: 2-SI for Chapter 2	196
A] Characterization of the pyrene derivatives by ¹H NMR and UV-Vis analysis	196
B] ¹H NMR characterization of the PyCX-PAMAM-GY dendrimers	199
C] Characterization of the PyCX-PAMAM-GY dendrimers by Mass Spectrometry (MS)	203
D] Global Analysis of Monomer and Excimer Decays using the Model-Free Analysis (MFA)	210
E] Parameters obtained from the MFA of the PyCX-PAMAM-GY dendrimers:	212
F] Determination of k_{diff} from plots of $\langle k \rangle$ as a function of [H-PyBA] in DMF and DMSO	216
G] Equations used for the radius of gyration and the end-to-end distance of the dendrimers	217
Appendix B: S3-SI for Chapter 3	218

A] Global Analysis of Monomer and Excimer Decays Using the Model-Free Analysis	218
B] Parameters retrieved from the MFA of the fluorescence decays:	220
C] Determination of k_{diff} from plots of $\langle k \rangle$ as a function of [H _x -PyBA] in DMF and DMSO .	236
Appendix C: S4- SI for Chapter 4	237
A] ¹ H NMR and UV-Vis characterization	237
B] Fluorescence Blob Model (FBM) Analysis.....	241
C] Parameters retrieved from the FBM analysis	243
D] Molecular Mechanic Optimization:	255
Appendix D: S5- SI for Chapter 5	258
A] ¹ H NMR and UV-vis characterization of the pyrenyl derivatives	258
B] Fluorescence Blob Model (FBM) analysis.....	259
C] Global analysis of the monomer and excimer fluorescence decays with the FBM	261
D] Molecular Mechanic Optimizations of PyCX(x)N-PNb-Ac	270

List of Figures

Figure 1.1 Illustration of how A) AFM and B) TEM images are acquired.	5
Figure 1.2 Schematic illustration of A) MC and B) MD simulations. The above figure only represents one iteration of the several thousands typically conducted in a simulation.	6
Figure 1.3 Illustration of the experimental set up for small (SAXS) and wide (WAXS) angle X-ray scattering.	9
Figure 1.4 Jablonski diagram	13
Figure 1.5 Illustration of integrative macromolecular science combining the FBM analysis of fluorescence decays with molecular mechanics optimizations for the characterization of macromolecular conformations.	17
Figure 1.6 Schematic illustration of dendrimer structure and their cascade-like synthesis	21
Figure 2.1 Chemical parametrization. A) Chemical structure of PyC4-PAMAM-G1 and B) its parametrized equivalent.	40
Figure 2.2 Comparison of R_g determined via (○) SAXS, ¹⁶ (Δ) computer simulations, ²⁰ and (□) with Equation 2.6.	44
Figure 2.3 Steady-state fluorescence spectra for the PyCX-PAMAM-GY dendrimers of generation A,D) 0, B,E) 1 and C,F) 2 that have been labeled with 1-pyrene-butyric (purple), -octanoic (blue), and dodecanoic (green) acid. Fluorescence spectra in Figures 2.3A-C and 2.3D-F were acquired in DMF and DMSO, respectively.....	45
Figure 2.4 Plot of A) $(I_E/I_M)^{SSF}$ as a function of $n_{Py}/(L_{Py}/l)^3$, B) $(I_E/I_M)^{TRF}$ as a function of $(I_E/I_M)^{SSF}$, and $(I_E/I_M)^{TRF}(f_{free}=f_{ES}=0)$. Triangle, diamond, and square for generation 0, 1, and 2 PAMAM dendrimers labeled with 1-pyrene-butyric, -octanoic, and -dodecanoic acid in purple, blue, and green, respectively. Empty and full symbols are for DMF and DMSO, respectively.	47

Figure 2.5 Plot of the molar fractions f_{free} (\blacklozenge), f_{diff} (\blacktimes), and f_{agg} (\blacktriangle) determined from the MFA of the fluorescence decays as a function of $n_{\text{Py}}/(\langle L_{\text{Py}} \rangle)^3$ in A) DMF and B) DMSO..... 48

Figure 2.6 Plot of $\langle k \rangle$ as a function of $[\text{Py}]_{\text{loc}}$ for PyCX-PAMAM-GY samples acquired in A) DMF and B) DMSO and PyC4-HMPA-GY samples acquired in C) DMF and D) DMSO. \blacktriangle , \blacklozenge and \blacksquare represent PAMAM generation 0, 1 and 2, respectively, while purple, blue and green represent PyCX-PAMAM-GY dendrimers labeled with 1-pyrene-butyric, -octanoic, and -dodecanoic acid, respectively. (\odot) and (\bullet) for the PyC4-HMPA-GY samples in DMF and DMSO, respectively..... 49

Figure 2.7 Plot of $\langle k \rangle$ as a function of $n_{\text{Py}}/(\langle L_{\text{Py}} \rangle)^3$ for A) the PyCX-PAMAM-GY samples and B) the PyCX-PAMAM-GY and PyC4-HMPA-GY samples. \blacktriangle , \blacklozenge and \blacksquare represent PAMAM generation 0, 1 and 2, respectively, while purple, blue and green represent PyCX-PAMAM-GY dendrimers labeled with 1-pyrene-butyric, -octanoic, and -dodecanoic acid, respectively. (\odot , \bullet) for the PyC4-HMPA-GY samples. Hollow for DMF and solid for DMSO. C) Plot of (solid) R_g and (hollow) r_{EE} as a function of dendrimer ends for the unlabeled (\blacktriangle , \blacktriangle) PAMAM and (\odot , \bullet) HMPA dendrimers..... 51

Figure 3.1 Fluorescence spectra of the PyCX-PAMAM-GY samples in DMF (top row) and DMSO (bottom row) with 5 mM HCl for X = 4 (\blacklozenge), 8 (\blacklozenge), or 12 (\blacklozenge) and Y = 0 (A & D), 1 (B & E), and 2 (C & F). 64

Figure 3.2 A plot of A) $(I_E/I_M)^{\text{SSF}}$ as a function of $n_{\text{Py}}/(\langle L_{\text{Py}} \rangle^{2/2}/l)^3$, B) $(I_E/I_M)^{\text{TRF}}$ as a function of $(I_E/I_M)^{\text{SSF}}$ and $(I_E/I_M)^{\text{TRF}}(f_{\text{free}}=0)$ as a function of $n_{\text{Py}}/(\langle L_{\text{Py}} \rangle^{2/2}/l)^3$ acquired in C) DMF (\blacksquare , \blacklozenge) or D) DMSO (\blacktimes , \blacktimes) without (black) or with (red) 5 mM HCl. 66

Figure 3.3 A plot of the molar fractions f_{free} (◊, ◊), f_{diff} (✕, ✕), and f_{agg} (▲, ▲) determined from the MFA of the fluorescence decays as a function of $n_{\text{Py}}/(\langle L_{\text{Py}}^2 \rangle^{1/2}/l)^3$ acquired in A) DMF and B) DMSO without (black) and with (red) of 5 mM HCl. 68

Figure 3.4 Plot of $\langle k \rangle$ as a function of $n_{\text{Py}}/(\langle L_{\text{Py}}^2 \rangle^{1/2}/l)^3$ in A) DMF (◻, ◻) and B) DMSO (✕, ✕) in the absence (black) and presence (red) of 5 mM HCl..... 69

Figure 3.5 Plot of $\langle k \rangle$ as a function of $n_{\text{Py}}/(\langle L_{\text{Py}}^2 \rangle^{1/2}/l)^3$ in DMF without (◻) and with (◻) 5 mM NaOH. 71

Figure 3.6 The monomer decay of PyC8-PAMAM-G0 acquired in A) DMF, B) DMF with 5 mM HCl, and C) DMF with 5 mM HCl and 10 mM NaOH. D) Overlap of the monomer decays obtained in Figure 3.6A), B), and C)..... 72

Figure 3.7. A) Plot of $\langle k \rangle$ as a function of $n_{\text{Py}}/(\langle L_{\text{Py}}^2 \rangle^{1/2}/l)^3$ for the PyCX-PAMAM-GY samples acquired in 1st experiment: DMF (black, empty), 2nd experiment: DMF with 5 mM HCl (red, empty), 3rd experiment: DMF with 5 mM NaOH (green, empty), and 4th experiment: DMF (black, full), followed by addition of 5 mM HCl (red, full), followed by addition of 10 mM NaOH (green, full). B) Plot of the slope of the straight lines shown in Figure 3.7A..... 73

Figure 3.8. A plot of $\langle k \rangle$ as a function of $n_{\text{Py}}/(\langle L_{\text{Py}}^2 \rangle^{1/2}/l)^3$ for 1-pyrenebutyric acid-labeled 2,2,-bis(hydroxymethyl propionic) acid-based dendrimers (PyC4-HMPA-GY) acquired in A) DMF and B) DMSO in the absence (◻) and presence (◻) of 5 mM HCl..... 75

Figure 3.9. A) A plot of the $\langle k \rangle/k_{\text{diff}}$ ratio as a function of $n_{\text{Py}}/(\langle L_{\text{Py}}^2 \rangle^{1/2}/l)^3$ for decays acquired in DMF (◻) or DMSO (✕, ✕) in the absence (black) or presence (red) of 5 mM HCl. B) A plot of the average $\langle k \rangle/k_{\text{diff}}$ (●, ●) values acquired in DMF and DMSO as a function of $n_{\text{Py}}/(\langle L_{\text{Py}}^2 \rangle^{1/2}/l)^3$ acquired without (black) and with (red) of the 5 mM HCl. 77

Figure 4.1 Plot of the molar ellipticity as a function of wavelength for (solid) PLGA and (dashed) PDLGA acquired with 10 mM of (black) NaOH or (red) HCl..... 94

Figure 4.2 Region between 3.7 and 4.6 ppm of the ¹H NMR spectrum showing the signal from the α-CH proton for (black) PLGA and (purple) PDLGA acquired in A) d₇-DMF and B) d₆-DMSO. [PLGA] = 1 mg/mL and [PDLGA] = 10 mg/mL..... 96

Figure 4.3 A) SSF spectra for the PyC4N-PLGA samples in DMF. Plots of I_E/I_M as a function of pyrene content for (○) PyC8N-PLGA, (●) PyC4N-PLGA, (◐) PyC8N-PDLGA, and (◑) PyC4N-PDLGA in B) DMF and C) DMSO. Lines: Samples labeled with (solid) PyC4N and (dashed) PyC8N..... 97

Figure 4.4 A) Plot of $N_{\text{blob}}^{\text{exp}}$ as a function of pyrene content for (black) PLGA and (purple) PDLGA labeled with (◊) 1-pyrene butylamine or (○) 1-pyrene octylamine in (hollow) DMF and (filled) DMSO. B) Plot of $\langle N_{\text{blob}}^{\text{exp}} \rangle$ as a function of the *blob* diameter in (hollow) DMF and (filled) DMSO for (◻) PLGA and (▲) PDLGA. $\langle N_{\text{blob}}^{\text{exp}} \rangle$ data shown in green¹⁷ and red¹⁹ were taken from previous reports on PLGA and PDLGA labeled with 1-pyrenemethylamine^{17,19} and 1-pyrenebutylamine.¹⁹ 100

Figure 4.5 A side and top view of a PLGA chain generated in silico with an α-, 3₁₀-, and PPII-helical and a random coil conformation..... 101

Figure 4.6 Plot of the number of carbon atoms (n_C) in the frame of the reference pyrene overlapping the frame of the secondary pyrene as a function of the number (#Glu) of Glu residues separating the reference from the secondary pyrene for A) PyC4N (◊) and B) PyC8N (○) attached onto a PLGA construct adopting a (blue) PPII-, (red) 3₁₀-, and (black) α-helical conformation or (purple) a random coil conformation. The lines presented in each plot are a means

to guide the eye only. C) Schematic representation of the MMOs conducted with two pyrenyl labels showing good (top), partial (middle), and no (bottom) overlap. 104

Figure 4.7 Plot of $\langle N_{\text{blob}}^{\text{exp}} \rangle$ for (\blacktriangle) PyC1N,¹⁸ (\blacklozenge) PyC4N, and (\bullet) PyC8N labeled A) PDLGA in (hollow) DMF or (filled) DMSO and PLGA in B) DMF or C) DMSO as a function of $N_{\text{blob}}^{\text{MMO}}$ for (purple) a random coil or (blue) a PPII-, (red) 3_{10} -, and (black) α -helix. The solid line represents the 1:1 diagonal. 106

Figure 5.1 A) Fluorescence spectra acquired for the PyC1(x)-PNb-Ac samples in DMF. Plots of I_E/I_M ratio for the PyCX(x)-PNb-Ac samples, where X equals B) 1 (methyl, \bullet), C) 4 (butyl \blacklozenge), D) 8 (octyl, \blacktriangle), and E) 12 (dodecyl, \blacksquare), in DMF (non-filled) and DMSO (filled). 119

Figure 5.2 Plots of A) $N_{\text{blob}}^{\text{exp}}$ as a function of the pyrene content in (empty symbols) DMF and (filled symbol) DMSO for the PyCX(x)-PNb-Ac samples where X equals (\circ, \bullet) 1, ($\blacklozenge, \blacklozenge$) 4, ($\blacktriangle, \blacktriangle$) 8, and (\square, \blacksquare) 12 and B) $\langle N_{\text{blob}}^{\text{exp}} \rangle$ as a function of the PEF length scale (L_{PEF}). 121

Figure 5.3 PNb-Ac backbone used to conduct the molecular mechanic optimizations where the backbone is A) a random coil or B) a 6_1 helix. 124

Figure 5.4 An illustration of the construct representing a PyC1N labeled PNb-Ac random coil where A) the different reference pyrene positions are highlighted in red, B) the carbon atoms selected to apply the restraints used in the MMOs are colored in red, C) the head-to-head and head-to-tail arrangements are shown, and D) the number of atoms (shown with red circles) separating the pyrenyl dye from the α -C in the PNb-Ac backbone for a hypothetical 1-pyrenepropylamine derivative. The hydrogen atoms and carbonyl oxygen of the f groups were hidden from the chemical structures shown in Figure 5.4. 126

Figure 5.5 Plots of the carbon-carbon overlap between the reference and secondary pyrenyl labels for a 32-residue PNb-Ac random coil construct labeled with PyC8N where the reference pyrene

was attached to a residue located at position A) 1 (●), B) 2 (◆), C) 3 (▲), D) 10 (■), and E) 32 (✕). F) Plot of $\langle N_{\text{blob}}^{\text{MMO}}(\text{RC}) \rangle$ as a function of the number of atoms (n_{Sp}) separating the dye from the α -C of the PNB-Ac backbone for a random coil. The red squares represent the extrapolated $\langle N_{\text{blob}}^{\text{MMO}}(\text{RC}) \rangle$ value for PyC8N and PyC12N. 128

Figure 5.6 Plots of $n_{\text{C-C}}$ for a 66-residue PNB-Ac helix labeled with PyC1N where the reference pyrene group was placed on the A) 9th (●), B) 10th (◆), C) 11th (▲), and D) 12th (■) SU. E) Plot of $N_{\text{blob}}^{\text{MMO}}(\text{H})$ as a function of the position of the reference pyrenyl group. The lines provided are only a means to guide the eye. The red symbols in plots B) and D) represent positions where the frames of the pyrenyl dyes were not planar, and thus were not used in the calculation of $N_{\text{blob}}^{\text{MMO}}(\text{H})$ 130

Figure 5.7 Plot of $n_{\text{C-C}}$ for a 132-residue PNB-Ac helical construct labeled with PyC1N attached onto the 69th (A & B) and 70th (C & D) residues with the reach of the reference pyrenyl label being probed on the left (▲) and right (■). The lines provided are only a means to guide the eye. . 131

Figure 5.8 Plots of $n_{\text{C-C}}$ for a 132-residue PNB-Ac helix labeled with A) PyC4N, B) PyC8N, and C) PyC12N. The reference residue used was position 70 and $n_{\text{C-C}}$ was counted from left-to-right (✕) and right-to-left (■). D) Plot of $N_{\text{blob}}^{\text{MMO}}(\text{H})$ as a function of the number (n_{Sp}) of atoms separating the dye from the α -C of the PNB-Ac backbone. 132

Figure 5.9 A) Plot of $\langle N_{\text{blob}}^{\text{exp}} \rangle$ as a function of (black square) $N_{\text{blob}}^{\text{MMO}}(\text{H})$ and (hollow square) $\langle N_{\text{blob}}^{\text{MMO}}(\text{RC}) \rangle$. B) Plot of f_{RC} and f_{H} as a function of L_{PEF} 134

List of Tables

Table 2.1 Expected molecular weight, m/z ratio, and number of pyrenes of the PyCX-PAMAM-GY dendrimers.....	34
Table 2.2 Chemical structure of the PyCX-PAMAM-GY samples.....	36
Table 2.3 Distances separating Py1* from groups with given numbers of ground-state pyrenyl labels for the PyC4-PAMAM-G1 sample.....	41
Table 3.1. Chemical structure for each PyCX-PAMAM-GY construct where $X = 4, 8,$ and 12 for 1-pyrene-butyryl, -octanoyl, and -dodecanoyl labels, respectively.	62
Table 5.1 Chemical structure of the PyCX(x)N-PNb-Ac samples.....	116

List of Abbreviations

3D	3-dimensional
CD	circular dichroism
CoM	center of mass of the pyrene moiety
DCM	dichloromethane
DIC	<i>N, N'</i> -diisopropylcarbodiimide
DIW	deionized water
DMAP	4-(dimethylamino)pyridine
DMF	<i>N, N</i> -dimethylformamide
DMSO	dimethyl sulfoxide
DP	degree of polymerization
Et-PyDA	<i>n</i> -ethyl-1-pyrenedodecanamide
Et-PyOA	<i>n</i> -ethyl-1-pyreneoctanamide
FBM	fluorescence <i>blob</i> model
FCQ	fluorescence collisional quenching
FRET	fluorescence resonance energy transfer
FTIR	Fourier transform infrared
Glu	glutamic acid
HMPA	2,2-bis(hydroxymethyl)propionic acid
Hx-PyBA	<i>n</i> -hexyl-1-pyrenebutyramide
IRF	instrument response function
MDS	molecular dynamic simulations
MFA	model free analysis
MMOs	molecular mechanic optimizations
Nb	norbornene
NMR	nuclear magnetic resonance
PAMAM	polyamidoamine
PBDLG	poly(γ -benzyl- <i>D, L</i> -glutamate)
PDLGA	poly(<i>D, L</i> -glutamic acid)
PEF	pyrene excimer formation
PGA	poly(glutamic acid)
PLGA	poly(<i>L</i> -glutamic acid)
PNb-Ac	poly(norbornene acid)
PPII	polyproline type II-helix
PyC1N	1-pyrenemethylamine
PyC4-HMPA-GY	1-pyrenebutyric acid-labeled HMPA dendrimer where <i>Y</i> is the generation number of the dendrimer
PyC4N	1-pyrenebutylamine
PyC4N-Ac	1-pyrenebutylacetamide
PyC8N	1-pyreneoctylamine
PyC8N-Ac	1-pyreneoctylacetamide
PyC12N	1-pyrenedodecylacetamide

PyCX(x)N-PDLGA	pyrene-labeled PDLGA where X and x are equal to the number of carbon atoms in the linker of the pyrene derivative and the molar percentage of pyrene-labeled glutamic acid, respectively.
PyCX(x)N-PGA	pyrene-labeled PGA where X and x are equal to the number of carbon atoms in the linker of the pyrene derivative and the molar percentage of pyrene-labeled glutamic acid, respectively.
PyCX(x)N-PLGA	pyrene-labeled PLGA where X and x are equal to the number of carbon atoms in the linker of the pyrene derivative and the molar percentage of pyrene-labeled glutamic acid, respectively.
PyCX(x)N-PNb-Ac	pyrene-labeled PNb-Ac where X and x are equal to the number of carbon atoms in the linker of the pyrene derivative and the molar percentage of residues labeled with pyrene, respectively.
PyCX-PAMAM-GY	pyrene-labeled PAMAM dendrimers where X and Y are equal to the number of carbon atoms in the linker of the pyrene derivative and the dendrimer generation number, respectively.
PyLM	pyrene-labeled macromolecule
Py-PDLGNa	pyrene-labeled poly(sodium <i>D,L</i> -glutamate)
Py-PLGNa	pyrene-labeled poly(sodium <i>L</i> -glutamate)
RB	round bottom
ROA	Raman optical activity
RT	room temperature
SANS	small angle neutron scattering
SAXS	small angle X-ray scattering
SLS	static light scattering
SSF	steady-state fluorescence
TFA	trifluoroacetic acid
TRF	time-resolved fluorescence
WAXS	wide angle X-ray scattering
WF	Wilemski and Fixman

List of Symbols

α -C	alpha carbon on the polymer backbone
ϵ_{Py}	molar absorption coefficient of a pyrene derivative
η	solvent viscosity
λ_{DS}	mass ratio of solids in the dialysate
λ_{Py}	moles of pyrene per gram of polymer
ρ_{loc}	local density of a macromolecule
τ_D	lifetime of an improperly stacked pyrene excimer
$\tau_{D\text{-FRET}}$	lifetime of a donor dye in a FRET experiment
τ_{E0}	lifetime of a properly stacked pyrene excimer
τ_{ES}	lifetime of a short-lived pyrene dimer
τ_{M}	lifetime of the pyrene monomer
b	absorption cell pathlength
D^*	improperly stacked pyrene excimer
$d_{\text{Py-aC}}$	distance separating the center of mass of the pyrene moiety from the α -carbon of the structural unit the pyrenyl derivative is attached to
E_{ET}	FRET efficiency
$E0^*$	excimer generated by two properly stacked pyrenyl labels
ES^*	short-lived pyrene dimer
f_{agg}	molar fraction of pyrene dyes that form pyrene excimer by direct excitation of pyrene aggregates
f_{diff}	molar fraction of pyrene dyes that form pyrene excimer by diffusion
f_{free}	molar fraction of pyrene dyes that do not form excimer and emit as if they were free in solution
f_{H}	fraction of helical segments along the polynorbornene backbone
f_{k_2}	molar fraction of pyrene dyes that form pyrene excimer via a rapid rearrangement with a rate constant k_2
f_{Py}	molar fraction of structural units labeled with pyrene
f_{RC}	fraction of randomly coiled segments along the polynorbornene backbone
I_{E}	fluorescence intensity of the pyrene excimer
$(I_{\text{E}}/I_{\text{M}})^{\text{SSF}}$	ratio of excimer over monomer fluorescence intensity determined from steady-state fluorescence measurements
$(I_{\text{E}}/I_{\text{M}})^{\text{TRF}}$	ratio of excimer over monomer fluorescence intensity determined from time-resolved fluorescence decay measurements
$(I_{\text{E}}/I_{\text{M}})^{\text{TRF}}(f_{\text{free}}=0)$	ratio of excimer over monomer fluorescence intensity determined from time-resolved fluorescence decay measurements where the molar fraction of free pyrene is set to equal 0.
I_{M}	fluorescence intensity of the pyrene monomer
$\langle k \rangle$	average rate constant of pyrene excimer formation
k_2	rate constant for pyrene excimer produced via a rapid rearrangement of two nearby pyrenyl labels
k_{blob}	rate constant for the diffusive encounter between two structural units bearing an excited and a ground-state pyrenyl labels located inside a same <i>blob</i>

k_{diff}	bimolecular rate constant of pyrene excimer formation by diffusive encounters between an excited and a ground-state pyrenyl label
k_{ET}	rate constant for energy transfer
l	bond length normalization constant
L_{PEF}	maximum length scale over which PEF can occur
L_{Py}	square root of the average squared end-to-end distance
m_{DS}	mass of solids in the dialysate
M_{GNa}	molar mass of sodium glutamate
M_{NbA}	molar mass of the unlabeled norbornene unit
$M_{\text{PyCXN-NbA}}$	molar mass of the pyrene-labeled norbornene unit
$M_{\text{Py-Glu}}$	molar mass of a pyrene-labeled glutamate residue
$m_{\text{Py-PLGNa}}$	mass of Py-PLGNa solids
$m_{\text{Py-PLGNa/DS}}$	mass of solids constituted of Py-PLGNa and excess sodium hydroxide
$\langle n \rangle$	average number of ground state pyrenyl labels inside a <i>blob</i>
$\langle N_{\text{blob}}^{\text{exp}} \rangle$	average number of norbornene units per <i>blob</i>
$N_{\text{blob}}^{\text{MMO}}$	number of norbornene units per <i>blob</i> enabling PEF between two pyrenyl labels determined by molecular mechanics optimization for a given macromolecular conformation
$N_{\text{blob}}^{\text{MMO}}(\text{H})$	$N_{\text{blob}}^{\text{MMO}}$ for a helical conformation
$N_{\text{blob}}^{\text{MMO}}(\text{RC})$	$N_{\text{blob}}^{\text{MMO}}$ for a random coil conformation
N_0	number of structural units enabling PEF between a secondary and reference pyrenyl label located on one side of the reference structural unit
N_0^{L}	number of structural units labeled with a secondary pyrene located to the left of the reference structural unit labeled with the primary pyrene and enabling PEF between the primary and secondary pyrenes
N_0^{R}	number of structural units labeled with a secondary pyrene located to the right of the reference structural unit labeled with the primary pyrene and enabling PEF between the primary and secondary pyrenes
$n_{\text{C-C}}$	number of carbons of one pyrenyl label overlapping the frame of a second pyrenyl label
n_{Py}	number of ground state pyrene dyes in a pyrene-labeled dendrimer
n_{Sp}	number of atoms in the spacer linking the pyrenyl moiety to the α -carbon in the PNb-Ac backbone
p	probability of forming an excimer upon encounter between an excited and ground-state pyrene dye.
Py_{agg}^*	pyrene dyes that form excimer via direct excitation of pre-aggregated pyrene
Py_{diff}^*	pyrene dyes that diffuse through the solution to form excimer
Py_{free}^*	pyrene dyes that do not form excimer and emit as if they were free in solution
Py_{k2}^*	pyrene dyes that form pyrene excimer via a rapid rearrangement between two nearby pyrenyl units
r	distance separating a donor and acceptor dye
r_{EE}	average end-to-end distance
R_{G}	radius of gyration
$R_{\text{G}}(N)$	radius of gyration where N is the generation of the dendrimer
R_0	Förster radius

T_g
 $V_{\text{dendrimer}}$

glass transition temperature
volume of a dendrimer

Chapter 1: Introduction

1.0 Introduction

The conformation of isolated synthetic and biological macromolecules in solution has a major impact on their properties, directly influencing their respective applications. Gels made of synthetic polymers with a bottlebrush architecture constitute a case in point. The persistence length (l_p) of a polymer bottlebrush (PBB), used to describe chain flexibility, depends on the length of the linear side chains of the PBB,¹ with longer side chains resulting in larger l_p . Since PBB with larger l_p do not coil as easily, they generate gels with a lower entanglement density and a lower elastic modulus than PBB with shorter side chains and smaller l_p .¹ In the context of biological macromolecules, conformation is an important part of their catalytic activity, which can play a positive or detrimental role for an organism. For instance, in prion-based diseases, sporadic misfolding of proteins induces a conformational change facilitating prion-protein interactions, ultimately leading to the propagation of misfolding in other proteins and resulting in a wide array of different neurodegenerative disorders.² Given the importance of conformation in both synthetic and biological macromolecules, considerable research effort has been dedicated to the characterization of macromolecular conformations and their changes induced by different chemical or physical triggers.¹⁻³⁴ The wide variety of experimental tools available for macromolecular characterization can be broadly divided into four main categories, namely microscopy,²⁷⁻³⁰ scattering,⁴⁻¹⁶ computation,⁶⁻²⁶ and spectroscopy experiments.¹⁹⁻³⁵ The subsequent sections focus on the type of information extracted from each type of experiment and how it can be applied to characterize the conformation of macromolecules.

1.1 Techniques Applied to Characterize Macromolecules

1.1.1 Microscopy-Based Techniques

While microscopy-based experiments have traditionally been employed to study the morphology of macromolecules rather than their conformation,^{36–38} advancements in instrumentation have increased their use for gaining conformational insight about macromolecules.^{27–43} The primary strength of all microscopy-based experiments lies in their ability to directly image the samples being studied. Although various types of microscopy-based experiments exist, the two most commonly encountered ones for studying the conformation of macromolecules are atomic force microscopy (AFM) and transmission electron microscopy (TEM). As such, a discussion and applications of these two types of microscopy are presented to illustrate how images are generated and the type of information extracted from these experiments.

AFM employs a cantilever fitted with a tip that has a ~10 nm apex radius to scan the topographical features of a sample surface.^{39,40} Depending on the type of instrumentation, desired information, and sample properties and preparation, the probe can be scanned in the x,y,z-plane across the sample.⁴⁴ While various modes, such as contact, tapping, non-contact, etc, can be applied to study macromolecules by AFM, the contact and tapping modes are the most commonly encountered.⁴⁴ In the contact mode, the tip of the cantilever maintains constant contact with the sample surface. Such studies require that the material be ‘hard’ to resist the lateral forces induced by the tip as it travels across the surface. In contrast, the tapping mode is typically employed for ‘soft’ materials. An AFM cantilever operated in the tapping mode probes interactions between the probe tip and the sample surface as the surface of the sample is scanned. By operating the AFM with different modes, images can be generated to visualize isolated macromolecules, chain movements, crystallization behaviour, stereocomplexes, chain packing, etc.⁴⁰ An illustrative

example demonstrating the resolving power of AFM has been presented in a recent study by Kuchuk et al., where AFM was utilized to observe the conformation of an isolated DNA macromolecule under near-physiological conditions.²⁹ Their study provides nanometer-level spatial details enabling the observation of the major and minor grooves within a single DNA double helix. Such information is not only useful to better understand the conformation of macromolecules, but can also be used as a form of integrative macromolecular science to guide simulations.^{28,42,43}

In contrast to AFM, TEM images are generated by transmitting a coherent beam of electrons through a thin sample (< 200 nm thick).⁴¹ As the electron beam passes through electron-rich and -poor domains, variation in electron density in the sample are used to generate an image of the macromolecules.³⁰ Analysis of the images, in turn, provides rich information about the structure and morphology of the macromolecules. Although TEM images are effectively produced from electron density differences in the sample, application of TEM to soft materials, such as amorphous polymers, is rather limited.⁴⁵ However, recent improvements in TEM instrumentation such as the cameras, fluorescence screens, preparation protocols are poised to make TEM a powerful experimental technique to gain conformational insight about macromolecules.^{30,45} As highlighted in a recent review by Zorzi et al., cryogenic TEM, which is an offshoot of TEM, can be used to probe the conformational dynamics of numerous receptors.³⁰ By using powerful computer algorithms, snapshots of different conformational states can be identified, albeit with some limitation.³⁰ An illustration of how AFM and TEM images are generated is provided in Figures 1.1A-B.

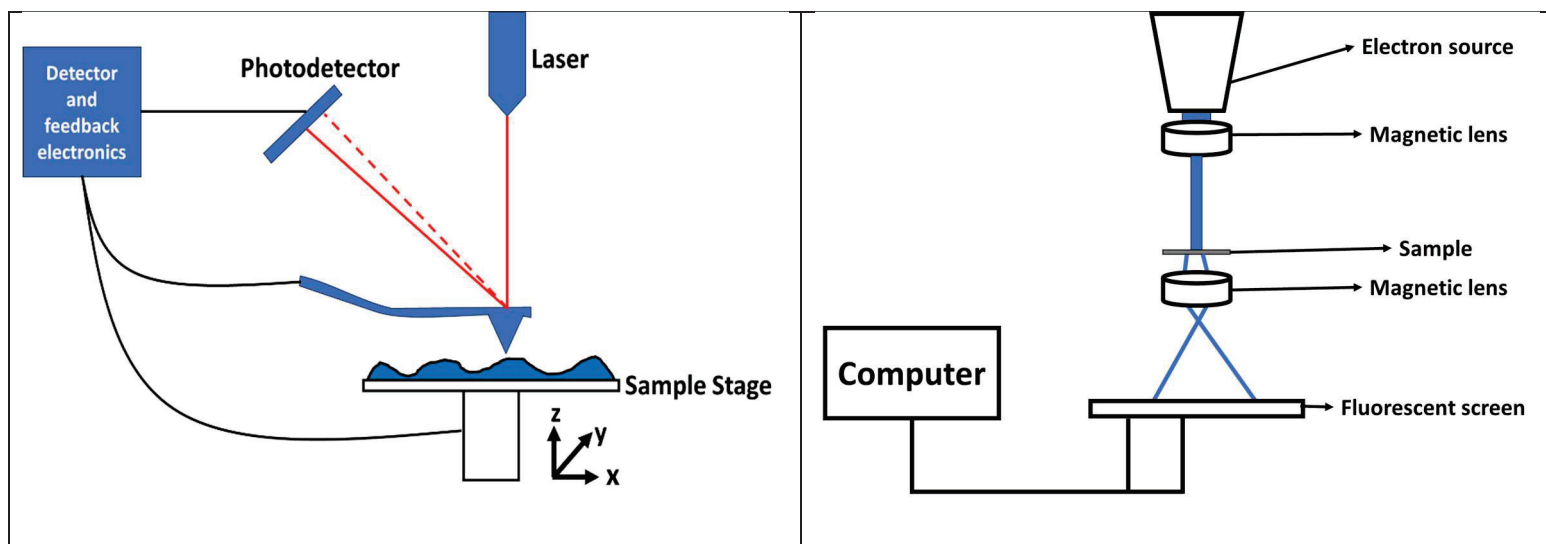


Figure 0.1 Illustration of how A) AFM and B) TEM images are acquired.

1.1.1 Computational Techniques

In contrast to microscopy experiments that provide 2D representations of macromolecules adsorbed on a substrate surface, computation-based simulations offer a means to generate detailed 3D images of isolated macromolecules by considering the primary interactions within a specified system.^{9,46–49} This methodology provides the experimentalist with unprecedented control over the type of information retrieved. Depending on the specific information sought, simulations are conducted on different time and length scales broadly categorized into quantum (10^{-10} minutes), atomistic (10^{-9} minutes), mesoscopic (10^{-6} minutes), and macroscopic (10^{-3} minutes) scales.⁴⁹ Although each time scale provides useful information, insight about conformation is obtained from the atomistic time scales. Monte-Carlo (MC) and molecular dynamics (MD) simulations are the most common computation methods used to probe polymer conformations.^{46–49} MC simulations generate an ensemble average of representative configurations through stochastic displacement of atoms which can be accepted or rejected via comparison against some criteria.^{46–49} In many cases, the total energy potential of the system is used to determine if a proposed displacement should be rejected or accepted. Each move is associated with a distribution of probabilities of accepting or

rejecting the move according to the Boltzmann factor. However, since the simulation is skewed towards lower energy states, the system reaches equilibrium eventually.^{48,49} On the other hand, MD simulations employ Newton's equations of motion to calculate trajectories over time, facilitating the monitoring of the conformation as a function of time, under a given condition.^{46,47,49,50} The schematic representation in Figures 1.2A and B illustrates the fundamental distinction between MC and MD simulations. Although the advantages and disadvantages of each simulation type, as well as more specialized approaches, have been discussed elsewhere,^{46-48,50} it is pertinent to the present thesis to emphasize that computation-based approaches provide atomic coordinates within the macromolecules. In turn, these coordinates enable the generation of a 3D representation of the macromolecular conformation, which can be benchmarked against experimental data such as the radius of gyration (R_G) determined from scattering experiments.

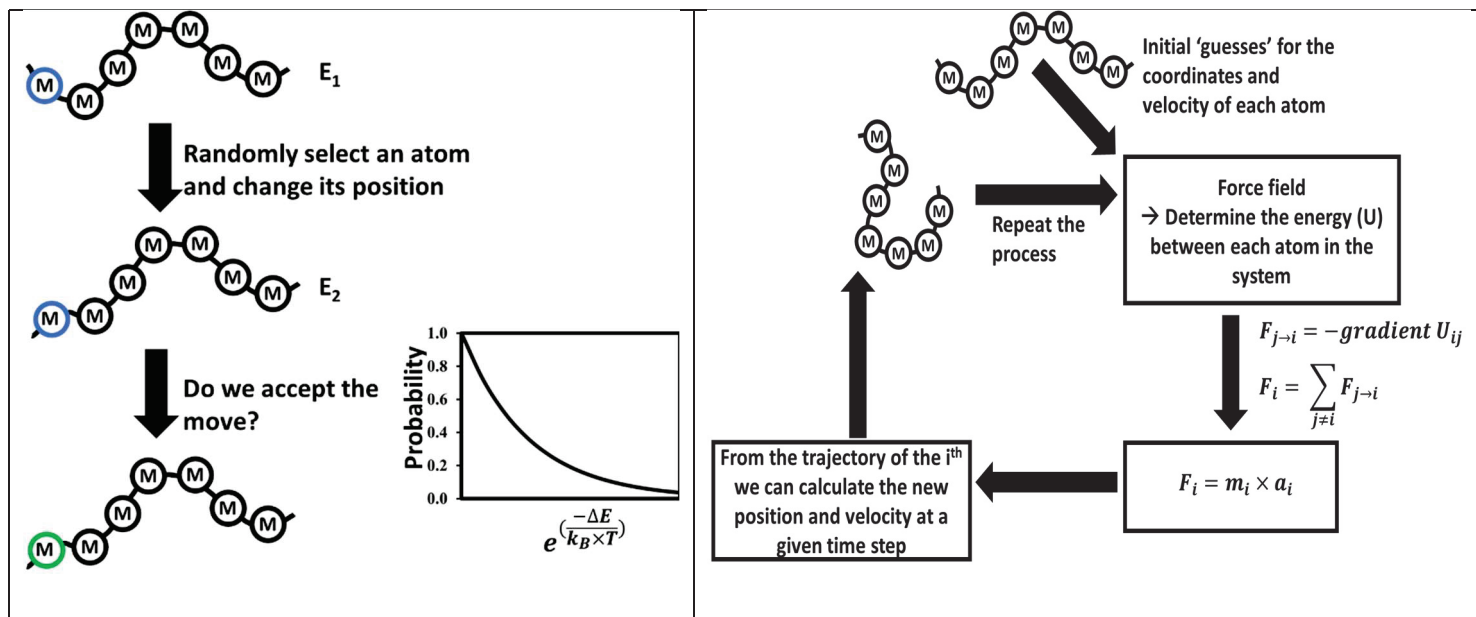


Figure 0.2 Schematic illustration of A) MC and B) MD simulations. The above figure only represents one iteration of the several thousands typically conducted in a simulation.

1.1.2 Scattering-Based Experiments

Scattering techniques, such as static light (SLS), small angle X-ray (SAXS), wide angle X-ray (WAXS), and small angle neutron (SANS) scattering have played a pivotal role in macromolecular science, specifically in probing macromolecular conformations in solution.^{5,6,8,9,16} Among the different scattering techniques, SAXS and WAXS stand out as the predominant tools employed to characterize macromolecular conformations. The underlying principle of any elastic scattering technique like SAXS and WAXS relies on their ability to probe the mass distribution of macromolecules with respect to their center of mass.⁵¹⁻⁵³ The illustration provided in Figure 1.3 describes the different steps taken during the acquisition of scattering data for a SAXS and WAXS experiment. In brief, the sample is irradiated with X-rays and the resulting scattered X-rays are recorded at various angles relative to the incident source, producing a 2D scattering profile.⁵² While this 2D scattering profile yields insights into the macromolecular shape, it is conventionally converted into a 1D scattering profile through the integration along the azimuthal plane at a defined distance from the incident beam.⁵³ This transformation yields a 1D scattering profile of the scattering intensity, $I(q)$, as a function of the scattering vector, q , which depends on the angle (θ) between the line linking the sample to the detector and the incident beam, as expressed in Equation 1.1.⁵² The limits of the scattering profile are defined by q_{\min} and q_{\max} which depend on the collimation system and fading of the scattering signal, respectively.⁵² The $I(q)$ scattering profile, after correcting for background scattering effects, consists of three components provided in Equation 1.2. K is a combination of constants that include particle contrast, volume, concentration, etc, while $P(q)$ and $S(q)$ are the form and structure factor, respectively.⁵² $P(q)$ contains information about the shape and internal density distribution, in the form of the radius of gyration (R_G), while $S(q)$ reflects particle-particle interactions such as inter-particle distances and degree of order.⁵² In

many cases, $S(q)$ is approximated as 1, i.e no interparticle effects, and the analysis of $P(q)$ yields information about the particle size through R_G and particle shape through subsequent data transformations from distinct regions in the $I(q)$ profile such as the Guinier and Fourier regions.⁵¹ The information retrieved through the analysis of the $I(q)$ scattering profile is particularly important for the characterization of macromolecular conformation.

$$q = \frac{4\pi \sin(\theta)}{\lambda} \quad (1.1)$$

$$I(q) = K \cdot P(q) \cdot S(q) \quad (1.2)$$

In the Guinier region of the scattering profile, corresponding to q vectors smaller than $1.3/R_G$, a plot of $\ln(I(q))$ as a function of q^2 yields a straight line, whose slope equals $-R_G^2/3$.⁵⁴ The significance of R_G lies in the fact that it reflects the mass distribution within the macromolecule with respect to its center of mass, and thus provides insight about particle size and conformation.^{51,52,53} In the Fourier region of the scattering profile, a pair distribution function, i.e. the distribution of distances between all electron pairs, can be calculated. In most cases, this is extracted by an indirect Fourier-transformation, where the pair distribution function expected for a given macromolecular conformation is calculated to simulate a scattering profile, which is then compared to the experimental scattering profile.^{54,55} A match between the simulated and experimental scattering profiles is taken as evidence that the macromolecular conformation assumed to simulate the scattering profile is representative of the macromolecule.

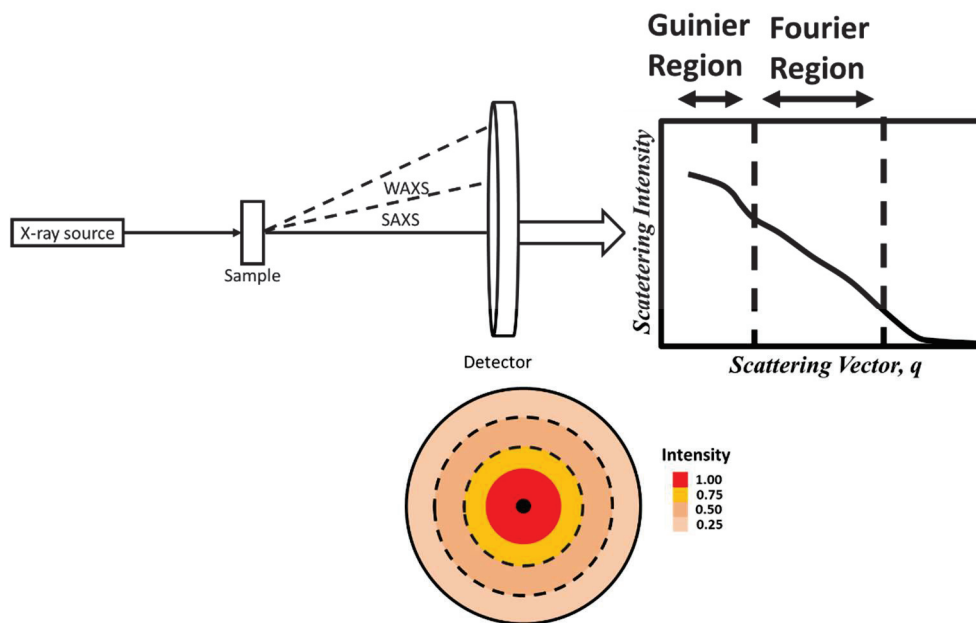


Figure 0.3 Illustration of the experimental set up for small (SAXS) and wide (WAXS) angle X-ray scattering.

1.1.3 Spectroscopy-Based Experiments

Various spectroscopy-based techniques such as nuclear magnetic resonance (NMR), circular dichroism (CD), and fluorescence can be used to probe macromolecular conformation. The primary advantage of these techniques resides in their ability to detect minute differences in the local environment of atoms, functional groups, and chromophores constituting macromolecules. However, the type of information obtained depends strongly on the specific technique applied.

For instance, NMR experiments can provide dihedral angles and inter-residue distances within a macromolecule. Dihedral angle information is retrieved through three-bond mediated vicinal coupling using the Karplus relationship.⁵⁶ Distance restraints, on the other hand, are retrieved from 2D NMR experiments based on the nuclear Overhauser effect (NOE), rotated frame NOE (ROESY), heteronuclear single-quantum coherence (HSQC), total correlation spectroscopy (TOCSY), and heteronuclear multiple-bond coherence (HMBC).⁵⁷ In turn, knowledge of the

dihedral angle and distance restraints between nuclei can be used in a form of integrative macromolecular science to generate a 3D conformation.

In contrast, CD-based experiments measure differences between the absorption of the left and right polarized light as it passes through the solution of a macromolecule to generate a spectrum whose features depend on the macromolecular conformation. For example, the CD spectrum of an α -helix displays two peak minima at ~ 222 and ~ 208 nm and a peak maximum at ~ 190 nm, whereas the CD spectrum of a random coil shows only one peak minimum at ~ 200 nm.¹⁸ For more complex macromolecules, the observed spectral features are averaged over all conformations adopted by the macromolecules in solution. In such cases, computer algorithms are employed to simulate a CD spectrum by assuming a specific macromolecular conformation, which can then be compared with the experimental CD spectrum.⁵⁸

Fluorescence studies are primarily based on Förster resonance energy transfer (FRET) experiments.⁵⁹ FRET experiments take advantage of the dependency of the FRET efficiency (E_{ET}) between a donor and acceptor dye on the distance (r) separating them as shown in Equation 1.3. In Equation 1.3, R_o is the Förster radius, which takes values between 1 and 10 nm depending on the donor-acceptor pair, which also represents the length scale being probed in FRET studies.^{59,60} The expression for the FRET rate constant (k_{ET}) is given in Equation 1.4, where τ_{D-FRET} is the donor lifetime. The distance dependency shown in Equations 1.3 and 1.4 for respectively, E_{ET} and k_{ET} explains why FRET was coined a spectroscopic ruler⁶¹ and rationalizes why FRET studies have been applied to probe the dynamics and conformations of macromolecules in solution.⁶²

$$E_{ET} = \frac{R_o^6}{r^6 + R_o^6} \quad (1.3)$$

$$k_{ET} = \frac{1}{\tau_{D-FRET}} \times \left(\frac{R_o}{r} \right)^6 \quad (1.4)$$

1.1.4 Current Limitations in the Characterization of Macromolecular Conformations

Despite the wealth of knowledge regarding macromolecular conformation retrieved from the different experimental tools discussed above, these tools are not without limitations. In many microscopy-based approaches, the macromolecule must be adsorbed onto a surface, which poses an obvious limitation, namely that the conformation of adsorbed macromolecules observed in 2D images may not accurately reflect the 3D conformation of the macromolecule in solution. Although recent advances in microscopy experiments aim to generate 3D images of macromolecules in solution,³⁰ such techniques are often selected for specific cases involving sample preparations that may not be universally applicable to all macromolecules.^{27,29} Similarly, simulations face one major limitation, namely that approximations are necessary for the sake of computational efficiency and expense associated with the precise determination of the position of each atom within a single macromolecule. This, in turn, requires prior knowledge of all important interactions within a complex system and the establishment of a set of mathematical equations describing these interactions, and the validity of these approximations must be experimentally confirmed.⁴⁶⁻⁵⁰ For scattering experiments, where scattering is the workhorse technique for the characterization of macromolecular conformations, two main challenges must be addressed. First, high concentrations, in the 0.1-20 g/L range,^{63,64} are required to yield sufficient scattering signal. Unfortunately, this requirement can lead to solubility issues resulting in aggregation and data analysis complications due to inter-macromolecular interactions, such as those induced by long-range electrostatic forces. Second, monodisperse macromolecules are preferred as broad molecular weight distributions complicate the analysis of the scattering signal that depends strongly on

macromolecular size.⁵¹ For spectroscopy-based experiments the major difficulty lies in the unambiguous assignment of peak shifts or spectral changes associated with a specific conformation.

The limitations described above for the existing experimental tools used to probe macromolecular conformations justify the search for alternative analytical methods that would overcome these complications. Ideally, such methods would be expected to provide unambiguous assignments between different conformations, require low sample concentrations, and be applicable to both mono- and polydisperse samples. A promising candidate for fulfilling these criteria is fluorescence collisional quenching (FCQ) between dyes and quenchers covalently attached onto a macromolecule, where the FCQ rate constant could be employed to gain conformational information about complex macromolecules in solution as a form of integrative macromolecular science.^{92,93} How FCQ could be applied in this context is described in the following discussion.

1.2 Fluorescence

Fluorescence is the phenomenon by which an excited molecule in its singlet state relaxes to its ground-state by emitting a photon.⁶⁵ This process is illustrated by the Jablonski diagram provided in Figure 1.5. Fluorescence begins with the absorption of a photon with an energy hc/λ_{ex} , where h , c , and λ_{ex} are Planck's constant, the speed of light, and the excitation wavelength, respectively. Absorption of a photon results in the rapid excitation of the fluorophore from the lowest electronic state ($S_{0,0}$) to one of the vibrational levels of a higher electronic state within a few femtoseconds. The excited fluorophore undergoes a process known as internal conversion, which is where the excited molecule relaxes to the lowest vibration level in the S_1 electronic state ($S_{1,0}$). This process

typically takes a few picoseconds. The excited molecule relaxes then from the $S_{1,0}$ level to one of the vibrational levels in the S_0 electronic state via the emission of a photon.⁶⁵ The time scale for this process varies significantly depending on the fluorescent dye chosen. For the dye pyrene used in the present thesis, the lifetime can be as high as 400 ns in degassed cyclohexane.⁶⁶

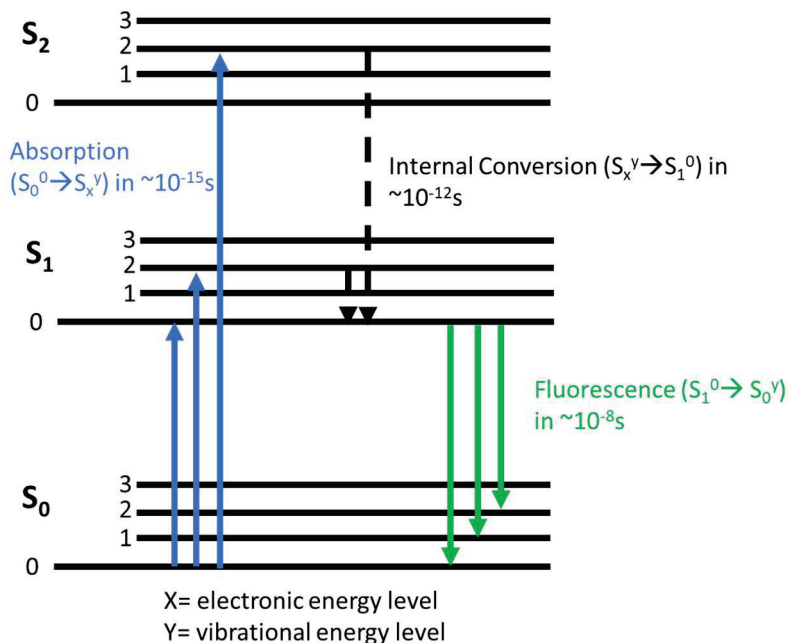


Figure 0.4 Jablonski diagram

1.2.2 Fluorescence Collisional Quenching (FCQ)

Fluorescence collisional quenching (FCQ) refers to the process whereby the fluorescence of a fluorophore is quenched upon encounter with a quencher. When the dye and quencher are covalently bound to a large macromolecule, FCQ occurs over a short length scale since the dye and quencher must touch within the time the dye remains excited. The quenching rate constant (k_q) is equal to the product $k_{diff} \times [Q]_{loc}$, where k_{diff} is the bimolecular rate constant for diffusive encounters between the excited dye and the quencher and $[Q]_{loc}$ is the local quencher concentration. A theoretical study published in 1974 by Wilemski and Fixman (WF) demonstrated

that the collisional encounters between one dye and one quencher attached to the opposite ends of a monodisperse, linear chain are well described by a single rate constant of cyclization (k_{cy}). In turn, the excited dye of such end-labeled monodisperse constructs would yield a monoexponential decay from which k_{cy} could be easily retrieved.^{67,68} Since a flexible chain would yield a larger k_{cy} than a stiffer chain, k_{cy} was determined for many polymer chains to characterize the internal dynamics of fluorescently end-labeled linear monodisperse polymer chains.⁶⁹⁻⁷³ This intense focus on the characterization of polymer chain dynamics resulted in the oversight that k_{cy} was also equal to the product $k_{diff} \times [Q]_{loc}$, and thus contained information about the local density of the macromolecule. Since the local density of a macromolecule is directly related to its conformation, these FCQ experiments could provide information about macromolecular conformations in a manner that could complement scattering studies. Unfortunately, coupled with this oversight, another hurdle affecting the general application of FCQ experiments to study macromolecular conformations stemmed from the realization that if a dye and quencher separated by one chain length yielded one FCQ rate constant and a monoexponential decay, macromolecules labeled with more than one dye and one quencher would yield several FCQ rate constants and the associated fluorescence decay would be multiexponential. The well-known challenges revolving around the quantitative analysis of multiexponential decays with sums of exponentials^{88,89} combined with the underreckoning, that the FCQ rate constant is directly proportional to $[Q]_{loc}$, rationalize why to date, so few studies have utilized FCQ to study macromolecular conformation in solution. In the present thesis, pyrene excimer formation (PEF), a classic example of FCQ, was applied to demonstrate that quantitative information about macromolecular conformations can be retrieved from the analysis of multiexponential decays obtained with macromolecules bearing more than two pyrenyl labels.

1.2.3 Pyrene

Although many dyes are available commercially to probe macromolecules by fluorescence, pyrene offers several advantages. First, self quenching of an excited pyrene monomer by a ground state pyrene to form a pyrene excimer is a classic example of FCQ, whose photochemistry is well-known and understood.^{69,74-79} Second, the high molar absorption coefficient and high fluorescence quantum yield of pyrene⁸⁰ enables the study of pyrene-labeled macromolecules (PyLM) at polymer concentrations that can be as low as ~1 mg/L, a concentration which is considerably lower than those used for scattering studies. Since such low concentrations ensure that no diffusive intermacromolecular encounters occur while a pyrenyl label remains excited, PyLM can be probed as isolated macromolecules in solution. Third, and perhaps most importantly, the 0-0 transition of pyrene is strongly reduced,⁸¹⁻⁸⁴ which means that no energy hopping takes place during PEF and that the excitation remains localized on a single pyrenyl label until the energy is released via emission of a photon or quenching by a ground state pyrenyl dye to produce the excimer. Fourth, the long lifetime of pyrene, typically on the order of ~200 ns for the many pyrene derivatives used to label macromolecules, provides the experimentalist with a large temporal window enabling the study of slow dynamic processes encountered in large macromolecules. Finally, the Duhamel group has introduced two models for the quantitative analysis of multiexponential fluorescence decays acquired with macromolecules bearing more than two pyrenyl labels. These models are the fluorescence *blob* model (FBM) and the model free analysis (MFA), whose application depends on the type of information desired. Although these models have been described in detail elsewhere,^{76,85-90} a brief discussion of each model is provided hereafter.

1.2.4 Fluorescence *Blob* Model (FBM)

The fluorescence *blob* model (FBM) was introduced in 1999⁸⁵ to circumvent the experimental deadlock that resulted from the 1974 WF study^{67,68} and prevented the quantitative analysis of multiexponential decays. The FBM acknowledges that when pyrene is covalently attached onto a large macromolecule, the pyrenyl dyes cannot probe the full macromolecular volume; rather they can only probe equally sized sub-volumes, denoted as *blobs*, while the pyrene dye remains excited. The *blobs* can be used to compartmentalize the macromolecular volume into a cluster of *blobs* among which the pyrenyl dyes distribute themselves according to a Poisson distribution. Conceptually, an ensemble of pyrene dyes randomly distributed amongst *blobs* is the same as for pyrene dyes distributed amongst surfactant micelles. As such, the robust mathematical treatment used to determine the average number of ground state pyrene dyes per micelles⁹¹ can be applied to determine the average number of ground state pyrene dyes per *blob* ($\langle n \rangle$). Combining $\langle n \rangle$ with the molar fraction of pyrene dyes per structural unit (x), determined by UV-vis measurements, and the molar fraction (f_{Mfree}) of pyrenyl dyes that do not form excimer in the monomer decay yields the number of structural units ($N_{\text{blob}}^{\text{exp}}$) within a *blob* according to Equation 1.5. Since a same pyrene derivative attached onto a macromolecule probes a similar *blob*, N_{blob} reflects the local density of the macromolecule with more or less flexible macromolecules yielding a larger or smaller $N_{\text{blob}}^{\text{exp}}$ value, respectively. As a form of integrative macromolecular science,^{92,93} the $N_{\text{blob}}^{\text{exp}}$ value can be compared with $N_{\text{blob}}^{\text{MMO}}$ obtained from molecular mechanic optimizations (MMOs) conducted on an assumed conformation of the macromolecule labeled with the same pyrene derivative. A match between $N_{\text{blob}}^{\text{exp}}$ and $N_{\text{blob}}^{\text{MMO}}$ enables the assignment of a given macromolecular conformation. Figure 1.5 illustrates the implementation of this methodology. This procedure has already been applied to study the conformation of polysaccharides⁹⁴⁻⁹⁶ and

polypeptides.^{97–101} One of the many advantages of the FBM is that it can be applied to study PyLM where the pyrene dye has been randomly attached to the macromolecule. One unfortunate consequence, however, is that the FBM cannot be applied to study macromolecules that have been labeled at specific positions, such as the chain ends of dendrimers.⁸⁶ It is in cases like these that the model free analysis (MFA) is being used as it can handle the fluorescence decays of any PyLM.⁸⁸

$$N_{blob} = \frac{\langle n \rangle}{x} \times (1 - f_{Mfree}) \quad (1.5)$$

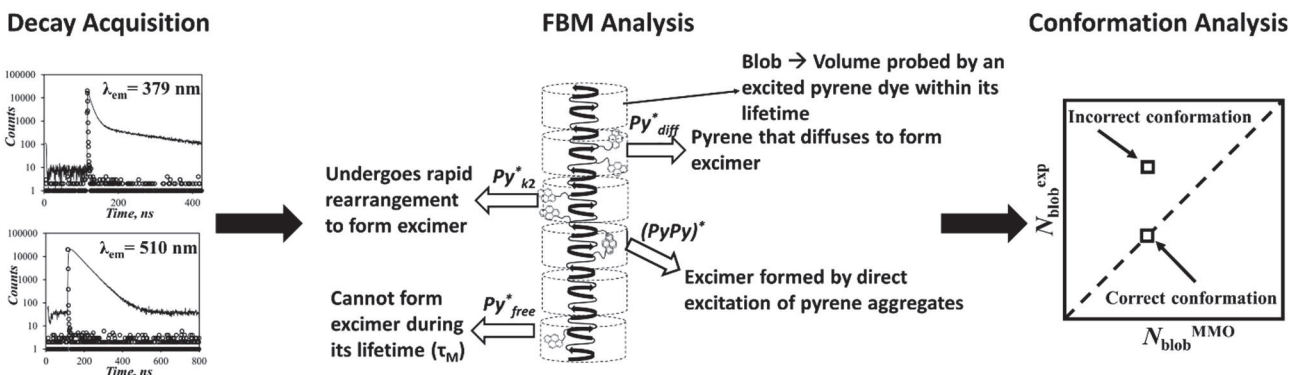


Figure 0.5 Illustration of integrative macromolecular science combining the FBM analysis of fluorescence decays with molecular mechanics optimizations for the characterization of macromolecular conformations.

1.2.5 Model Free Analysis (MFA)

In contrast to the FBM, the model free analysis (MFA) was developed to globally analyze the monomer and excimer fluorescence decays by making no assumption on how the pyrenyl labels were attached to the macromolecule.^{88,89} Its development was based off the observation that any fluorescence decay can be fitted with a sum of exponentials, whose pre-exponential factors (a_i) and decay times (τ_i) can be combined to yield a pseudo-unimolecular average rate constant of

excimer formation ($\langle k \rangle$) according to Equation 1.6. $\langle k \rangle$ equals the product of the rate constant (k_{diff}) for diffusive encounters between an excited and a ground-state pyrenyl label and the local pyrene concentration ($[Py]_{loc}$) as described in Equation 1.7. In further contrast to the FBM, the MFA does not decouple k_{diff} from $[Py]_{loc}$, which rationalizes why PEF studies almost exclusively use the MFA to gain insight about the internal dynamics of the PyLM.¹⁰²⁻¹⁰⁴

$$\langle k \rangle = \frac{\sum_{i=1}^n a_i}{\sum_{i=1}^n a_i \times \tau_i} - \frac{1}{\tau_M} \quad (1.6)$$

$$\langle k \rangle = k_{diff} \times [Py]_{loc} \quad (1.7)$$

1.2.6 Application of the Fluorescence *Blob* Model (FBM) and Model Free Analysis (MFA)

Since their introduction, the analysis of the multiexponential decays of macromolecules labeled with more than two pyrenyl dyes according to the FBM or MFA has been shown to yield quantitative information about the internal dynamics and conformation of PyLM.^{74-77,85-87,94-105} Despite the numerous reports illustrating various aspects of the application of the FBM or MFA to retrieve quantitative information about PyLM, there have been few studies which have clearly established that $\langle k \rangle$ is directly proportional to the local pyrene concentration ($[Py]_{loc}$).^{74,75} Yet, the $\langle k \rangle$ -vs.- $[Py]_{loc}$ relationship reflects the underlying principle that enables the quantitative analysis of the fluorescence decays acquired with any PyLM. As such, the focus of the present thesis is to establish this fundamental relationship and demonstrate that PEF can be applied to probe not only the internal dynamics of macromolecules but also their conformation. With these objectives in mind, the macromolecules that will be investigated in this thesis are described in more detail in the following section.

1.3 Macromolecules under Study

The overarching goal of the present thesis is to establish that PEF is well-suited to probe the conformation of macromolecules in solution. To this end, the conformation of polyamidoamine (PAMAM) dendrimers, poly(glutamic acid) (PGA), and poly(norbornene acid) (PNb-Ac) was characterized in solution by labeling these macromolecules with different pyrene derivatives and analyzing their fluorescence decays with the FBM and MFA. These three constructs were carefully selected for their interesting properties which are described hereafter.

1.3.1 Dendrimers

Dendrimers are well-defined monodisperse tree-like macromolecules, which originated from the pioneering work conducted in 1978 by Vögtle and co-workers, who initially referred to them as ‘cascade molecules’.¹⁰⁶ Between 1979 and 1983, Denkwalter et al. at the Allied Corporation filed several patents dealing with the synthesis of polypeptide-based dendrimers.^{107–109} In 1985, Newkome¹¹⁰ and Tomalia¹¹¹ independently published different synthetic routes to yield dendrimer constructs. These constructs, however, garnered limited attention until a 1990 publication by Tomalia et al.,¹¹² which proposed a large number of potential applications. The term ‘dendrimer’ itself had been coined earlier by Tomalia et al. in 1985.¹¹¹ Figure 1.6 highlights the general structure of these constructs. Their synthesis can be achieved through divergent^{106–113} or convergent^{114,115} synthesis, with the former expanding from the focal point outward and the latter progressing from the exterior inward. One common feature of dendrimers is that the number of chain ends grows exponentially while the volume of the dendrimer grows linearly with increasing generation number.^{90,112} This feature is responsible for the strong interest in dendrimers for their potential use in light harvesting^{116–118} and in applications for nanomedicines,^{119,120} gene delivery,^{121,122} catalysis,^{123,124} and multifunction sensors.^{125,126} In the context of this PhD thesis,

these features make them ideal candidates to establish that the rate constant of PEF is directly proportional to the local concentration of pyrene ($[Py]_{loc}$) since their chemical structure is so well-defined. In fact, earlier studies^{74,75,127} aimed to demonstrate the $\langle k \rangle$ -vs.- $[Py]_{loc}$ relationship with 2,2-bis(hydroxymethyl) propionic acid based dendrimers end-labeled with 1-pyrenebutyric acid (PyC4-HMPA-GY). While successful in establishing this relationship, these earlier studies were unable to benchmark the methodology used to parameterize $[Py]_{loc}$ as the actual macromolecular volume of the HMPA dendrimers remains unknown. In contrast to this earlier work,^{74,75,127} the present thesis employed PAMAM dendrimers. The reason for this was 3-fold. First, unlike the HMPA dendrimers, a large body of research has been conducted on PAMAM dendrimers, typically through a combination of scattering and computation based experiments.^{7-15,31-34} This, in turn, provides a means to benchmark the methodology developed to parameterize the chemical structure of the dendrimers and estimate their dimension used in the calculation of $[Py]_{loc}$ against other experimental parameters such as R_G determined by scattering techniques. Second, unlike HMPA dendrimers, PAMAM dendrimers have both primary and tertiary amines that should induce a conformational change upon protonation at low pH.^{8-11,13,15,31-34} Despite the many studies aiming to characterize this pH-induced conformational change in PAMAM dendrimers, some have concluded that R_G is not a suitable parameter for this purpose.⁹ This statement stems, in part, from the high concentrations of PAMAM dendrimers required for scattering experiments, which introduce long-range electrostatic interactions between neighbouring dendrimers, preventing their study as isolated macromolecules in solution. This factor is not being adequately accounted for in most computation-based simulations aiming to characterize the conformation of individual dendrimers. In contrast, PEF-based experiments operate at significantly lower concentrations, and thus should offer an experimental means to probe intramacromolecular conformational changes.

Third, PAMAM dendrimers are commercially available in high purity, which should ease the synthetic burden for preparing pyrene-labeled dendrimers.

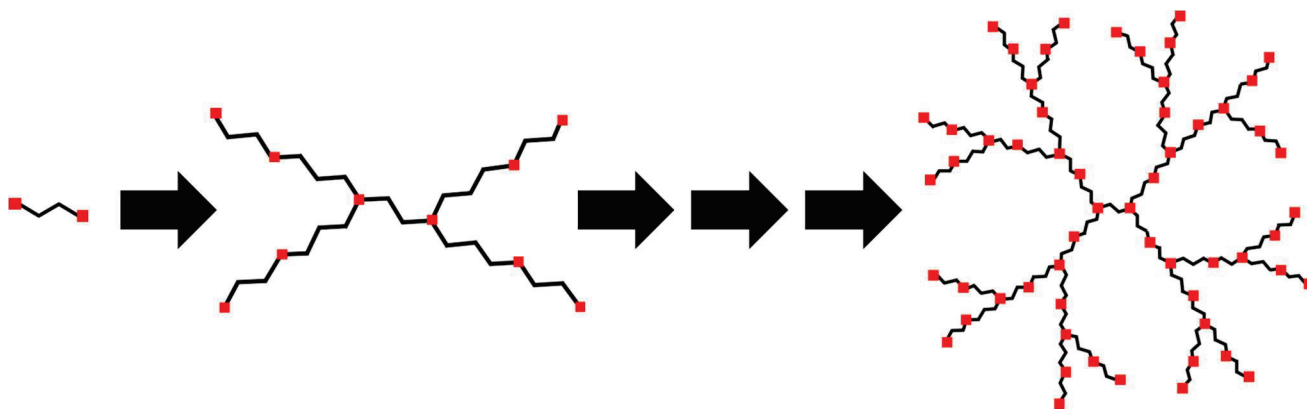


Figure 0.6 Schematic illustration of dendrimer structure and their cascade-like synthesis

1.3.2 Poly(glutamic acid) (PGA)

PGA is a natural, biodegradable, non-immunogenic, and environmentally friendly biopolymer which has many different applications ranging from the biomedical^{128,129} to agricultural¹³⁰ fields. For a given application, the conformation of a macromolecule is important, as it governs its physical properties. As such, significant effort has focused on characterizing the conformation of PGA in solution, typically in water^{16–19,131–134} or organic solvents.^{20–22,97,100,101,135–138} Poly(*L*-glutamic acid) (PLGA) in aqueous solutions is known to be a random coil and α -helix at high and low pH, respectively.^{16–19,131–134} PLGA in *N,N*-dimethylformamide (DMF), a helicogenic solvent, is known to adopt an α -helical conformation.^{21,136,137} However, the conformation of PLGA in dimethyl sulfoxide (DMSO) is still not fully understood.^{21,22,137,136}

In the context of the present thesis, PLGA samples are ideal candidates to study for two reasons. First, their conformation in DMF is known to be a rigid α -helix. As such, pyrene derivatives with different linker lengths could be employed to adjust the range over which PEF occurs, ideally on length scales comparable to those used in FRET studies. Second, since the exact

conformation of PLGA in DMSO is unknown, the methodology developed to probe the conformation of macromolecules over different length scales with pyrene derivatives having different linker lengths could be applied to investigate the conformational change experienced by PLGA upon changing the solvent from DMF to DMSO.

1.3.3 Polynorbornene

Norbornene (Nb) is a bicyclic monomer, that can undergo polymerization via ring-opening, cationic, or vinyl type addition polymerization.^{139–143} While ring opening polymerization of Nb is common,^{24,25,139–141} significant effort has been devoted towards the vinyl-type addition polymerization. This, in part, is due to the unique physical properties imparted on the macromolecules from the retention of the bicyclic ring in the polymer backbone. Such properties include a high T_g (>220 °C)^{24,25,140–143} and good thermostability,^{141,144–147} chemical resistivity,^{140,146,148,149} dielectric^{24,140,143,146} and mechanical properties,¹⁴¹ and optical transparency.^{142,149} These properties are highly dependent on the polymerization conditions.^{140,150–152} Although polynorbornene (PNb) has been described as adopting a rigid random coil conformation, some contrary evidence has suggested that PNb adopts a helix-kink conformation.^{24–26,140} Unfortunately, since these macromolecules tend to be polydisperse and poorly soluble, they cannot be easily studied by solution scattering experiments which require high concentrations and monodisperse samples. Furthermore, it would be difficult to employ 2D NMR to probe their conformation in solution owing to the spectral overlap between the different signals obtained with PNb samples, which is a common problem for synthetic macromolecules.¹⁵³ These considerations explain why few experimental tools can be used to probe the conformation of PNb. However, unlike the limitations associated with the scattering and NMR experiments, PEF should be able to retrieve quantitative information about the PNb conformation for the following reasons.

First, application of the FBM to study macromolecules, that have been randomly labeled with pyrene, shifts the focus of the study from the entire macromolecule to the *blob* sub-volume probed by the excited dye, which eliminates the impact of polydispersity on the data analysis. Second, PEF studies require only low concentrations around 1-10 mg/L of PyLM which should facilitate the solubilization of the PNb samples. Third, if pyrene derivatives with different linker lengths are employed to study the PNb samples, the conformation of PNb can be probed over different length scales and conformational heterogeneity of PNb can be assessed. In summary, these three important advantages of PEF over more traditional techniques suggest that application of PEF to study pyrene-labeled PNb samples should yield information about the conformation of PNb in solution.

1.4 Research Objective and Thesis Outline

The overarching goal of the present thesis was to confirm that PEF, a classic example of FCQ, can yield quantitative conformational information about complex macromolecules in solution. Specifically, the present thesis focusses on the characterization of PAMAM dendrimer, PGA, and PNb-Ac samples to demonstrate how quantitative conformational information about each macromolecule can be extracted from PEF-based experiments. Following the Introduction presented in Chapter 1 of this thesis, the first research goal, presented in Chapter 2, was two-fold. First, it aimed to establish the fundamental relationship between the average rate constant ($\langle k \rangle$) for PEF, retrieved from the MFA of multiexponential decays acquired with PyLM, and the local pyrene concentration ($[Py]_{loc}$) in the macromolecular volume. Second, to demonstrate that $[Py]_{loc}$ for a PyLM is well-represented by the ratio of the number (n_{Py}) of ground-state pyrenyl labels in the vicinity of an excited pyrene divided by the cube of the average end-to-end distance ($\langle L_{Py} \rangle$)

separating every two pyrene dyes. The assumptions made to derive $\langle L_{Py} \rangle$, such as having the internal segments of low generation PAMAM dendrimers obey Gaussian statistics, can then be validated by comparing $\langle k \rangle$ and the ratio $n_{Py}/\langle L_{Py} \rangle^3$, thus establishing a methodology providing conformational insight about a macromolecule in a manner that complements scattering experiments. The establishment of the $\langle k \rangle$ -vs.- $[Py]_{loc}$ relationship for the pyrene end-labeled PAMAM dendrimers led to its application to study the intramacromolecular conformational changes occurring upon protonation of the internal tertiary amines of PAMAM dendrimers in Chapter 3. In contrast to the working concentrations in the 10-50 g/L range commonly employed in scattering experiments for PAMAM dendrimers,^{8-10,12} PEF studies were conducted at a significantly lower working concentration of ~ 1 mg/L that enabled the conformational analysis of isolated macromolecules in solution. The third research objective, presented in Chapter 4, was two-fold. Its first aim was to extend the length scale over which PEF studies can be conducted, and in turn, demonstrate that PEF can probe length scales, that are on par with FRET, the golden standard of fluorescence-based experiments to probe conformational changes in macromolecules. Its second aim was to introduce a new methodology which can be applied to study conformational homogeneity and changes experienced by a macromolecule over different length scales. To this end, two PGA constructs, one prepared from L-glutamic acid (PLGA) and another from a racemic mixture of D- and L-glutamic acid (PDLGA), were labeled with 1-pyrenebutylamine and 1-pyreneoctylamine. The methodology using PEF with different pyrene derivatives to probe the conformation of macromolecules in solution over different length scales was validated first by confirming the conformations of PDLGA, known to adopt a random coil conformation in DMF and DMSO, and PLGA, known to adopt an α -helical conformation in DMF. It was then applied to demonstrate that the unknown conformation of PLGA in DMSO is that of a 3_{10} -helix. The ability

to probe the conformation of macromolecules over different length scales established in Chapter 4 was taken advantage of in Chapter 5 to probe the conformation of PNb-Ac constructs. Contrary to the PGA samples studied in Chapter 4, which were prepared with a narrow molecular weight distribution, the PNb-Ac sample studied in Chapter 5 was polydisperse. Given that scattering techniques typically require monodisperse samples for conformational analysis, the study conducted in Chapter 5 illustrates the advantage of using the PEF-based methodology since it does not suffer from this limitation. One main outcome of Chapter 5 was that the conformation of PNb-Ac, determined by a combination of PEF, FBM, and MMO, appeared to be heterogeneous on the different length scales studied in contrast to the homogeneous conformation of the PGA samples described in Chapter 4. Consequently, this study demonstrated that the PEF-based approach can be applied to study macromolecules with richer conformation than the conformationally homogenous PGA samples. Furthermore, considering the lack of scattering experiments conducted on PNb samples in solution, this study should highlight another advantage of PEF-based experiments, namely that even samples with reduced solubility can be studied. The sixth and last chapter of the thesis summarizes the important contributions made in Chapters 2 – 5 and describes future experiments that could be conducted based on the fundamental principles established in this thesis supporting the notion that PEF is a robust and reliable methodology to probe the conformation of macromolecules in solution.

Chapter 2: Macromolecular Conformation of Low Generation PAMAM Dendrimers Probed by Pyrene Excimer Formation

Adapted with permission from Patel, S.; Duhamel, J. Macromolecular Conformation of Low-Generation PAMAM Dendrimers Probed by Pyrene Excimer Formation. *Macromolecules* **2023**, *56*, 4012-4021, Copyright 2023 American Chemical Society.

2.1 ABSTRACT

A series of pyrene-labeled PAMAM dendrimers (PyCX-PAMAM-GY, where X (= 4, 8, or 12) and Y (= 0, 1, or 2) represent the number of atoms in the pyrenyl linker and the dendrimer generation, respectively) were studied by acquiring their time-resolved fluorescence decays in N,N -dimethylformamide (DMF) and dimethyl sulfoxide (DMSO). The fluorescence decays were fitted globally according to the model free analysis (MFA), that yielded the average rate constant $\langle k \rangle$ for pyrene excimer formation (PEF). $\langle k \rangle$ was compared with the local pyrene concentration $[Py]_{loc}$ inside the dendrimers, which was calculated by assuming that the segments constituting the dendrimer interior obey Gaussian statistics. $\langle k \rangle$ was found to increase linearly with $[Py]_{loc}$ in both solvents, but the straight lines had different slopes due to differences in solvent viscosity and polarity. These differences were accounted for by dividing $\langle k \rangle$ by k_{diff} , the bimolecular rate constant for PEF generated by n -hexyl-1-pyrenebutyramide used as a model compound. The $\langle k \rangle/k_{diff}$ ratios obtained for all the PyCX-PAMAM-GY samples in DMF and DMSO collapsed onto a single master line where $\langle k \rangle/k_{diff}$ increased linearly with $[Py]_{loc}$. The strong correlation found between $\langle k \rangle$ and $[Py]_{loc}$ suggested that the oligomeric segments constituting the interior of the low generation ($Y = 0, 1, \text{ and } 2$) PAMAM dendrimers obeyed Gaussian statistics. This fact was further supported by using the Gaussian approximation to calculate the radius of gyration (R_g) of PAMAM dendrimers and compare them to the R_g values obtained by molecular dynamics simulations (MDS). The excellent agreement obtained between the two sets of R_g values validated the assumption. Furthermore, the direct relationship between $\langle k \rangle$ and $[Py]_{loc}$ established in this study demonstrates that $\langle k \rangle$ provides a quantitative measure of the internal density of the dendrimers, an observation with considerable implications for the quantitative conformational characterization of macromolecules with a complex architecture in solution.

2.2 INTRODUCTION

The finding in 1974 by Wilemski and Fixman (WF), that the rate of encounter between a dye and its quencher covalently attached to the ends of a single chain could be handled by a single rate constant,^{1,2} ushered in a flurry of research activity to characterize the internal dynamics of fluorescently end-labeled linear monodisperse chains through fluorescence collisional quenching (FCQ) experiments.³⁻⁷ While the WF study opened an exciting new field of research, its unfortunate corollary was that a macromolecule labeled with more than one dye and one quencher would result in more than one quenching rate constant, whose values could not be extracted from the associated multiexponential fluorescence decay of the dye. This conclusion rationalizes why to this day, all quantitative FCQ studies of macromolecules in solution are conducted with linear monodisperse chains labeled at two specific positions, typically the chain ends, with a dye and a quencher.³⁻⁷ This experimental design is obviously extremely restrictive, as it not only prevents the FCQ study of the many macromolecules whose architecture departs from that of a linear chain,⁸⁻¹¹ but it also deprives the experimentalist from much needed information since the labeling of a macromolecule with more than one dye and one quencher increases the number of locations being probed on the macromolecule, thus providing a more detailed and accurate depiction of the macromolecule under study.¹² More importantly, the pseudo-unimolecular quenching rate constant retrieved from these FCQ experiments is directly proportional to the local quencher concentration, $[Q]_{\text{loc}}$, in the macromolecule.^{12,13} Since the quenchers are covalently attached onto the macromolecule, $[Q]_{\text{loc}}$ is directly related to the internal density (ρ_{loc}) of the macromolecule, a feature that should theoretically yield conformational information about a macromolecule and is hardly exploited by current FCQ techniques.¹²

Scattering techniques such as static light scattering (SLS), small angle X-ray (SAXS) or neutron (SANS) scattering are the workhorse characterization methods for determining the conformation of macromolecules in solution.¹⁴⁻¹⁷ Scattering techniques work by probing the local density of a macromolecule with respect to its center of gravity. Application of Guinier's law to scattering data yields the radius of gyration (R_g) of any macromolecule in solution with a decrease in R_g reflecting an increase in ρ_{loc} and a more compact macromolecular conformation.¹⁸ While the use of scattering techniques to probe macromolecular conformations is most widespread, scattering techniques do have stringent limitations. In particular, macromolecular objects must be large enough to generate a strong enough scattering signal for detection and be monodisperse.^{14,19} Although not acknowledged, FCQ techniques, which report on $[Q]_{loc}$ and thus ρ_{loc} , are ideally suited to handle small and/or polydisperse macromolecular objects in a manner that perfectly complements scattering techniques.

This point is illustrated in the present study where pyrene excimer formation (PEF), a classic example of FCQ,^{3,12,13} is applied to probe the conformation of three polyamidoamine PAMAM dendrimers with low generation numbers, namely G0, G1, and G2. Although these dendrimers are monodisperse, they are too small to generate sufficient scattering signal and their conformation in solution is typically predicted from molecular dynamics simulations (MDS).²⁰ The pseudo-unimolecular rate constant $\langle k \rangle$ of PEF for the G0, G1, and G2 PAMAM dendrimers labeled with 1-pyrene-butyric ($X = 4$), -octanoic ($X = 8$), and -dodecanoic ($X = 12$) acid (PyCX-PAMAM-GY with $X = 4, 8, \text{ and } 12$ and $Y = 0, 1, \text{ and } 2$) was compared to the local pyrene concentration $[Py]_{loc}$ of the PyCX-PAMAM-GY samples. $[Py]_{loc}$ was estimated from the ratio $n_{Py}/(L_{Py}/l)^3$ of the known number of ground-state pyrenes in the dendrimer (n_{Py}) divided by the cubed square root of the averaged squared end-to-end distance (L_{Py}^2) normalized by the bond

length (l), namely $(L_{\text{Py}}/l)^3$, between the pyrenyl labels. L_{Py}^2 was determined by applying the same methodology developed for a series of six dendrimers with a 2,2-bis(hydroxymethyl) propionic acid (HMPA) backbone labeled with 1-pyrenebutyric acid (PyC4-HMPA-GY), which had assumed that the oligomeric segments constituting the interior of the dendrimers obeyed Gaussian statistics.^{21,22}

An excellent correlation was observed between $\langle k \rangle$ and $n_{\text{Py}}/(L_{\text{Py}}/l)^3$ in *N,N*-dimethylformamide (DMF) and dimethyl sulfoxide (DMSO), the two solvents where the PyCX-PAMAM-GY samples were fully soluble. The effect of solvent viscosity and PEF efficiency could be accounted for by normalizing $\langle k \rangle$ by k_{diff} , the bimolecular rate constant for diffusive PEF for the model compound hexyl-1-pyrenebutyramide, as was done earlier.^{22,23} Furthermore, all $\langle k \rangle/k_{\text{diff}}$ ratios obtained for the PyCX-PAMAM-GY and PyC4-HMPA-GY samples in DMF and DMSO clustered around a master line when plotted as a function of $n_{\text{Py}}/(L_{\text{Py}}/l)^3$,^{21,22} suggesting that these trends are general and could also apply to a wider range of pyrene-labeled constructs. Consequently, two conclusions can be drawn from this study. First, this study demonstrates that the conformation of low generation dendrimers can be predicted by assuming Gaussian statistics for the oligomeric segments constituting a dendrimer interior. Second and perhaps more importantly, this study also indicates that PEF reports on the local density of macromolecules in solution in the same manner as scattering techniques do and thus opens the path for using PEF for the quantitative conformational characterization of complex macromolecules in solution.

2.3 EXPERIMENTAL

Chemicals: Oxalyl chloride and EDC-HCl were purchased from Oakwood Chemicals. Suberic acid monomethyl ester and 12-methoxy-12-oxodecanoic acid were purchased from Fisher

Scientific and Ambeed chemicals, respectively. The PAMAM dendrimers of generation G0, G1, and G2 and all other reagents/solvents were purchased from Sigma-Aldrich. All reagents and solvents were used without further purification.

Synthesis of 1-pyreneoctanoic acid: The synthesis of 1-pyreneoctanoic acid was adapted from a procedure reported previously.²⁴ In brief, a 100 mL round bottom (RB) flask was charged with dichloromethane (DCM, 15 mL) and suberic acid monomethyl ester (2 mL, 11.2 mmol). The solution was purged with nitrogen for 5 minutes followed by the careful addition of oxalyl chloride (1.2 mL, 14.5 mmol, 1.3 eq). After 20 minutes, excess DCM and oxalyl chloride was evaporated via a steady stream of nitrogen gas. The activated acid was redissolved in DCM (50 mL) followed by the addition of pyrene (6.8 g, 33.5 mmol, 3 eq) and aluminum trichloride (5.4 g, 17.9 mmol, 1.6 eq). The reaction was stirred vigorously at room temperature (RT). After 30 minutes, the reaction was cooled to 0 °C, followed by the slow addition of 1 M HCl to quench excess aluminium trichloride. The precipitate was removed from the product via suction filtration and the solvent was evaporated. The resultant product was off-white to yellow in color. Without further purification, the crude product (5.4 g, ~14.4 mmol) was dissolved in trifluoroacetic acid (TFA, 25 mL) followed by the addition of triethyl silane (5.8 mL, 36.1 mmol, 2.5 eq). The reaction was allowed to proceed for 1.5 hours at room temperature. TFA was removed under vacuum to obtain an off-white to yellow product. The resultant product was purified by three 50 mL rinses with cold hexane to obtain the off-white methyl 1-pyreneoctanoate product. A 100 mL RB flask was charged with methyl 1-pyreneoctanoate, methanol (15 mL), and 6 M sodium hydroxide (8 mL). Once fully dispersed, the mixture was refluxed for 5-6 hours. The solution was cooled to RT and the resultant precipitate was recovered from the filtrate via suction filtration. Residual methanol was removed by a steady stream of air overnight. The crude product was rinsed with DCM (300 mL) followed

by 1 M HCl (50 mL). The resultant off-white product was dried overnight under vacuum to obtain the pure 1-pyreneoctanoic acid (1.5 g, 38 %). The ^1H NMR spectrum of 1-pyreneoctanoic acid in d_6 -DMSO can be found in Figure S2.1 in Supporting Information (SI).

Synthesis of 1-pyrenedodecanoic acid: The synthesis of 1-pyrenedodecanoic acid was conducted in the same manner as described for 1-pyreneoctanoic acid using 12-methoxy-12-oxododecanoic acid instead of monomethyl suberate ester as the starting material. The 1-pyrenedodecanoic acid product (1.5 g, 39 %) was obtained as an off-white solid and its ^1H NMR spectrum in d_6 -DMSO can be found in Figure S2.2.

*Synthesis of *n*-hexyl-1-pyrenebutyramide:* A 50 mL RB flask equipped with a magnetic stir bar was charged with 1-pyrenebutyric acid (0.2 g, 0.69 mmol, 1 eq) and 20 mL of DCM. The mixture was purged with nitrogen and stirred rapidly for 20 minutes to obtain a homogenous dispersion. Under continuous stirring, oxalyl chloride (0.09 mL, 1.0 mmol, 1.5 eq) was slowly added. After 30 minutes, DCM and excess oxalyl chloride were removed via a steady stream of nitrogen gas. Once dried, the activated 1-pyrenebutyric acid was redissolved in DCM (15 mL) followed by the addition of *n*-hexylamine (13 mL, 99 mmol, 100 e.q). The reaction was allowed to proceed overnight at room temperature. The crude reaction mixture was diluted with DCM (15 mL) and purified via liquid-liquid extractions (3×1 M HCl, $3 \times$ brine, and $3 \times$ deionized water (DIW)). The crude product was further purified by column chromatography with a mobile phase made of a mixture of ethyl acetate (5 %) and hexane (95 %). The ^1H NMR spectrum of *n*-hexyl-1-pyrenebutyramide (Hx-PyBA) in CDCl_3 can be found in Figure S2.3 in SI. The molar extinction coefficient of Hx-PyBA in DMF equaled $37,500 \text{ M}^{-1} \cdot \text{cm}^{-1}$ at 345 nm. A plot of the absorbance as a function of concentration is provided in Figure S2.6 in SI.

Synthesis of n-ethyl-1-pyreneoctanamide: A 20 mL vial equipped with a magnetic stir bar was charged with 1-pyreneoctanoic acid (0.2 g, 0.58 mmol, 1 eq) and EDC-HCl (0.44 g, 2.3 mmol, 4 eq). DMF (4 mL) was subsequently added to the solids and the mixture was vigorously mixed until the solids completely dissolved. Once fully dissolved, ethyl amine (0.18 mL, 2.3 mmol, 3.9 eq) was added and the reaction was allowed to proceed at room temperature overnight. The crude reaction mixture was combined with DCM (20 mL) and partially purified via liquid-liquid extractions (3 × 1 M NaOH, 1 M HCl, brine, and DIW). The product was further purified by flash chromatography with a mobile phase of ethyl acetate (50 %) and hexane (50 %). The ¹H NMR spectrum of ethyl-1-pyreneoctanamide (Et-PyOA) in CDCl₃ can be found in Figure S2.4 in SI.

Synthesis of n-ethyl-1-pyrenedodecanamide: n-Ethyl-1-pyrenedodecanamide (Et-PyDA) was synthesized and purified in a similar manner as described for Et-PyOA, with one deviation. For this sample, no liquid-liquid extraction was conducted prior to purification via column chromatography. The ¹H NMR spectrum of Et-PyDA in CDCl₃ can be found in Figure S2.5 in SI.

Pyrene labeling of PAMAM dendrimers: PAMAM dendrimers were labeled via an EDC-HCl coupling reaction. A brief description of the labeling reaction and purification will be presented hereafter for a PAMAM-G0 dendrimer which had been labeled with 1-pyrenebutyric acid. In a 20 mL vial equipped with a magnetic stir bar, 0.1 g of a 20 wt% PAMAM-G0 (0.039 mmol, 4 eq of primary amines) solution in methanol was weighed. Methanol was removed under a steady stream of air for 10 minutes. The dried PAMAM-G0 was dispersed in a mixture of DMSO (1 mL) and DMF (3 mL). Once fully dispersed, 1-pyrenebutyric acid (0.37 g, 0.93 mmol, 6 eq relative to the number of primary amines) was added to the solution and vigorously stirred for 25 minutes, followed by the addition of EDC-HCl (0.19 g, 1.0 mmol, 6.6 eq). Under continuous stirring, the reaction was left at RT in the dark for 2 days. The reaction mixture was purified via

4-7 precipitations in cold diethyl ether (50 mL) followed by 3-4 rinses with deionized water (DIW, 50 mL). The purified product was dried overnight under vacuum and subsequently characterized by ¹H NMR and MALDI-TOF. The spectra for ¹H NMR (Figures S2.7 – S2.15) and MALDI-TOF (Figures S2.17 – S2.24) can be found in the SI. A summary of the expected molecular weight, m/z ratios obtained from MALDI-TOF, and the number of pyrenes per dendrimer determined from ¹H NMR is provided in Table 2.1. The chemical structure of the PyCX-PAMAM-GY samples can be found in Table 2.2.

Table 0.1 Expected molecular weight, m/z ratio, and number of pyrenes of the PyCX-PAMAM-GY dendrimers.

UV-Vis Spectroscopy: Absorption measurements were conducted on a Varian Cary 100 Bio spectrophotometer (Varian, Palo Alto, CA, USA) using a quartz cuvette with a 1 cm pathlength. Absorption measurements ensured that the absorbance at 345 nm of the pyrene-labeled dendrimer solutions equaled 0.1, which corresponds to a pyrene concentration of about 2.5×10^{-6} M. At such a low concentration intermolecular pyrene excimer formation is prevented.

Generation	1-Pyrenebutyric Acid			1-Pyreneoctanoic acid			1-Pyrenedodecanoic acid		
	Expected MW (g/mol)	m/z	#Py calculated (expected) from NMR	Expected MW (g/mol)	m/z	#Py calculated (expected) from NMR	Expected MW (g/mol)	m/z	#Py calculated (expected) from NMR
0	1598	1600	4.0 (4)	1823	1825	3.9 (4)	2047	2047	3.8 (4)
1	3593	3592	8.0 (8)	4041	4042	7.6 (8)	4490	4493	7.6 (8)
2	7582	7578	16.2 (16)	8479	8484	16.1 (16)	9391	<i>n.a.</i>	16.1 (16)

Steady-State Fluorescence Spectroscopy: All steady-state fluorescence (SSF) spectra were acquired on a QM-400 spectrofluorometer equipped with a Xenon arc lamp. Prior to acquisition of the fluorescence spectra, the samples were degassed for 35 minutes by bubbling pure nitrogen through the solution. The spectra were acquired with an excitation wavelength of 345 nm from 355 to 600 nm. Analysis of the SSF spectra yielded the fluorescence intensity ratio $(I_E/I_M)^{SSF}$, where the fluorescence intensity of the excimer (I_E) taken from 500 to 530 nm was divided by the fluorescence intensity of the monomer (I_M) taken from 376 to 382 nm.

Time-Resolved Fluorescence: Time-resolved fluorescence (TRF) decays were acquired on a HORIBA Ultima Ultrafast time-resolved fluorometer (HORIBA, Piscataway, NJ, USA) equipped with a DeltaDiode laser centered at 336 nm. A 370 nm and 490 nm cut-off filters were used at the entrance of the emission monochromator for acquisition of the monomer (379 nm) and excimer (510 nm) fluorescence decays, respectively, to minimize stray light from reaching the detector. The instrument response function was obtained with an aluminium reflective monolith by setting the emission wavelength at 336 nm. All fluorescence decays were acquired with 20,000 counts at the decay maximum over 1,024 channels. Time-per-channels of 0.10, 0.44, or 0.87 ns/channel were used. The monomer and excimer fluorescence decays were fitted globally according to the model free analysis (MFA). The quality of the fluorescence decay fits was assessed from the low χ^2 values (< 1.3) and the random distribution of the residuals and

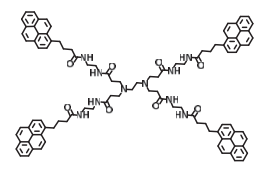
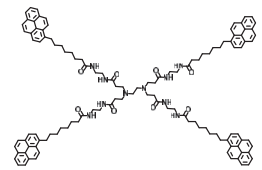
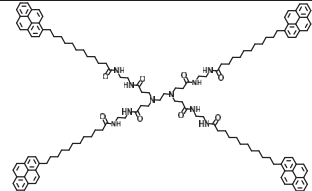
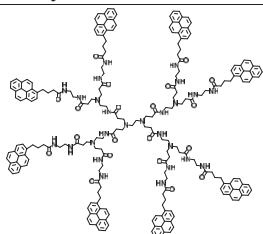
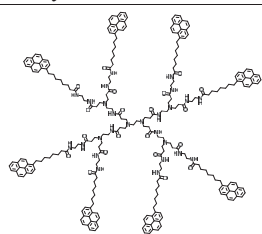
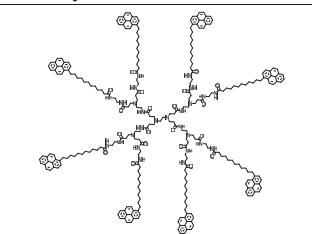
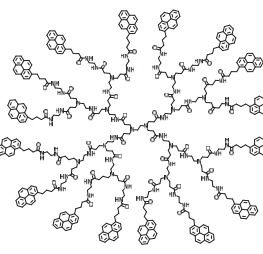
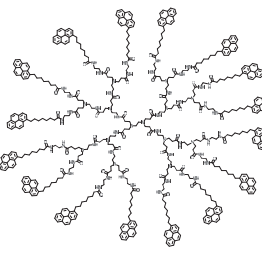
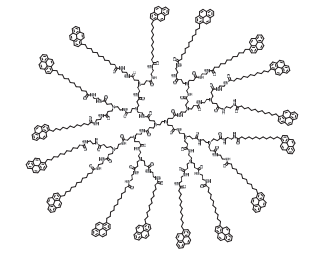
Generation	Pyrene butyric acid	Pyrene octanoic acid	Pyrene dodecanoic acid
0			
	PyC4-PAMAM-G0	PyC8-PAMAM-G0	PyC12-PAMAM-G0
1			
	PyC4-PAMAM-G1	PyC8-PAMAM-G1	PyC12-PAMAM-G1
2			
	PyC4-PAMAM-G2	PyC8-PAMAM-G2	PyC12-PAMAM-G2

Table 0.2 Chemical structure of the PyCX-PAMAM-GY samples.

autocorrelation of the residuals around zero. An example of the fit quality and the equations used in the MFA can be found in the Supporting Information. The front-face geometry was used to acquire the TRF decays with concentrated solutions of the Hx-PyBA model compound to determine the bimolecular rate constant k_{diff} for PEF in DMF and DMSO, while all the TRF decays of the pyrene-labeled dendrimer solutions with about 2.5×10^{-6} M pyrene concentration were acquired in the normal right-angle geometry.

Model-Free Analysis (MFA) of the Fluorescence Decays: All monomer and excimer fluorescence decays were fitted globally according to the model free analysis (MFA).^{25,26} In brief, after absorption of a photon, an excited pyrene can fluorescence with its monomer lifetime, τ_M , or it can diffuse through the solution and encounter a ground-state pyrene to form one of two types of excimer depending on whether the two pyrenes are properly ($E0^*$) or improperly (D^*) stacked. The corresponding lifetimes of these two excimer species are τ_{E0} and τ_D , respectively. The dendrimers labeled with 1-pyrenebutyric acid showed a short contribution in the excimer decays attributed to a short-lived pyrene dimer (ES^*) with a lifetime τ_{ES} . Due to its much shorter-lived fluorescence compared to all other pyrene species, ES^* was not considered in the discussion of the fluorescence data. Consequently, three pyrene species were expected to be present in the sample, namely Py_{free}^* , Py_{diff}^* , and Py_{agg}^* , which corresponded to unreacted pyrene, pyrene excimer formed by diffusive encounters, and pyrene excimer formed through direct excitation of a pyrene aggregate, respectively. MFA of the monomer and excimer decays yields the molar fractions f_{free} , f_{diff} , and f_{agg} of the Py_{free}^* , Py_{diff}^* , and Py_{agg}^* species, respectively. The fluorescence intensity ratio of the pyrene excimer over the monomer, namely the $(I_E/I_M)^{\text{TRF}}$ ratio, and the average rate constant of pyrene excimer formation, $\langle k \rangle$, were calculated with the decay times (τ_i) and their pre-exponential factors (a_i) retrieved from the MFA of the decays and their expressions are provided

in Equations 2.1 and 2.2, respectively. τ_M for the PyCX-PAMAM-GY dendrimers was fixed during the MFA and was determined from the model compounds. The τ_M values equaled 173, 161, and 161 ns in DMF, whereas τ_M values of 138, 130, and 130 ns were obtained in DMSO for the *n*-hexyl-1-pyrenebutyramide, *n*-ethyl-1-pyreneoctanamide, and *n*-ethyl-1-pyrenedodecanamide model compounds, respectively.

While the fluorescence intensity ratios $(I_E/I_M)^{SSF}$ and $(I_E/I_M)^{TRF}$ are obtained by different fluorescence techniques, namely steady-state (SSF) and time-resolved (TRF) fluorescence, respectively, they are related to one another according to the following reasoning. The MFA decomposes the overall steady-state fluorescence signal I_M^{SSF} for the pyrene monomer into that of the pyrene monomer species Py_{diff}^* and Py_{free}^* , which emit as monomer with the radiative rate constant for the pyrene monomer ($k_{rad,M}$). Similarly, the overall steady-state fluorescence signal I_E^{SSF} for the pyrene excimer is represented by that of the pyrene monomer species Py_{diff}^* and Py_{agg}^* , which lead to excimer formation and result in excimer emission with the radiative rate constant for the pyrene excimer ($k_{rad,E}$). The fluorescence intensity of the pyrene monomer (I_M^{SSF}) is obtained by multiplying $k_{rad,M}$ by the integral under the respective fluorescence decays of Py_{diff}^* and Py_{free}^* defined by $\langle\tau\rangle$ and τ_M and weighing these contributions with the molar fractions f_{diff} and f_{free} of the pyrene species detected in the fluorescence decay of the pyrene monomer, respectively. Similarly, the fluorescence intensity of the excimer (I_E^{SSF}) is obtained by multiplying $k_{rad,E}$ by the integral under the respective fluorescence decays of Py_{diff}^* and Py_{agg}^* defined by the products $\langle k \rangle \cdot \langle \tau \rangle \cdot \tau_X$ and τ_X , where X stands for a short-lived ($E0$) or long-lived (D) excimer and weighing these contributions with the molar fractions f_{diffX} and f_X of the pyrene species detected in the fluorescence decay of the pyrene excimer, respectively. Consequently, the ratio $(I_E/I_M)^{SSF}$ is found to equal $(k_{rad,E}/k_{rad,M}) \times (I_M/I_E)^{TRF}$, where the expression for $(I_M/I_E)^{TRF}$ is given in Equation

2.1. While $(I_E/I_M)^{SSF}$ is a relative measure of the pyrene excimer formation efficiency, which depends on the fluorometer and the method applied to determine the fluorescence intensities I_M^{SSF} and I_E^{SSF} , $(I_M/I_E)^{TRF}$ is an absolute value. The direct relationship between $(I_E/I_M)^{SSF}$ and $(I_M/I_E)^{TRF}$ has been demonstrated in numerous reports.^{21,22,28-29}

$$(I_E / I_M)^{TRF} = \frac{(f_{diffE0}\tau_{E0} + f_{diffD}\tau_D) \langle k \rangle \langle \tau \rangle + f_{E0}\tau_{E0} + f_D\tau_D}{(f_{diffE0} + f_{diffD}) \langle \tau \rangle + f_{free}\tau_M} \quad (2.1)$$

$$\langle k \rangle = \frac{\sum_{i=1}^n a_i}{\sum_{i=1}^n a_i \tau_i} - \frac{1}{\tau_M} = \frac{1}{\langle \tau \rangle} - \frac{1}{\tau_M} \quad (2.2)$$

2.3 RESULTS AND DISCUSSION

Calculation of the end-to-end distance and radius of gyration of the pyrene-labeled PAMAM dendrimers: The same molecular parametrization was applied to all of the PyCX-PAMAM-GY dendrimers as was done earlier for a series of dendrons, that were prepared with a 2,2-bis(hydroxymethyl)propionic acid (HMPA) backbone and labeled with 1-pyrenebutyric acid (PyC4-HMPA-GY with Y = 1 – 6).²¹⁻²² The methodology is described in more detail for the PyC4-PAMAM-G1 dendrimer shown in Figure 2.1. The black acyl spacer connecting the pyrenyl label to the dendrimer was made of a atoms, which equalled 4, 8, or 12 atoms depending on whether the dendrimer was labeled with 1-pyrene-butyl, -octanoyl, or -dodecanoyl groups, respectively. The green aminoethyl propionamide building block of the PAMAM dendrimer contained b (= 7) atoms and the red ethylene diamine core was made of c (= 4) atoms. The corresponding schematic representation of PyC4-PAMAM-G1 is shown in Figure 2.1B.

The squared average end-to-end distance ($L_{Py}^2(1)$) of PyC4-PAMAM-G1 was then calculated by selecting Py1 as being the excited pyrene, and thus the reference pyrene, and accounting for the number of atoms separating Py1* from Py2, Py1* from Py3 and Py4, and Py1* from Py5, Py6, Py7, and Py8 and considering each segment separating Py1* from a ground-state pyrene as a Gaussian chain. L_{Py}^2 needed to be weighed by the number of pyrenyl labels being separated by a same number of atoms from Py1* (see Table 2.2) yielding Equation 2.3. l in Equation 2.3 is a normalization factor equivalent to the bond length.

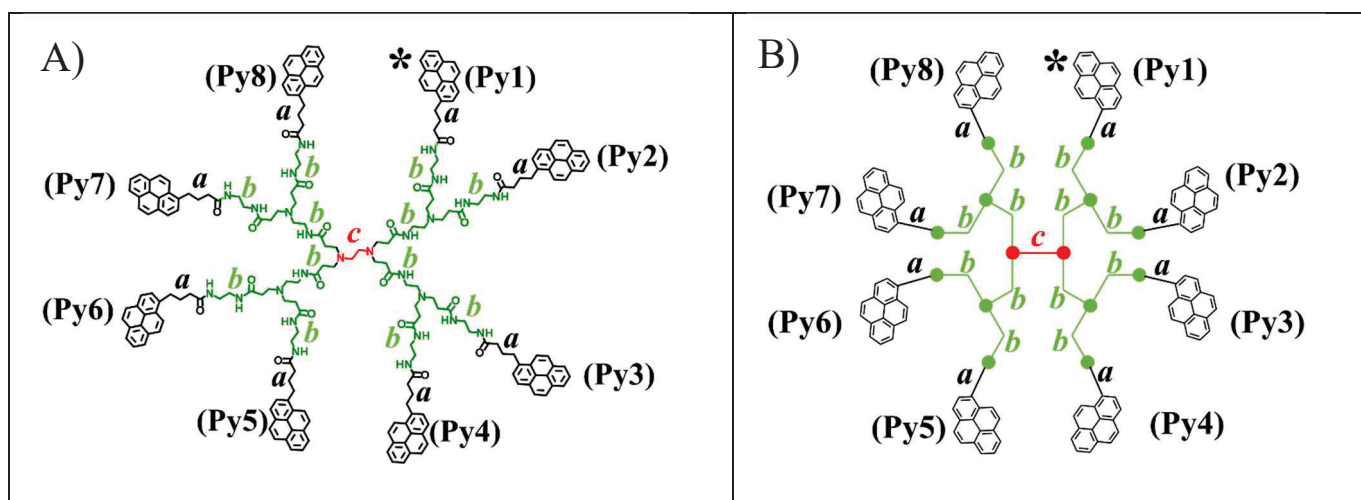


Figure 0.1 Chemical parametrization. A) Chemical structure of PyC4-PAMAM-G1 and B) its parametrized equivalent.

$$L_{Py}^2(1) = \frac{1 \times (2a + 2b + 1) + 2 \times (2a + 4b + 1) + 4 \times (2a + 4b + c)}{1 + 2 + 4} \times l^2 = \frac{14a + 26b + 4c + 3}{7} \times l^2 \quad (2.3)$$

Table 0.3 Distances separating Py1* from groups with given numbers of ground-state pyrenyl labels for the PyC4-PAMAM-G1 sample.

Distance between	# of atoms	# of ground-state pyrenes
Py1* from Py2	$2a + 2b + 1$	1
Py1* and Py3 and Py4	$2a + 4b + 1$	2
Py1* and Py5, Py6, Py7, and Py8	$2a + 4b + c$	4

$L_{Py}^2(1)$ for PyC4-PAMAM-G1 calculated with Equation 2.3 could be generalized to determine $L_{Py}^2(N)$ for all PyCX-PAMAM-GY dendrimers as a function of the generation number (N) as shown in Equation 2.4.

$$L_{Py}^2(N) = \left(2a + \frac{[2 - 2^{N+2} + (N+1) \times 2^{N+3}]b + 2^{N+1}c + 2^{N+1} - 1}{2^{N+2} - 1} \right) \times l^2 \quad (2.4)$$

Assuming that the dendrimer volume is a sphere of diameter $L_{Py}(N)$, the local pyrene concentration $[Py]_{loc}$ could be obtained by applying Equation 2.5 where the number of ground-state pyrenyl groups (# GS Py) is divided by the dendrimer volume. The term $2^{N+2} - 1$ in the nominator of Equation 2.5 represents the number (n_{Py}) of ground-state pyrenyl labels in a PyCX-PAMAM-GY dendrimer of generation $Y = N$ from which one pyrenyl group was subtracted to account for the excited pyrene. The validity of Equation 2.5 can be tested by comparing the average rate constant, $\langle k \rangle$, of PEF obtained from the MFA of the PyCX-PAMAM-GY fluorescence decays and given by Equation 2.2 in the Experimental section with the quantity $n_{Py}/(L_{Py}(N)/l)^3$ taken as a measure of $[Py]_{loc}$. Since $\langle k \rangle$ is directly equal to the product $k_{diff} \times [Py]_{loc}$, where k_{diff} is the bimolecular rate constant for PEF by diffusive encounters between an excited and a ground-state pyrene,^{12,13,26} $\langle k \rangle$

would be expected to increase linearly with increasing $n_{Py}/(L_{Py}(N)/l)^3$ used to represent $[Py]_{loc}$. Another advantage of considering the quantity $n_{Py}/(L_{Py}(N)/l)^3$ is that it avoids the $(\pi/6)$ term characteristic of a sphere, since numerous studies expect dendrimers to be better described as ellipsoids.^{20,30}

$$[Py]_{loc} = \frac{\#GS Py}{V_{Den}} = \frac{2^{N+2} - 1}{\frac{\pi}{6} L_{Py}^3(N)} \quad (2.5)$$

The calculation of $L_{Py}^2(N)$ was based on the simple assumption that the internal segments of the dendrimers obey Gaussian statistics. The validity of this assumption was supported from the linear relationship that was obtained earlier between $\langle k \rangle$ and $n_{Py}/(L_{Py}(N)/l)^3$ for six PyC4-HMPA-GY dendrimers with Y ranging from 1 to 6.^{21,22} Compared to the HMPA dendrimers, PAMAM dendrimers have been studied in much more detail and the profile of their radius of gyration as a function of generation number ($R_g(N)$) has been reported.^{16,20} Consequently, the assumption that the oligomeric segments constituting the interior of dendrimers might follow Gaussian statistics was applied to derive an expression for the radius of gyration of PAMAM dendrimers taking the center of the ethylene diamine linker located at the core of the dendrimer as the center of mass in Figure 2.1B. The average distance between the center of mass of the PAMAM dendrimer and an atom linked to the center of mass by i atoms would thus be $\sqrt{i} \times l$, where l is a normalization factor equivalent to a bond length. This relationship was taken advantage of to derive Equation 2.6 for a dendrimer of generation N , where the nominator represents the sum of all the $\sqrt{i} \times l$ distances multiplied by the corresponding number of branches and the denominator represents the total number of atoms. Although the formalism applied to derive Equation 2.6 could be extended to

determine $R_g(N)$ of the PyCX-PAMAM-GY dendrimers, Equation 2.6 was derived for the naked PAMAM dendrimers, so that it could be compared to the $R_g(N)$ values obtained by molecular dynamics simulations (MDS).²⁰

$$R_g(N) = \frac{2 \times \left[2^{N+1} \sum_{i=1}^{c/2+(N+1) \times b} \sqrt{i} - \sum_{k=0}^N 2^k \sum_{i=1}^{c/2+k \times b} \sqrt{i} \right]}{c + 4(2^{N+1} - 1)} \times l \quad (2.6)$$

$R_g(N)$ obtained with Equation 2.6 was plotted as a function of N in Figure 2.2 and the $R_g(N)$ values obtained with Equation 2.6 were compared to those determined from MDS conducted by Maiti et al.²⁰ An excellent agreement between the $R_g(N)$ values obtained with Equation 2.6 and MDS was observed up to the 4th generation PAMAM dendrimer. The discrepancy between the $R_g(N)$ values obtained with Equation 2.6 and MDS must result from the crowding of the dendrimer interior for the higher generation dendrimers, which prevents the segments from adopting the Gaussian conformation, that was assumed in the derivation of Equation 2.6. For lower generation numbers, it is quite satisfying that $R_g(N)$ obtained with Equation 2.6 reproduces closely the $R_g(N)$ - vs - N trend obtained by MDS, since the chain segments constituting the dendrimer interior are likelier to adopt a Gaussian conformation for the lower generation dendrimers, that are much less dense than the higher generation dendrimers. In turn, the good agreement observed in Figure 2.2 validates the calculation of $L_{Py}^2(N)$ in Equation 2.4 and its use in Equation 2.5 to calculate $[Py]_{loc}$. $[Py]_{loc}$ can be compared in the following sections to the average rate constant $\langle k \rangle$ for PEF obtained with Equation 2.2 from the MFA of the PyCX-PAMAM-GY fluorescence decays.

Steady-state fluorescence spectra: The steady-state fluorescence (SSF) spectra of all samples were acquired and can be found in Figures 2.3A-F. They showed the typical spectral features expected

from the pyrene monomer and excimer fluorescence, with the monomer exhibiting sharp fluorescence peaks between 370 and 410 nm and the excimer displaying a broad structureless emission centered at 480 nm.¹² The fluorescence spectra were analyzed to determine the fluorescence intensity of the excimer (I_E) and monomer (I_M), whose $(I_E/I_M)^{SSF}$ ratio represents a measure of the efficiency of pyrene excimer formation. $(I_E/I_M)^{SSF}$ was plotted as a function of $n_{Py}/(L_{Py}/l)^3$ taken as a measure of $[Py]_{loc}$ in Figure 2.4A. Contrary to expectations,¹³ Figure 2.4A illustrates an apparent lack of trend between $(I_E/I_M)^{SSF}$ and $[Py]_{loc}$. This outcome is expected since dealing with the $(I_E/I_M)^{SSF}$ ratio is notoriously sensitive to the presence of minute amount of unreacted pyrene derivative, whose fluorescence quantum yield can be more than 100 times larger than the quantum yield of the pyrene monomer covalently attached to a pyrene-labeled dendrimer.^{26,31,32} The first task when dealing with fluorescence data obtained with pyrene-labeled dendrimers is to eliminate the contribution from unattached pyrenyl labels from the monomer fluorescence. This task is easily accomplished from the analysis of the fluorescence decays.^{21,22,26}

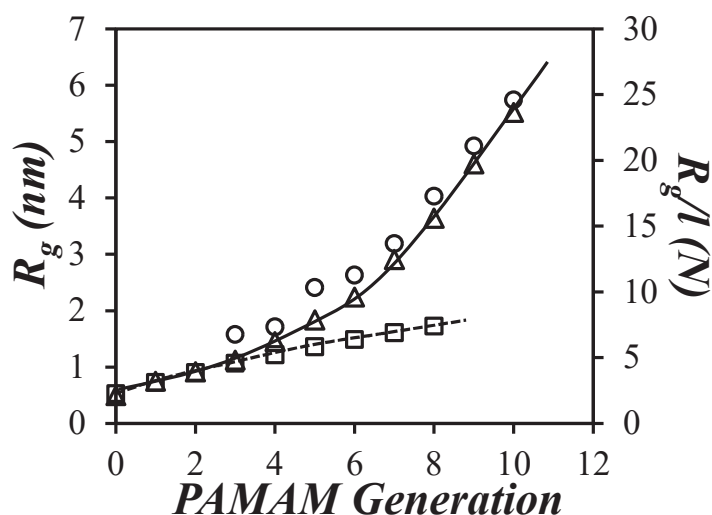


Figure 0.2 Comparison of R_g determined via (\bigcirc) SAXS,¹⁶ (\triangle) computer simulations,²⁰ and (\square) with Equation 2.6.

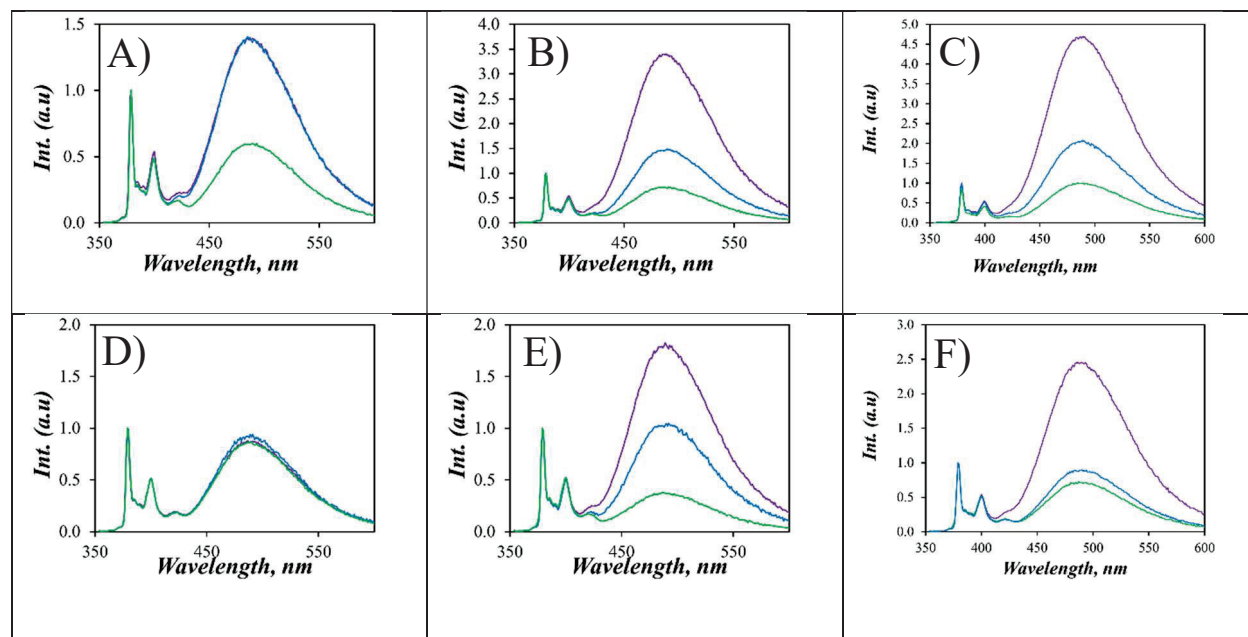


Figure 0.3 Steady-state fluorescence spectra for the PyCX-PAMAM-GY dendrimers of generation A,D) 0, B,E) 1 and C,F) 2 that have been labeled with 1-pyrene-butyric (purple), -octanoic (blue), and dodecanoic (green) acid. Fluorescence spectra in Figures 2.3A-C and 2.3D-F were acquired in DMF and DMSO, respectively.

Model Free Analysis of the Fluorescence Decays: The pyrene monomer and excimer fluorescence decays were fitted globally according to the model free analysis (MFA) and the ratio $(I_E/I_M)^{\text{TRF}}$ was calculated with Equation 2.1 from the MFA parameters listed in Tables S2.1 – S2.6. The excellent correlation found between the $(I_E/I_M)^{\text{TRF}}$ and $(I_E/I_M)^{\text{SSF}}$ ratios in Figure 2.4B demonstrated that the MFA parameters provided an accurate representation of the fluorescence signals emitted by the pyrene monomer and excimer as already described in numerous reports.^{21,22,27-29} It also afforded the ability to eliminate the contribution from unreacted pyrene derivatives by setting the molar fraction f_{free} of unreacted pyrene derivatives equal to zero in Equation 2.1 to yield the $(I_E/I_M)^{\text{TRF}}(f_{\text{free}}=0)$ ratio, which was plotted as a function of $n_{\text{Py}}/(L_{\text{Py}}/l)^3$ in Figure 2.4C. While some scatter in the data remained, the data points clustered along two main lines for DMF and DMSO

with a Pearson correlation coefficient equal to 0.92 and 0.98, respectively. The fact that these Pearson correlation coefficients approached unity implied that a strong correlation existed between $(I_E/I_M)^{\text{TRF}}(f_{\text{free}}=0)$ and $[Py]_{\text{loc}}$ as would be theoretically expected.^{12,13,26}

The molar fractions f_{diff} , f_{free} , and f_{agg} of the pyrenyl labels, that a) formed excimer by diffusion, b) were unable to form excimer and emitted as if they were free pyrene in solution, and c) were aggregated, respectively, were plotted as a function of $n_{\text{Py}}/(L_{\text{Py}}/l)^3$ in Figure 2.5. The large f_{diff} values obtained in DMF and DMSO indicated that pyrene excimer formation (PEF) occurs mostly through diffusive encounters between the pyrenyl labels. The fact that PEF is diffusion-controlled rationalizes why the $(I_E/I_M)^{\text{TRF}}(f_{\text{free}}=0)$ ratios in Figure 2.4C took lower values in DMSO than in DMF. Since DMSO has a higher viscosity ($\eta = 1.99$ mPa.s at 25 °C) than DMF ($\eta = 0.79$ mPa.s at 25 °C), PEF is hindered in DMSO compared to DMF and the $(I_E/I_M)^{\text{TRF}}(f_{\text{free}}=0)$ ratios are lower in DMSO than in DMF. While the $(I_E/I_M)^{\text{TRF}}(f_{\text{free}}=0)$ ratios are somewhat informative, they involve the excimer decays and are thus affected by the contributions from the different excimers $E0^*$ and D^* , which also complicates the interpretation of the results. A much simpler parameter to interpret is the average rate constant $\langle k \rangle$ for pyrene excimer formation, whose expression was provided in Equation 2.2. $\langle k \rangle$ is a pseudo-unimolecular rate constant that is equal to the product $k_{\text{diff}} \times [Py]_{\text{loc}}$ and is thus directly proportional to $[Py]_{\text{loc}}$ as described in Equation 2.7. $\langle k \rangle$ was plotted as a function of $n_{\text{Py}}/(L_{\text{Py}}/l)^3$ in Figure 2.6.

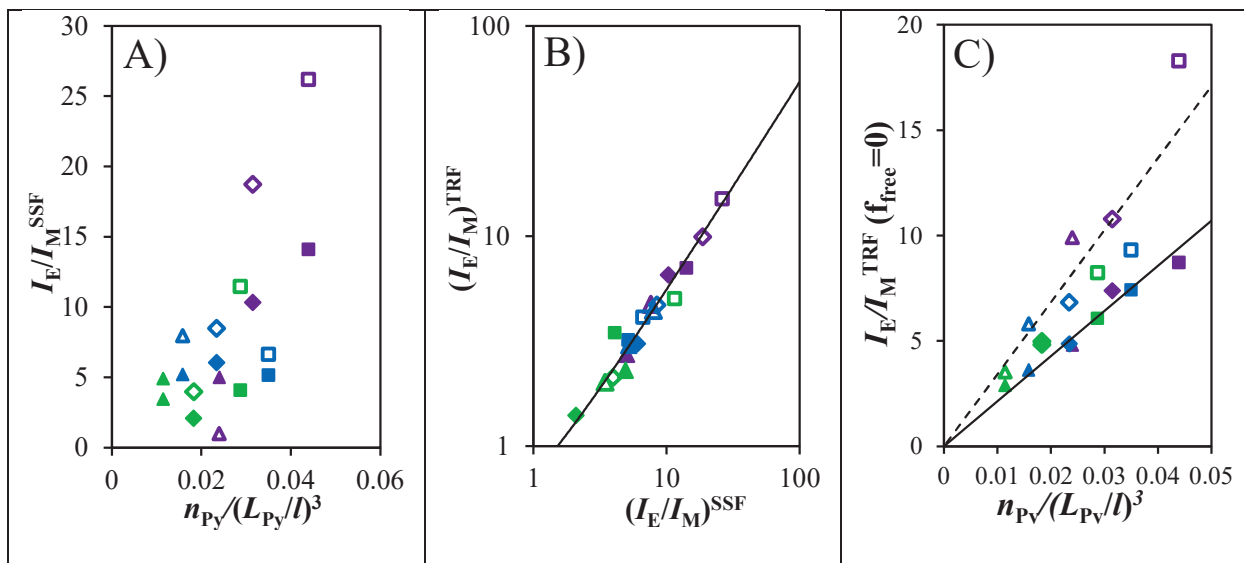


Figure 0.4 Plot of A) $(I_E/I_M)^{SSF}$ as a function of $n_{Py}/(L_{Py}/l)^3$, B) $(I_E/I_M)^{TRF}$ as a function of $(I_E/I_M)^{SSF}$, and $(I_E/I_M)^{TRF}(f_{free}=f_{ES}=0)$. Triangle, diamond, and square for generation 0, 1, and 2 PAMAM dendrimers labeled with 1-pyrene-butyric, -octanoic, and -dodecanoic acid in purple, blue, and green, respectively. Empty and full symbols are for DMF and DMSO, respectively.

$$\langle k \rangle = k_{diff} \times [Py]_{loc} \propto k_{diff} \times \frac{n_{Py}}{(L_{Py}/l)^3} \quad (2.7)$$

The plots in Figure 2.6A for DMF and 2.6B for DMSO showed excellent correlations between $\langle k \rangle$ and $n_{Py}/(L_{Py}/l)^3$ with Pearson correlation coefficients equal to 0.97 and 0.99, respectively. Pearson correlation coefficients close to unity indicate a strong correlation between two parameters. Consequently, the strong correlations found between $\langle k \rangle$ and $n_{Py}/(L_{Py}/l)^3$ in Figures 2.6A and B provide strong support for the notion that $\langle k \rangle$ is an accurate measure of $[Py]_{loc}$ and that the assumption, that the internal segments of low generation PAMAM dendrimers obey Gaussian statistics, is justified.

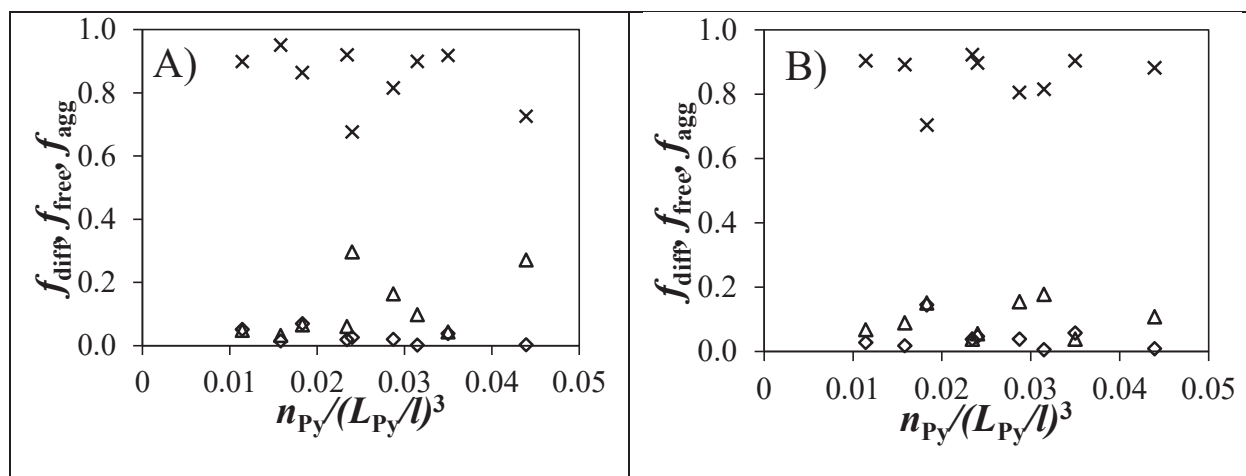


Figure 0.5 Plot of the molar fractions f_{free} (\diamond), f_{diff} (\times), and f_{agg} (\triangle) determined from the MFA of the fluorescence decays as a function of $n_{\text{Py}}/(L_{\text{Py}}/l)^3$ in A) DMF and B) DMSO.

Furthermore, the $\langle k \rangle$ values obtained in DMF and DMSO for the PyCX-PAMAM-GY dendrimers were compared to those obtained earlier for the PyC4-HMPA-GY dendrons^{21·22} in Figures 2.6C and D, respectively. All data points clustered around a master straight line between the two types of dendrimers and up to the 5th generation for the PyC4-HMPA-GY series. The Pearson correlation coefficient for the data shown in Figures 2.6C and D took a same value of 0.995 indicating an extremely strong correlation between $\langle k \rangle$ and $[Py]_{\text{loc}}$. Visual inspection of Figure 2.5 indicates that different trends obtained with different linker lengths of the different pyrene derivatives employed to fluorescently label the PAMAM and HMPA dendrimers were satisfyingly accounted for by applying Equations 2.4 and 2.5, since all data points clustered along master lines. It also suggests that $\langle k \rangle$ responds directly to $[Py]_{\text{loc}}$ and that this dependency can be employed to draw conclusions about the macromolecule under study. In the case of the low generation PAMAM and HMPA dendrimers, their internal chain segments appear to be well described by Gaussian statistics.

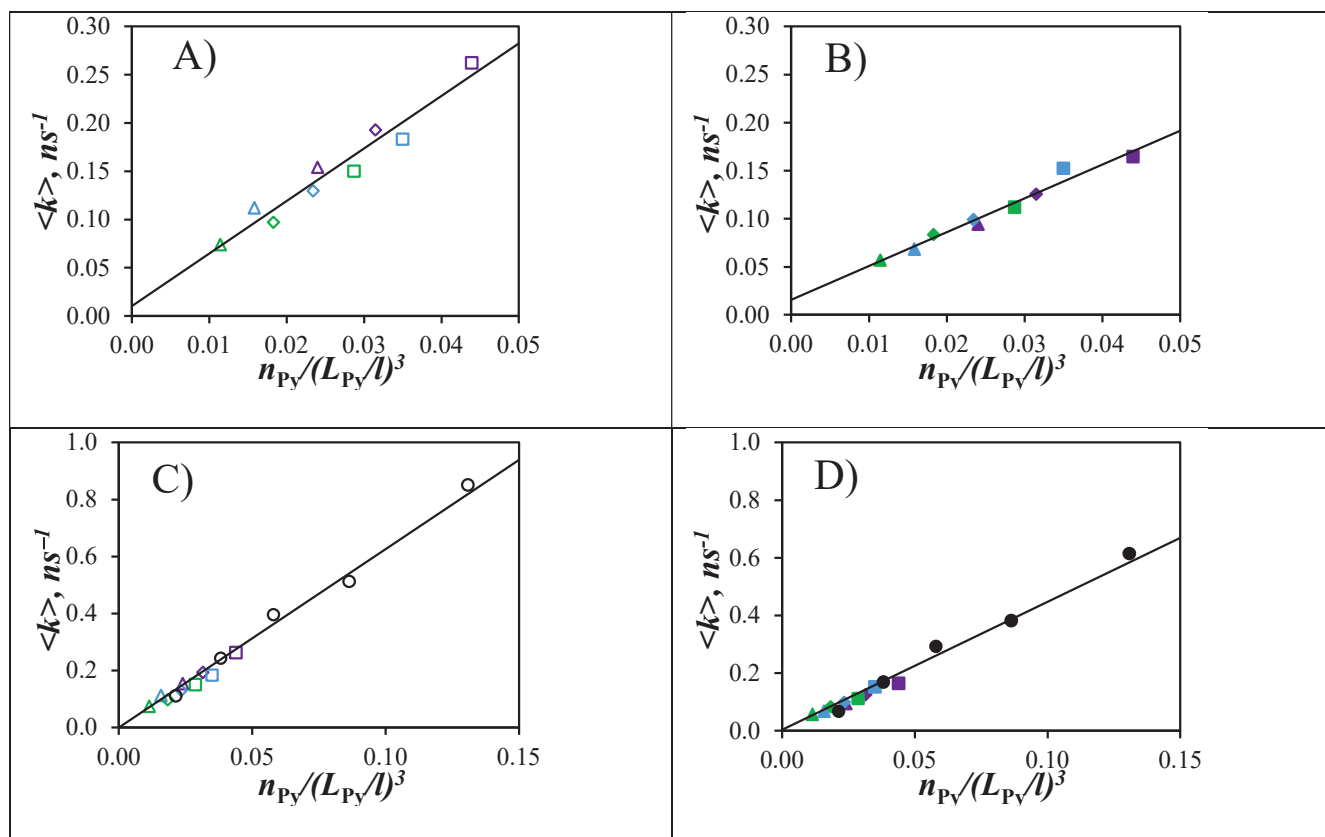


Figure 0.6 Plot of $\langle k \rangle$ as a function of $[Py]_{loc}$ for PyCX-PAMAM-GY samples acquired in A)

DMF and B) DMSO and PyC4-HMPA-GY samples acquired in C) DMF and D) DMSO. \triangle , \diamond and \square represent PAMAM generation 0, 1 and 2, respectively, while purple, blue and green represent PyCX-PAMAM-GY dendrimers labeled with 1-pyrene-butyric, -octanoic, and -dodecanoic acid, respectively. \odot and \bullet for the PyC4-HMPA-GY samples in DMF and DMSO, respectively.

It is however noticeable that the trends in Figure 2.6 are solvent-dependent. The lower slope obtained in DMSO compared to DMF is a consequence of PEF being diffusion-controlled in the pyrene-labeled dendrimers (see large f_{diff} values in Figure 2.5). Since $\langle k \rangle$ equals the product $k_{diff} \times [Py]_{loc}$, the higher solvent viscosity of DMSO ($\eta = 1.99$ mPa.s at 25 °C) than DMF ($\eta = 0.79$ mPa.s at 25 °C) implies that k_{diff} , which is inversely proportional to solvent viscosity, is lower in

DMSO than in DMF. At first glance, differences in solvent viscosities could be dealt with by simply multiplying $\langle k \rangle$ by the solvent viscosity. Unfortunately, k_{diff} depends also on the probability (p) of forming an excimer upon encounter between an excited and a ground-state pyrene and this probability depends on the solvent.⁹ Instead, the effect of solvent on $\langle k \rangle$ can be accounted for by determining k_{diff} for a model compound.²² Since k_{diff} accounts for solvent viscosity and p , dividing $\langle k \rangle$ by k_{diff} yields the ratio $\langle k \rangle/k_{\text{diff}}$ which no longer depends on solvent viscosity and p .

The bimolecular rate constant k_{diff} was determined for hexyl-1-pyrenebutyramide (Hx-PyBA) by acquiring the monomer and excimer fluorescence decays in DMF and DMSO with Hx-PyBA concentrations ranging from 10 to 30 mmol/L. The fluorescence decays were fitted with the MFA to yield the $\langle k \rangle$ values, which were plotted as a function of the Hx-PyBA concentration in Figure S26. Straight lines were obtained whose slopes yielded k_{diff} found to equal 1.05 (± 0.01) and 0.700 (± 0.003) $\text{M}^{-1} \cdot \text{ns}^{-1}$ in DMF and DMSO, respectively.

k_{diff} was then used to calculate the $\langle k \rangle/k_{\text{diff}}$ ratio, which was plotted against $n_{\text{Py}}/(L_{\text{Py}}/l)^3$ in Figure 2.7A for the PyCX-PAMAM-GY samples. All the data points clustered around a master line with a Pearson correlation coefficient equal to 0.97 indicating a strong correlation. A plot of $\langle k \rangle/k_{\text{diff}}$ against $n_{\text{Py}}/(L_{\text{Py}}/l)^3$ is provided in Figure 2.7B for all PyCX-PAMAM-GY and PyC4-HMPA-GY dendrimers. A strong correlation with a Pearson correlation coefficient equal to 0.99 was obtained demonstrating the direct relationship existing between $\langle k \rangle/k_{\text{diff}}$ and $n_{\text{Py}}/(L_{\text{Py}}/l)^3$.

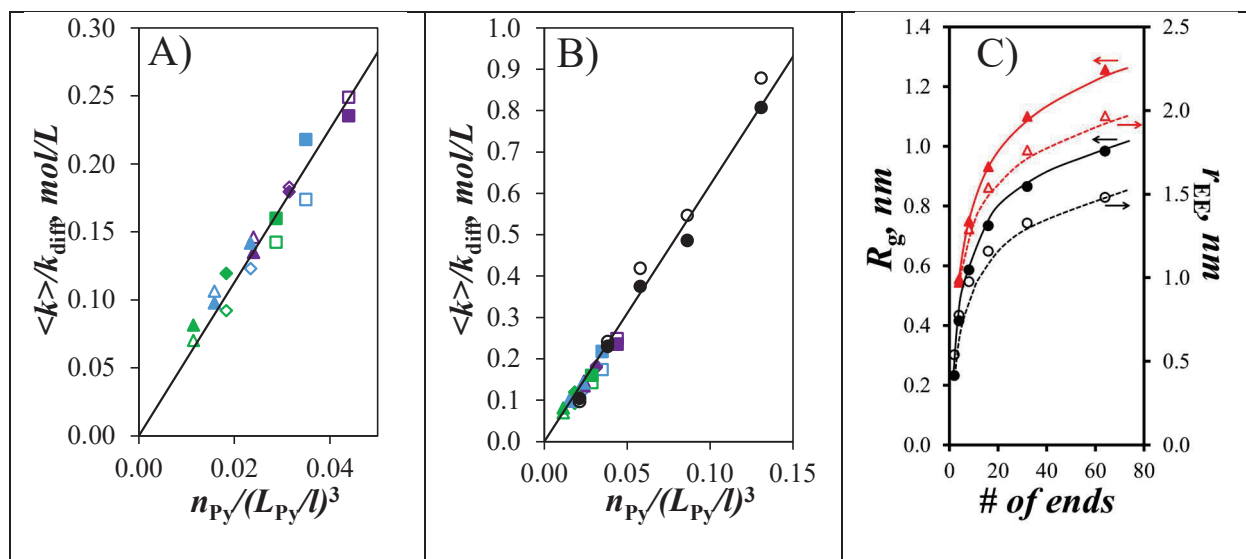


Figure 0.7 Plot of $\langle k \rangle$ as a function of $n_{Py}/(L_{Py}/l)^3$ for A) the PyCX-PAMAM-GY samples and B)

the PyCX-PAMAM-GY and PyC4-HMPA-GY samples. \blacktriangle , \blacklozenge and \blacksquare represent PAMAM generation 0, 1 and 2, respectively, while purple, blue and green represent PyCX-PAMAM-GY dendrimers labeled with 1-pyrene-butyric, -octanoic, and -dodecanoic acid, respectively. (\bullet , \bullet) for the PyC4-HMPA-GY samples. Hollow for DMF and solid for DMSO. C) Plot of (solid) R_g and (hollow) r_{EE} as a function of dendrimer ends for the unlabeled (\blacktriangle , \blacktriangle) PAMAM and (\bullet , \bullet) HMPA dendrimers.

Since the strong correlations found between $\langle k \rangle / k_{diff}$ and $n_{Py}/(L_{Py}/l)^3$ for the low generation PAMAM and HMPA dendrimers with different chemical compositions were obtained by assuming that the internal oligomeric segments constituting the dendrimer interior obeyed Gaussian statistics, R_g and the average end-to-end distance (r_{EE}) of the unlabeled PAMAM and HMPA dendrimers could be determined using the equations listed in Table S2.9 in SI. Since a same generation number yields different numbers of terminals for the PAMAM and HMPA dendrimers, R_G and r_{EE} were plotted as a function of the number of unlabeled ends in Figure 2.7C. These calculations were performed up to a maximum of 64 ends corresponding to a G4 PAMAM

dendrimer or a G6 HMPA dendrimer. R_G and r_{EE} were smaller for the HMPA dendrimers compared to the PAMAM dendrimers for a same number of end groups indicating that the HMPA dendrimers are denser than the PAMAM dendrimers. This conclusion agrees with the finding that $\langle k \rangle$, and thus $[Py]_{loc}$, is much larger for the PyC4-HMPA-GY dendrimers than for the PyC4-PAMAM-GY dendrimers for a same number of end groups as found experimentally in Figure 2.7B.

2.4 CONCLUSIONS

This study has established that the pseudo-unimolecular rate constant for PEF $\langle k \rangle$ responds directly to $[Py]_{loc}$ and that the relationship between $\langle k \rangle$ and $[Py]_{loc}$ can be employed to characterize the conformation of complex macromolecules labeled with more than two pyrenes. This represents a major departure from the current employment of fluorescence collisional quenching experiments for the quantitative characterization of macromolecules in solution, since such experiments are solely applied to linear monodisperse chains labeled at their opposite ends with a dye and a quencher. In contrast, the experiments presented in this study were conducted with PAMAM dendrimers decorated with a minimum of 4 and up to 16 pyrenyl labels, where $[Py]_{loc}$ was adjusted in a controlled manner by increasing either the generation number of the PAMAM dendrimers from 0 to 2 or the length of the linker connecting the pyrenyl labels to the PAMAM dendrimers from 4 to 12 carbon atoms. The linear response between $\langle k \rangle$ and $[Py]_{loc}$ found not only for the nine PyCX-PAMAM-GY samples but also the five PyC4-HMPA-GY samples suggests that the direct relationship between $\langle k \rangle$ and $[Py]_{loc}$ is general and can be applied to characterize the conformation of the numerous macromolecules with an architecture much more complex than linear polymer chains such as the dendrimers probed in the present study. The PEF experiments

described herein appear to nicely complement the scattering experiments typically conducted to characterize the conformation of large macromolecules, but which fail with small macromolecules that do not provide sufficient scattering signal as illustrated herein with the low generation PAMAM and HMPA dendrimers.

Chapter 3: Intra-Macromolecular Conformational Changes in Low Generation PAMAM Dendrimers Probed by Pyrene Excimer Formation

Adapted with permission from Patel, S.; McNelles, S.; Adrovnov, A.; Duhamel, J. Intramacromolecular Conformational Changes in Low Generation PAMAM Dendrimers Probed by Pyrene Excimer Formation. *J. Phys. Chem. B* **2023**, *127*, 8040-8048, Copyright 2023 American Chemical Society.

3.1 ABSTRACT

Pyrene excimer formation (PEF) was used to probe the intra-macromolecular conformational change experienced by low generation pyrene-labeled PAMAM dendrimers referred to as PyCX-PAMAM-GY, where X (= 4, 8, or 12) and Y (= 0, 1, or 2) represent the number of atoms in the pyrenyl linker and the dendrimer generation, respectively. Each sample was studied in *N,N*-dimethylformamide (DMF) and dimethyl sulfoxide (DMSO) with and without 5 mM HCl. Global analysis of the monomer and excimer time-resolved fluorescence decays using the model free analysis (MFA) yielded the average rate constant of excimer formation, $\langle k \rangle$, which was compared with the local pyrene concentration ($[Py]_{loc}$) of the PyCX-PAMAM-GY samples calculated by assuming that the oligomeric segments constituting the dendrimer's interior obeyed Gaussian statistics. A notable decrease in $\langle k \rangle$ was observed upon the addition of 5 mM HCl to the PyCX-PAMAM-GY solutions and was attributed to swelling of the dendrimers resulting from the protonation of the internal tertiary amines. The reversibility of this conformational change could also be monitored via PEF. Solvent differences between DMF and DMSO were accounted for by dividing $\langle k \rangle$ by k_{diff} , the bimolecular rate constant for diffusive PEF of a *n*-hexyl-1-pyrenebutyramide model compound, to yield the $\langle k \rangle/k_{diff}$ ratio. Comparison between the $\langle k \rangle/k_{diff}$ ratios obtained for all the PyCX-PAMAM-GY samples with and without 5 mM HCl revealed a 13 % increase in the radius of the PAMAM-GY dendrimers upon protonation of their internal tertiary amines in agreement with earlier reports. These experiments illustrate that PEF represents a powerful experimental means to quantitatively probe the intra-conformational changes of complex macromolecules in solution, in a manner that complements scattering techniques.

3.2 INTRODUCTION

Since their introduction in 1985, PAMAM dendrimers have led to thousands of studies. Yet despite this intense scrutiny, few experimental studies have been able to quantitatively characterize the conformation of low generation PAMAM dendrimers (G0 – G3) in solution. Getting quantitative information about the conformation of low generation dendrimers is challenging due to their weak scattering which complicates their conformational characterization through the determination of their radius of gyration (R_G), a measure of the mass distribution in space of the macromolecule, by scattering techniques like static light scattering (SLS) or small angle X-ray (SAXS) or neutron (SANS) scattering. Another complication in the study of protonated PAMAM dendrimers is the existence of long range electrostatic interactions that must be accounted for due to the relatively high 10 – 50 g/L concentrations typically used to study PAMAM dendrimers by scattering techniques.¹⁻⁴ The difficulty in accounting for intermacromolecular interactions between PAMAM dendrimers might be one reason why conclusions drawn from scattering techniques about the conformation of protonated PAMAM dendrimers differ somewhat from those obtained by molecular dynamics simulations (MDS) on isolated PAMAM dendrimers. Based on R_G values, scattering studies indicate that the volume of PAMAM dendrimers does not change much upon protonation, although a rearrangement of the internal segments in the PAMAM dendrimers is observed during protonation.¹⁻⁴ In fact the invariance of R_G obtained by scattering techniques for PAMAM dendrimers upon protonation has led some to conclude that *R_G is not suitable as the index parameter to characterize the dendrimer conformation change.*³ In contrast, the R_G values obtained from MDS have been shown to increase upon protonation by 4 to up to 180 %.⁵⁻⁹ More recently, full atomistic MDS have found a 28 (± 4) % increase in R_G upon protonation of PAMAM dendrimers for generations between G1 and G6.¹⁰

Since the high PAMAM concentrations used in scattering experiments induce intermacromolecular interactions that might be difficult to account for, techniques capable of probing the conformation of macromolecules at much lower polymer concentration to prevent intermacromolecular interactions are of interest. In this context, a methodology based on pyrene excimer formation (PEF) could prove useful. It was recently applied to characterize the conformation of PAMAM dendrimers using polymer concentration of 0.001 g/L,¹¹ more than 4 orders of magnitude lower than scattering techniques.^{1-4,12,13} The pyrene end-labeled PAMAM dendrimers were referred to as PyCX-PAMAM-GY, where $X = 4, 8,$ and 12 represents a 1-pyrenebutyryl, -octanoyl, and -dodecanoyl label and Y indicates the generation number equal to 0, 1, and 2. The square root of the average squared end-to-end distance $\langle L_{py}^2 \rangle^{1/2}$ separating every two pyrenyl labels for the nine PyCX-PAMAM-GY samples was calculated by assuming that the internal segments of the PAMAM dendrimers obeyed Gaussian statistics. This assumption was validated by applying it to calculate the radius of gyration (R_G) of low generation PAMAM dendrimers and demonstrating that the calculated R_G showed the same trend as a function of generation number found by MDS.⁷ $\langle L_{py}^2 \rangle^{1/2}$ was used to demonstrate that the average rate constant $\langle k \rangle$ for PEF was proportional to the local pyrene concentration $[Py]_{loc}$ inside a dendrimer expressed as $n_{py} / \langle L_{py}^2 \rangle^{3/2}$, where n_{py} is the number of ground-state pyrenes in a pyrene end-labeled dendrimer. L_{py} accounts for the length of the linker connecting the pyrenyl moiety to the PyCX-PAMAM-GY sample with $\langle L_{py}^2 \rangle^{1/2}$ being equal to the average end-to-end distance (r_{EE}) in the hypothetical case where the pyrenyl group could be covalently linked directly onto the reactive ends of a PAMAM dendrimer. In essence, this first study established a new way to probe the local density of PAMAM dendrimers through PEF measurements providing a means to determine R_G and r_{EE} for low generation PAMAM dendrimers at extremely low polymer concentration.¹¹

To further expand the methodology combining PEF measurements to determine $\langle k \rangle$ and the mathematical derivation of R_G , r_{EE} , or $\langle L_{py}^2 \rangle^{1/2}$, the extreme sensitivity of PEF was employed to probe the conformational change undergone by the pyrene end-labeled PAMAM dendrimers upon protonation at a concentration of 1 mg/L. A 1 mg/L PAMAM concentration is so low that in the case of G0 PAMAM dendrimers, each macromolecule would be separated by an average of 172 nm, a distance long enough to eliminate intermolecular interactions between protonated PAMAM dendrimers induced by long range electrostatic forces and enabling the conformational study of protonated low generation PAMAM dendrimers as isolated macromolecules in solution. The PEF experiments conducted with 5 mM HCl on the protonated pyrene end-labeled dendrimers indicated a 33 % reduction in $\langle k \rangle$ corresponding to a 13 % increase in R_G or r_{EE} . Although only the internal tertiary amines were protonated for the PyCX-PAMAM-GY samples, the 13 % increase in R_G expected from the PEF measurements was in good agreement with the ~16 % increase in R_G found by MDS for PAMAM dendrimers of generation G4, G5, and G6⁷ and the 13 % increase for generation G8^{6,10} and G9¹⁰ with protonated internal tertiary and terminal primary amines. However, the increase in R_G found by PEF upon protonation of PAMAM dendrimers was lower than that of 28 (± 4) % determined by more recent all atom MDS for generations between G1 and G6.¹⁰ Nevertheless, the expansion in the PAMAM dendrimer volume detected in the present study upon protonation stands in stark contrast with the invariance of R_G deduced from scattering experiments at much larger PAMAM concentrations.¹⁴ It also suggests that PEF-based methodologies enable the characterization of the conformation of protonated PAMAM dendrimers that are isolated in solution, a capability that could be extended to the study of any macromolecule in solution.

3.3 EXPERIMENTAL

Chemicals: The preparation of the PyCX-PAMAM-GY dendrimers, where $X = 4, 8,$ and 12 and $Y = 0, 1,$ or $2,$ and the model compounds *n*-hexyl-1-pyrenebutyramide (Hx-PyBA), *n*-ethyl-1-pyreneoctanamide (Et-PyOA), and *n*-ethyl-1-pyrenedodecanamide (Et-PyDA) used to determine the natural lifetime τ_M of the different pyrene derivatives was described in an earlier publication.¹¹ All other chemicals were purchased from Sigma-Aldrich. The ¹H NMR and MALDI-TOF spectra of all the constructs can be found in an earlier publication¹¹ while the chemical formula for each PyCX-PAMAM-GY construct is given in Table 3.1.

Instrumentation: The same instruments described in the study of the PyCX-PAMAM-GY samples without HCl were used in the present study.¹¹ In brief, a Varian Cary 100 Bio spectrophotometer (Varian, Palo Alto, CA, USA) was employed to acquire the absorption spectra with a 1 cm pathlength quartz cuvette. The solution for fluorescence measurements were diluted to ensure that the absorbance at 345 nm equaled 0.1 equivalent to a pyrene concentration of about 2.5×10^{-6} M or a dendrimer concentration varying between 1.0 and 1.5 mg/L, low enough to prevent intermolecular pyrene excimer formation. The solutions were then degassed for 35 minutes by bubbling N₂ before acquiring the fluorescence spectra and decays on a QM-400 spectrofluorometer and a FluoroHub time-resolved fluorometer from HORIBA, respectively. The PyCX-PAMAM-GY constructs were excited at 345 nm. The fluorescence spectra were recorded from 355 to 600 nm. The $(I_E/I_M)^{SSF}$ ratio describing the PEF efficiency was calculated by taking the ratio of the fluorescence intensity of the excimer, I_E , integrated from 500 to 530 nm over that of the monomer, I_M , integrated from 376 to 382 nm. For the time-resolved fluorescence experiments, the PyCX-PAMAM-GY solutions were excited with a 336 nm DeltaDiode laser and the monomer and excimer fluorescence decays were acquired at 379 and 510 nm with a 370 and 490 nm cut-off

filter, respectively, to minimize stray light from reaching the detector through the emission monochromator. A reflective aluminium monolith was used to acquire the instrument response function (IRF) by monitoring the signal reflected off its surface at 336 nm, the wavelength emitted by the exciting laser. Each fluorescence decay was acquired with up to 20,000 counts at its maximum over 1,024 channels. Time-per-channel values of 0.1, 0.44, or 0.87 ns were used. The quality of the global decay fits with the model free analysis (MFA)^{14,15} was assessed from the random distribution of the residuals and autocorrelation of the residuals around zero and a low χ^2 (< 1.3). An example of the fits can be found in Figure S3.1 of the SI. The fluorescence decays for the Hx-PyBA model compound to determine k_{diff} were acquired at high Hx-PyBA concentrations with the front-face geometry, while all the other fluorescence decays were acquired with the normal right-angle geometry.

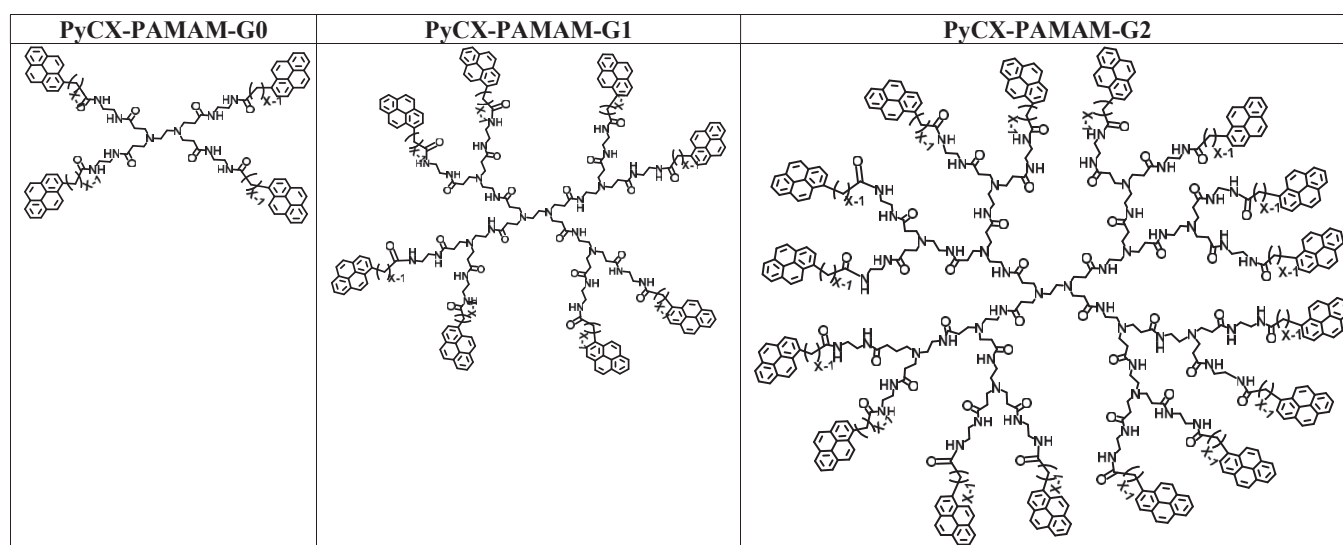
Model-Free Analysis (MFA) of the Fluorescence Decays: The monomer and excimer fluorescence decays of the PyCX-PAMAM-GY samples were fitted globally according to the MFA with Equations S3.1 and S3.2 provided in the SI. According to the MFA, the pyrenyl labels can be in one of three states. The species Py_{free}^* represents the isolated pyrenes that are unable to form excimer and emit as if they were free in solution with the lifetime τ_M , the species Py_{diff}^* forms excimer upon diffusive encounter with a ground-state pyrene, and the species Py_{agg}^* describes these excited pyrenyl labels that are aggregated with ground-state pyrenes. Depending on whether Py_{agg}^* forms a well-stacked ($E0^*$) or poorly stacked (D^*) dimer, Py_{agg}^* emits with a lifetime equal to either τ_{E0} or τ_D , respectively. The PyC4-PAMAM-GY samples showed a short-lived excimer species (ES^*), which was accounted for by adding an extra exponential with a lifetime τ_{ES} equal to 3.5 ns that was fixed in the decay analysis. Since it was much shorter-lived than the other pyrenyl species, its contribution was not accounted for to calculate the molar fractions. Global analysis of

the monomer and excimer fluorescence decays yields the pre-exponential factors (a_i) and decay times (τ_i), which are used in Equation 3.2 to calculate the average lifetime ($\langle \tau \rangle$) of the monomer decay (excluding the contribution from $P_{y_{free}^*}$) and the average rate constant $\langle k \rangle$ for PEF, as well as the molar fractions f_{free} , f_{diff} , and f_{agg} for the pyrenyl species $P_{y_{free}^*}$, $P_{y_{diff}^*}$, and $P_{y_{agg}^*}$, respectively. The parameters retrieved from the MFA can be used to calculate the absolute I_E/I_M ratio ($(I_E/I_M)^{TRF}$) with Equation 3.1 and $\langle k \rangle$ with Equation 3.2. The lifetime τ_M in the decay analysis was fixed to equal 173 ns, 161 ns, and 161 ns in DMF and 138 ns, 130 ns, and 130 ns in DMSO based on the lifetime of the model compounds Hx-PyBA, Et-PyOA, and Et-PyDA in the same solvents without 5 mM HCl, respectively. All τ_M values remained the same with 5 mM HCl except for Hx-PyBA in DMF, which had a lifetime of 169 ns.

$$(I_E / I_M)^{TRF} = \frac{(f_{diffE0}\tau_{E0} + f_{diffD}\tau_D) \langle k \rangle \langle \tau \rangle + f_{E0}\tau_{E0} f_D\tau_D}{(f_{diffE0} + f_{diffD}) \langle \tau \rangle + f_{free}\tau_M} \quad (3.1)$$

$$\langle k \rangle = \frac{\sum_{i=1}^n a_i}{\sum_{i=1}^n a_i \tau_i} - \frac{1}{\tau_M} = \frac{1}{\langle \tau \rangle} - \frac{1}{\tau_M} \quad (3.2)$$

Table 0.1. Chemical structure for each PyCX-PAMAM-GY construct where $X = 4, 8,$ and 12 for 1-pyrene-butryryl, -octanoyl, and -dodecanoyl labels, respectively.



3.4 RESULTS AND DISCUSSION

Parameterization of the PyCX-PAMAM-GY dendrimers to obtain $[Py]_{loc}$: Based on the parametrization introduced earlier for the PyCX-PAMAM-GY dendrimers,¹¹ the local pyrene concentration ($[Py]_{loc}$) would be expected to take the expression provided in Equation 3.3. In Equation 3.3, n_{Py} represents the number of ground-state pyrenes equal to $2^{N+2} - 1$ in a PAMAM dendrimer of generation N , $V_{dendrimer}$ is the dendrimer volume approximated as a sphere of diameter equal to the square root of $\langle L_{Py}(N)^2 \rangle$, which is the average squared end-to-end distance of the dendrimer whose expression is provided in Equation 3.4, and l is a normalization parameter that can be viewed as a bond length. In Equation 3.4, b (= 7) and c (= 4) correspond to the aminoethyl propionamide building block and ethylene diamine core in the PAMAM dendrimer, respectively, and a represents the number of atoms in the 1-pyrene-butyryl, -octanoyl, or -dodecanoyl derivatives equal to 4, 8, or 12, respectively. Combination of Equations 3.3 and 3.4 yields $n_{Py}/(\langle L_{Py}^2 \rangle^{1/2}/l)^3$ which was taken to represent $[Py]_{loc}$. The validity of Equations 3.3 and 3.4 was established for the PyCX-PAMAM-GY dendrimers in an earlier publication.¹¹

$$[Py]_{loc} = \frac{n_{Py}}{V_{dendrimer}} = \frac{n_{Py}}{(\pi/6) \times \langle L_{Py}(N)^2 \rangle^{3/2}} \propto \frac{n_{Py}}{(\langle L_{Py}(N)^2 \rangle / l^2)^{3/2}} \quad (3.3)$$

$$\langle L_{Py}^2(N) \rangle = \left(2a + \frac{[2 - 2^{N+2} + (N+1) \times 2^{N+3}] b + 2^{N+1} c + 2^{N+1} - 1}{2^{N+2} - 1} \right) \times l^2 \quad (3.4)$$

Steady-state fluorescence spectra: The steady-state fluorescence (SSF) spectra for all samples were acquired with 5 mM HCl in *N,N*-dimethylformamide (DMF) and dimethyl sulfoxide (DMSO) and they are shown in Figure 3.1. These fluorescence spectra display the typical features expected

from the pyrene monomer and excimer, with sharp peaks between 370 and 410 nm and a broad band centred at 480 nm, respectively. The fluorescence spectra were analyzed by determining the $(I_E/I_M)^{\text{SSF}}$ ratio obtained by dividing the intensity of the excimer from 500 to 530 nm (I_E) by the intensity of the monomer from 376 to 382 nm (I_M) to represent the efficiency of pyrene excimer formation. The $(I_E/I_M)^{\text{SSF}}$ ratios obtained for the PyCX-PAMAM-GY samples in DMF and DMSO with 5 mM HCl were plotted in Figure 2A as a function of $n_{\text{Py}}/(\langle L_{\text{Py}}^2 \rangle^{1/2}/l)^3$ taken as a measure of $[\text{Py}]_{\text{loc}}$ along with the $(I_E/I_M)^{\text{SSF}}$ ratios of the same PyCX-PAMAM-GY solutions obtained earlier without HCl.¹¹

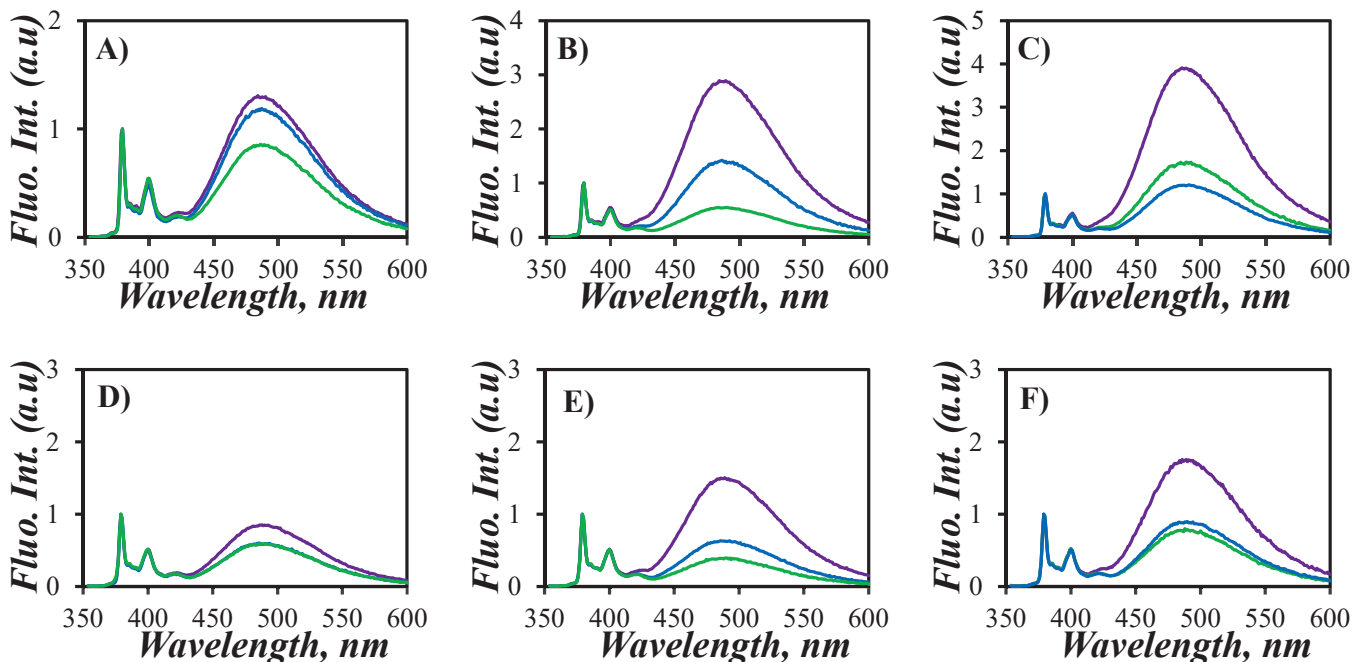


Figure 0.1 Fluorescence spectra of the PyCX-PAMAM-GY samples in DMF (top row) and DMSO (bottom row) with 5 mM HCl for $X = 4$ (—), 8 (—), or 12 (—) and $Y = 0$ (A & D), 1 (B & E), and 2 (C & F).

No discernible trend was observed between the $(I_E/I_M)^{\text{SSF}}$ ratios and $[\text{Py}]_{\text{loc}}$ contrary to expectation.¹⁶ However, this outcome was not surprising considering that $(I_E/I_M)^{\text{SSF}}$ is extremely

sensitive to the presence of a minute amount of unattached pyrene, whose fluorescence quantum yield can be 100 times larger than that of a pyrenyl monomer attached onto macromolecules.¹⁷⁻¹⁹ Clearly, quantitative information about the conformation of PyCX-PAMAM-GY samples in solution cannot be extracted from fluorescence spectra and the interpretation of $(I_E/I_M)^{SSF}$ ratios requires that the contribution of unattached pyrenyl labels be eliminated. This is accomplished through the analysis of the time-resolved fluorescence decays.

Model Free Analysis of the Fluorescence Decays: The time-resolved fluorescence (TRF) decays for all PyCX-PAMAM-GY samples were acquired in DMF and DMSO with 5 mM HCl, in DMF with 5 mmol NaOH, or in DMF with 5 mM HCl followed by the addition of 10 mM NaOH. The decays were globally fitted in accordance with the model free analysis (MFA) and all parameters from the decay fits can be found in Supporting Information (SI) in Tables S3.1 to S3.24. The results obtained for the PyCX-PAMAM-GY samples with 5 mM HCl were compared to those obtained for the same dendrimers without HCl earlier.¹¹ The $(I_E/I_M)^{TRF}$ ratios were calculated with Equation 3.1 by using the parameters obtained from the MFA of the decays and they were compared to the $(I_E/I_M)^{SSF}$ ratios in Figure 3.2B. They showed a strong correlation with a Pearson correlation coefficient equal to 0.97. The strong positive correlation between $(I_E/I_M)^{SSF}$ and $(I_E/I_M)^{TRF}$ suggests that the MFA parameters obtained from the global analysis of the fluorescence decays provided an accurate representation of the fluorescence of the PyCX-PAMAM-GY samples shown in the fluorescence spectra in Figure 3.1. However, unlike the $(I_E/I_M)^{SSF}$ ratios, the $(I_E/I_M)^{TRF}$ ratios can be calculated in the absence of unattached pyrene by setting f_{free} , the molar fraction of unattached pyrene, to zero which yields the ratio $(I_E/I_M)^{TRF}(f_{free}=0)$. Contrary to the $(I_E/I_M)^{SSF}$ ratios in Figure 3.2A, the $(I_E/I_M)^{TRF}(f_{free}=0)$ ratios plotted as a function of $n_{Py}/(\langle L_{Py}^2 \rangle^{1/2}/l)^3$ yielded distinct lines in

Figures 3.2C and D with Pearson correlation coefficients equal to 0.92 in DMF without HCl, 0.96 in DMF with 5 mM HCl, 0.98 in DMSO without HCL, and 0.90 in DMSO with 5 mM HCl. In each case the Pearson correlation coefficients approached unity, indicating a strong positive correlation between $(I_E/I_M)^{\text{TRF}}(f_{\text{free}}=0)$ and $[Py]_{\text{loc}}$.

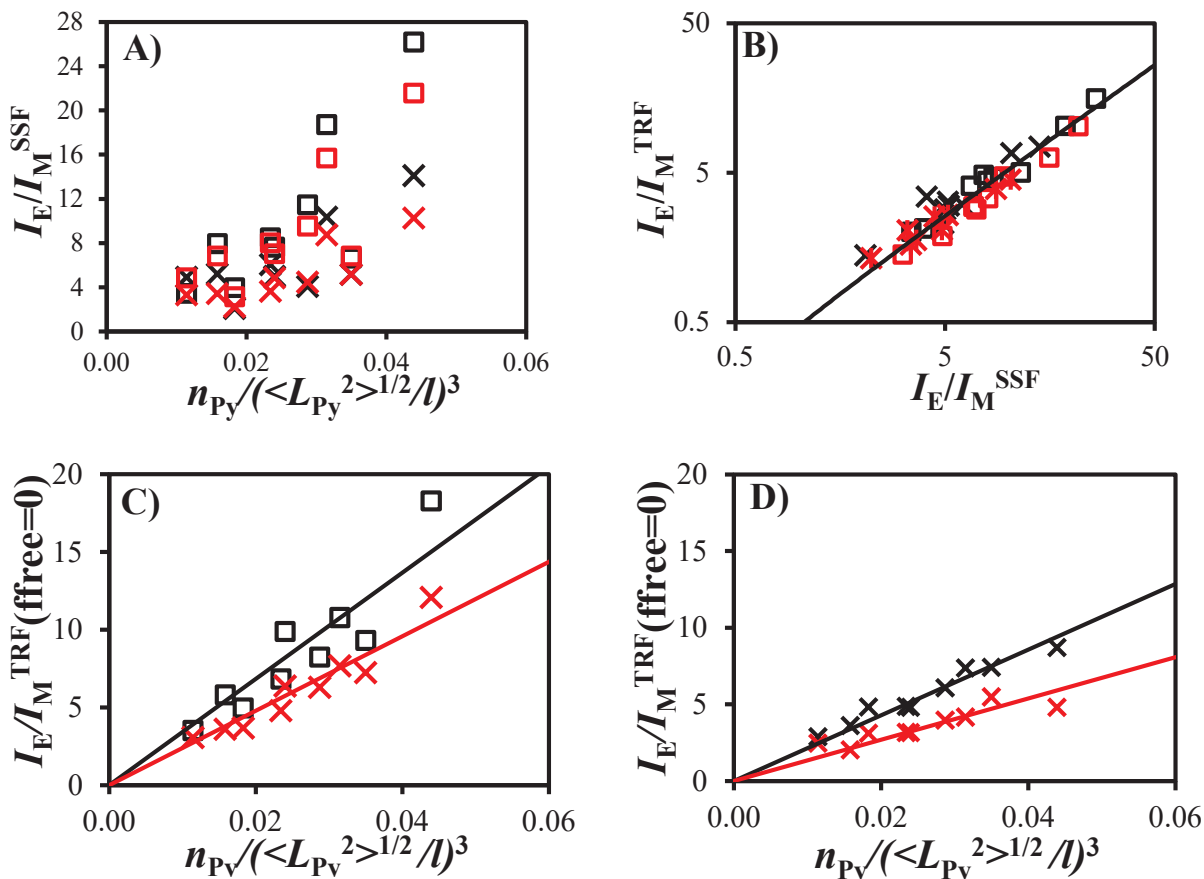


Figure 0.2 A plot of A) $(I_E/I_M)^{\text{SSF}}$ as a function of $n_{\text{Py}}/(\langle L_{\text{Py}}^2 \rangle^{1/2}/l)^3$, B) $(I_E/I_M)^{\text{TRF}}$ as a function of $(I_E/I_M)^{\text{SSF}}$ and $(I_E/I_M)^{\text{TRF}}(f_{\text{free}}=0)$ as a function of $n_{\text{Py}}/(\langle L_{\text{Py}}^2 \rangle^{1/2}/l)^3$ acquired in C) DMF (\blacksquare , $\color{red}\square$) or D) DMSO (\blacktimes , $\color{red}\times$) without (black) or with (red) 5 mM HCl.

Considering the strong relationship between $(I_E/I_M)^{\text{TRF}}(f_{\text{free}}=0)$ and $n_{\text{Py}}/(\langle L_{\text{Py}}^2 \rangle^{1/2}/l)^3$ taken as a measure of $[Py]_{\text{loc}}$ in Figures 3.2C and D, the reduction in the slopes of the straight lines in red obtained for the PyCX-PAMAM-GY dendrimers in both solvents with 5 mM HCl compared to the straight lines in black obtained without HCl implied that $[Py]_{\text{loc}}$ was lower with 5 mM HCl. A lower $[Py]_{\text{loc}}$ would be expected if protonation of the internal tertiary amines of the PyCX-PAMAM-GY dendrimers induced by HCl would result in a larger macromolecular volume, which would dilute the pyrenyl labels. In turn, this conclusion indicates that PEF measurements can probe the expansion of the interior of PAMAM dendrimers under acidic conditions.

Regardless of the presence or absence of 5 mM HCl in the solvents, the $(I_E/I_M)^{\text{TRF}}(f_{\text{free}}=0)$ ratios obtained in DMSO were also consistently lower compared to their corresponding values in DMF. Considering that PEF is a diffusion-controlled process and that DMSO has a higher viscosity ($\eta = 1.99$ mPa.s at 25 °C) compared to DMF ($\eta = 0.79$ mPa.s at 25 °C), this trend is not surprising and serves to further demonstrate that the $(I_E/I_M)^{\text{TRF}}(f_{\text{free}}=0)$ ratios calculated from the MFA parameters respond to solvent effects, as expected. The molar fractions f_{diff} , f_{free} , and f_{agg} of the pyrenyl species Py_{diff}^* , Py_{free}^* , and Py_{agg}^* were calculated and they were plotted as a function of $n_{\text{Py}}/(\langle L_{\text{Py}}^2 \rangle^{1/2}/l)^3$ in Figure 3.3. In both DMF and DMSO with or without HCl, f_{diff} was above 0.80 for all but three samples, prepared with PyBA, that seemed to generate more pyrene aggregation. Nevertheless, the majority of f_{diff} values approached unity indicating that PEF occurred primarily through diffusive encounters. Furthermore, the molar fractions f_{free} and f_{agg} remained relatively low, suggesting a low amount of unattached and aggregated pyrenyl labels, respectively. Despite the low amount of Py_{free}^* species, their large fluorescence quantum yield was sufficient to scramble the $(I_E/I_M)^{\text{SSF}}$ ratios resulting in the absence of any discernable trend in Figure 3.2A.

Although the $(I_E/I_M)^{\text{TRF}}(f_{\text{free}}=0)$ ratio and the molar fractions provide quantitative information about the PyCX-PAMAM-GY constructs, their calculations are more complicated due to the involvement of the excimer decays. A simpler parameter to interpret is the pseudo-unimolecular average rate constant of excimer formation ($\langle k \rangle$) given in Equation 3.2. $\langle k \rangle$ is equal to $k_{\text{diff}} \times [Py]_{\text{loc}}$ and should thus increase linearly with the $[Py]_{\text{loc}}$. Consequently, $\langle k \rangle$ was plotted as a function of $n_{\text{Py}}/(\langle L_{\text{Py}}^2 \rangle^{1/2}/l)^3$ in Figure 3.4. $\langle k \rangle$ increased linearly with $n_{\text{Py}}/(\langle L_{\text{Py}}^2 \rangle^{1/2}/l)^3$ regardless of solvent conditions. Pearson correlation coefficients were found to equal 0.97 in DMF without HCl, 0.98 in DMF with 5 mM HCl, 0.99 in DMSO without HCl, and 0.93 in DMSO with 5 mM HCl. The strong positive correlation between $\langle k \rangle$ and $n_{\text{Py}}/(\langle L_{\text{Py}}^2 \rangle^{1/2}/l)^3$ evidenced by the Pearson correlation coefficients approaching unity implied that the parametrization of the dendrimers, based on the assumption that the internal oligomeric segments constituting the PyCX-PAMAM-GY samples obey Gaussian statistics, was valid in both DMF and DMSO with and without 5 mM HCl.

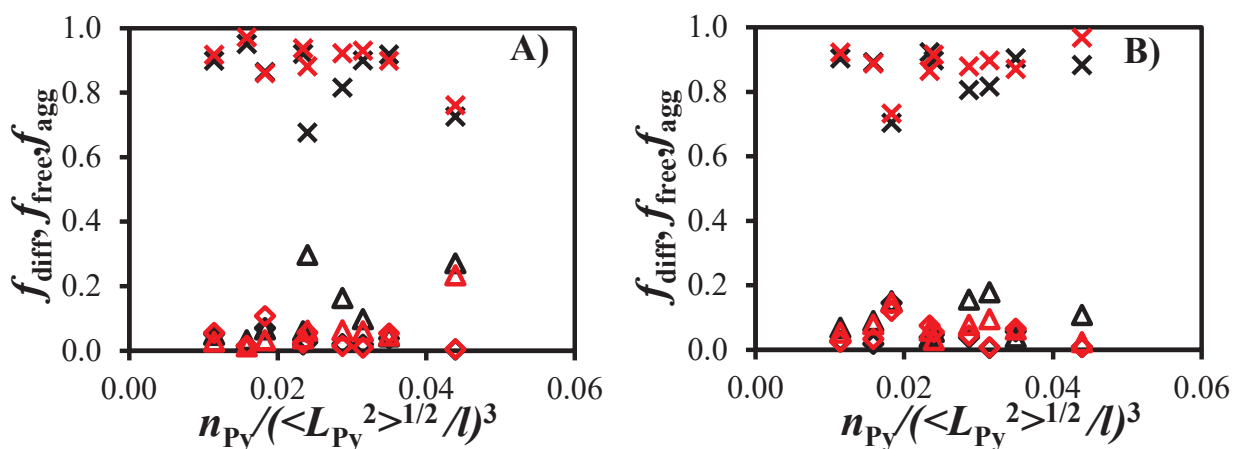


Figure 0.3 A plot of the molar fractions f_{free} ($\blacklozenge, \redlozenge$), f_{diff} (\blackcross, \redcross), and f_{agg} ($\blacktriangle, \redtriangle$) determined from the MFA of the fluorescence decays as a function of $n_{\text{Py}}/(\langle L_{\text{Py}}^2 \rangle^{1/2}/l)^3$ acquired in A) DMF and B) DMSO without (black) and with (red) of 5 mM HCl.

As for the $I_E/I_M^{\text{TRF}}(f_{\text{free}}=0)$ ratios in Figure 3.2C, the trends for $\langle k \rangle$ in Figure 3.4 yielded slopes with 5 mM HCl that were clearly smaller than the slopes obtained without HCl. Specifically, the addition of 5 mM HCl in either DMF or DMSO resulted in a 34 (± 5) % or 55 (± 8) % decrease in the slopes, respectively. This observation suggests that the pyrenyl groups in the PyCX-PAMAM-GY constructs experienced a 45 (± 10) % lower $[Py]_{\text{loc}}$ upon addition of 5 mM HCl. Considering that the internal tertiary amines of the PAMAM dendrimers can be protonated upon addition of 5 mM HCl, the resulting ammonium cations would induce electrostatic repulsion inside the PAMAM dendrimer resulting in the swelling of their interior. This, in turn, would effectively increase the dendrimer volume and lower $[Py]_{\text{loc}}$ for each sample. This observation represents a significant departure from scattering studies, which report an invariance of R_G upon protonation of PAMAM dendrimers implying a constant macromolecular volume.¹⁻⁴

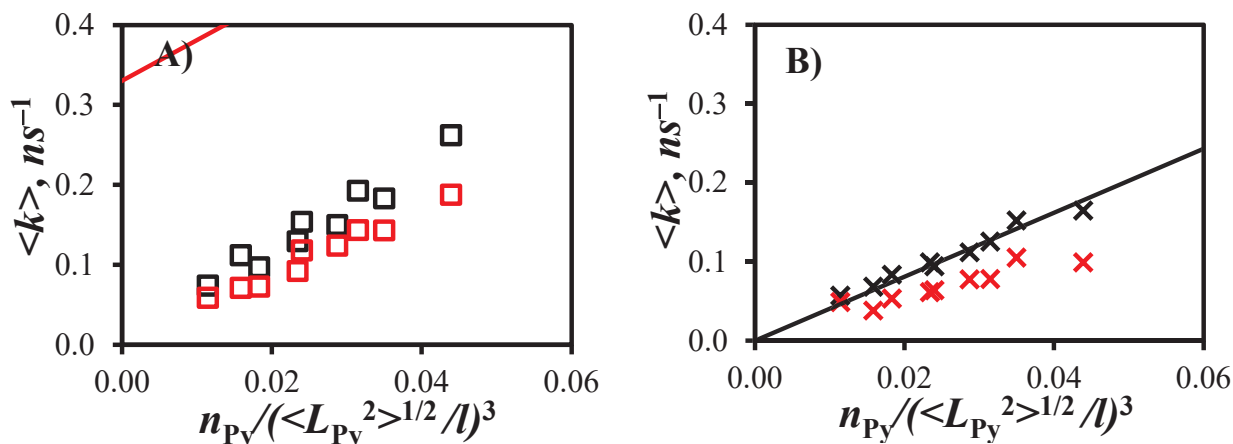


Figure 0.4 Plot of $\langle k \rangle$ as a function of $n_{\text{Py}}/(\langle L_{\text{Py}}^2 \rangle^{1/2}/l)^3$ in A) DMF (\square , \square) and B) DMSO (\times , \times) in the absence (black) and presence (red) of 5 mM HCl.

To solidify this rationale, four additional control experiments were conducted. First, the protonation state of the PyCX-PAMAM-GY constructs in DMF and DMSO without HCl was assigned. Second, the reversibility of the conformational change experienced by the protonation and deprotonation of the tertiary amines was determined. Third, the effect of HCl on $\langle k \rangle$ was assessed by determining whether $\langle k \rangle$ for a pyrene-labeled macromolecule without protonatable groups is affected by the presence of HCl. Fourth, the effect of HCl on k_{diff} , the bimolecular rate constant of excimer formation, which depends on both the solvent viscosity (η) and the probability of excimer formation (p),²⁰ was investigated since HCl might affect p .

To characterize the protonation state of the PyCX-PAMAM-GY dendrimers in DMF without HCl, their $\langle k \rangle$ value was determined in DMF with 5 mM NaOH. The presence of 5 mM NaOH should ensure that all of the tertiary amines in the PyCX-PAMAM-GY samples were deprotonated so that comparison between the $\langle k \rangle$ values obtained in pure DMF and DMF with 5 mM NaOH should provide some insight on the protonation state of the samples. A similar study was also attempted in DMSO with 5 mM NaOH. However, DMSO turned yellowish upon addition of NaOH and the fluorescence experiments were abandoned. The fluorescence decays of the PyCX-PAMAM-GY dendrimers were acquired in DMF with 5 mM NaOH and fitted globally with the MFA to yield $\langle k \rangle$, which was plotted as a function of $n_{\text{Py}}/(\langle L_{\text{Py}}^2 \rangle^{1/2}/l)^3$ in Figure 3.5. Visual inspection of Figure 3.5 reveals excellent agreement between the $\langle k \rangle$ values in pure DMF and those acquired in DMF with 5 mM NaOH. The excellent agreement between the data sets in Figure 3.5 demonstrates that the tertiary amines in the PyCX-PAMAM-GY constructs were most likely deprotonated in the pure solvents and it provides further support that protonation of the tertiary amines upon addition of HCl was most likely responsible for the decrease in $\langle k \rangle$ observed in Figure 3.4.

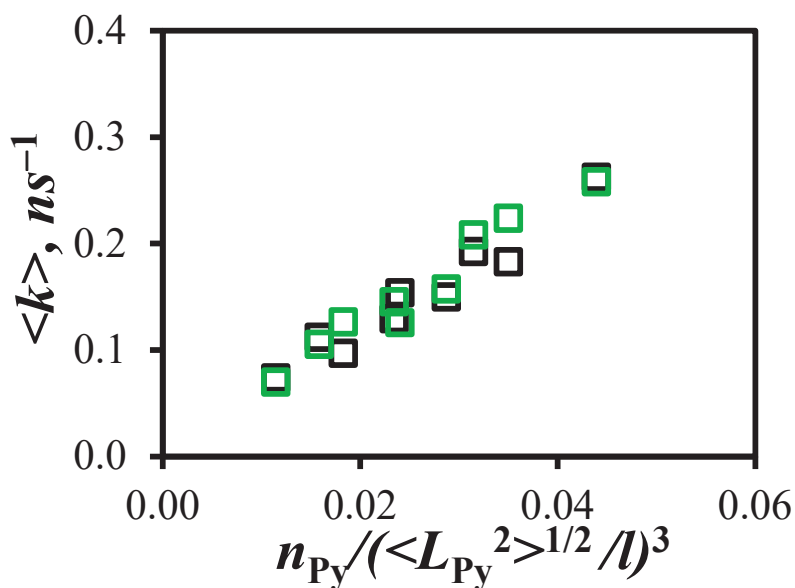


Figure 0.5 Plot of $\langle k \rangle$ as a function of $n_{Py}/(\langle L_{Py}^2 \rangle^{1/2}/l)^3$ in DMF without (■) and with (■) 5 mM NaOH.

Since the tertiary amines located inside the dendrimers are not protonated in DMF with 5 mM NaOH, the good fits obtained by applying the global MFA to the fluorescence decays of the PyCX-PAMAM-GY samples also suggest that the tertiary amines do not seem to quench the pyrenyl labels. It is possible that the tertiary amines, which are well-known quenchers of pyrene, might be too sterically hindered to allow access and induce quenching of the pyrenyl labels.

To assess the reversibility of the conformational change experienced by PyCX-PAMAM-GY samples in DMF, the fluorescence decays were reacquired. Initially, the fluorescence decays of each PyCX-PAMAM-GY sample were obtained in DMF. Subsequently, the fluorescence decays of the same solutions were reacquired in DMF with 5 mM HCl. Finally, the fluorescence decays were acquired after 40 μ L of 1 M NaOH was added to 4 mL of the PyCX-PAMAM-GY solutions in DMF with 5 mM HCl to yield a final concentration of 10 mM NaOH with 5 mM HCl. Using this experimental design, the conformational changes experienced by the samples could be monitored as the tertiary amines transitioned from an initial deprotonated state (pure DMF) to a

protonated state (DMF with 5 mM HCl) and then back to a deprotonated state (DMF with 5 mM HCl and 10 mM NaOH). As depicted in Figure 3.6, the fluorescence decays showed a visible difference depending on whether the tertiary amines were deprotonated (Figures 3.6A and C) or protonated (Figure 3.6B). Specifically, the earlier portion of the monomer fluorescence decay, which yields dynamic information for PEF, exhibits a longer decay when the tertiary amines are protonated compared to when deprotonated. Given that $\langle k \rangle$ is inversely related with $\langle \tau \rangle$, since $\langle k \rangle$ is much larger than τ_M^{-1} , the slower decay indicates that $\langle k \rangle$ is lower when the tertiary amines are protonated. The difference between the decays is further illustrated in Figure 3.6D where the monomer fluorescence decays under each condition were overlapped. Most importantly, Figure 3.6D clearly demonstrates that the fluorescence decay returns to its original form in DMF (Figure 3.6A), where the tertiary amines were deprotonated, upon the addition of NaOH (Figure 3.6C) to the protonated samples (Figure 3.6B). This illustrates the reversibility of the conformational change experienced by the PyCX-PAMAM-GY samples with or without HCl.

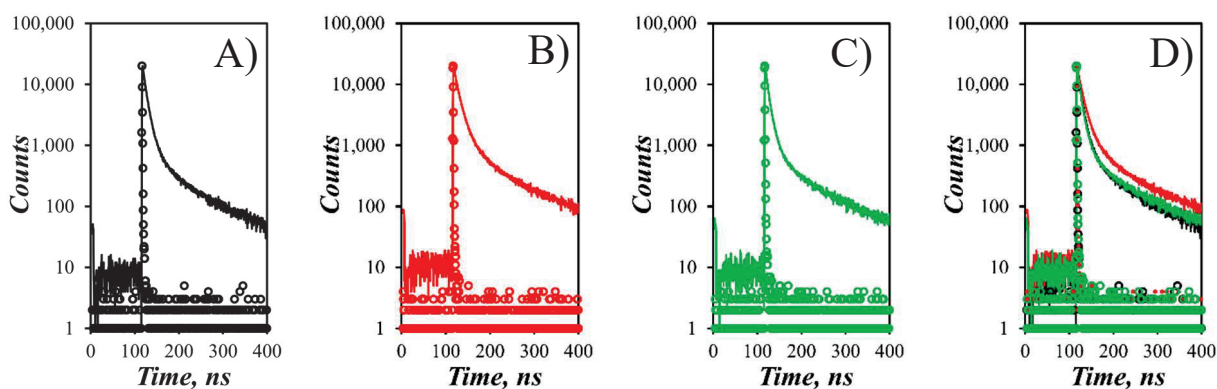


Figure 0.6 The monomer decay of PyC8-PAMAM-G0 acquired in A) DMF, B) DMF with 5 mM HCl, and C) DMF with 5 mM HCl and 10 mM NaOH. D) Overlap of the monomer decays obtained in Figure 3.6A), B), and C).

Although the reversibility of the conformational change experienced by the PyCX-PAMAM-GY samples with or without HCl can be confirmed from the visual inspection of the monomer fluorescence decays, a more quantitative analysis would be based on $\langle k \rangle$ determined under each condition. As seen in Figure 3.7, $\langle k \rangle$ values obtained in DMF are clearly higher than the values obtained in the same solution with 5 mM HCl, as observed previously in Figure 3.4A. Upon addition of NaOH to a same PyCX-PAMAM-GY solution with HCl, the $\langle k \rangle$ values returned to the same line, within experimental error, as obtained initially in pure DMF. This behavior demonstrates the reversibility of the conformational change experienced by the PAMAM dendrimers. Interestingly, comparison of $\langle k \rangle$ obtained independently in Figures 3.4, 3.5 and 3.7 revealed that $\langle k \rangle$ varied by at most 2% under a given condition. The reproducibility and reliability of the $\langle k \rangle$ measurements not only confirm the reversibility of the conformational change experienced by the PyCX-PAMAM-GY samples but also demonstrate the robustness of the methodology applied to globally analyze the fluorescence decays.

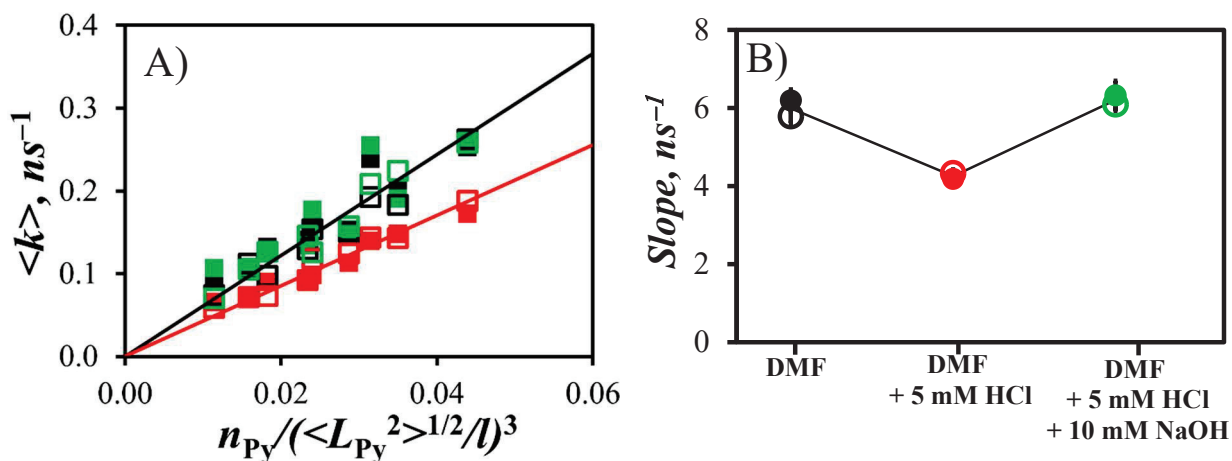


Figure 0.7. A) Plot of $\langle k \rangle$ as a function of $n_{Py}/(\langle L_{Py}^2 \rangle^{1/2}/l)^3$ for the PyCX-PAMAM-GY samples acquired in 1st experiment: DMF (black, empty), 2nd experiment: DMF with 5 mM HCl (red, empty), 3rd experiment: DMF with 5 mM NaOH (green, empty), and 4th experiment: DMF (black,

full), followed by addition of 5 mM HCl (red, full), followed by addition of 10 mM NaOH (green, full). B) Plot of the slope of the straight lines shown in Figure 3.7A.

To evaluate how $\langle k \rangle$ might be affected by 5 mM HCl when dealing with a pyrene-labeled macromolecule without protonatable groups, the fluorescence decays of a series of 2,2-*bis*(hydroxymethyl)propionic acid-based dendrimers labeled with 1-pyrenebutyric acid (PyC4-HMPA-GY) with Y ranging from 1 to 5, that were characterized in pure DMF and DMSO in an earlier study,^{21,22} were acquired in DMF and DMSO with 5 mM HCl. The fluorescence decays were analyzed using the MFA and their parameters can be found in Tables S3.25 to S3.28 in the SI. The $\langle k \rangle$ values obtained in DMF and DMSO without HCl and with 5 mM HCl were compared in Figures 3.8A and B for DMF and DMSO, respectively. The identical trends observed in Figures 3.8A and B for the solvents without and with 5 mM HCl demonstrate that within experimental error, the $\langle k \rangle$ values for the PyC4-HMPA-GY samples are unaffected by the presence of 5 mM HCl. Consequently, if $\langle k \rangle$ for a macromolecule without protonatable groups is unaffected by the presence of 5 mM HCl, the comparison conducted in Figure 3.8 supports the notion that the decrease in $\langle k \rangle$ observed in Figure 3.4 was likely due to the presence of the protonatable groups, namely the tertiary amines of the PyCX-PAMAM-GY constructs.

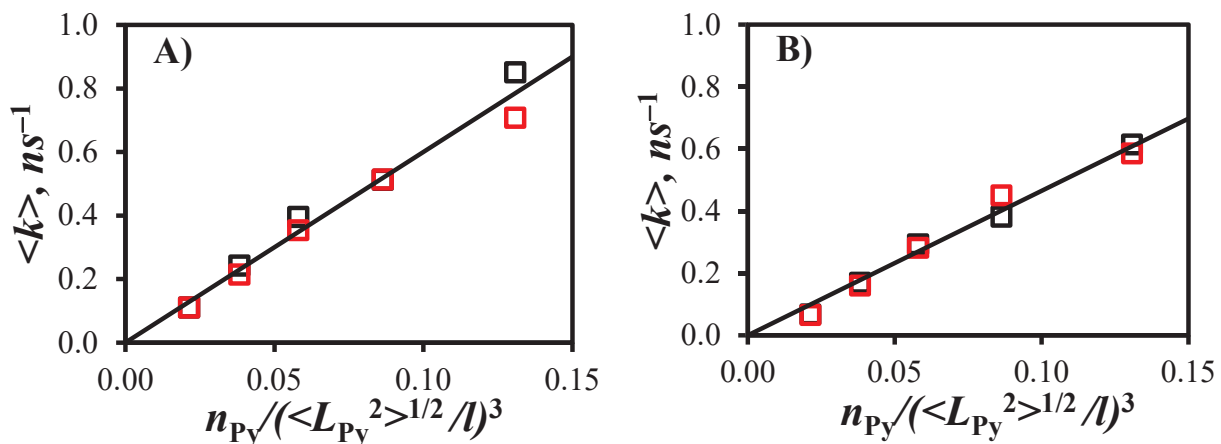


Figure 0.8. Plot of $\langle k \rangle$ as a function of $n_{Py}/(\langle L_{Py}^2 \rangle^{1/2}/l)^3$ for 1-pyrenebutyric acid-labeled 2,2,-bis(hydroxymethyl)propionic acid-based dendrimers (PyC4-HMPA-GY) acquired in A) DMF and B) DMSO in the absence (■) and presence (◻) of 5 mM HCl.

Proper parametrization of macromolecules such as the PyC4-HMPA-GY and PyCX-PAMAM-GY dendrimers yields an expression of $[Py]_{loc}$, that results in a linear relationship between $\langle k \rangle$ and $[Py]_{loc}$ as observed in Figures 3.4 – 3.8. However, $\langle k \rangle$ being equal to the product $k_{diff} \times [Py]_{loc}$, where k_{diff} depends on solvent viscosity (η) and the probability (p) of forming an excimer upon encounter between an excited and a ground-state pyrene, the lines shown in Figure 3.4 have different slopes in DMF and DMSO, since DMF and DMSO have different η and p values. Furthermore, the η and p values in these solvents could be further affected by the addition of 5 mM HCl. To assess the effect of HCl on k_{diff} , k_{diff} was determined for the formation of intermolecular pyrene excimer with the model compound *n*-hexyl-1-pyrenebutyramide (Hx-PyBA). To this end, the fluorescence decays of Hx-PyBA solutions in DMF and DMSO with 5 mM HCl were acquired for Hx-PyBA concentrations ranging from 11 to 26 mM and they were fitted according to the MFA to yield $\langle k \rangle$. Plotting $\langle k \rangle$ as a function of Hx-PyBA concentration in

Figures S3.2A and B for DMF and DMSO with 5 mM HCl resulted in two straight lines whose slope yielded k_{diff} equal to $1.06 (\pm 0.01) \mu\text{s}^{-1}$ and $0.71 (\pm 0.01) \mu\text{s}^{-1}$ in DMF and DMSO with 5 mM HCl, respectively. Within experimental error, these values are identical to those of $1.05 (\pm 0.01) \mu\text{s}^{-1}$ and $0.70 (\pm 0.00) \mu\text{s}^{-1}$ obtained earlier in pure DMF and DMSO,¹¹ respectively, leading to the conclusion that 5 mM HCl does not affect k_{diff} in DMF and DMSO, as was already suggested by the PyC4-HMPA-GY study in Figure 3.8, where similar $\langle k \rangle$ values were obtained without and with 5 mM HCl.

Dividing $\langle k \rangle$ by k_{diff} for Hx-PyBA yielded the ratio $\langle k \rangle / k_{\text{diff}}$, which no longer depends on solvent viscosity and p . The $\langle k \rangle / k_{\text{diff}}$ values were plotted as a function of $n_{\text{Py}} / (\langle L_{\text{Py}}^2 \rangle^{1/2} / l)^3$ in Figure 3.9A. The $\langle k \rangle / k_{\text{diff}}$ ratios obtained for the pure solvents without HCl clustered around a straight line whose slope was larger than the slope of the straight line along which the $\langle k \rangle / k_{\text{diff}}$ ratios for the samples in the solvents with 5 mM HCl distributed themselves. Pearson correlation coefficients of 0.99 and 0.98 were found for the solutions without and with 5 mM HCl, respectively, reflecting a very strong positive correlation between the $\langle k \rangle / k_{\text{diff}}$ ratio and $n_{\text{Py}} / (\langle L_{\text{Py}}^2 \rangle^{1/2} / l)^3$, thus validating the assumption that the oligomeric segments constituting the interior of the PyCX-PAMAM-GY constructs obey Gaussian statistics.

Averaging the $\langle k \rangle / k_{\text{diff}}$ ratios obtained for the same construct in DMF and DMSO yielded the trend shown in Figure 3.9B, which highlights the difference in slopes for the $\langle k \rangle$ values obtained without and with 5 mM HCl. Addition of 5 mM HCl reduces the slope by $1.45 (\pm 0.05)$ times, which would suggest a 33 % increase in the dendrimer volume. The cube root of the volume increase indicates by how much the average end-to-end distance $\langle L_{\text{Py}}^2 \rangle^{1/2}$, used to calculate the ratio $n_{\text{Py}} / (\langle L_{\text{Py}}^2 \rangle^{1/2} / l)^3$, increased after protonating the interior tertiary amines. This calculation

suggests that the average end-to-end distance of the PAMAM dendrimers increased by 13 (± 1) % upon exposure to 5 mM HCl.

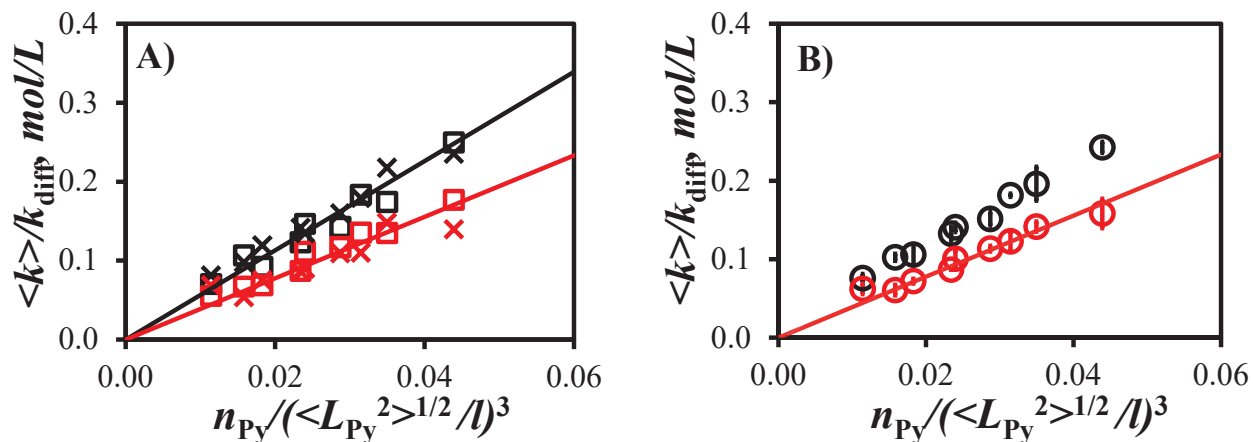


Figure 0.9. A) Plot of the $\langle k \rangle / k_{\text{diff}}$ ratio as a function of $n_{\text{Py}} / (\langle L_{\text{Py}}^2 \rangle^{1/2} / l)^3$ for decays acquired in DMF (\blacksquare) or DMSO (\times , \times) in the absence (black) or presence (red) of 5 mM HCl. B) Plot of the average $\langle k \rangle / k_{\text{diff}}$ (\bullet , \circ) values acquired in DMF and DMSO as a function of $n_{\text{Py}} / (\langle L_{\text{Py}}^2 \rangle^{1/2} / l)^3$ acquired without (black) and with (red) of the 5 mM HCl.

Although scattering experiments cannot be used to study changes in R_G for isolated non-interacting polyelectrolytes,¹⁻⁴ molecular dynamics simulations (MDS) can. MDS conducted on PAMAM dendrimers of generation 4, 5, and 6 found an increase in R_G of 13, 20, and 15%, respectively, going from a completely unprotonated to a fully protonated (both primary and tertiary amines) construct.⁷ While only the internal tertiary amines of the PyCX-PAMAM-GY samples were protonated in the present study, the 13 (± 1) % increase in the end-to-end distance observed for these samples upon adding 5 mM HCl is in excellent agreement with the 16 (± 3) % average increase in R_G found for the PAMAM-GY samples with $Y = 4, 5,$ and 6 by MDS.⁷ It is however

lower than the 28 (± 4) % determined by all atom MDS conducted more recently for PAMAM dendrimers with generations between G1 and G6.¹⁰ The lower increase in R_G probed for the PyCX-PAMAM-GY samples upon protonation could reflect the expansion of the PAMAM dendrimers induced by the sole internal tertiary amines, which is different from the MDS, which consider the naked PAMAM dendrimer with protonated internal tertiary amines and terminal primary amines. While MDS describe the unmodified PAMAM dendrimers, the PyCX-PAMAM-GY samples are actually more representative of the many PAMAM dendrimers used for applications in the scientific literature since their terminal groups are taken advantage of for chemical modification.

3.5 CONCLUSIONS

This study provides another application of the PEF-based methodology developed for pyrene end-labeled dendrimers to characterize their conformation.^{11,21,22} The combination of the pseudo-unimolecular rate constant of excimer formation, $\langle k \rangle$, together with the parameterization of a series of pyrene-labeled PAMAM dendrimers to obtain a measure of $[Py]_{loc}$ through the quantity $n_{Py}/(\langle L_{Py}^2 \rangle^{1/2}/l)^3$ was applied to characterize the conformational changes occurring intramolecularly in solution under conditions where the PAMAM dendrimers were characterized as isolated macromolecules without undergoing intermolecular interactions. Such experimental conditions are inaccessible to scattering experiments, in part, due to their use of significantly higher polymer concentrations. Specifically, the PEF studies revealed that the radius of low generation PAMAM dendrimers increased by 13 (± 1) % upon protonation of their interior tertiary amines. This result differs significantly from scattering studies, which have found little change in R_G upon protonation of PAMAM dendrimers.¹⁻⁴ Furthermore, the 13 % increase in the dimensions of the pyrene end-labeled PAMAM dendrimers was found to be in excellent agreement with the

increase predicted by MDS in the radius of gyration of PAMAM dendrimers of generation 4, 5, and 6 as they transition from an unprotonated state to a fully protonated state.⁷ This study represents the first example where PEF was applied to quantitatively characterize the conformational change happening to low generation PAMAM dendrimers upon protonation of their internal tertiary amines. Additionally, and perhaps more importantly, these studies further illustrate how PEF can be applied to macromolecules bearing more than two pyrenyl labels to extract quantitative information about the conformation of macromolecules in solution in a manner that complements scattering experiments.

Chapter 4: Extending the Range of Distances Used to Characterize the Conformation of Macromolecules by Pyrene Excimer Formation: Application to the Conformation of Poly(*L*-glutamic acid) in Dimethyl Sulfoxide

4.1 ABSTRACT

Pyrene excimer formation (PEF) was applied to study the homopolypeptides poly(*D,L*-glutamic acid) (PDLGA) and poly(*L*-glutamic acid) (PLGA), collectively referred to as the PGA samples, in *N,N*-dimethylformamide (DMF) and dimethyl sulfoxide (DMSO). The polypeptides were labeled with 1-pyrenebutylamine (PyC4N) or 1-pyreneoctylamine (PyC8N) and were described as PyCX(*x*)N-PGA where *X* equals 4 or 8, respectively, and *x* represents the molar percentage of pyrene-labeled glutamic acid (Glu). The fluorescence results obtained with these polypeptides were compared with the results obtained earlier with the same polypeptides randomly labeled with 1-pyrenemethylamine (PyC1N). Analysis of the fluorescence decays of the PyCX(*x*)N-PGA samples with the fluorescence blob model (FBM) yielded $\langle N_{\text{blob}}^{\text{exp}} \rangle$, which is the average number of Glu units per *blob*, where a *blob* is the sub-volume probed by an excited pyrenyl label. The $\langle N_{\text{blob}}^{\text{exp}} \rangle$ values obtained for the PyCX(*x*)N-PGA samples in DMF and DMSO were compared with the $N_{\text{blob}}^{\text{MMO}}$ values determined via molecular mechanics optimizations (MMO) conducted for PLGA constructs adopting four different conformations and labeled with either PyC1N, PyC4N, or PyC8N. The good agreement obtained between the $\langle N_{\text{blob}}^{\text{exp}} \rangle$ and $N_{\text{blob}}^{\text{MMO}}$ values for PDLGA in DMF and DMSO and PLGA in DMF, whose conformation was known to be a random coil and an α -helix, respectively, validated the PEF-based methodology. It was then applied to determine that the as yet unknown conformation of PLGA in DMSO was that of a 3_{10} -helix. Since PyC8N probed a spherical volume whose 7.7 nm diameter was almost double that of PyC1N, these experiments significantly extended the range of distances over which PEF can be applied to characterize macromolecular conformations, making PEF competitive with Förster resonance energy transfer (FRET).

4.2 INTRODUCTION

The characterization of the conformation of biomacromolecules is a fundamental area of study, given that conformation governs the underlining functions of the biomacromolecules used as the building blocks of living organisms. Although much simpler than proteins, synthetic polypeptides are excellent model compounds to gain insight into the physical principles underlining the structure-property relationships of proteins.⁸ One of the best characterized homopolypeptides is poly(*L*-glutamic acid) (PLGA), whose conformation is typically monitored in aqueous solutions⁹⁻¹⁶ or organic solvents.¹⁷⁻²⁷ One particularly important organic solvent regarding peptide conformation is dimethyl sulfoxide (DMSO), owing, in part, to its widespread use for the storage of biomacromolecules²⁸ and to handle biological samples, drugs, and cosmetics.²⁹ Since DMSO is also viewed as a denaturant,³⁰⁻³⁵ the effect that DMSO has on the conformation of biomacromolecules must be carefully assessed, particularly since a large body of evidence also suggests that several biomacromolecules retain some structure in DMSO.^{20-22,45,36-38}

Numerous techniques can be applied to characterize the conformation of biomacromolecules in solution. They are mainly based on scattering,^{9,10,12,31,34,39} NMR,^{17,19,27,32,36-38,40} circular dichroism (CD),^{35,41-43,56} Raman optical activity (ROA),^{22,44-46} and Fourier transform infrared (FTIR) spectroscopy.^{22,33,47-49} Despite the wealth of knowledge extracted from these experimental techniques, limitations do exist. Scattering experiments used for biological and synthetic macromolecules often require high concentrations (~ 0.1 – 20 mg/mL) of macromolecules to generate sufficient scattering signal,^{50,51} which can complicate the conformational analysis of macromolecules if long range intermacromolecular interactions occur.^{52,53} On the other hand, multidimensional NMR experiments can be used to probe the conformation of small biomacromolecules,^{32,36-38} with a molecular weight typically up to 100

kDa,⁵⁴ but its use has been less prevalent for synthetic polymers, such as homopolypeptides, in part due to the similarity/overlap of the backbone resonances.⁵⁵ Consequently, the characterization of the conformation of homopolypeptides by solution NMR typically involves monitoring shifts of the position of the α -CH proton signal in the ^1H NMR spectrum to infer the presence of secondary structure.^{17,19,27,40} Conformational information obtained by CD and ROA requires measuring the difference between, respectively, the absorbance or scattering of left and right polarized light as a function of wavelength. Comparison of the resulting spectra against spectra, that are either simulated or acquired experimentally with macromolecules of known conformation, provides a means to characterize macromolecular conformations and conformational changes. The interpretation of the CD and ROA spectra, however, can be complicated by solvent effects^{56,57} in the characteristic regions of the spectrum used to assess macromolecular conformations. In contrast to CD and ROA, FTIR spectroscopy monitors the stretching and bending motions between atoms resulting in spectral shifts in the amide region, which are commonly analyzed to gain conformational insight about polypeptides. However, accurate assignment of the shifts within the amide region can be challenging because they are relatively small, making it difficult to unambiguously determine if the shifts are due to structural differences or changes in the local environment experienced by the polypeptide.⁵⁸ In summary, although the combination of these experimental techniques has provided valuable conformational information about polypeptides, the above discussion illustrates that limitations still remain stemming mainly from the high concentrations of macromolecules used in these experiments and the difficulty in assigning specific spectral features to a given macromolecular conformation. These problems are further highlighted in the following section focusing on the conformation of PLGA in DMSO.

Although PLGA is mostly studied by NMR in D₂O⁵⁹⁻⁶³ rather than DMSO, some conformational information about PLGA in DMSO can be inferred from NMR studies conducted with its benzyl protected analog, namely poly(γ -benzyl-*L*-glutamate) (PBLG). The α -CH proton of PBLG, used to assess conformational changes, has been found to shift up-field in DMSO for PBLGA with a degree of polymerization (DP) greater than seven compared to the α -CH proton of PBLGA chains with a DP smaller than seven, known to adopt a random coil conformation.¹⁹ This result indicates that long PBLGA chains in DMSO adopt a secondary structure suggesting that PLGA chains could also do so. Beside NMR, a combination of electric birefringence, scattering, and viscosity measurements of PLGA in various helicogenic organic solvents (methanol, *N,N*-dimethylformamide, dioxane-water mixtures, etc...) led to the conclusion that PLGA most likely adopts an α -helical conformation in each solvent with the exception of DMSO where PLGA adopted a distinctly different helical conformation.^{20,21} Although the authors could not determine the type of helix, they suggested that the helical conformation adopted by PLGA in DMSO was less compact than that of an α -helix.²¹ A recent study using a combination of FTIR, ROA, and small angle X-ray scattering (SAXS) proposed that the PLGA molecules constituting β -amyloid fibres in DMSO adopted a long rigid helical conformation, which was suggested to be that of an α -helix, but which could not be unambiguously assigned.²² Furthermore, the aggregation of PLGA into fibers at high polypeptide concentrations between 10 and 45 mg/mL could result in some long range intermacromolecular effects, that could affect the conformation expected for an isolated macromolecule. In summary, numerous lines of evidence suggest that PLGA in DMSO adopts a helical conformation, but its exact type has not been conclusively demonstrated to date using the traditional techniques typically employed to probe the conformation of homopolypeptides in solution.

In 2003, an alternate methodology based on pyrene excimer formation (PEF) upon contact between an excited and ground-state pyrene dye was introduced to characterize the conformation in solution of PLGA after it had been labeled with 1-pyrenemethylamine (PyC1N).²³ These experiments yield the number ($N_{\text{blob}}^{\text{exp}}$) of glutamic acids (Glu) located inside the volume probed by an excited pyrenyl label also referred to as a *blob*.^{64,69} Since $N_{\text{blob}}^{\text{exp}}$ represents the maximum number of Glu units separating two Glu bearing a pyrenyl label, while still enabling good stacking of the pyrene moieties conducive of PEF, $N_{\text{blob}}^{\text{exp}}$ can be compared to $N_{\text{blob}}^{\text{MMO}}$ obtained by conducting molecular mechanics optimizations (MMO) on a pyrene-labeled PLGA construct adopting a given conformation. A good match between $N_{\text{blob}}^{\text{exp}}$ with PLGA in solution and the $N_{\text{blob}}^{\text{MMO}}$ value determined for a given conformation of PLGA enables the assignment of this conformation for PLGA in the solvent of interest. Upon labeling samples of poly(*D,L*-glutamic acid) (PDLGA) and poly(*L*-glutamic acid) (PLGA) with PyC1N, $N_{\text{blob}}^{\text{exp}}$ values of 10 (± 1) in DMF²⁴ and 11 (± 2) in DMSO²⁴ for PyC1N-PDLGA and 21 (± 1)²⁴ and 22 (± 2)²⁶ in DMF and 18 (± 1) in DMSO²⁴ for PyC1N-PLGA could be compared with the $N_{\text{blob}}^{\text{MMO}}$ values of 10 (± 1), 13, 19, and 23 for a pyrene-labeled PLGA adopting the conformation of a random coil, polyproline type II-helix (PPII), 3_{10} -helix, and α -helix, respectively. This comparison indicated that PDLGA was randomly coiled in DMF and DMSO and that PLGA was an α -helix in DMF and a 3_{10} -helix in DMSO.²⁴ However, since the $N_{\text{blob}}^{\text{exp}}$ values are typically obtained with $\sim 10\%$ uncertainty, the $N_{\text{blob}}^{\text{exp}}$ values of 18 (± 1) and 21 (± 2) for a PLGA 3_{10} - and α -helix, respectively, were deemed too close for the unambiguous assignment of the PLGA conformation in DMSO as a 3_{10} -helix.

The relatively narrow range of $N_{\text{blob}}^{\text{exp}}$ values between 10 and 22 found experimentally when using PyC1N to label PDLGA or PLGA,^{24,26} collectively referred to as the PGA samples, is due to the short reach of the pyrenyl dye, which is limited by the 5 atom-long linker connecting

pyrene to the polypeptide backbone. Since longer linkers would extend the reach of the pyrenyl label, yield larger $N_{\text{blob}}^{\text{exp}}$ values, and result in a more clear-cut difference between the $N_{\text{blob}}^{\text{exp}}$ values obtained for PLGA in DMF and DMSO, PLGA and PDLGA samples were labeled with 1-pyrenebutylamine (PyC4N) and 1-pyreneoctylamine (PyC8N) to yield series of PyCX(x)N-PLGA and PyCX(x)N-PDLGA samples, where X equals 4 or 8, respectively, and x represents the mole percent of Glu units labeled with pyrene. The longer linkers resulted in much larger $N_{\text{blob}}^{\text{exp}}$ values, which enabled the unambiguous assignment of PLGA as a 3_{10} -helix in DMSO. The longer linkers increased the reach of the pyrenyl labels from 4.0 to 5.7 and 7.7 nm, when the polypeptides were labeled with PyC1N, PyC4N, and PyC8N, respectively. As it turns out, these distances are comparable to those available with many fluorescence resonance energy transfer (FRET) donor and acceptor pairs. Since PEF and FRET probe similar distances at the molecular level, PEF can be viewed as a novel spectroscopic ruler.⁶⁵ The main advantage of PEF over FRET is that the PEF efficiency is directly proportional to the local concentration ($[Py]_{\text{loc}}$) of ground-state pyrenyl labels whereas the FRET efficiency is only related to the local concentration of acceptors.⁶⁶ These appealing features enabled the use of PEF in the present study to unambiguously assign the conformation of PLGA in DMSO as a 3_{10} -helix thanks to the significant increase in the reach of the pyrene moieties achieved by labeling the PGA samples with PyC4N and PyC8N compared to PyC1N used in earlier studies.^{23,24,26}

4.3 EXPERIMENTAL

Chemicals: All reagents were purchased from Sigma-Aldrich and used without further purification. Poly(*L*-glutamic acid) (PLGA) and poly(*D,L*-glutamic acid) (PDLGA) were purchased from Alamanda Polymers and had a number-average degree of polymerization equal to

830 and 784, respectively. Oxalyl chloride and EDC-HCl were purchased from Oakwood Chemicals, while monomethyl suberate was purchased from Fisher Scientific.

Synthesis of 1-pyrene butylamine (PyC4N): The synthesis of 1-pyrenebutylamine was adapted from a previously reported procedure.⁶⁷ In brief, a 100 mL round bottom flask equipped with a magnetic stir bar was charged with 1-pyrenebutyric acid (2 g, 6.9 mmol, 1 eq.), dichloromethane (DCM, 20 mL) and a catalytic amount of anhydrous *N,N*-dimethylformamide (DMF, ~3 drops). The dispersion was vigorously stirred and purged with pure nitrogen (99.99%, anhydrous) for 5 minutes. Under continuous stirring, the solution was subsequently placed in an ice bath (0 °C) and the nitrogen flow was stopped. Oxalyl chloride (0.77 mL, 9.0 mmol, 1.3 eq.) was added dropwise and the reaction mixture was allowed to proceed for 30 minutes. DCM and excess oxalyl chloride were removed via a steady stream of dry nitrogen to yield a crude off-white to yellow solid (1-pyrenebutyryl chloride). Without further purification, the solid was redissolved in DCM (50 mL) and ammonia gas was bubbled through the solution at room temperature for 30 minutes, which resulted in the formation of a white precipitate. Ammonia gas was generated in the fumehood by the dropwise addition of aqueous ammonium hydroxide (28–30 wt%, 12 mL) with a syringe to sodium hydroxide pellets (4 g) placed in a sealed container capped with a septum and kept under positive nitrogen pressure. The generated ammonia gas was evacuated from the container through another syringe connected to Tygon tubing terminated at the other end with a glass tube to allow direct bubbling of the gas into the flask containing the 1-pyrenebutyryl chloride solution in DCM. The ammonia gas was bubbled through the solution for 30 minutes in the fumehood. The crude mixture was filtered through Whatman #5 filter paper followed by the evaporation of the filtrate via a steady stream of air. The resulting off white solid corresponds to the crude 1-pyrenebutylamine product. Without further purification, the crude product was dissolved in doubly

distilled tetrahydrofuran (20 mL) followed by the addition of lithium aluminum hydride (0.52 g, 14 mmol, 10 eq.). The solution was vigorously stirred and refluxed for 2 hours, after which the solution was cooled for 10 minutes in an ice bath followed by the careful dropwise addition of deionized water (2 mL), 1 M sodium hydroxide (1 mL), and deionized water (1 mL). The mixture was filtered (Whatman #5) and the precipitate was discarded while the filtrate was recovered and concentrated to ~5 mL. Under continuous stirring, concentrated 12 M HCl (0.06 mL) was added to the solution which resulted in the immediate precipitation of the 1-pyrenebutylamine hydrochloride salt. The precipitate was recovered by suction filtration (Whatman #5) and dried under vacuum overnight. The ^1H NMR spectrum of the product can be found in Figure S4.1 in the Supporting Information (SI).

Synthesis of 1-pyreneoctylamine (PyC8N): PyC8N was prepared in the same manner as PyC4N using 1-pyreneoctanoic acid as the starting material. The synthesis of 1-pyreneoctanoic acid has been reported in an earlier publication.⁶⁸ The ^1H NMR spectrum of 1-pyreneoctylamine hydrochloride can be found in Figure S4.2 in the SI.

Synthesis of 1-pyrenebutyl acetamide (PyC4N-Ac): A 20 mL vial equipped with a stir bar was charged with 1-pyrenebutylamine (200 mg, 0.66 mmol) and EDC-HCl (0.191 mg, 1.0 mmol, 1.5 eq.) which were dissolved in DMF (4 mL). Following the complete dissolution of the reactants, glacial acetic acid (2 mL, 35 mmol, 53 eq.) was added to the reaction mixture with vigorous stirring and the reaction was allowed to proceed overnight in the dark. The crude mixture was diluted with DCM (20 mL) and purified via liquid-liquid extractions (3×50 mL of 1 M HCl, 1 M NaOH, deionized water (DIW), and brine) to yield an off-white PyC4N-Ac product. The maximum absorption peak in DMF was found at 345 nm and the corresponding molar absorbance coefficient was found to equal $35,950 \text{ M}^{-1} \cdot \text{cm}^{-1}$. The ^1H NMR spectrum and plot of the absorbance-vs-

[PyC4N-Ac] to obtain the molar absorbance coefficient are provided in Figure S4.3 and Figure S4.5 in the Supporting Information (SI), respectively.

Synthesis of 1-pyreneoctyl acetamide (PyC8N-Ac): The synthesis of PyC8N-Ac was done in the same manner as PyC4N-Ac by replacing PyC4N by PyC8N. The molar absorbance coefficient for this model compound was found to equal $39,300 \text{ M}^{-1} \cdot \text{cm}^{-1}$ at 345 nm in DMF. The ^1H NMR spectrum and plot of absorbance-vs.-[PyC8N-Ac] are provided in Figures S4.4 and S4.6 in the SI, respectively.

Pyrene-labeling of PLGA and PDLGA samples: Prior to labeling the PLGA and PDLGA samples with pyrene, collectively referred to as the PGA samples from here on, the amino terminus of the PGA samples was capped using succinimidyl acetate as described elsewhere.^{24,25} To cap the homopolypeptides, a PGA sample (200 mg, $1.7 \mu\text{mol}$) was fully dissolved in DIW (8 mL) and diluted with DMF (8 mL). Succinimidyl acetate (31 mg, $200 \mu\text{mol}$) was subsequently added, and the reaction mixture was allowed to react overnight. The samples were then purified via dialysis against 1 L of DIW 3-5 times, followed by pH 9 DIW. The dialysate was recovered by lyophilization and subsequently used for pyrene-labeling reactions. The procedure applied to label PGA was adapted from previous publications²⁴⁻²⁶ and a brief description of the procedure employed to label PLGA with 4.1 mol% of 1-pyrenebutylamine is described hereafter. A 20 mL vial equipped with a magnetic stir bar was charged with PLGA (20 mg, 0.17 mmol eq. of glutamic acid (Glu)) and dissolved in 4 mL of deionized water (DIW). Upon complete dissolution, DMF (4 mL), EDC-HCl (1.8 mg, $9 \mu\text{mol}$), and 1-pyrenebutylamine (2.4 mg, $7.6 \mu\text{mol}$) was added to the solution. The reaction mixture was covered with aluminum foil and allowed to react for 2-3 days at room temperature. The reaction mixture was transferred to dialysis tubing (16 kDa, regenerated cellulose) and dialyzed in 6-hour increments 2-3 times against 1 L of pure DMF followed by an

80, 50, 20, and 0 vol % of DMF in DIW solution. Once the sample was in DIW, it was further dialyzed against 1 L of pH 6 DIW and then 1 L of pH 9 DIW for 6 hours. A final dialysis was conducted with 1 L of pH 9 DIW overnight. Before discarding the dialysis waste, a ~20 mL aliquot was freeze dried to determine the mass ratio (λ_{DS}) of solids other than Py-PLGNa per gram of dialysis solution. The Py-PLGNa solution was accurately weighed into vials and λ_{DS} was used to determine the mass of solid (m_{DS}) in the dialysate that was not Py-PLGNa by multiplying the mass of Py-PLGNa solution to be lyophilized by λ_{DS} . The Py-PLGNa solution was lyophilized to remove water and the mass of solid ($m_{Py-PLGNa/DS}$) was recorded. The mass of Py-PLGNa ($m_{Py-PLGNa}$) was obtained by subtracting m_{DS} from $m_{Py-PLGNa/DS}$.

Pyrene Content: The mole fraction (f_{Py}) of Glu labeled with pyrene was determined using Equation 4.1. For these experiments, the pyrene-labeled PGA samples were in their deprotonated form (Py-PGNa). In Equation 4.1, λ_{Py} represents the moles of pyrene per gram of Py-PGNa sample. It is calculated by dividing the absorbance (*Abs*) of a solution of Py-PGNa sample by the product of the mass ($m_{Py-PGNa}$) of Py-PGNa sample used to prepare the solution with the molar absorption coefficient (ϵ) of the pyrene derivatives used to label the polypeptides ($\lambda_{Py} = Abs/(\epsilon \times m_{Py-PGNa})$). M_{GNa} and M_{Py-Glu} represent the molar mass of the sodium glutamate residue ($151 \text{ g} \cdot \text{mol}^{-1}$) and the pyrene-labeled glutamate residue, equal to 384 and 441 mol/g for 1-pyrenebutyl- γ -glutamide and 1-pyreneoctyl- γ -glutamide, respectively. To ensure accurate determination of λ_{Py} , and thus f_{Py} , a minimum of 5 mg of freshly freeze dried Py-PGNa was weighed ($m_{Py-PGNa}$). Prior to UV-vis measurements, Py-PGNa was dissolved in 1 mL of DIW, followed by the addition of 1 mL of 1 M HCl. The suspension was vortexed for 30 seconds and freeze-dried. All UV-vis measurements to determine f_{Py} were done in DMF using the molar extinction coefficients determined for the 1-pyrenebutylacetamide (PyC4N-Ac) and 1-pyreneoctylacetamide (PyC8N-Ac) model compounds.

$$f_{Py} = \frac{M_{GNa}}{\lambda_{Py}^{-1} + M_{GNa} - M_{Py-Glu}} \quad (4.1)$$

Circular dichroism: All circular dichroism (CD) measurements were conducted with a Jasco J-715 spectropolarimeter in a quartz cell with a 0.1 mm pathlength at a concentration of 1 mg/mL. The spectra were averaged over 10 scans from 190 to 250 nm and baseline corrected to DIW with either 10 mM NaOH or HCl.

NMR spectrometer: All NMR spectra were acquired on a Bruker 300 MHz NMR spectrometer equipped with a Bruker SampleXpress Lite autosampler. Each NMR spectrum was analyzed using SpinWorks 4 (version 4.2.10.0).

Steady-state fluorescence: The steady-state fluorescence spectra were acquired on a QM-400 fluorometer equipped with an Arc-Xenon lamp with 4 mL of polypeptide solutions having a 2.5×10^{-6} M concentration of pyrene with 20 μ L of 1 M HCl. Prior to acquisition, the samples were purged with nitrogen for 35 minutes. All spectra were acquired from 355 to 600 nm with an excitation wavelength of 345 nm and analyzed by integrating the fluorescence signal of the excimer (I_E) from 500 to 530 nm and dividing it by the integrated fluorescence signal of the monomer (I_M) from 376 to 382 nm to yield the I_E/I_M ratio, which was used as a measure of the PEF efficiency.

Time-resolved fluorescence: The fluorescence decays were acquired using an IBH time-correlated single photon counting (TC-SPC) fluorometer equipped with a NanoLED-340. The monomer and excimer fluorescence decays were acquired at 379 and 510 nm using a 370 and 495 nm cut-off filter with an excitation wavelength of 344 nm. The monomer and excimer fluorescence decays were acquired with 40,000 and 20,000 counts at the decay maximum over 1,024 channels with

time-per-channels of 2.04 and 1.02 ns, respectively. The instrument response function (IRF) was collected at 344 nm using a LUDOX dispersion in water with a peak maximum of 20,000 counts.

Fluorescence Blob Model (FBM): All fluorescence decays were globally analyzed with the fluorescence blob model (FBM), which was derived in an earlier publication.⁶⁹ According to the FBM, a macromolecule randomly labeled with pyrene is compartmentalized into segments of equal volume, denoted as *blobs*, representing the volume probed by a pyrenyl label while it remains excited. The random labeling of the macromolecule ensures that the pyrenyl dyes distribute themselves among the *blobs* according to a Poisson distribution. Within the framework of the FBM, the four excited pyrene species Py_{free}^* , $Py_{k_2}^*$, Py_{diff}^* , and Py_{agg}^* can be present inside a *blob*. Py_{free}^* represents isolated pyrene dyes that are excited but do not form excimer within their lifetime, τ_M . $Py_{k_2}^*$ represents excited pyrene dyes close to a ground-state pyrenyl label that form excimer via a rapid rearrangement process with a rate constant k_2 . Py_{diff}^* represents excited pyrene dyes which diffuse through the solution with a rate constant k_{blob} to generate the $Py_{k_2}^*$ species. Py_{agg}^* represents pre-associated pyrenyl labels which form two excimer types through direct excitation. In the present work, the two excimer species $E0^*$ and D^* were detected and represent pyrene aggregates forming excimer with two well or two poorly stacked pyrenyl moieties, respectively. Equations S4.1 and S4.2, provided in the SI, were used for the global analysis of the monomer and excimer fluorescence decays, respectively. Each pair of monomer and excimer fluorescence decays acquired for a given polypeptide was fitted globally with the program *globmis90lbg*, where k_2 was allowed to float during the analysis. For a given polymer series, the k_2 values obtained for each polypeptide sample were averaged and the decays were reanalyzed with the program *globmis90obg* with k_2 fixed to its average value. This procedure has been found to narrow the spread between $N_{\text{blob}}^{\text{exp}}$ values. The quality of each fit using the FBM was assessed

by applying three criteria, namely that the χ^2 value needed to remain below 1.3 and the residuals and autocorrelation of the residuals had to be randomly distributed around zero. Among other parameters, the global analysis of each monomer and excimer fluorescence decay pair yielded the molar fractions f_{diff} , f_{agg} , f_{free} , and f_{k2} of the pyrenyl species Py_{diff}^* , Py_{agg}^* , Py_{free}^* , and Py_{k2}^* and $\langle n \rangle$, the average number of ground-state pyrenes per *blob*. $N_{\text{blob}}^{\text{exp}}$ was calculated with Equation 4.2, where f_{Mfree} represents the molar fraction of Py_{free}^* detected in the monomer fluorescence decays (i.e. omitting Py_{agg}^*) and f_{Py} was defined in Equation 4.1.

$$N_{\text{blob}}^{\text{exp}} = \frac{\langle n \rangle}{x} \times (1 - f_{\text{Mfree}}) \quad (4.2)$$

4.4 RESULTS AND DISCUSSION

Conformational analysis of the PGA samples by circular dichroism: Prior to labeling the PGA samples with pyrene, their secondary structure in aqueous solutions at high and low pH was determined to establish the behaviour of each polymer. To achieve high and low pH conditions, a 10 mM concentration of NaOH and HCl was used, respectively, while the polymer concentration was maintained at 1 mg/mL. As shown in Figure 4.1, a plot of the molar ellipticity of PDLGA showed the same spectral features at high and low pH, namely a peak maximum centered at ~220 nm followed by a peak minimum centered at ~199 nm. These features were consistent with those of a polypeptide adopting a random coil conformation¹³ and serve to demonstrate that the PDLGA sample used in the present study adopts a random coil conformation regardless of pH. PDLGA is expected to retain its random coil conformation in DMF and DMSO, the two organic solvents used for the fluorescence study.

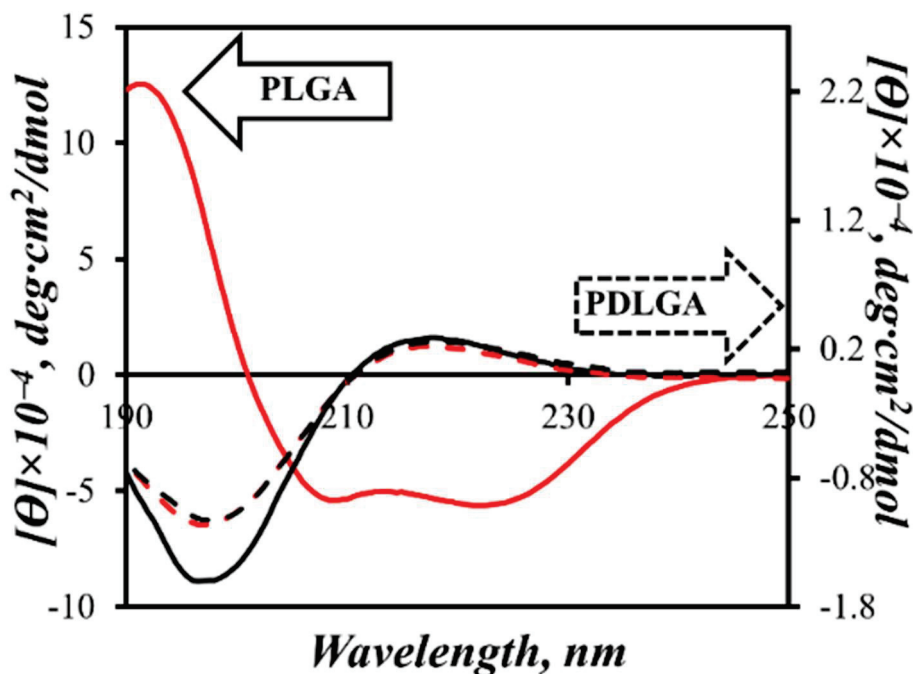


Figure 4.1 Plot of the molar ellipticity as a function of wavelength for (solid) PLGA and (dashed) PDLGA acquired with 10 mM of (black) NaOH or (red) HCl.

At high pH, the carboxylic acids of the PLGA side chains are deprotonated and electrostatic repulsion between the neighbouring side chains destabilizes the α -helical conformation adopted by PLGA at low pH.¹⁶ Considering the striking spectral similarities between PLGA at high pH and PDLGA at high and low pH, it can be concluded that PLGA at high pH most likely adopts a random coil conformation similar to PDLGA.

Contrary to PLGA at high pH, Figure 4.1 clearly demonstrates that the plot of ellipticity obtained for PLGA at low pH has substantially different spectral features, namely a double peak minimum at ~ 222 and ~ 209 nm followed by a peak maximum at ~ 198 nm. The protonated side chains of PLGA at lower pH are no longer ionized and are not subject to electrostatic repulsion between the Glu residues allowing helix formation. The spectral features of PLGA at low pH are

identical to those typically observed for α -helices⁴¹ leading to the conclusion that PLGA at low pH adopts an α -helical conformation. It should be noted that the behavior described in Figure 4.1 for the PLGA sample used in this study agrees with that reported in an earlier publication.¹³

Conformational analysis of the PGA samples by NMR: Although the exact conformation for synthetic homopolypeptides can not be determined from the chemical shift of the α -CH proton signal obtained in a ¹H NMR spectrum, the existence of secondary structure can still be inferred. Specifically, the signal for the α -CH proton obtained for randomly coiled polypeptides is shifted downfield relative to that of polypeptides with a secondary structure. The CD measurements presented in Figure 4.1 have demonstrated that PDLGA adopts a random coil conformation, and thus the chemical shift of the α -CH proton for PDLGA can be compared with the chemical shift of the α -CH proton for PLGA in DMF and DMSO to assess the presence of secondary structure, if any. As seen in Figure 4.2, the broad peaks associated with the α -CH proton for PDLGA were found to be centered at ~ 4.37 ppm in *d*₇-DMF and ~ 4.17 ppm in *d*₆-DMSO whereas they were found at ~ 4.27 ppm in *d*₇-DMF and ~ 3.85 ppm in *d*₆-DMSO for PLGA. In both solvents, the signal from the α -CH proton of PLGA is shifted up-field relative to the α -CH proton of PDLGA. This shift suggests that PLGA in both DMF and DMSO adopts a secondary structure, which agrees with a previous report for PBLGA samples.¹⁹

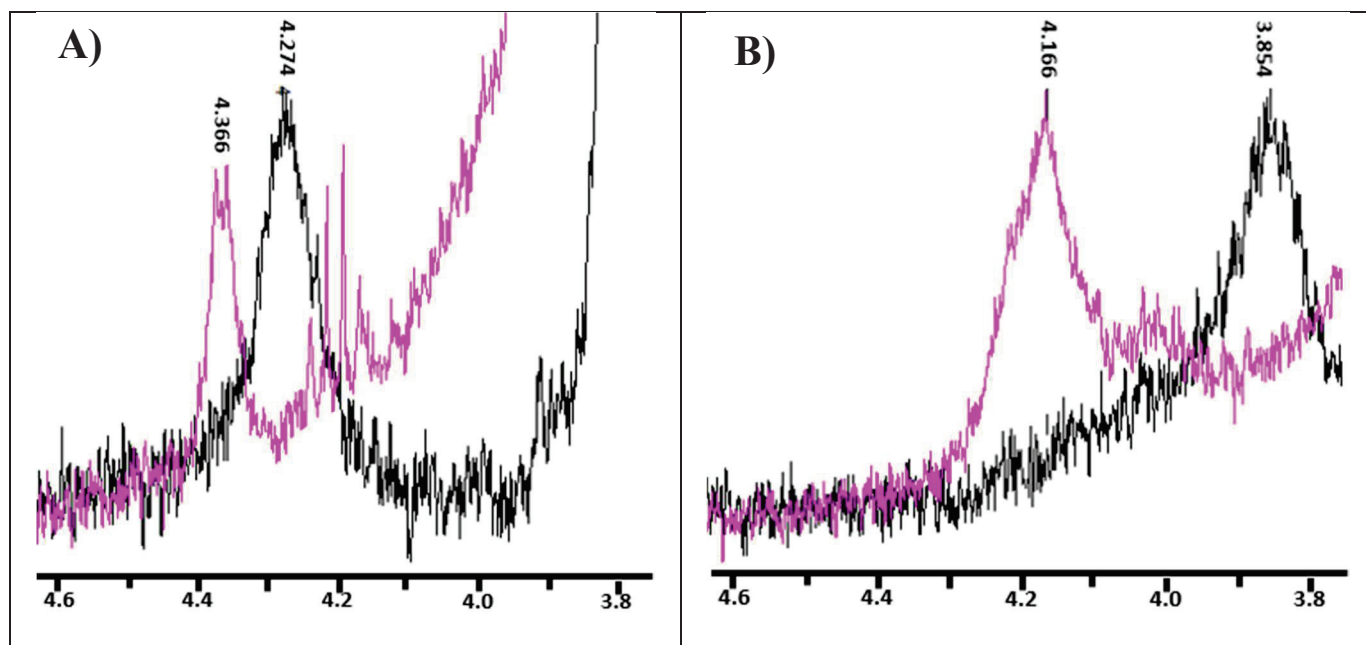


Figure 4.2 Region between 3.7 and 4.6 ppm of the ^1H NMR spectrum showing the signal from the α -CH proton for (black) PLGA and (purple) PDLGA acquired in A) d_7 -DMF and B) d_6 -DMSO. [PLGA] = 1 mg/mL and [PDLGA] = 10 mg/mL.

Steady-State Fluorescence: The steady-state fluorescence spectra of PyC4N-PLGA in DMF were normalized at the 0-0 transition and are shown in Figure 4.3A. These spectra present the typical features expected from a pyrene-labeled macromolecule, namely the sharp fluorescence peaks observed for the pyrene monomer between 360 and 440 nm and the broad structureless emission of the excimer centered at 480 nm. The I_E/I_M ratio was calculated and plotted as a function of the pyrene content for each sample in DMF (Figure 4.3B) and DMSO (Figure 4.3C). Figures 4.3B and C display three important trends which were similar in DMF and DMSO. First, for each construct and regardless of solvent, the I_E/I_M ratio increased with increasing pyrene content, which is consistent with trends observed for pyrene covalently bound onto macromolecules.²³⁻²⁶ This trend is reasonable since an increase in pyrene content results in more pyrene-pyrene encounters and

thus PEF. Second, the I_E/I_M ratio for PyC8N-PLGA and PyC8N-PDLGA was larger than that for the respective PyC4N-PLGA and PyC4N-PDLGA samples. This effect is a consequence of the longer reach of the pyrenyl label attached to the polypeptide backbone via a longer linker, which allows the excited pyrene to probe a larger volume along the macromolecule, that will contain more ground-state dyes.^{26,70} Third, the I_E/I_M ratio is higher in a same solvent and for a same pyrene content of a same pyrene derivative for the PLGA samples compared to their PDLGA counterparts.

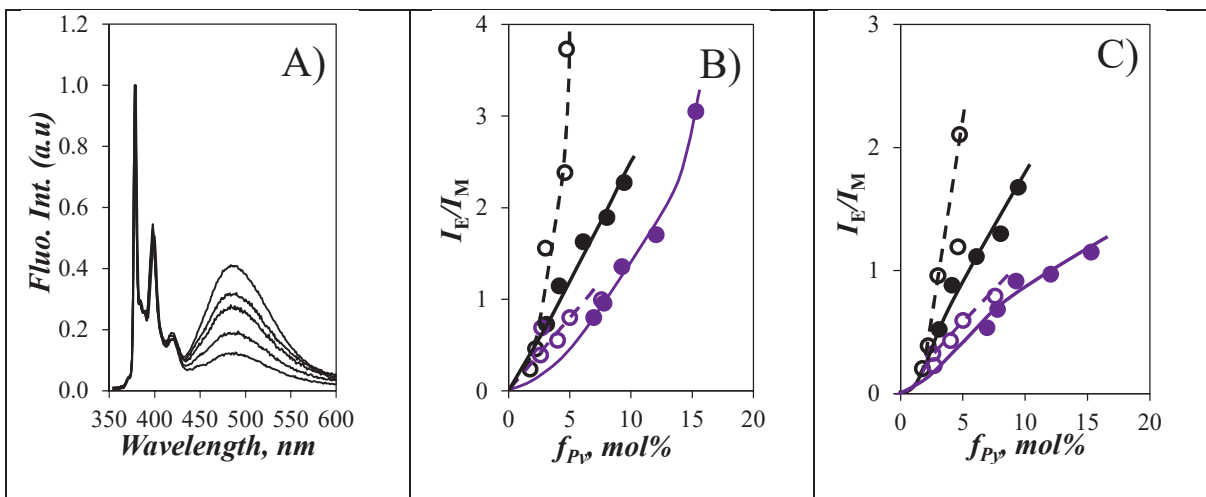


Figure 4.3 A) SSF spectra for the PyC4N-PLGA samples in DMF. Plots of I_E/I_M as a function of pyrene content for (○) PyC8N-PLGA, (●) PyC4N-PLGA, (○) PyC8N-PDLGA, and (●) PyC4N-PDLGA in B) DMF and C) DMSO. Lines: Samples labeled with (solid) PyC4N and (dashed) PyC8N.

The larger I_E/I_M ratio observed for the PLGA rather than the PDLGA samples indicates that an excited pyrenyl label attached to PLGA experiences a larger $[Py]_{loc}$, and thus local density, compared to the PDLGA samples. Since this observation is made in DMF and DMSO and since a larger $[Py]_{loc}$ is typically obtained for a structured, and thus more condensed macromolecule, it would suggest that PLGA is structured in both DMF and DMSO but that PDLGA is not. Unfortunately, the SSF spectra only allow a qualitative characterization of the conformation of the

different polypeptide constructs. Quantitative characterization of the conformation of the constructs can be achieved through the analysis of the time-resolved fluorescence decays as described in the following section.

Analysis of the fluorescence decays with the fluorescence blob model: The fluorescence decays of the PGA samples labeled with PyC4N and PyC8N were acquired in DMF and DMSO and they were globally analyzed with the fluorescence *blob* model (FBM) to yield the number ($N_{\text{blob}}^{\text{exp}}$) of Glu inside a *blob*. $N_{\text{blob}}^{\text{exp}}$ was calculated with Equation 4.2 and was plotted as a function of pyrene content (f_{Py}) in Figure 4.4A. Within experimental error, the $N_{\text{blob}}^{\text{exp}}$ values remained constant with pyrene content for the PyC4N-PDLGA and PyC8N-PDLGA samples yielding an average $\langle N_{\text{blob}}^{\text{exp}} \rangle$ value of 15 (± 2) and 21 (± 2), respectively, regardless of solvent. The constancy of $\langle N_{\text{blob}}^{\text{exp}} \rangle$ in DMF ($\eta = 0.79 \text{ mPa}\cdot\text{s}$)⁷¹ and much more viscous DMSO ($\eta = 1.99 \text{ mPa}\cdot\text{s}$)⁷¹ indicates that for these rigid constructs, the volume probed by an excited pyrenyl label (*i.e.* the *blob*) is unaffected by the changes in solvent viscosity. The main dynamic change observed between DMF and DMSO is a 30% reduction in k_2 from 0.09 to 0.06 ns⁻¹ for the PyC4N-PDLGA samples (see Tables S4.13 and S4.16) and a 30% reduction in k_{blob} from 16 (± 3) to 11 (± 1) μs^{-1} for the PyC8N-PDLGA samples (see Tables S4.19 and S4.22), respectively, which did not affect $\langle N_{\text{blob}}^{\text{exp}} \rangle$. Contrary to PDLGA where the same $\langle N_{\text{blob}}^{\text{exp}} \rangle$ values were obtained in DMF and DMSO, $\langle N_{\text{blob}}^{\text{exp}} \rangle$ values of 30 (± 3) for PyC4N(*x*)-PLGA and 42 (± 3) for PyC8N(*x*)-PLGA were found in DMF, while $\langle N_{\text{blob}}^{\text{exp}} \rangle$ took a lower value of 24 (± 3) for PyC4N(*x*)-PLGA and 33 (± 3) for PyC8N(*x*)-PLGA in DMSO.

The larger $\langle N_{\text{blob}}^{\text{exp}} \rangle$ value obtained for the Py-PLGA constructs in both DMF and DMSO compared to $\langle N_{\text{blob}}^{\text{exp}} \rangle$ obtained for the Py-PDLGA samples indicated that in both solvents, the

pyrenyl labels were held closer to each other for the Py-PLGA samples than for the Py-PDLGA samples, thus reflecting the denser conformation adopted by PLGA. In turn, this observation confirmed that PLGA adopted a secondary structure in both solvents compared to the randomly coiled PDLGA. Furthermore, since PDLGA was randomly coiled in both DMF and DMSO, the fact that $\langle N_{\text{blob}}^{\text{exp}} \rangle$ remained unchanged in both solvents for either the PyC4N(x)-PDLGA or PyC8N(x)-PDLGA samples indicated that changing the solvents from DMF to DMSO would not affect $\langle N_{\text{blob}}^{\text{exp}} \rangle$ for a same conformation of the polypeptide despite the large increase in solvent viscosity from DMF (0.79 mPa.s at 25 °C) to DMSO (1.99 mPa.s at 25 °C).⁷¹ However, since $\langle N_{\text{blob}}^{\text{exp}} \rangle$ increased going from Py-PLGA in DMSO to Py-PLGA in DMF, it suggested that the conformation of PLGA in DMF was different from and denser than that of PLGA in DMSO.

As mentioned earlier, the overarching goal of the present study was to probe the conformation of PLGA and PDLGA on longer length scales via the use of pyrene derivatives with linkers that were longer than that of PyC1N used in earlier studies.^{24,26} To ensure that a larger volume was probed with a longer linker, $\langle N_{\text{blob}}^{\text{exp}} \rangle$ was compared with the distance corresponding to the diameter of a *blob*, whose calculation is provided in the SI. In brief, HyperChem was used to attach a 1-pyrene-methyl-, -butyl-, or -octyl-amine derivative onto a Glu residue. The distance ($d_{\text{Py}-\alpha\text{C}}$) between the α -C of the Glu unit and the center of mass (CoM) of the pyrenyl label was determined and multiplied by 4 to represent the diameter of a *blob*, since an excited pyrene located at a distance $d_{\text{Py}-\alpha\text{C}}$ from a given α -C can form an excimer with a ground-state pyrene located at a same distance from another α -C on one side of the PGA backbone. The same holds true on the other side of the PGA backbone leading to a maximum distance (L_{PEF}) probed by PEF equal to $4 \times d_{\text{Py}-\alpha\text{C}}$ and found to equal 4.0, 5.7, and 7.7 nm for a methyl, butyl, and octyl linker, respectively. As shown in Figure 4.4B, $\langle N_{\text{blob}}^{\text{exp}} \rangle$ determined from this and previous works^{24,26} increased

linearly with the diameter of a *blob*, which is dictated by the linker length of the pyrene derivative used. This reasoning demonstrates that increasing the linker length separating the pyrenyl dye from the main chain increases the volume, that it can probe, and that this volume can be directly monitored via $\langle N_{\text{blob}}^{\text{exp}} \rangle$.

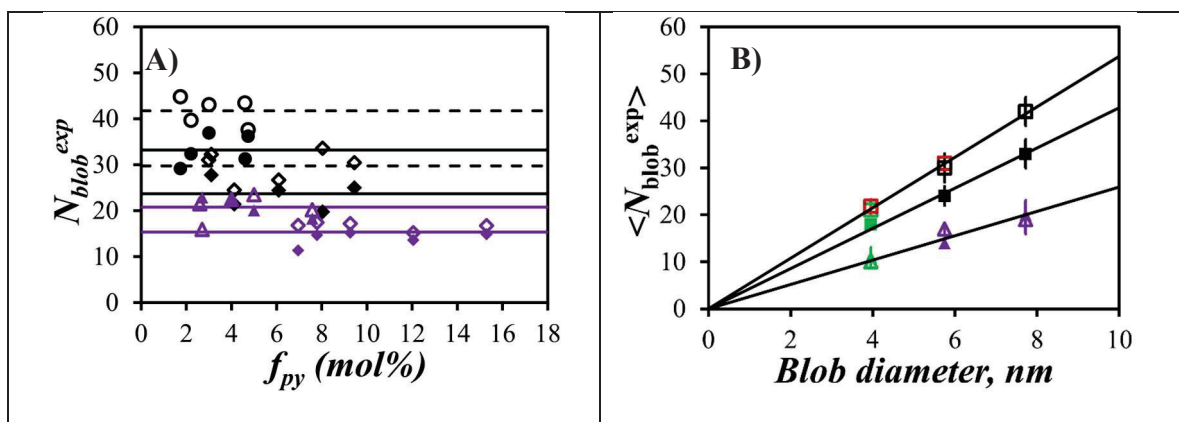


Figure 4.4 A) Plot of $N_{\text{blob}}^{\text{exp}}$ as a function of pyrene content for (black) PLGA and (purple) PDLGA labeled with (\diamond) 1-pyrene butylamine or (\circ) 1-pyrene octylamine in (hollow) DMF and (filled) DMSO. B) Plot of $\langle N_{\text{blob}}^{\text{exp}} \rangle$ as a function of the *blob* diameter in (hollow) DMF and (filled) DMSO for (\square) PLGA and (\triangle) PDLGA. $\langle N_{\text{blob}}^{\text{exp}} \rangle$ data shown in green²⁴ and red²⁶ were taken from previous reports on PLGA and PDLGA labeled with 1-pyrenemethylamine^{24,26} and 1-pyrenebutylamine.²⁶

Molecular mechanics optimizations (MMO): To elucidate the conformation of the PLGA and PDLGA constructs in DMF and DMSO, $\langle N_{\text{blob}}^{\text{exp}} \rangle$ was compared with the $N_{\text{blob}}^{\text{MMO}}$ values obtained by molecular mechanic optimizations (MMO) conducted with PLGA constructs of known conformations. All MMO were conducted using HyperChem (version 8.0.7) in the same manner as in previous reports.²⁴⁻²⁶ The Fletcher-Reeves Conjugate gradient *in vacuo* with a termination condition of an RMS gradient of $0.1 \text{ kcal}\cdot\text{\AA}^{-1}\cdot\text{mol}^{-1}$ was used for all simulations.

PLGA constructs in HyperChem were set to have the conformation of a random coil or a PPII- ($\phi = -75^\circ$, $\psi = 145^\circ$, $\omega = 180^\circ$), 3_{10} - ($\phi = -49^\circ$, $\psi = -26^\circ$, $\omega = 180^\circ$), or α - ($\phi = -58^\circ$, $\psi = -47^\circ$, $\omega = 180^\circ$) helix and the simulations were conducted for PLGA constructs labeled with PyC4N and PyC8N since the MMO with PyC1N had been conducted earlier.^{24,26} To generate a randomly coiled PLGA construct, a constraint of 999 Å was placed between the amino and carboxyl terminus of an α -helical PLGA construct. With the restraints in place the structure was optimized to fully stretch the PLGA chain. The restraints were subsequently removed, and the optimization of the backbone was conducted again to yield the randomly coiled construct. A side and top view of each PLGA conformation is provided in Figure 4.5.

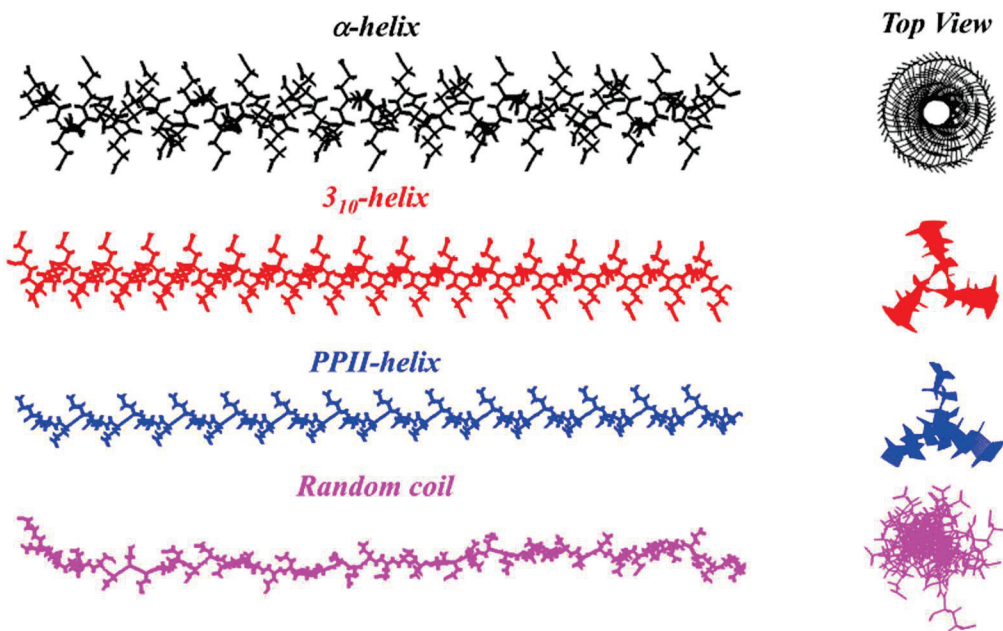


Figure 4.5 A side and top view of a PLGA chain generated in silico with an α -, 3_{10} -, and PPII-helical and a random coil conformation.

Visual inspection of Figure 4.5 suggests that within a same volume, the largest number of carboxylic acids per unit volume is obtained for an α -helix followed by the 3_{10} -helix, the PPII-

helix, and the random coil conformation. This trend is expected since α -, 3_{10} -, and PPII-helices have 3.6,⁷² 3.2⁷³ and 3.0⁷⁴ amino acid residues per turn, respectively, reflecting a decrease in the local density of the construct.

Several reports have described the methodology applied to determine $N_{\text{blob}}^{\text{MMO}}$ with molecular mechanics optimizations (MMO),²⁴⁻²⁶ and a succinct description of the methodology is provided for an α -helical PLGA construct labeled with 1-pyrenebutylamine. In brief, a 50 residue PLGA α -helix was generated *in silico* using the built-in amino acid database of HyperChem and the backbone was fixed in place using the 'FIX ATOM' constraint. One PyC4N was attached to the 7th glutamic acid residue from the amino terminal of the construct and was denoted as the reference pyrene. A second PyC4N was attached onto the adjacent Glu residue moving towards the C-terminal of the construct and it was referred to as the secondary pyrene. Restraints of 3.4 Å were placed between the reference and the secondary pyrene and a geometry optimization was conducted to induce stacking of the two pyrene moieties. Following the MMO, the number of carbon atoms ($n_{\text{C-C}}$) of one pyrene overlapping the frame of the second pyrene was determined and recorded. The reference pyrene was kept at the same position while the secondary pyrenyl label was moved to the next Glu towards the C terminus. The MMO were repeated until 3 consecutive positions had returned a zero-value for $n_{\text{C-C}}$, indicating that the reference and secondary pyrenyl labels were now too far apart. A plot of $n_{\text{C-C}}$ as a function of the number of Glu (#Glu) separating the secondary pyrenyl dye from the reference one is given in Figure 4.6. For PEF to occur, two conditions must be met. First, the dyes must remain planar at the end of the MMO and second, an $n_{\text{C-C}}$ value of 7 or more carbon atoms must be obtained to ensure the good overlap conducive of PEF.⁷⁵ An example of good, poor, and no overlap is provided in Figure 4.6C. From Figure 4.6A, it was found that for PyC4N attached to PLGA constructs, that adopted a PPII-, 3_{10} -, and α -helical

conformation, the reference and secondary pyrenyl labels showed good overlap, when they were separated by up to 8, 11, and 14 Glu, respectively, whereas for PLGA in a random coil conformation, a good overlap between the reference and the secondary pyrene was observed when they were separated by ~ 7 Glu. These numbers include the Glu bearing the secondary pyrene and are referred to as N_0 .

For constructs labeled with PyC8N, a good overlap was obtained for PLGA constructs adopting a PPII-, 3_{10} -, or α -helical conformation, if the reference and secondary pyrene were separated by 11, 16, and 21 Glu, whereas PLGA in a random coil conformation yielded 9 Glu with sufficient carbon atom overlap between the reference and secondary pyrene. Since PEF for a pyrene-labeled macromolecule can occur on either side of the reference pyrene attached on a PLGA construct, $N_{\text{blob}}^{\text{MMO}}$ was calculated as $2 \times N_0 + 1$ where “1” is added to account for the Glu bearing the reference pyrene. Based on this definition, $N_{\text{blob}}^{\text{MMO}}$ values of 17, 23, and 29 were obtained when PyC4N was attached on PLGA constructs, that adopted a PPII-, 3_{10} -, and α -helical conformation, respectively. Similarly, $N_{\text{blob}}^{\text{MMO}}$ values of 23, 33, and 43 were obtained when PyC8N was attached onto PLGA constructs adopting a PPII-, 3_{10} -, and α -helical conformation, respectively. For randomly coiled PLGA constructs labeled with PyC4N and PyC8N, $N_{\text{blob}}^{\text{MMO}}$ was found to equal 14 (± 1) and 20 (± 2), respectively.

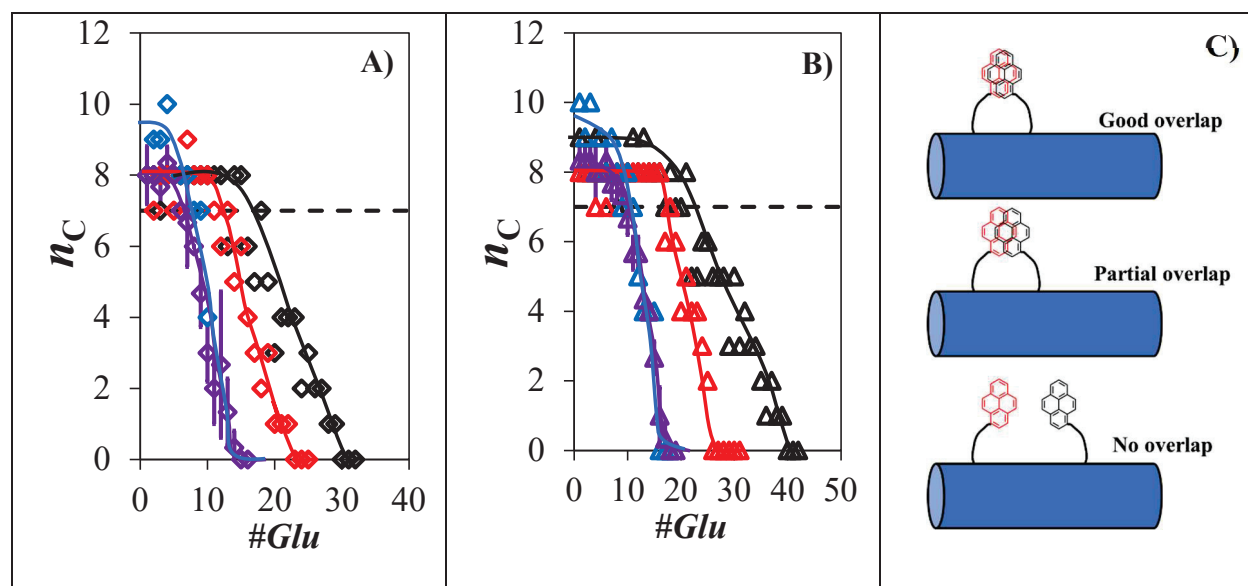


Figure 4.6 Plot of the number of carbon atoms (n_C) in the frame of the reference pyrene overlapping the frame of the secondary pyrene as a function of the number (#Glu) of Glu residues separating the reference from the secondary pyrene for A) PyC4N (\blacklozenge) and B) PyC8N (\bullet) attached onto a PLGA construct adopting a (blue) PPII-, (red) 3_{10} -, and (black) α -helical conformation or (purple) a random coil conformation. The lines presented in each plot are a means to guide the eye only. C) Schematic representation of the MMO conducted with two pyrenyl labels showing good (top), partial (middle), and no (bottom) overlap.

Comparison of N_{blob}^{exp} and N_{blob}^{MMO} : Comparison between $\langle N_{blob}^{exp} \rangle$ obtained experimentally for a given pyrene-labeled PLGA and PDLGA construct with N_{blob}^{MMO} determined for a given PLGA conformation yields conformational insight into the secondary structure of the polypeptide in solution. As such, $\langle N_{blob}^{exp} \rangle$ determined for the PLGA and PDLGA samples labeled with PyC1N,^{24,26} PyC4N,²⁶ and PyC8N was plotted as a function of N_{blob}^{MMO} obtained for each PLGA conformation in Figure 4.7. As shown in Figure 4.4B, $\langle N_{blob}^{exp} \rangle$ obtained for either PDLGA in DMF and DMSO, PLGA in DMSO, and PLGA in DMF increased linearly with increasing linker

length, and the magnitude of the slope depended on the conformation adopted by the polypeptide, a random coil for PDLGA in both DMF and DMSO and an α -helix for PLGA in DMF. Consequently, the relative position of each series of data points in the $\langle N_{\text{blob}}^{\text{exp}} \rangle$ -vs.- $N_{\text{blob}}^{\text{MMO}}$ plots shown in Figure 4.7 was expected to yield a good correlation around the main diagonal between $\langle N_{\text{blob}}^{\text{exp}} \rangle$ and $N_{\text{blob}}^{\text{MMO}}$ for a matching conformation.

To assess the validity of this methodology, $\langle N_{\text{blob}}^{\text{exp}} \rangle$ obtained for the pyrene-labeled PDLGA, which should adopt a random coil conformation in DMF and DMSO (see Figures 4.1 and 4.2), was first analyzed. As seen in Figure 4.7A for the pyrene-labeled PDLGA constructs, the $\langle N_{\text{blob}}^{\text{exp}} \rangle$ values determined in either DMF or DMSO yielded the closest match with the $N_{\text{blob}}^{\text{MMO}}$ values expected for a random coil conformation, while all other conformations resulted in the $\langle N_{\text{blob}}^{\text{exp}} \rangle$ data points appearing below the 1:1 diagonal. The excellent agreement between $\langle N_{\text{blob}}^{\text{exp}} \rangle$ and the $N_{\text{blob}}^{\text{MMO}}$ values predicted for a random coil further confirmed that PDLGA adopts a random coil conformation in DMF and DMSO, which agrees with the earlier CD experiments (Figure 4.1), and supports the validity of the PEF-based approach to determine the conformation of a polypeptide in solution. The $\langle N_{\text{blob}}^{\text{exp}} \rangle$ values obtained for the pyrene-labeled PLGA constructs in DMF, a well-known helicogenic solvent,⁷⁶ were found to land on the 1:1 diagonal for the $N_{\text{blob}}^{\text{MMO}}$ values corresponding to an α -helical conformation. Additionally, all other conformations for PLGA in DMF were clearly above the 1:1 diagonal and underestimated the local density of the macromolecule. Consequently, Figure 4.7B confirmed that PLGA adopts an α -helical conformation in DMF.

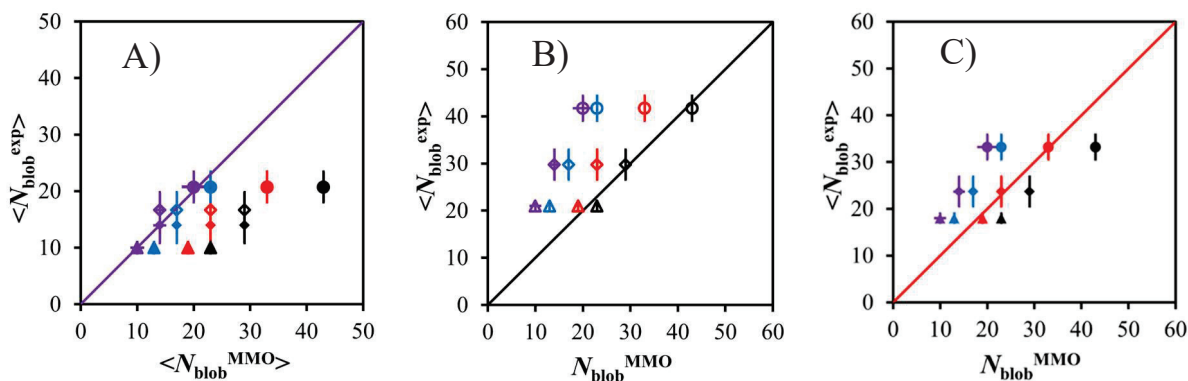


Figure 4.7 Plot of $\langle N_{\text{blob}}^{\text{exp}} \rangle$ for (\blacktriangle) PyC1N,²⁵ (\blacklozenge) PyC4N, and (\bullet) PyC8N labeled A) PDLGA in (hollow) DMF or (filled) DMSO and PLGA in B) DMF or C) DMSO as a function of $N_{\text{blob}}^{\text{MMO}}$ for (purple) a random coil or (blue) a PPII-helix, (red) 3_{10} -helix, and (black) α -helix. The solid line represents the 1:1 diagonal.

Since the methodology based on the comparison of $\langle N_{\text{blob}}^{\text{exp}} \rangle$ and $N_{\text{blob}}^{\text{MMO}}$ had correctly predicted the random coil conformation of PDLGA in DMF and DMSO and the α -helical conformation of PLGA in DMF, it was applied to assess the conformation of PLGA in DMSO. As shown in Figure 4.7C, a surprisingly good match was found between $\langle N_{\text{blob}}^{\text{exp}} \rangle$ for the pyrene-labeled PLGA in DMSO and $N_{\text{blob}}^{\text{MMO}}$ obtained for a 3_{10} -helix. Consequently, this result indicates that PLGA in DMSO adopts a 3_{10} -helical conformation, which represents the first unambiguous assignment of the conformation of PLGA in this solvent.

4.5 CONCLUSIONS

This study has expanded the use of the methodology, whereby $N_{\text{blob}}^{\text{exp}}$ obtained through PEF experiments conducted on a macromolecule randomly labeled with pyrene is compared to $N_{\text{blob}}^{\text{MMO}}$ obtained from MMO conducted *in silico* on the same pyrene-labeled macromolecule adopting an

assumed conformation. Up to now, the methodology had been mostly confined to pyrene-labeled macromolecules where the pyrenyl moiety was connected to the macromolecular backbone via a linker made of 5 – 6 non-hydrogen atoms, which resulted in a maximum length scale of about 4.0 nm. By attaching PyC4N and PyC8N to PDLGA and PLGA, linkers made of 8 and 12 non-hydrogen atoms were created that afforded maximum length scales probed by PEF of 5.7 and 7.7 nm, respectively. Such distances are comparable to those probed with FRET donor and acceptor pairs making PEF a worthy alternative to FRET as a novel spectroscopic ruler.⁶⁵ The PEF-based methodology was applied to determine that the unknown conformation of PLGA in DMSO is that of a 3_{10} -helix. Not only does this study represent, to the best of our knowledge, the first report to unambiguously demonstrate that PLGA adopts a 3_{10} -helical conformation in DMSO, but more importantly, it illustrates that the combination of PEF and MMOs provides a robust methodology to characterize the unknown conformation of complex macromolecules in solution. Furthermore, the ability of PEF-based methods to probe the local macromolecular conformation implies that the methodology is applicable to macromolecules that are mono- or poly-disperse at extremely dilute macromolecular concentrations in the 1-10 mg/L range in a manner that nicely complements the more traditional techniques such as scattering, NMR, CD, ROA, FRET, or FTIR, to name but a few, currently used for this purpose.

SUPPORTING INFORMATION

¹H NMR and UV-Vis characterization; Fluorescence Blob model (FBM) analysis; Parameters retrieved from the FBM analysis; Molecular Mechanic Optimization; and References.

Chapter 5: Pyrene Excimer Formation as a Tool for Probing Polymer Microstructure – Application to Poly(norbornene Acid)

5.1 ABSTRACT

The microstructure of a poly(norbornene acid) (PNb-Ac) sample was characterized on different length scales using pyrene excimer formation (PEF) between excited and ground-state pyrene labels that had been randomly attached onto the PNb-Ac sample via four linkers of different

lengths to yield four series of PyCX(x)N-PNb-Ac samples. X and x in PyCX(x)N-PNb-Ac represent the number of carbons in the linker of the pyrene derivative used in the labeling reactions and the mole fraction of residues labeled with pyrene, respectively. In this study, PNb-Ac was labeled with 1-pyrene-methyl- (PyC1N), -butyl- (PyC4N), -octyl- (PyC8N), and -dodecyl- (PyC12N) amine for X equal to 1, 4, 8, and 12, respectively. The fluorescence decays of the pyrene monomer and excimer of the PyCX(x)N-PNb-Ac samples were acquired in N,N -dimethylformamide (DMF) and dimethyl sulfoxide (DMSO) before being globally analyzed with the fluorescence *blob* model (FBM) to yield $\langle N_{\text{blob}}^{\text{exp}} \rangle$, the average number of norbornene units per *blob*. Based on the FBM, a *blob* is the volume probed by an excited pyrenyl label covalently attached onto the PNb-Ac construct. The $\langle N_{\text{blob}}^{\text{exp}} \rangle$ values for the PyCX(x)N-PNb-Ac samples were compared with $N_{\text{blob}}^{\text{MMO}}$ determined by molecular mechanic optimizations (MMO) for PNb-Ac constructs adopting a random coil or helical conformation. This comparison led to the finding that on short length scales of 4.1 and 5.8 nm generated by the PyC1N and PyC4N derivatives, respectively, PNb-Ac appeared to have a local conformation similar to that of a 6_1 -helix while on the longer length scales of 7.8 and 9.9 nm, generated by PyC8N and PyC12N, respectively, PNb-Ac could be viewed as a random coil. Consequently, this study demonstrated that PNb-Ac becomes less dense when probed over increasing length scales and that PEF can quantitatively characterize the local microstructure of pyrene-labeled macromolecules in solution on different length scales.

5.2 INTRODUCTION

The length scale over which macromolecules maintain a homogeneous configuration has a profound impact on their physical properties. The conformation of a polymer can be broadly defined by the distribution and types of arrangements adopted by structural units along the main chain and it has a major impact on polymer microstructure. Consequently, chain length distribution,¹ main chain regio/stereochemistry,²⁻⁴ monomer or segment sequence,^{5,6} and architecture⁷ are some of the many factors impacting polymer microstructure. The current experimental tools available for microstructure characterization can be divided into four main categories based on microscopy,^{8,9} computation,¹⁰⁻¹⁹ scattering,²⁰⁻²⁹ and spectroscopy.³⁰⁻³⁸ Since microscopy-based experiments tend to focus more on polymer morphologies instead of microstructure, polymer microstructure is often characterized by using computation, spectroscopy, and scattering. Computational approaches excel at generating 3D images of a macromolecule and predicting polymer behavior, dynamics, physical properties, structure-property relationships, etc.¹⁰ However, the numerous interactions, that must be accounted for in computational studies conducted for microstructure determination, typically require the use of approximations and unique/modified force fields, whose results must be validated against experimental data.^{10,39} Spectroscopy-based approaches to study macromolecules usually involve nuclear magnetic resonance (NMR) spectroscopy. The main appeal of NMR stems from its ability to sense minute differences in the local chemical environment of a given nucleus and its proximity to adjacent nuclei, which in turn can be used to generate a 3D structure of the macromolecule.³⁵ Unfortunately, these minute differences in local environment are difficult to detect for large synthetic macromolecules constituted of a same structural unit.³⁶ Furthermore, the assignment of chemical shifts for a microstructure generated by the given configuration of a structural unit can be

challenging despite the use of model compounds,⁴⁰⁻⁴³ although methodologies have been implemented to predict the microstructure of some polyolefins from the analysis of their chemical shifts.⁴⁴⁻⁴⁹ Small angle X-ray (SAXS) or wide angle X-ray (WAXS) scattering experiments provide insight about the size and shape of macromolecules by probing their local density. Depending on the macromolecule, scattering experiments require high polymer concentrations in the 0.1 to 20 mg/mL range to generate sufficient scattering signal and monodisperse samples are usually preferred for analysis.^{25,26} Since the scattering signal depends strongly on macromolecular size, analysis of scattering data is complicated by any broadening of the size distribution of a macromolecule. A broadening of the size distribution can be due to the unavailability of synthetic techniques capable of producing the macromolecule of interest with a narrow molecular weight distribution (MWD) or uncontrolled macromolecular aggregation caused by stronger interactions generated at the polymer concentrations used in scattering experiments.^{25,26}

This list of limitations highlights a need for alternate experimental techniques to better characterize macromolecular microstructures. Ideally such techniques would A) use low polymer concentrations to minimize intermacromolecular interactions and avoid solubility issues, B) be insensitive to macromolecular dispersity, C) probe the microstructure of a macromolecule on different length scales to determine how far it is retained, and D) yield experimental parameters representative of a given macromolecular conformation to be compared to those obtained *in-silico* as a form of integrative structural macromolecular science.^{50,51} One technique particularly well suited for this task is based on fluorescence collisional quenching (FCQ).

The advantages of FCQ experiments are described hereafter. First, fluorescence is an extremely sensitive technique enabling one to work at macromolecular concentrations as low as 1 mg/L, thereby limiting both solubility issues and inter-macromolecular interactions.⁵² Second,

FCQ processes, like pyrene excimer formation (PEF) between an excited and a ground-state pyrenyl labels covalently attached onto a macromolecule,^{52–55} occur over a few nanometers due to the restricted mobility experienced by the dyes and quenchers attached onto a macromolecule. In turn, the length scale over which collisions take place is defined by the volume probed by the excited dye, referred to as a *blob*, which can be used to compartmentalize the macromolecule into a cluster of *blobs*. Compartmentalization of the macromolecule into identical *blobs* shifts the focus of the study from a polydisperse macromolecule to a *blob*, thus eliminating issues associated with polydispersity. Third, since the quenching rate constant is proportional to the local concentration ($[Q]_{\text{loc}}$) of the quencher in the macromolecular volume, it is directly related to the local density of the macromolecule and can be used to predict its conformation.^{53–55} Fourth, the size of a *blob*, which defines the length scale over which the macromolecule is being probed by the dye and quencher, is controlled not only by the local dynamics and density of a macromolecule but also by the length of the linker connecting the dyes and quenchers to the macromolecule. Consequently, the observation length scale can be easily modified by adjusting the linker length.^{56–62} Fifth, the size of a *blob* defined by the number ($N_{\text{blob}}^{\text{exp}}$) of structural units located inside a *blob*, can be determined with the fluorescence *blob* model (FBM), which was introduced to study macromolecules randomly labeled with pyrene.^{63–70} A match between $N_{\text{blob}}^{\text{exp}}$ and $N_{\text{blob}}^{\text{MMO}}$, obtained by conducting molecular mechanics optimizations (MMO) on different conformations of the same macromolecule labeled with the same pyrenyl derivative, provides a means for assigning a given conformation to the macromolecule. Consequently, N_{blob} can be viewed as a structural parameter that could be used in integrative structural macromolecular science.^{56,62,65–70}

The present study takes advantage of the appealing features of PEF, a well-known example of FCQ, to characterize the length scale over which the conformational homogeneity of a

poly(norbornene acid) (PNb-Ac) sample is maintained. The PNb-Ac sample was selected due to the excellent physical properties displayed by products obtained through the vinyl-addition polymerization of norbornene.^{16–19,34,37,40,42,46,71,72} Beside being optically transparent,^{73,74} polynorbornenes (PNb) have a high T_g (≥ 220 °C)^{29,37,71–73} and excellent thermostability,^{73–76} chemical resistivity,^{37,38,77} and dielectric^{29,37,71,75,78} and mechanical⁷⁴ properties. This broad range of properties is a consequence of the varied PNb microstructures, which can be adjusted depending on the polymerization conditions.^{29,79–81} For example, it was shown in a recent study conducted with 3 copolymers, where the ratio of norbornene and hexylnorbornene was adjusted, that T_g was consistently 20 °C higher when the copolymers were produced with a Pd- *versus* a Ni-catalyst.²⁹ The difference in T_g was rationalized by assuming that the copolymers adopted a helix-kink conformation, as proposed in several computation-based studies of PNb.^{16,20–22} These results suggested that the Pd-catalyzed copolymers had fewer kinks compared to the Ni-catalyzed copolymers so that the latter copolymer had a lower packing efficiency and thus a lower T_g . This discussion highlights the need for developing techniques capable of probing the microstructure of macromolecules in general and PNb in particular over different length scales.

To probe the conformation of the PNb-Ac sample over different length scales, the length scale over which the PEF measurements were conducted was adjusted by randomly labeling PNb-Ac with four pyrene derivatives, where the pyrene moiety was linked to the main chain via four different spacer lengths. The pyrene-labeled PNb-Ac samples were referred to as PyCX(x)N-PNb-Ac, where X equals 1, 4, 8, or 12 depending on whether 1-pyrene-methyl- (PyC1N), -butyl- (PyC4N), -octyl- (PyC8N), or -dodecyl- (PyC12N) amine was used for the labeling, respectively, and x represents the molar fraction of pyrene-labeled norbornene units. Global analysis of the monomer and excimer fluorescence decays of the PyCX(x)N-PNb-Ac samples with the FBM

yielded $N_{\text{blob}}^{\text{exp}}$, whose value increased with increasing length of the linker of the pyrene derivative as had been observed for other macromolecules.^{62,67,70} Comparison of $N_{\text{blob}}^{\text{exp}}$ and $N_{\text{blob}}^{\text{MMO}}$ obtained by conducting MMO on two PNB-Ac constructs that adopted either a random coil or helical conformation led to the conclusion that PNB-Ac had a more or less dense microstructure similar to that of a 6_1 helix or a random coil over length scales shorter or larger than 6 nm, respectively. The heterogeneous nature of the PNB backbone characterized by PEF for PNB-Ac over different length scales might rationalize why different properties are observed for PNB samples prepared by different synthetic methods and resulting in different microstructures over different length scales.

5.3 EXPERIMENTAL

Chemicals: Unless otherwise stated, all reagents were purchased from Sigma-Aldrich and used without further purification. Oxalyl chloride, monomethyl suberate, and 12-methoxy-12-oxo-decanoic acid were purchased from Oakwood Chemicals, Fisher Scientific, and Ambeed Inc, respectively. The synthesis of the poly(norbornene acid) (PNB-Ac) sample has been described earlier.⁸²

Gel permeation chromatography (GPC): The molecular weight distribution of the PNB-Ac sample ($M_n = 21.5 \text{ kg}\cdot\text{mol}^{-1}$, PDI = 1.3 with $dn/dc = 0.212$, using the mass of injected polymer) was determined with an aqueous Agilent GPC instrument equipped with a triple detection system that included a differential refractive index, dynamic light scattering, and viscosity detectors. The eluent was an aqueous solution of 100 mM NaNO_3 , 50 mM NaHCO_3 , 20 mM triethyl amine, and 5 mM NaN_3 .

Pyrene derivatives: PyC1N was purchased from Aldrich. The synthesis of PyC4N, PyC8N, and PyC12N has been described elsewhere.⁷⁰

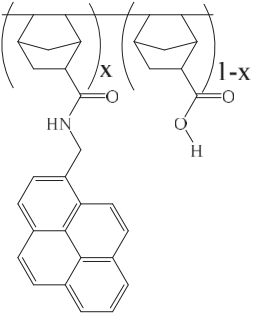
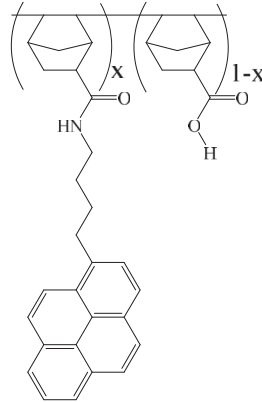
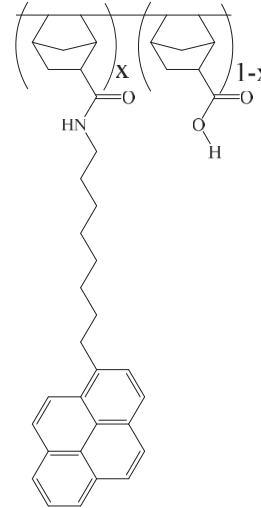
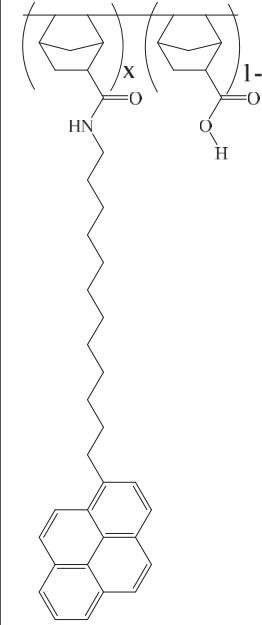
Pyrene labeling: All pyrene labeled PNb-Ac samples were prepared via a standard DIC coupling reaction and a brief description of the procedure is provided hereafter for a PNb-Ac sample labeled with 5.6 mol % of PyC4N. A 20 mL vial equipped with a magnetic stir bar was charged with PNb-Ac (0.05 g, 0.36 mmol of polymer), PyC4N (33 μmol , 0.090 e.q), 4-(dimethylamino)pyridine (DMAP, 49 μmol , 0.13 e.q), and *N,N*-dimethylformamide (DMF, 3 mL). Upon complete dissolution via vigorous stirring, *N,N'*-diisopropylcarbodiimide (DIC, 59 μmol , 0.16 e.q) was added dropwise to the reaction mixture. The reaction was left in the dark overnight under continuous stirring. The following day the sample was precipitated 6-8 times in diethyl ether. The solid product was dried in *vacuum* overnight prior to pyrene content determination. The chemical structure of the PyCX(*x*)N-PNb-Ac samples is presented in Table 5.1.

Pyrene content determination: All absorption measurements were conducted using a quartz cuvette with a 1 cm pathlength on a Cary 100 UV-Vis spectrophotometer. Absorption measurements were carried out in DMF to determine λ_{py} , which represents the moles of pyrene per gram of polymer. λ_{py} was obtained by dividing the concentration of pyrene determined from the solution absorbance as $[Py] = Abs/(\epsilon_{\text{py}} \times b)$, where ϵ_{py} and b are the molar absorption coefficient of the pyrene derivative and the cell pathlength (1 cm), by the polymer mass concentration. The molar absorption coefficients of PyC1N, PyC4N, and PyC8N at 344 nm in DMF have been reported to equal 40,000,⁶² 36,000,⁶² and 39,300⁷⁰ $\text{M}^{-1} \cdot \text{cm}^{-1}$, respectively. The molar absorption coefficient of 43,900 $\text{M}^{-1} \cdot \text{cm}^{-1}$ at 344 nm for PyC12N in DMF was determined experimentally. The mole fraction (*x*) of norbornene units bearing a pyrene label was calculated using Equation 5.1, where M_{NbA} and $M_{\text{PyCXN-NbA}}$ represent the molar mass of the unlabeled norbornene acid (138 g/mol) and

the norbornene acid labeled with either a 1-pyrene-methyl- (350 g/mol), -butyl- (388 g/mol), -octyl- (449 g/mol), and -dodecyl- (511 g/mol) amine group, respectively.

$$x = \frac{M_{NbA}}{\lambda_{Py}^{-1} - M_{PyCXN-NbA} + M_{NbA}} \quad (5.1)$$

Table 5.1 Chemical structure of the PyCX(x)N-PNb-Ac samples.

PyC1(x)N-PNb-Ac	PyC4(x)N-PNb-Ac	PyC8(x)N-PNb-Ac	PyC12(x)N-PNb-Ac
			
$x = 5.6 - 15.0 \text{ mol\%}$	$x = 8.2 - 12.4 \text{ mol\%}$	$x = 2.0 - 11.0 \text{ mol\%}$	$x = 3.2 - 6.4 \text{ mol\%}$

Steady-state fluorescence: All steady-state fluorescence (SSF) spectra were acquired at an excitation wavelength of 345 nm on a QM-400 spectrofluorometer equipped with a Xenon arc lamp. The excitation and emission slit width were set to 1 nm. For each sample, the pyrene concentration was maintained at 2.5×10^{-6} M in DMF and DMSO. Prior to the fluorescence spectra

acquisition, the solutions were vigorously purged with nitrogen for 35 minutes to remove dissolved oxygen, a known quencher of pyrene fluorescence. The SSF spectra were analyzed to determine the fluorescence intensity ratio of the excimer over the monomer, the I_E/I_M ratio, by integrating the monomer (I_M) and excimer (I_E) fluorescence intensity between 376 and 382 nm and between 500 and 530 nm, respectively.

Time-resolved fluorescence: Time-resolved fluorescence (TRF) decays of the same solutions used for the fluorescence spectra were acquired using a 345 nm excitation wavelength on an IBH time-resolved fluorometer. The monomer and excimer fluorescence decays were collected at an emission wavelength of 379 and 510 nm, respectively. To minimize stray light from reaching the detector, 370 and 495 nm cut-off filters were employed for the monomer and excimer fluorescence decays, which were acquired with 40,000 and 20,000 counts at the decay maximum, respectively. The instrument response function was acquired with a LUDOX solution by setting the emission wavelength equal to the excitation wavelength.

Analysis of the TRF decays: The monomer and excimer TRF decays for all samples were globally analyzed using the fluorescence *blob* model (FBM) with the equations provided in Supporting Information. The FBM has been described in detail elsewhere^{58,59} and a brief overview is provided hereafter. The FBM acknowledges that when a macromolecule has been covalently labeled with pyrene dyes, excited pyrenyl dyes cannot probe the full macromolecular volume. Rather they probe equally sized sub-volumes, denoted as *blobs*, used to compartmentalize the macromolecule into a cluster of *blobs*. The pyrenyl dyes distribute themselves amongst these *blobs* according to a Poisson distribution. Within the FBM framework, PEF is the result of the interplay between four different pyrene species denoted as $P_{y_{\text{free}}}$, $P_{y_{\text{diff}}}$, $P_{y_{k2}}$, and $P_{y_{\text{agg}}}$. $P_{y_{\text{free}}}$ represents the pyrenes which are located in pyrene-poor domains, do not form excimer, and thus emit as if they were free

in solution with a lifetime equal to τ_M . Py_{diff}^* represents the pyrenes undergoing diffusive motion with a rate constant k_{blob} until they come close to a ground-state pyrene and generate the species $Py_{k_2}^*$, which forms a pyrene excimer through the rapid rearrangement of the two pyrene labels with a rate constant k_2 . Py_{agg}^* represents the pre-aggregated pyrene dyes which form excimer instantaneously upon excitation. The fluorescence decays were first fitted using the program *globmis90gbg*, where k_2 was optimized. Once the analysis was completed for a given series of PyCX(x)N-PNb-Ac samples, the k_2 values were averaged and the decays were reanalyzed using the program *globmis90bbg*, where k_2 was set to equal $\langle k_2 \rangle$. This procedure significantly reduces error in the other parameters retrieved through the FBM analysis of the decays such as the average number $\langle n \rangle$ of ground-state pyrenes per *blob*, k_{blob} , and the molar fractions f_{free} , f_{diff} , f_{k_2} , and f_{agg} of the pyrene species Py_{free}^* , Py_{diff}^* , $Py_{k_2}^*$, and Py_{agg}^* , respectively. In all cases, the fits were deemed acceptable if the χ^2 value was below 1.3 and the residuals and the autocorrelation of the residuals were randomly distributed around zero. An example fit has been provided as Figure S5.3 in the SI.

Molecular Mechanic Optimization (MMO) simulations: All molecular mechanic optimizations (MMO) were conducted using HyperChem (version 8.0.7) as described elsewhere.^{58,62–70} The Fletcher-Reeves Conjugate gradient *in vacuo* with a termination condition of an RMS gradient of $0.1 \text{ kcal}\cdot\text{\AA}^{-1}\cdot\text{mol}^{-1}$ was used.

5.4 RESULTS AND DISCUSSION

Analysis of the Steady-State Fluorescence Spectra: All steady-state fluorescence (SSF) spectra were normalized at 379 nm and the fluorescence spectra for the PyC1N(x)-PNb-Ac samples in DMF are shown in Figure 5.1A. The typical spectral features expected for pyrene-labeled macromolecules (PyLM) were found in all fluorescence spectra.^{52,54–70} Specifically, sharp

fluorescence peaks were observed for the pyrene monomer between 360 and 410 nm, while the broad structureless emission centered at 480 nm was characteristic of the excimer fluorescence. For each sample dissolved in either DMF or DMSO, the I_E/I_M ratio was calculated and plotted as a function of pyrene content in Figures 5.1B-E.

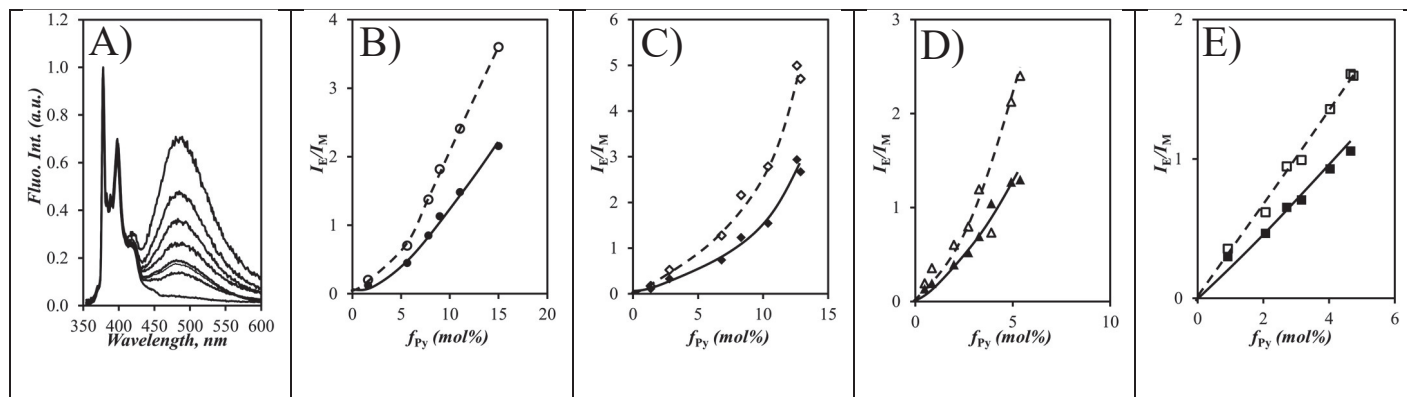


Figure 5.1 A) Fluorescence spectra acquired for the PyC1(x)-PNb-Ac samples in DMF. Plots of the I_E/I_M ratio for the PyCX(x)-PNb-Ac samples, where X equals B) 1 (methyl, ●), C) 4 (butyl ◆), D) 8 (octyl, ▲), and E) 12 (dodecyl, ■), in DMF (non-filled) and DMSO (filled).

Two important trends were observed in Figures 5.1B-E. First, the I_E/I_M ratio for all samples increased with increasing pyrene content (x) regardless of solvent. This trend is reasonable since an increase in pyrene content results in more pyrene-pyrene encounters and thus more PEF as already found with other PyLM.^{52,54-70} Second, for a given series of PyCX(x)N-PNb-Ac samples, the I_E/I_M ratio in DMF was higher than in DMSO. Since the I_E/I_M ratio is proportional to the product $k_{diff} \times [Py]_{loc}$,⁵²⁻⁵⁵ where k_{diff} is the bimolecular rate constant for PEF and $[Py]_{loc}$ is the local concentration of ground-state pyrenyl labels, it depends on solvent viscosity and the probability of PEF upon contact between an excited and a ground-state pyrene. Considering that DMSO ($\eta =$

1.99 mPa.s at 25 °C) is much more viscous than DMF ($\eta = 0.79$ mPa.s at 25 °C), the larger I_E/I_M ratios obtained in DMF than in DMSO are reasonable. While these results are qualitatively interesting, quantitative information about the PyCX(x)N-PNb-Ac samples was obtained through the analysis of their time-resolved fluorescence decays as described hereafter.

Analysis of the Fluorescence Decays with the Fluorescence Blob Model: The monomer and excimer fluorescence decays of the PyCX(x)N-PNb-Ac samples in DMF and DMSO were acquired and globally analyzed with the fluorescence *blob* model (FBM). The FBM analysis yielded the average number ($\langle n \rangle$) of ground-state pyrenes per *blob*, which was used to determine $N_{\text{blob}}^{\text{exp}}$ according to Equation 5.2. $N_{\text{blob}}^{\text{exp}}$ was plotted as a function of pyrene content in Figure 5.2A. Interestingly, $N_{\text{blob}}^{\text{exp}}$ remained relatively constant regardless of solvent for a given series of PyCX(x)N-PNb-Ac samples. This observation suggests first that PNb-Ac must adopt a similar conformation in both DMF and DMSO. Second, since the $N_{\text{blob}}^{\text{exp}}$ values are similar in DMF which is much less viscous than DMSO, it implies that within a *blob*, the backbone of the PNb-Ac must be rigid and that the pyrenyl labels probe a same volume around the polynorbornene backbone, albeit at a different rate. Indeed, the k_2 and k_{blob} values listed in Tables S5.1-S5.24 were found to be on average 18 (± 7)% lower in DMSO than in DMF reflecting the difference in solvent viscosity. Considering that PNb-Ac is often described as adopting a rigid random coil conformation,¹⁶ it is not surprising that the solvent did not induce a conformational change and that $N_{\text{blob}}^{\text{exp}}$ was minimally affected by the solvent viscosity. Since the $N_{\text{blob}}^{\text{exp}}$ values remained constant as a function of pyrene content within experimental error for a given series of PyCX(x)N-PNb-Ac samples and in both DMF and DMSO, $N_{\text{blob}}^{\text{exp}}$ was averaged over all pyrene contents in both DMF and DMSO for a given series to yield $\langle N_{\text{blob}}^{\text{exp}} \rangle$. $\langle N_{\text{blob}}^{\text{exp}} \rangle$ was found to increase with the linker

length of the pyrenyl derivative from 15 (± 1) to 23 (± 4), 29 (± 4), and 49 (± 4) for PyCX(x)N-PNb-Ac, where X equals 1 (methyl), 4 (butyl), 8 (octyl), and 12 (dodecyl), respectively. This trend suggests that a longer linker enables the pyrenyl moiety to probe a larger sub-volume. Such a trend is reasonable and has already been reported for other polymers labeled with different pyrene derivatives.^{62,64,68,70}

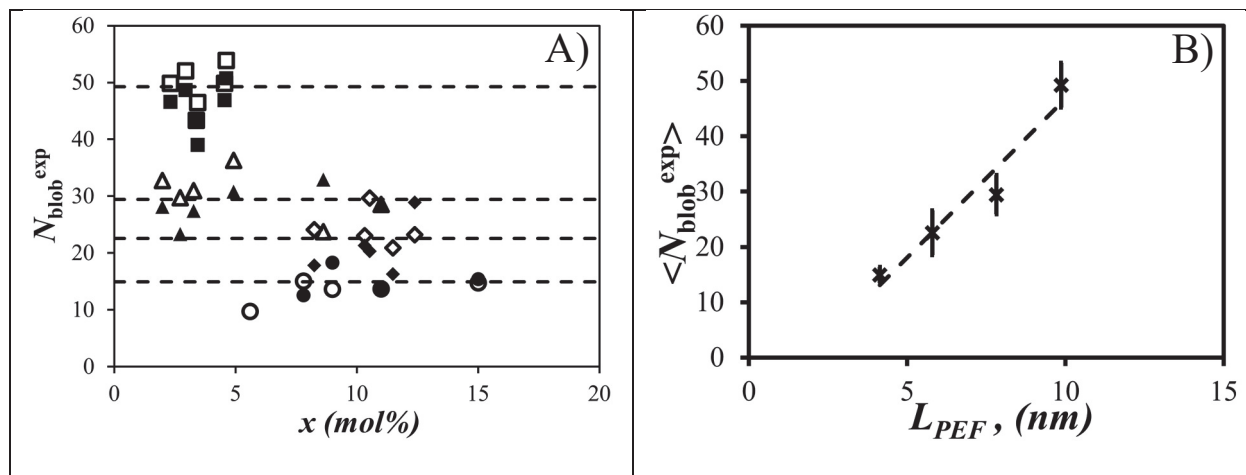


Figure 5.2 Plots of A) N_{blob}^{exp} as a function of the pyrene content in (empty symbols) DMF and (filled symbol) DMSO for the PyCX(x)-PNb-Ac samples where X equals (\circ, \bullet) 1, (\diamond, \blacklozenge) 4, ($\triangle, \blacktriangle$) 8, and (\square, \blacksquare) 12 and B) $\langle N_{blob}^{exp} \rangle$ as a function of the PEF length scale (L_{PEF}).

$$N_{blob}^{exp} = \frac{\langle n \rangle}{x} \times (1 - f_{Mfree}) \quad (5.2)$$

To ensure that the pyrene derivatives with a longer linker did in fact probe a larger volume, the $\langle N_{blob}^{exp} \rangle$ values obtained for the PyCX(x)N-PNb-Ac samples were compared in Figure 5.2B with the expected distance over which PEF could occur (L_{PEF}) as described in a previous report.⁷⁰ In brief, HyperChem was used to generate a norbornene monomeric unit which had been labeled

with PyC1N, PyC4N, PyC8N, and PyC12N. The distance $d_{\text{Py-}\alpha\text{C}}$ separating the center of mass (CoM) of the pyrene moiety and the α -carbon of the norbornene monomer that would be incorporated in the polymer backbone was determined. $d_{\text{Py-}\alpha\text{C}}$ was then multiplied first by 2 to reflect that a reference pyrenyl label located at the center of a *blob* can probe the polynorbornene backbone on both sides of the structural unit it is attached to, and second by 2 again to account for those pyrenyl labels located in the two *blobs* flanking the *blob* hosting the reference pyrene. The product $4 \times d_{\text{Py-}\alpha\text{C}}$ representing the maximum distance separating the attachment points of two ground-state pyrenes capable of forming an excimer with an excited pyrene attached at the midpoint along the backbone would thus represent the length scale (L_{PEF}) over which PEF occurs. L_{PEF} was found to equal 4.1, 5.8, 7.8, and 9.9 nm for PyC1N, PyC4N, PyC8N, and PyC12N, respectively. Since a *blob* represents the volume probed by an excited pyrenyl label, its diameter should equal $2 \times d_{\text{Py-}\alpha\text{C}}$ or $L_{\text{PEF}}/2$. As seen in Figure 5.2B, $\langle N_{\text{blob}}^{\text{exp}} \rangle$ increased linearly with L_{PEF} . Since L_{PEF} depends solely on the length of the linker connecting the pyrenyl label to the polynorbornene backbone, the trend in Figure 5.2B indicates that the four pyrenyl derivatives enabled the study of the PyCX(x)N-PNb-Ac samples over length scales ranging from 4.1 to 9.9 nm.

Molecular Mechanic Optimizations: To assess how homogeneous the conformation remains along the PNb-Ac backbone as a function of L_{PEF} , $\langle N_{\text{blob}}^{\text{exp}} \rangle$ was compared with $N_{\text{blob}}^{\text{MMO}}$ determined from molecular mechanic optimizations (MMO) conducted for the PNb-Ac constructs given in Figures 5.3A and B that adopted a random coil and helical conformation, respectively. The random coil conformation, provided in Figure 5.3A, was generated by Prof. Jérôme Claverie from the University of Sherbrooke. First, a norbornene acid dimer was created and minimized

using density function theory calculations that employed M06-2X functionals with 6-311g(d,p) basis set in a similar manner as reported earlier.⁸³ Two dimers were then attached together, however due to the computational cost of density function theory calculations, molecular dynamics using the AMBER force field was employed. Since the bicyclic ring of a norbornene unit is rigid, no significant difference between the geometry of the norbornene unit between AMBER or DFT optimization occurs. This process was repeated until a 32-mer was generated.

To generate the helical PNb-Ac construct, a *cis-exo*-disyndiotactic dodecamer was built by placing norbornene units with a dihedral angle of 130 ° and -70 ° between two monomers, which corresponds to the primary and secondary energy minima, respectively, that had been calculated from the equilibrium position of two monomers attached to the organometallic catalyst.⁸³ The stereochemical arrangement for each main chain carbon was an alternation of SS and RR configurations, consistent with a 2,3-*exo*-disyndiotactic structure reported earlier.⁸⁴ Once generated, the geometry of the construct was optimized using an Amber force-field, imported into HyperChem and extended by overlapping the two last structural units of one dodecamer with the two first structural units of another dodecamer to generate a 22-mer. This process was repeated several times to generate a construct with 66 and 132 structural units. We note that earlier molecular mechanics calculations for 2,3 *exo*-disyndiotactic PNb heptamers with a helical conformation had suggested distorted *gauche* and *skew* conformations with torsion angles of $\pm 80^\circ$ and $\pm 130^\circ$, respectively,⁸⁵ a value which is consistent with the angle between norbornene monomers used to generate the helical construct in the present work. Furthermore, visual inspection of the generated helical conformation used in the present work suggests that the present construct was similar to that reported for a 2,3 *exo*-disyndiotactic heptamer,⁸⁴ which had 6 norbornene units per turn (6_1).

Interestingly, visual inspection of Figures 5.3A and B suggests that some short sections of the randomly coiled PNb-Ac backbone in Figure 5.3A exhibit some local conformation similar to that of the 6_1 helix shown in Figure 5.3B even though the overall conformations are clearly different. Those segments, that look similar to that of a 6_1 helix, would also be expected to exhibit a local compactness similar to that of the 6_1 helix. This discussion suggests that the PNb-Ac polymer might have a locally heterogeneous microstructure, and that this heterogeneity might be reflected in our PEF-based experiments aimed to probe the polymer conformation over different length scales.

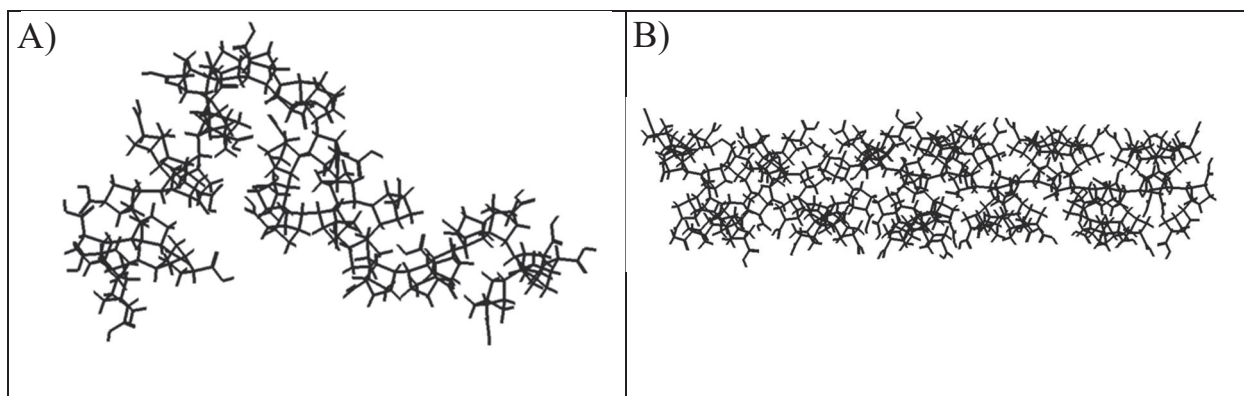


Figure 5.3 PNb-Ac backbone used to conduct the molecular mechanic optimizations where the backbone is A) a random coil or B) a 6_1 helix.

The MMOs for the randomly coiled PNb-Ac construct made of 32 residues, shown in Figure 5.3A, were conducted in the same manner as described in previous reports.^{58,62,63,66,70} The simulations were carried out by attaching a first pyrene onto one of five reference structural units (SU) selected for the MMO and shown in red in Figure 5.4A and a secondary pyrene onto a SU adjacent to the SU bearing the reference pyrene. The reference and secondary pyrenyl labels were then induced to approach each other by restraining the atoms shown in Figure 5.4B to come within 3.4 Å from each other without affecting the atoms of the main chain. Stacking between the

reference pyrene (red) and the secondary pyrene (black) resulted in a head-to-head or head-to-tail contact as illustrated in Figure 5.4C. As long as one of the two simulations resulted in one pyrene moiety overlapping the frame of the second pyrene with a number (n_{C-C}) of carbons that was equal to or greater than 7 and as long as the pyrene frames remained planar during the optimizations, this n_{C-C} value was considered conducive of PEF.⁸⁶ The number (N_0) of SU bearing a secondary pyrenyl label located on the same side of the reference pyrenyl label along the PNb chain, that resulted in PEF, was increased by one unit. The secondary pyrene was then moved to the following SU along the PNb backbone and away from the reference SU, one SU at a time, and the procedure was repeated until three consecutive positions yielded a n_{C-C} value of zero. At this point, N_0 represented the number of norbornene units which would enable PEF if they were labeled with pyrene on one same side of the reference pyrenyl label. Since PEF occurs between pyrenyl labels attached on both sides of the reference norbornene unit, $N_{\text{blob}}^{\text{MMO}}(\text{RC})$ for the random coil conformation was calculated as $2 \times N_0 + 1$, where “1” is added to account for the reference pyrene dye. The MMOs were repeated for five reference positions and averaged to yield $N_{\text{blob}}^{\text{MMO}}(\text{RC})$. The obtained results for each MMO have been provided in Figures S5.4-S5.6 in SI, while the results obtained for the MMOs for the PNb-Ac labeled with 1-pyrenebutylamine are shown in Figure 5.5A-E for further discussion.

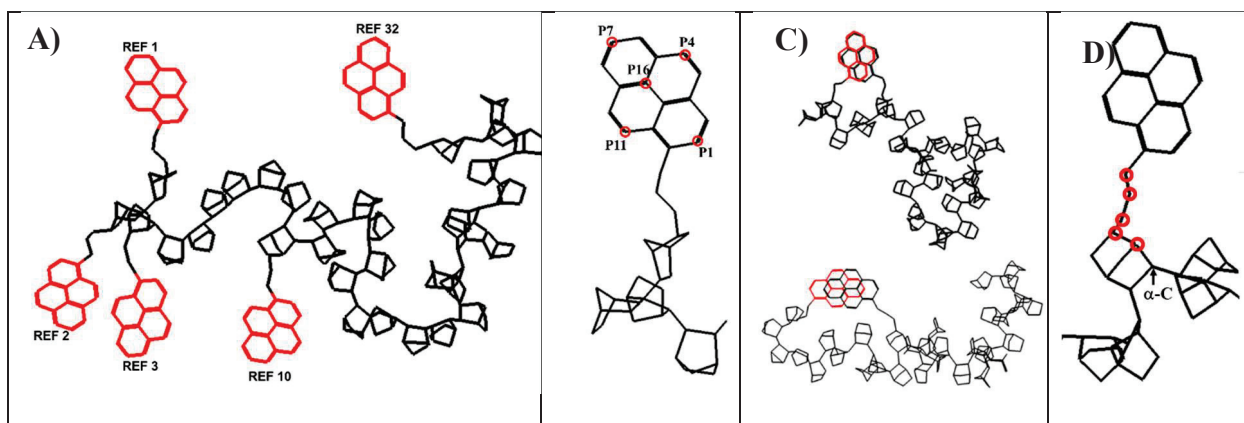


Figure 5.4. Illustration of the construct representing a PyC1N labeled PNb-Ac random coil where A) the different reference pyrene positions are highlighted in red, B) the carbon atoms selected to apply the restraints used in the MMOs are colored in red, C) the head-to-head and head-to-tail arrangements for two stacked pyrenyl labels are shown, and D) the number of atoms (shown with red circles) separating the pyrenyl dye from the α -C in the PNb-Ac backbone for a hypothetical 1-pyrenepropylamine derivative. The hydrogen atoms and carbonyl oxygen of the acetic acid groups were hidden from the chemical structures shown in Figure 5.4.

Visual inspection of Figures 5.5A-E indicates that the n_{C-C} values follow different behaviors depending on the reference SU used in the MMO. The variation in the MMO trends obtained with different reference SU, however, is not unexpected due to the heterogeneous microstructure of the randomly coiled PNb-Ac backbone. Despite these differences, the N_o values, and thus the $N_{\text{blob}}^{\text{MMO}}(\text{RC})$ values equal to $2 \times N_o + 1$, showed little variation. In the case of the PNb-Ac randomly coiled construct labeled with PyC4N on the 1st, 2nd, 3rd, 10th, and 32nd SU, $N_{\text{blob}}^{\text{MMO}}(\text{RC})$ values of 17, 17, 19, 19, and 17 were obtained, respectively, taking an average $\langle N_{\text{blob}}^{\text{MMO}}(\text{RC}) \rangle$ value of 18 (± 1). This consistency suggests that similar $N_{\text{blob}}^{\text{MMO}}(\text{RC})$ values were obtained despite differences in the trends shown in Figure 5.5. This was also true for the $N_{\text{blob}}^{\text{MMO}}(\text{RC})$ values obtained with 1-pyrene-methyl, -ethyl, and -propyl derivatives, which

yielded $\langle N_{\text{blob}}^{\text{MMO}}(\text{RC}) \rangle$ values of $7 (\pm 2)$, $12 (\pm 3)$, and $15 (\pm 2)$, respectively. These $\langle N_{\text{blob}}^{\text{MMO}}(\text{RC}) \rangle$ values were plotted as a function of the number of atoms (n_{Sp}) in the spacer linking the pyrene moiety to the α -carbon on the PNB-Ac construct, as shown in Figure 5.5F. A straight line was obtained in Figure 5.5F indicating that $\langle N_{\text{blob}}^{\text{MMO}}(\text{RC}) \rangle$ increases linearly with increasing linker length. The linear relationship between $\langle N_{\text{blob}}^{\text{MMO}}(\text{RC}) \rangle$ and n_{Sp} was then utilized to extrapolate $N_{\text{blob}}^{\text{MMO}}(\text{RC})$ for a randomly coiled PNB-Ac construct labeled with PyC8N and PyC12N, which are two pyrene derivatives used in the present study. This approach to determine $N_{\text{blob}}^{\text{MMO}}(\text{RC})$ was adopted for two reasons. First, to conduct a complete series of MMOs for the PyC8N and PyC12N derivatives, a PNB-Ac construct made of more than 32 norbornene units must be generated *in silico*. This, unfortunately, proved to be a rather challenging task. Second, to yield accurate $N_{\text{blob}}^{\text{MMO}}$ values representative of the entire construct, several reference positions across the construct should be used. Doubling the construct size, in turn, would mean doubling the number of simulations to be conducted for each pyrene derivative, which would become too time-consuming. In the end, $\langle N_{\text{blob}}^{\text{MMO}}(\text{RC}) \rangle$ values for the random coil conformation were found to equal $7 (\pm 2)$, $18 (\pm 1)$, $33 (\pm 5)$, and $47 (\pm 6)$ for PyC1N, PyC4N, PyC8N, and PyC12N, respectively, with the two latter $\langle N_{\text{blob}}^{\text{MMO}}(\text{RC}) \rangle$ values being obtained through extrapolation with Figure 5.5F.

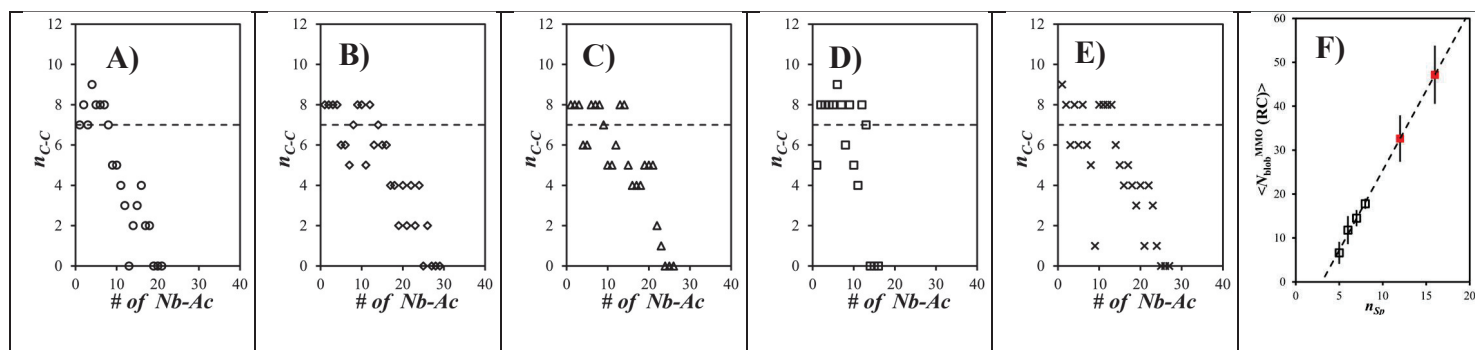


Figure 5.5 Plots of the number (n_{C-C}) of overlapping carbons between the reference and secondary pyrenyl labels for a 32-residue construct for a PNb-Ac random coil labeled with PyC4N where the reference pyrene was attached to a residue located at position A) 1 (●), B) 2 (◆), C) 3 (▲), D) 10 (■), and E) 32 (×). F) Plot of $\langle N_{\text{blob}}^{\text{MMO}}(\text{RC}) \rangle$ as a function of the number of atoms (n_{Sp}) separating the dye from the α -C of the PNb-Ac backbone for a random coil. The red squares represent the extrapolated $\langle N_{\text{blob}}^{\text{MMO}}(\text{RC}) \rangle$ value for PyC8N and PyC12N.

Compared to the PNb-Ac random coil in Figure 5.3A, a single reference position is typically used for the constructs of structured polymers such as the PNb-Ac helix in Figure 5.3B due to the symmetry of the selected conformation.^{58,63,65–70} For these constructs, $N_{\text{blob}}^{\text{MMO}}$ is taken as $(2 \times N_0 + 1)$ as was done for the randomly coiled PNb-Ac construct. The expression $N_{\text{blob}}^{\text{MMO}} = 2 \times N_0 + 1$ assumes that the pyrenyl dye has the same reach on the left and right side of the reference pyrene on the construct. However, this assumption was no longer valid for the PNb-Ac helix generated *in silico* using SS and RR dimers since they have different configurations. This is illustrated with a 66-residue-long PNb-Ac helix, where the reference PyC1N was placed on either the 9th, 10th, 11th, or 12th residues, and $N_{\text{blob}}^{\text{MMO}}$ was calculated in the same manner as done earlier.^{58,63,65–70} The data from these simulations are shown in Figures 5.6A-D and they present several interesting features. First, for all reference positions, the first 2 norbornene residues were

always conducive of PEF regardless of the reference pyrene position along the PNb-Ac construct. Second, as the number of residues separating the reference from the secondary pyrenyl labels was increased, n_{C-C} took values greater than or equal to 7, followed by a decrease, before increasing back to values greater than or equal to 7, and eventually decreasing to zero. This oscillatory feature reflects the placement of the secondary pyrene along the PNb-Ac backbone as it passes behind and in front of the helix, where overlap between pyrenyl labels is hindered or favored, respectively. Third, the trends obtained by MMO show that the n_{C-C} pattern exhibits three and two maxima depending on whether the reference pyrene is labeled onto an odd or an even numbered SU, respectively. This consistent trend suggests that for the PNb-Ac helical construct, the position of the reference pyrene might impact the $N_{\text{blob}}^{\text{MMO}}$ value obtained for the 6_1 helix ($N_{\text{blob}}^{\text{MMO}}(\text{H})$). Since the second maximum observed represents one full turn around the helical construct, these trends suggest that the n_{C-C} positions conducive of PEF depend on the placement of the reference pyrene. The plots shown in Figure 5.6A-D yielded N_o values equal to 6, 3, 8, and 4 resulting in $N_{\text{blob}}^{\text{MMO}}(\text{H})$ values ($= 2 \times N_o + 1$) of 13, 7, 17, and 9 when the reference pyrene was placed on the 9th, 10th, 11th, and 12th SU, respectively. These $N_{\text{blob}}^{\text{MMO}}$ values for the PyC1N labeled PNb-Ac helix would yield an average of 12 (± 4). This 33% error on $\langle N_{\text{blob}}^{\text{MMO}}(\text{H}) \rangle$ for a well-defined helical conformation seemed unlikely. The likeliest explanation for the large variations observed for the $N_{\text{blob}}^{\text{MMO}}(\text{H})$ values was that $N_{\text{blob}}^{\text{MMO}}$ took different values of 15 (± 2) or 8 (± 1), when odd (#9 and 11) or even (#10 and 12) reference positions were used, respectively. This discrepancy was attributed to the SS and RR dimers used to prepare the PNb-Ac helix, which might yield a different reach between the left and right side of the reference pyrenyl residue.

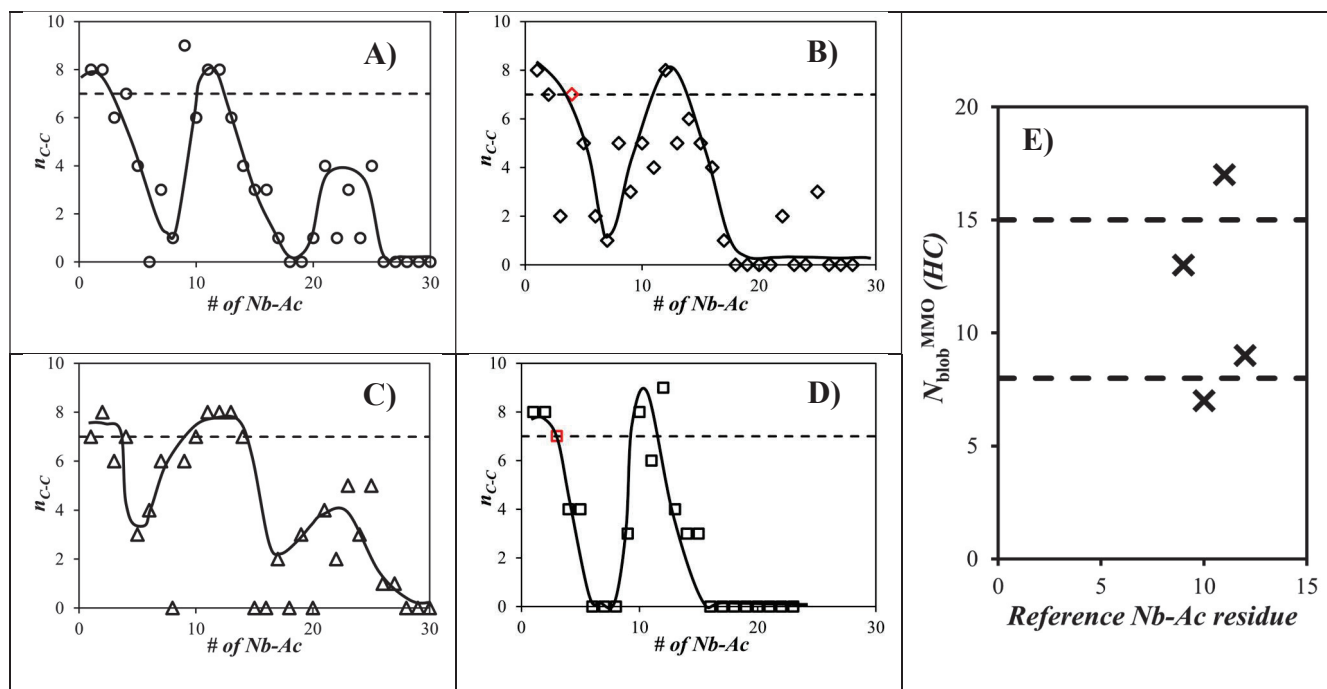


Figure 5.6 Plots of n_{C-C} for a 66-residue PNB-Ac helix labeled with PyC1N where the reference pyrene group was placed on the A) 9th (●), B) 10th (◆), C) 11th (▲), and D) 12th (■) SU. E) Plot of $N_{\text{blob}}^{\text{MMO}}(\text{H})$ as a function of the position of the reference pyrenyl group. The lines provided are only a means to guide the eye. The red symbols in plots B) and D) represent positions where the frames of the pyrenyl dyes were not planar, and thus were not used in the calculation of $N_{\text{blob}}^{\text{MMO}}(\text{H})$.

In an effort to reduce the errors for $N_{\text{blob}}^{\text{MMO}}(\text{H})$, the methodology applied to determine $N_{\text{blob}}^{\text{MMO}}$ was modified. The MMO were carried out by considering the number of SU labeled with a secondary pyrene on the left (N_o^L) and right (N_o^R) of the reference pyrene along the helical PNB-Ac construct that yielded n_{C-C} values, equal to or larger than 7. According to this new methodology, $N_{\text{blob}}^{\text{MMO}}(\text{H})$ was then taken as $N_o^L + N_o^R + 1$. To ensure that this modified methodology yielded consistent $N_{\text{blob}}^{\text{MMO}}(\text{H})$ values for the PNB-Ac helix, two sets of MMO were conducted for a

PyC1N labeled PNB-Ac helix made of 132 residues. The resulting n_{C-C} trends are shown in Figures 5.7A-D.

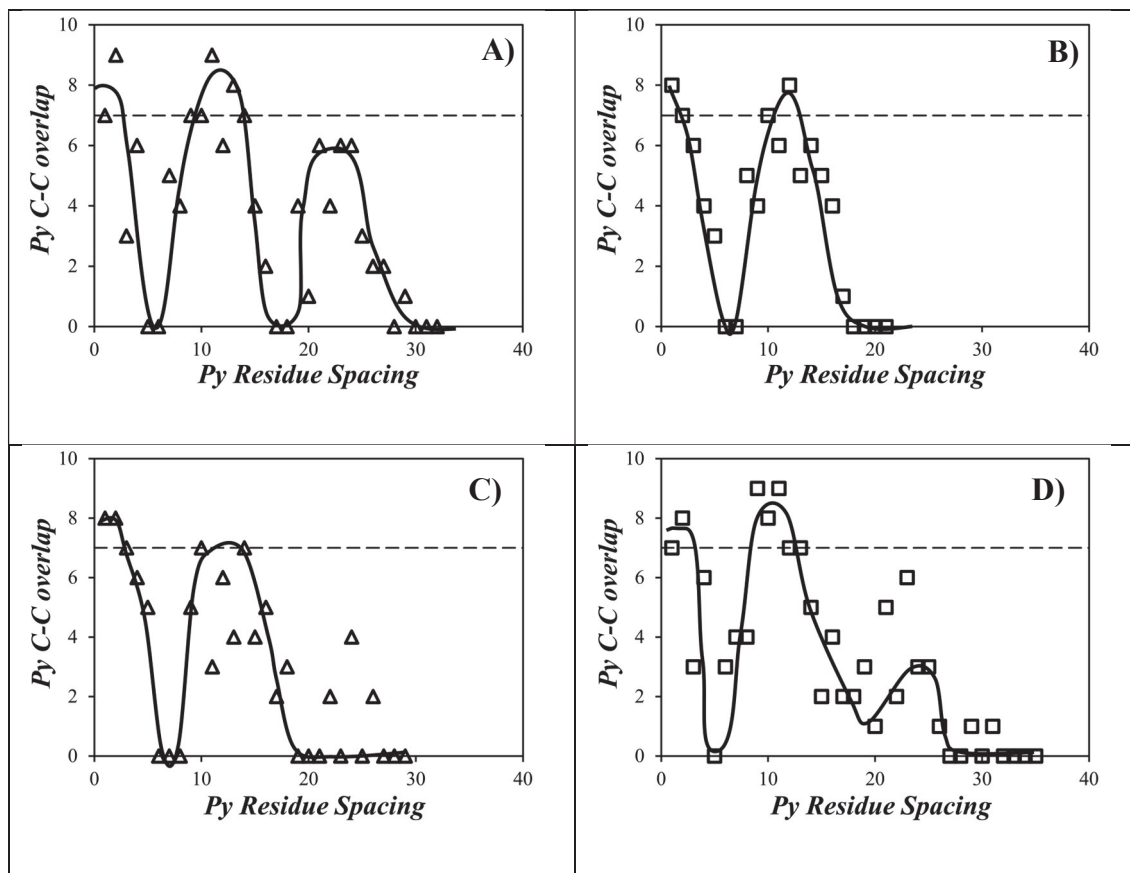


Figure 5.7 Plot of n_{C-C} for a 132-residue PNB-Ac helical construct labeled with PyC1N attached onto the 69th (A & B) and 70th (C & D) residues with the reach of the reference pyrenyl label being probed on the left (\blacktriangle) and right (\blacksquare). The lines provided are only a means to guide the eye.

With a reference pyrene on the 69th and 70th SU, the MMO yielded N_0^L equal to 7 and 5, respectively, while N_0^R was equal to 4 and 7, respectively. Consequently, $N_{\text{blob}}^{\text{MMO}}(\text{H})$ was found to equal 13 and 12 for the 69th and 70th reference positions, respectively, which represents a more reasonable spread of the $N_{\text{blob}}^{\text{MMO}}(\text{H})$ values.

The MMOs for the PNB-Ac helix labeled with the other pyrene derivatives were conducted in the same manner by determining N_o^L and N_o^R for each pyrene reference attached onto the 70th residue. The $N_{\text{blob}}^{\text{MMO}}(\text{H})$ values for the helical constructs were found to equal 13, 29, 55, and 77 for PyC1N, PyC4N, PyC8N, and PyC12N, respectively. Plots of $n_{\text{C-C}}$ as a function of the number of residues separating the reference from the secondary residues are shown for PyC4N, PyC8N, and PyC12N in Figures 5.8A-C. Additionally, the $N_{\text{blob}}^{\text{MMO}}$ values for each pyrene derivative were plotted in Figure 5.8D as a function of the number of atoms (n_{Sp}) of the spacer for a given pyrene derivative separating the pyrenyl group from the α -C of the PNB-Ac backbone (see Figure 5.4D). Similar to $\langle N_{\text{blob}}^{\text{MMO}}(\text{RC}) \rangle$ in Figure 5.5F, $N_{\text{blob}}^{\text{MMO}}(\text{H})$ was found to increase linearly with n_{Sp} in Figure 5.8D.

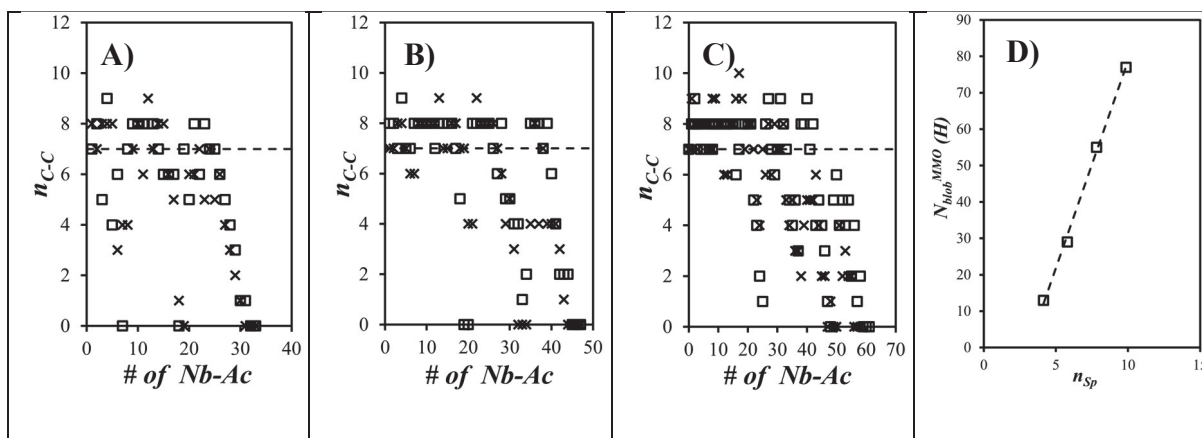


Figure 5.8 Plots of $n_{\text{C-C}}$ for a 132-residue PNB-Ac helix labeled with A) PyC4N, B) PyC8N, and C) PyC12N. The reference residue used was position 70 and $n_{\text{C-C}}$ was counted from left-to-right (x) and right-to-left (■). D) Plot of $N_{\text{blob}}^{\text{MMO}}(\text{H})$ as a function of the number (n_{Sp}) of atoms separating the dye from the α -C of the PNB-Ac backbone.

Comparison of $N_{\text{blob}}^{\text{exp}}$ and $N_{\text{blob}}^{\text{MMO}}$. To investigate whether PEF could probe the conformational homogeneity along the PNB-Ac backbone on different length scales, $\langle N_{\text{blob}}^{\text{exp}} \rangle$ was compared with

$\langle N_{\text{blob}}^{\text{MMO}}(\text{RC}) \rangle$ and $N_{\text{blob}}^{\text{MMO}}(\text{H})$ for a PNb-Ac construct with a random coil or helical conformation in Figure 5.9A. On the shortest PEF length scale investigated ($L_{\text{PEF}} = 4.1$ nm) obtained with PyC1N, plotting $\langle N_{\text{blob}}^{\text{exp}} \rangle$ as a function of $N_{\text{blob}}^{\text{MMO}}(\text{H})$ yielded a point that landed on the 1:1 diagonal, denoted by the dashed line in Figure 5.9A, indicating a good match between $\langle N_{\text{blob}}^{\text{exp}} \rangle$ and $N_{\text{blob}}^{\text{MMO}}(\text{H})$ and thus a dense conformation for the PNb-Ac backbone. For an L_{PEF} of 5.8 nm obtained with PyC4N, the points obtained by plotting $\langle N_{\text{blob}}^{\text{exp}} \rangle$ as a function of $N_{\text{blob}}^{\text{MMO}}(\text{H})$ and $\langle N_{\text{blob}}^{\text{MMO}}(\text{RC}) \rangle$ were evenly separated from the diagonal reflecting a decrease in local density. For L_{PEF} equal to 7.8 and 9.9 nm corresponding to PyC8N and PyC12N, plotting $\langle N_{\text{blob}}^{\text{exp}} \rangle$ as a function of $\langle N_{\text{blob}}^{\text{MMO}}(\text{RC}) \rangle$ yielded two points that landed on the 1:1 diagonal indicating a good match suggesting that these pyrene derivatives probed the randomly coiled PNb-Ac backbone. This analysis of the $\langle N_{\text{blob}}^{\text{exp}} \rangle$ values suggests some heterogeneity in the local conformation of the PNb-Ac backbone depending on the length scale of observation. This conclusion was further supported by the more quantitative analysis conducted in Figure 5.9B. In Figure 5.9B, $\langle N_{\text{blob}}^{\text{exp}} \rangle$ was assumed to be the result of a linear combination of random coil and helical conformations with a corresponding $\langle N_{\text{blob}}^{\text{MMO}}(\text{RC}) \rangle$ and $N_{\text{blob}}^{\text{MMO}}(\text{H})$ values weighed by their respective molar fractions f_{RC} and f_{H} . f_{RC} and f_{H} were calculated for each pyrene derivative and plotted as a function of L_{PEF} . As L_{PEF} was increased from 4.1 to 9.9 nm, f_{RC} increased from zero to unity while f_{H} decreased from unity to zero. It would appear that for L_{PEF} smaller than 7.8 nm, the conformation of PNb-Ac is denser than expected for a random coil and that it exhibits a helical character. As L_{PEF} is increased past 7.8 nm, the random coil conformation of the PNb backbone is recovered and f_{RC} equals unity.

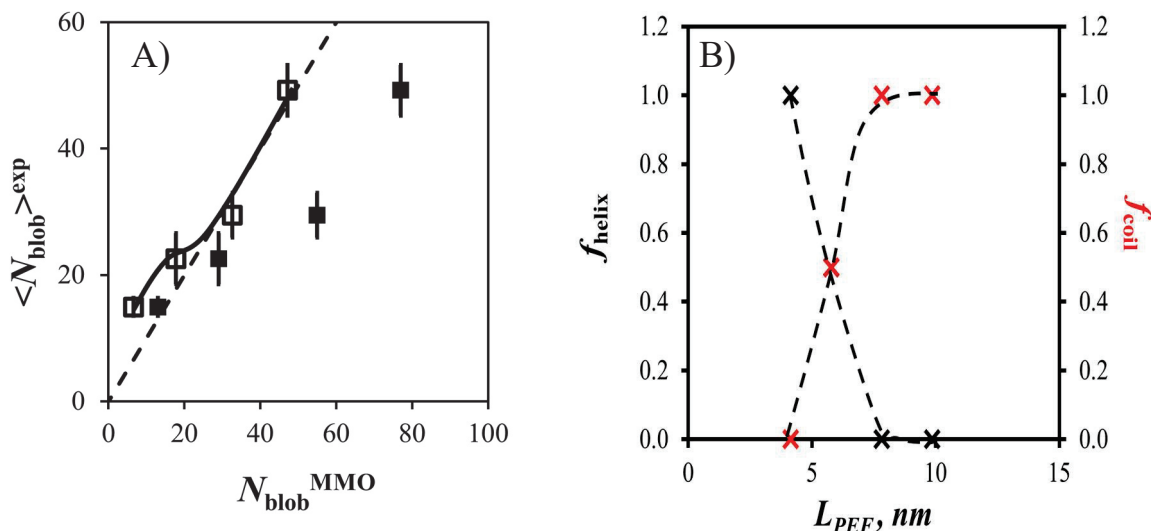


Figure 5.9 A) Plot of $\langle N_{\text{blob}}^{\text{exp}} \rangle$ as a function of (black square) $N_{\text{blob}}^{\text{MMO}}(\text{H})$ and (hollow square) $\langle N_{\text{blob}}^{\text{MMO}}(\text{RC}) \rangle$. B) Plot of f_{RC} and f_{H} as a function of L_{PEF} .

The change in local conformation of PNB-Ac observed from the differences in $\langle N_{\text{blob}}^{\text{exp}} \rangle$ with L_{PEF} described in Figure 5.9 contrasts with what was reported in Chapter 4 for poly(*D,L*-glutamic acid) (PDLGA) and poly(*L*-glutamic acid) (PLGA) in DMF and DMSO.⁷⁰ Based on the PEF results, PDLGA had been found to be randomly coiled in DMF and DMSO while PLGA adopted an α - and 3_{10} -helical conformation in DMF and DMSO, respectively. But when the poly(glutamic acid) constructs were labeled with PyC1N, PyC4N, and PyC8N, an excellent match was observed between $\langle N_{\text{blob}}^{\text{exp}} \rangle$ and $N_{\text{blob}}^{\text{MMO}}$ indicating that the same conformation of these polypeptide backbones extended over the different L_{PEF} probed by PyC1N, PyC4N, and PyC8N. Based on these results, it would appear that the microstructure of PNB-Ac is richer than that of the PDLGA and PLGA polypeptides. It is also worth noting that a full atomistic simulation conducted for a 2,3 erythro di-isotactic polynorbornene construct has suggested a helix-kink conformation.¹⁶ This result would agree with those obtained from the FBM analysis of the PyCX(*x*)N-PNB-Ac

samples, which suggest some heterogeneity in the microstructure of PNb along the polymer backbone.

5.5 CONCLUSIONS

This study has demonstrated the ability of PEF to probe the microstructure of a PNb-Ac sample on different length scales. This was achieved by randomly labeling a PNb-Ac sample with varying amounts of 1-pyrene-methyl, -butyl, -octyl, or -dodecyl-amine to yield four series of PyCX(*x*)N-PNb-Ac samples. Since the PNb-Ac is rigid, the pyrenyl labels could only form excimer by probing the space surrounding the PNb-Ac backbone via their flexible linker on different length scales depending on the linker length. Global analysis of the monomer and excimer fluorescence decays acquired with the PyCX(*x*)N-PNb-Ac samples yielded $\langle N_{\text{blob}}^{\text{exp}} \rangle$, which was used as a structural parameter to assess the conformation of the PNb-Ac backbone in solution. Over short length scales ($L_{\text{PEF}} = 4.1$ and 5.8 nm), the $\langle N_{\text{blob}}^{\text{exp}} \rangle$ values agreed more closely to $N_{\text{blob}}^{\text{MMO}}$ obtained for a helical PNb-Ac whereas on longer length scales ($L_{\text{PEF}} = 7.8$ and 9.9 nm), $\langle N_{\text{blob}}^{\text{exp}} \rangle$ matched $N_{\text{blob}}^{\text{MMO}}$ obtained for a randomly coiled PNb-Ac construct. This behavior was very different from that observed for structured and unstructured polypeptides for which $\langle N_{\text{blob}}^{\text{exp}} \rangle$ has been found to match $N_{\text{blob}}^{\text{MMO}}$ over three different length scales. Taking advantage of the recently demonstrated ability of PEF to probe the local density and thus the conformation of macromolecules in solution,⁵²⁻⁵⁵ this study illustrates the interesting microstructure of PNb-Ac being more and less dense like the conformation of a helix or a random coil on short and long observation length scales, respectively.

Chapter 6: Concluding remarks & Future Works

6.1 Thesis Conclusion

The overarching goal of the present thesis was to establish the applicability of fluorescence collisional quenching (FCQ) experiments, specifically pyrene excimer formation (PEF), to quantitatively characterize the conformation of complex macromolecules in solution. To achieve this goal, pyrene was attached onto samples of polyamidoamine (PAMAM) dendrimers, poly(glutamic acid) (PGA), and poly(norbornene acid) (PNb-Ac) to yield pyrene-labeled macromolecules (PyLM), whose multiexponential decays were subsequently analyzed using the model free analysis (MFA) or fluorescence blob model (FBM).

The conformation of the pyrene end-labeled PAMAM dendrimers was characterized in the two first research chapters. In Chapter 2, the relationship between the average rate constant ($\langle k \rangle$) for PEF and the local concentration ($[Py]_{loc}$) of ground state pyrenes was established for a series of PAMAM dendrimers, that were end-labeled with pyrene derivatives which had different linker lengths to yield the PyCX-PAMAM-GY samples where X (= 4, 8, and 12) and Y (= 0, 1, and 2) represent the number of carbon atoms in the linker and the dendrimer generation, respectively. It was found that irrespective of the solvent, $\langle k \rangle$ increased linearly as a function of $[Py]_{loc}$, as had been found in earlier reports for other types of pyrene end-labeled dendrimers.^{1,2} A methodology was introduced for the parametrization of the chemical structure of the PyCX-PAMAM-GY samples, which was used to determine the average end-to-end distance ($\langle L_{Py} \rangle$) between every two pyrenyl labels and $[Py]_{loc}$. This methodology could be validated by comparing the radius of gyration (R_G) calculated by adjusting the mathematical treatment used to determine $\langle L_{Py} \rangle$ and the R_G values determined by molecular dynamic simulations³ and scattering experiments.⁴ This comparison validated the methodology employed to determine $[Py]_{loc}$ and since $\langle k \rangle$ was found to increase linearly with $[Py]_{loc}$, it also demonstrated that this PEF-based methodology enables the

quantitative characterization of a macromolecular conformation in a manner that complements scattering studies. The PEF experiments were conducted at concentrations of PAMAM dendrimers that were 3-to-4 orders of magnitude lower than the concentrations used in scattering experiments, which enabled the study of isolated PAMAM dendrimers in solution. To illustrate this point further, Chapter 3 illustrated the superiority of PEF studies over scattering-based experiments to probe the intramacromolecular conformational change of isolated PyCX-PAMAM-GY samples upon protonation of their internal tertiary amines. The concentrations used in scattering experiments are so high for PAMAM dendrimers that intermolecular long range electrostatic forces distort the conformation of the dendrimers preventing their characterization as isolated macromolecules in solution. In contrast to the results obtained from scattering experiments which indicate a nominal change in the radius of PAMAM dendrimers,^{5,6,7,8} the PEF experiments yielded a 13% increase in the radius of the PAMAM dendrimers upon protonation of their internal tertiary amines, which was in good agreement with the conclusions reached from molecular dynamic simulations for G4, G5, G6, and G8 dendrimers.⁹

While the study of small macromolecules was described in Chapters 2 and 3, Chapters 4 and 5 shifted the focus to the study of larger macromolecules, specifically poly(glutamic acid) (PGA) and poly(norbornene acid) (PNb-Ac) samples, respectively. Chapter 4 established a methodology for extending the length scale over which PEF experiments can be conducted. This methodology, in turn, enabled the study of the homogeneity of a macromolecular conformation over different length scales which were found to be comparable to those achieved with Förster resonance energy transfer (FRET), leading to the suggestion that like FRET, PEF can be viewed as a spectroscopic ruler. To achieve this goal, poly(D,L-glutamic acid) (PDLGA) and poly(L-glutamic acid) (PLGA) samples were randomly labeled with pyrene derivatives that had different

linker lengths to yield the PyCX(*x*)N-PGA samples, where *X* and *x* equaled the number of carbon atoms in the linker of the pyrene derivative and the molar percentage of pyrene-labeled glutamic acids, respectively. The fluorescence decays of the monomer and excimer for each PyCX(*x*)N-PGA sample were acquired in DMF and DMSO, followed by their analysis with the FBM to determine $N_{\text{blob}}^{\text{exp}}$, the number of structural units per *blob*. Comparison of $N_{\text{blob}}^{\text{exp}}$ with the $N_{\text{blob}}^{\text{MMO}}$ values determined by molecular mechanic optimization (MMO) for different conformations of PLGA labeled with the different pyrene derivatives illustrated that the PGA samples exhibited a homogenous conformation over all the length scales studied by PEF. Specifically, PDLGA adopted a random coil conformation, as would be expected, in both DMF and DMSO, while PLGA adopted an α -helical conformation in DMF, a known helicogenic solvent. This analysis was further extended to determine the conformation of PLGA in DMSO, which was unknown before this study. PEF-based experiments revealed that the conformation of PLGA in DMSO was that of a 3_{10} -helix, which to the best of our knowledge, represents the first time this was unambiguously demonstrated.

Chapter 5 applied the methodology established in Chapter 4 to study the microstructure of poly(norbornene acid) (PNb-Ac) on different length scales. To this end, pyrene derivatives with different linker lengths were attached onto PNb-Ac to yield the PyCX(*x*)N-PNb-Ac samples, where *X* and *x* take the same definition as for the PyCX(*x*)N-PGA samples. Plots of $\langle N_{\text{blob}}^{\text{exp}} \rangle$ as a function of $N_{\text{blob}}^{\text{MMO}}$ based on MMO conducted for a randomly coiled and 6_1 -helical PNb-Ac construct revealed that on short observation length scales for PEF ($L_{\text{PEF}} = 4.1$ and 5.8 nm), PNb-Ac adopted a denser conformation similar to that of a 6_1 -helix than on longer observation length scales ($L_{\text{PEF}} = 7.8$ and 9.9 nm), where its conformation appeared less dense and similar to that of a random coil. These conclusions suggested that PNb-Ac had a heterogeneous conformation, when

probed over different length scales. Such level of details in the characterization of macromolecular conformation would be difficult to attain by techniques other than the combination of PEF, FBM, and MMO described in this thesis.

In summary, this thesis describes the successful application of PEF to study the conformation of PAMAM dendrimers and PGA and PNB-Ac samples. It not only established the relationship between $\langle k \rangle$ and $[Py]_{loc}$ for the pyrene end-labeled PAMAM dendrimers, but also demonstrated that $[Py]_{loc}$ provides valuable information about macromolecular conformation in a manner that complements scattering experiments. However, due to its sensitivity, PEF can be used at much lower polymer concentrations compared to other techniques, enabling PEF to probe isolated macromolecules in solution. Additionally, the length scale over which PEF occurs was extended to distances comparable to those probed in FRET-based experiments. The large body of results presented in this thesis is expected to offer a solid basis onto which further applications of PEF can be developed to gain quantitative information about the conformation of complex macromolecules, that can be labeled with more than two dyes.

6.2 Future Work

While the primary focus of this thesis was to establish PEF as a powerful tool for probing macromolecular conformations, each chapter opens numerous avenues for further investigation. For instance, the main aim of Chapters 2 and 3 was to demonstrate that $\langle k \rangle$ is directly proportional to $[Py]_{loc}$ for pyrene-labeled dendrimers. To establish this relationship, the oligomeric segments separating every two dyes in a pyrene end-labeled dendrimer were assumed to obey Gaussian statistics, an assumption that is valid for low generation dendrimers.^{10,11} However, it would be of interest to investigate whether the $\langle k \rangle$ -vs.- $[Py]_{loc}$ relationship observed for low generation

dendrimers would still hold for higher generation dendrimers with a rigid core and flexible ends, as the rigid core would exclude the dyes attached to the dendrimer ends, in effect restricting their motion to the periphery of the dendrimer. The increase in $\langle k \rangle$ for high generation dendrimers compared to what would be expected from the $\langle k \rangle$ -vs.- $[Py]_{loc}$ relationship determined for low generation dendrimers should provide a measure of the increase in the local concentration experienced by the ends of high generation dendrimers. Such information should prove valuable for applications for catalysis or drug delivery. The $\langle k \rangle$ -vs.- $[Py]_{loc}$ relationship determined for low generation dendrimers could also be used as a benchmark to assess whether restricted geometries might affect the conformation of the dendrimer. In this context, it would also be of interest to study the conformation of dendrimers that are isolated inside surfactant micelles, which could have implication for drug delivery applications. Considering that application of most conventional experimental tools, such as scattering and NMR experiments, would be complicated by the extremely low dendrimer concentrations used to ensure single occupancy of a surfactant micelle which would result in a signal dominated by empty micelles, PEF represents an appealing alternative since the signal generated by the pyrene end-labeled dendrimers would not be contaminated by the presence of empty micelles.

In Chapters 4, a methodology was established to extend the length scale over which PEF could be conducted. Based on this study, it should be possible to characterize the conformation of more complex macromolecules by PEF. For example, the introduction of varying levels of D-glutamic acid in an otherwise PLGA sample could unveil dynamic and conformational changes in the polymer backbone induced by the increased disorder associated with a more racemic composition of residues in the polypeptide. By monitoring how N_{blob}^{exp} changes with the content of D-glutamic acid in the PLGA construct, such studies could quantify the impact of disorder on

the rigid α - or 3_{10} - helix of PLGA in DMF or DMSO, respectively, which could be characterized on different length scales. In such a study, the copolymers prepared with mixtures of D- and L- glutamic acid could be viewed as model systems for intrinsically disordered proteins. Alternatively, it would be of interest to study how the conformation of PLGA is impacted in the presence of different surfactants. For example, under basic conditions induced by addition of NaOH, poly(L-sodium glutamate) (PLNaG) should adopt an extended random coil conformation, but addition of a positively charged surfactant could induce the condensation of PLNaG associated with a local conformational change, that could be probed quantitatively by monitoring how $N_{\text{blob}}^{\text{exp}}$ varies as a function of surfactant concentration. These experiments would take advantage of the low concentration of macromolecules used for PEF, which would minimize intermacromolecular interactions that might otherwise occur at the higher concentrations used with more traditional techniques. Such studies could lead to establishing relationships relating the conformation of the polypeptide to the surfactant type, which could have implications for gene delivery applications.

The PEF experiments conducted over different length scales to characterize the conformation of PNb-Ac led to the conclusion that PNb-Ac has a heterogenous microstructure. Given that polymerization conditions strongly influence the microstructure of polymers, it would be of interest to study PNb-Ac samples synthesized under different conditions and with other catalysts. These polymers could be studied using PEF to characterize their microstructure on different length scales, which, in turn, could be correlated with their physical properties. This line of research may prove valuable to better understand the relationship between synthetic conditions and the resulting polymer microstructures and physical properties.

Letters of Copyright Permission

Permission for reproduction of Chapter 2



Macromolecular Conformation of Low-Generation PAMAM Dendrimers Probed by Pyrene Excimer Formation

Author: Sanjay Patel, Jean Duhamel

Publication: Macromolecules

Publisher: American Chemical Society

Date: Jun 1, 2023

Copyright © 2023, American Chemical Society

PERMISSION/LICENSE IS GRANTED FOR YOUR ORDER AT NO CHARGE

This type of permission/license, instead of the standard Terms and Conditions, is sent to you because no fee is being charged for your order. Please note the following:

- Permission is granted for your request in both print and electronic formats, and translations.
- If figures and/or tables were requested, they may be adapted or used in part.
- Please print this page for your records and send a copy of it to your publisher/graduate school.
- Appropriate credit for the requested material should be given as follows: "Reprinted (adapted) with permission from {COMPLETE REFERENCE CITATION}. Copyright {YEAR} American Chemical Society." Insert appropriate information in place of the capitalized words.
- One-time permission is granted only for the use specified in your RightsLink request. No additional uses are granted (such as derivative works or other editions). For any uses, please submit a new request.

If credit is given to another source for the material you requested from RightsLink, permission must be obtained from that source.

BACK

CLOSE WINDOW

Permission for reproduction of Chapter 3



Intramacromolecular Conformational Changes in Low Generation PAMAM Dendrimers Probed by Pyrene Excimer Formation

Author: Sanjay Patel, Stuart A. McNelles, Alex Adronov, et al

Publication: The Journal of Physical Chemistry B

Publisher: American Chemical Society

Date: Sep 1, 2023

Copyright © 2023, American Chemical Society

PERMISSION/LICENSE IS GRANTED FOR YOUR ORDER AT NO CHARGE

This type of permission/license, instead of the standard Terms and Conditions, is sent to you because no fee is being charged for your order. Please note the following:

- Permission is granted for your request in both print and electronic formats, and translations.
- If figures and/or tables were requested, they may be adapted or used in part.
- Please print this page for your records and send a copy of it to your publisher/graduate school.
- Appropriate credit for the requested material should be given as follows: "Reprinted (adapted) with permission from {COMPLETE REFERENCE CITATION}. Copyright {YEAR} American Chemical Society." Insert appropriate information in place of the capitalized words.
- One-time permission is granted only for the use specified in your RightsLink request. No additional uses are granted (such as derivative works or other editions). For any uses, please submit a new request.

If credit is given to another source for the material you requested from RightsLink, permission must be obtained from that source.

BACK

CLOSE WINDOW

References

Chapter 1

1. Daniel, W.; Burdynska, J.; Vatankhah-Varnoosfaderani, M.; Matyjaszewski, K.; Paturej, J.; Rubinstein, M.; Dobrynin, A.; Sheuko, Sheiko, S. Solvent-FREE, Supersoft and Superelastic Bottlebrush Melts and Networks. *Nat. Mater.* **2016**, *15*, 183-188.
2. Soto, C.; Satani, N. The Intricate Mechanisms of Neurodegeneration in Prion Diseases. *Trends. Mol. Today*, **2011**, *17*, 14-24.
3. Nakano, T.; Okamoto, Y. Synthetic Helical Polymers: Conformation and Function. *Chem. Rev.* **2001**, *101*, 4013-4038.
4. Hofmann, H.; Soranno, A.; Borgia, A.; Gast, K.; Nettels, D.; Schuler, B. Polymer Scaling Laws of Unfolded and Intrinsically Disordered Proteins Quantified with Single-Molecule Spectroscopy. *Proc. Natl. Acad. Sci.* **2012**, *109*, 16155-16160.
5. Hammel, M. Validation of Macromolecular Flexibility in Solution by Small-Angle X-Ray Scattering. *Eur. Biophys. J.* **2012**, *41*, 789-799.
6. Venditti, V.; Egner, T. K.; Clore, G. M. Hybrid Approaches to Structural Characterization of Conformational Ensembles of Complex Macromolecular Systems Combining NMR Residual Dipolar Couplings and Solution X-ray Scattering. *Chem. Rev.* **2016**, *116*, 6305-6322.
7. Maiti, P. K.; Çağın, T.; Wang, G.; Goddard, W. A. Structure of PAMAM Dendrimers: Generations 1 through 11. *Macromolecules* **2004**, *37*, 6236–6254.

8. Chen, W.-R.; Porcar, L.; Liu, Y. ; Buttler, P. D.; Magid, L. J. Small Angle Neutron Scattering Studies of the Counterion Effects on the Molecular Conformation and Structure of Charged G4 PAMAM Dendrimers in Aqueous Solutions. *Macromolecules* **2007**, *40*, 5887-5898.
9. Porcar, L.; Hong, K.; Butler, P. D.; Herwig, K. W.; Smith, G. S.; Liu, Y.; Chen, W.-R. Intramolecular Structural Change of PAMAM Dendrimers in Aqueous Solutions Revealed by Small-Angle Neutron Scattering. *J. Phys. Chem. B* **2010**, *114*, 1751-1756.
10. Liu, Y.; Chen, Y-C.; Chen, L-H.; Hong, K.; Shew, Y-C.; Li, X.; Liu, L.; Melnichenko, Y.; Smith, G.; Herwig, K.; Porcar, L.; Chen, R-W. Electrostatic Swelling and Conformational Variation Observed in High-Generation Polyelectrolyte Dendrimers. *J. Phys. Chem. Lett.* **2010**, *1*, 2020-2024.
11. Welch, P.; Muthukumar, M. Tuning the Density Profile of Dendritic Polyelectrolytes. *Macromolecules* **1998**, *31*, 5892-5897.
12. Maiti, P.; Goddard, W. Solvent Quality Changes the Structure of G8 PAMAM Dendrimer, a Disagreement with Some Experimental Interpretations. *J. Phys. Chem. B* **2006**, *110*, 25628-25632.
13. Maiti, P.; Cagin, T.; Lin, S-T.; Goddard, W. Effect of Solvent and pH on the Structure of PAMAM Dendrimers. *Macromolecules* **2005**, *38*, 979-991.
14. Opitz, A. W.; Wagner, N. J. Structural Investigations of Poly(amido amine) Dendrimers in Methanol Using Molecular Dynamics. *J. Polym. Sci. B Polym. Phys.* **2006**, *44*, 3062-3077.
15. Liu, Y. Bryantsev, V.; Diallo, M.; Goddard, W. PAMAM Dendrimers Undergo pH Reponsive Conformational Changes without Swelling. *J. Am. Chem. Soc.* **2009**, *131*, 2798-2799.

16. Shimizu, S.; Nuroga, Y.; Hyono, T.; Kurita, K. Small-angle X-ray Scattering Study on the Conformation of Poly(sodium L-glutamate) in NaCl and NaF Aqueous Solutions. *J. Appl. Crystallogr.* **2007**, *40*, s553-s557.
17. Zagrovic, B.; Jayachandran, G.; Millet, I.; Doniach, S.; Pande, V. How Large is an α -Helix? Studies of the Radii of Gyration of Helical Peptides by Small-angle X-ray Scattering and Molecular Dynamics. *J. Mol. Biol.* **2005**, *353*, 232-241.
18. Myer, Y. The pH-Induced Helix-Coil Transition of Poly-L-lysine and Poly-L-Glutamic Acid and the 238-m μ Dichroic Band. *Macromolecules* **1969**, *2*, 624-628.
19. Barbone, G.; Crescenzi, V.; Quadrioglio, F. Conformational Transition of Poly(L-glutamic Acid) in Aqueous Solutions. *Biopolymers* **1966**, *4*, 529-538.
20. Doty, P.; Wada, A.; Yang, J. T.; Blout, E. Polypeptides. VIII. Molecular Configurations of Poly-L-Glutamic Acid in Water-Dioxane Solution. *J. Polym. Sci.* **1957** *23*, 851-861.
21. Matsumoto, M.; Watanabe, H.; Yoshioka, K. Electric and Hydrodynamic Properties of Polypeptides in Solution. II. Conformational Change of Poly(L-glutamic Acid) in Various Organic Solvents. *Biopolymers* **1970**, *9*, 1307-317.
22. Berbec, S.; Dec, R.; Molodenskiy, D.; Wielgus-Kutrowska, B.; Johannessen, C.; Hernik-Magon, A.; Tobias, F.; Bzowska, A.; Scibisz, G.; Keiderling, T.; Svergun, D.; Dzwolak, W. β -Type Amyloidlike Fibrils of Poly-L-glutamic Acid Convert into Long, Highly Ordered Helices upon Dissolution in Dimethyl Sulfoxide. *J. Phys. Chem. B* **2018**, *122*, 11895-11905.

23. Urayama, H.; Moon, S-I; Kimura, Y. Microstructure and Thermal Properties of Polylactides with Different L- and D- Unit Sequences: Importance of the Helical Nature of the L-sequenced Segments. *Macromol. Mater. Eng.* **2003**, *288*, 137-143.
24. Ahmed, S.; Ludovice, P.; Kohl, P. Microstructure of 2,3 Erythro Di-Isotactic Polynorbornene from Atomistic Simulations. *Comput. Theor. Polym. Sci.* **2000**, *10*, 221-233.
25. Ahmed, S.; Bidstrup, S-A.; Kohl, P.; Ludovice, P. Stereochemical Structure-Property Relationships in Polynorbornene from Simulation. *Macromol. Symp.* **1998**, *133*, 1-10.
26. Chung, W.; Henderson, C.; Ludovice, P. RIS Model of the Helix-Kink Conformation of Erythro Diisotactic Polynorbornene. *Macromol. Theory Simul.* **2010**, *19*, 421-431.
27. He, Y.; Lu, M.; Cao, J.; Lu, P. Manipulating Protein Conformation by Single-Molecular AFM-FRET Nanoscopy. *ACS Nano*, **2012**, *6*, 1221-1229.
28. Meeng, Y.; Shi, X.; Zhang, S.; Ding, K.; Nie, S.; Luo, C.; Xu, X.; Triple-Helix Conformation of a Polysaccharide Determined with Light Scattering, AFM, and Molecular Dynamics Simulation. *Macromolecules*, **2018**, *51*, 10150-10159.
29. Kuchuk, K.; Sivan, U. Hydration Structure of a Single DNA Molecule Revealed by Frequency-Modulation Atomic Force Microscopy. *Nano Lett.* **2018**, *18*, 2733-2737.
30. Zorzi D. R.; Mi, W.; Liao, M.; Walz, T. Single-Particle Electron Microscopy in the Study of Membrane Protein Structure. *Microscopy* **2016**, *65*, 81-96.
31. Dongen, M.; Orr, B.; Holl, M. Diffusion NMR Study of Generation-Five PAMAM Dendrimer Materials. *J. Phys. Chem. B* **2014**, *118*, 7195-7202.

32. Li, X.; Zamponi, M.; Hong, K.; Porcar, L.; Shew, C-Y.; Jekins, T.; Liu, E.; Smith, G.; Herwig, K.; Liu, Y.; Chen, W-R. pH Responsiveness of Polyelectrolyte Dendrimers: A Dynamical Perspective. *Soft Matter* **2011**, *7*, 618-622.
33. Jiménez, V.; Gavin, J. Scaling Trend in Diffusion Coefficients of Low Generation G0-G3 PAMAM Dendrimers in Aqueous Solution at High and Neutral pH. *Struct. Chem.* **2012**, *23*, 123-128.
34. Nisato, G.; Ivkov, R.; Amis, E. Size Invariance of Polyelectrolyte Dendrimers. *Macromolecules* **2000**, *33*, 4172-4176.
35. Kwan, A.; Mobli, M.; Gooley, P.; King, G.; Mackay, J. Macromolecular NMR Spectroscopy for the Non-Spectroscopist. *FEBS J.* **2011**, *278*, 687-703.
36. McPherson, A.; Kuznetsov, Y.; Malkin, A.; Plomp, M. Macromolecular Crystal Growth as Revealed by Atomic Force Microscopy. *J. Struct. Biol.* **2003**, *142*, 32-46.
37. Li, H.; Zhang, X.; Kuang, X.; Wang, J.; Wang, D.; Li, L.; Yan, S. A Scanning Electron Microscopy Study on the Morphologies of Isotactic Polypropylene Induced by its Own Fibers. *Macromolecules* **2004**, *37*, 2847-2853.
38. Chiellini, E.; Cineeli, P.; Fernandes, E.; Kenawy, E-R.; Lazzeri, A. Gelatin-Based Blends and Composites. Morphological and Thermal Mechanical Characterization. *Biomacromolecules* **2001**, *2*, 806-811.
39. Giannotti, M.; Vancso, G.; Interrogation of Single Synthetic Polymer Chains and Polysaccharides by AFM-Based Force Spectroscopy. *ChemPhysChem*, **2007**, *8*, 2290-2307.

40. Kumaki, J. Observation of Polymer Chain Structures in Two-dimensional Films by Atomic Force Microscopy. *Polym. J.* **2016**, *48*, 3-14.
41. Libera, M.; Egerton, R. Advances in the Transmission Electron Microscopy of Polymers. *Polym. Rev.* **2010**, *50*, 321-339.
42. Ding, J.; Lee, Y-T.; Bhandari, Y.; Schwieters, C.; Fan, L.; Yu, P.; Tarosov, S.; Stagno, J.; Ma, B.; Nussinov, R.; Rein, A.; Zhang, J.; Wang, Y-X. Visualizing RNA Conformational and Architectural Heterogeneity in Solution. *Nat. Commun.* **2023**, *14*, 1-11.
43. Amyot, R.; Marchesi, A.; Franz, C.; Casuso, I.; Flechsig, H. Simulation of Atomic Force Microscopy for Atomic Reconstruction of biomolecular Structures from Resolution-limited Experimental Images. *PLoS Comput. Biol.* **2022**, 1-15.
44. Gavara, N. A Beginner's Guide to Atomic Force Microscopy Probing for Cell Mechanics. *Microsc. Res. Tech.* **2017**, *80*, 75-84.
45. Libera, M.; Egerton, R. Advances in the Transmission Electron Microscopy of Polymers. *Polym. Rev.* **2010**, *50*, 321-339.
46. Frenkel, D. Simulations: The Dark Side. *Eur. Phys. J. Plus* **2013**, *128*, 1-21.
47. Gartner III, T.; Jayaraman, A. Modeling and Simulations of Polymers: A Roadmap. *Macromolecules* **2019**, *52*, 755-786.
48. Mavrantza, V. Using Monte Carlo to Simulate Complex Polymer Systems: Recent Progress and Outlook. *Front. Phys.* **2021**, *9*.
49. Xu, D.; Wan, H-X.; Yao, X-R.; Li, J.; Yan, L-T. Macromolecular Simulations in Macromolecular Science. *Chinese J. Polym. Sci.* **2023**, *41*, 1361-1370.

50. Hospital, A.; Goniñi J.; Orozco, M. Gelpi. Molecular Dynamics Simulations: Advances and Applications. *Adv. Appl. Bioinforma. Chem.* **2015**, *8*, 37-47.
51. Boldon, L.; Laliberte, F.; Liu, L. Review of the Fundamental Theories Behind Small Angle X-ray Scattering, Molecular Dynamics simulations and Relevant Integrated Applications. *Nano Rev.* **2015**, *6*, 1-21.
52. Schnablegger, H.; Singh, Y. The SAXS Guide. Getting Acquainted with the Principles, 3rd ed.; Anton Paar GmbH: Austria, 2013.
53. Kkhney, A.; Svergun, D. A Practical Guide to Small Angle X-ray Scattering (SAXS) of Flexible and Intrinsically Disordered Proteins. *FEBS Letters* **2015**, *589*, 2570-2577.
54. Svergun, D.; Koch, M. Small-angle Scattering Studies of Biological Macromolecules in Solution. *Rep. Prog. Phys.* **2003**, *66*, 1735-1782.
55. Hopkins, J. BioXTAS RAW. https://bioxtas-raw.readthedocs.io/en/latest/saxs_tutorial.html (accessed 2023-11-21).
56. Karplus, M. Vicinal Proton Coupling in Nuclear Magnetic Resonance. *J. Am. Chem. Soc.* **1963**, *85*, 2870-2871.
57. Elyashberg, M. Identification and Structure Elucidation by NMR Spectroscopy. *Anal. Chem.* **2015**, *69*, 88-97.
58. Miles, A.; Janes, R.; Wallace, B. Tools and Methods for Circular Dichroism Spectroscopy of Proteins: A Tutorial Review. *Chem. Soc. Rev.* **2021**, *50*, 8400-8413.
59. Algar, W.; Hildebrandt, N.; Vogel, S.; Medintz, I. FRET as a Biomolecular Research Tool- Understanding its Potential While Avoiding Pitfalls. *Nat. Methods* **2019**, *16*, 815-829.

60. Schuler, B. Single-molecule FRET of Protein Structure and Dynamics-A Primer. *J. Nanobiotechnology* **2013**, *11*, 1-17.
61. Stryer, L.; Haugland, R. P. Energy Transfer: A Spectroscopic Ruler. *Proc. Natl. Acad. Sci USA* **1967**, *58*, 719-726.
62. Mazal, H.; Haran, G. Single-Molecular FRET Methods to Study the Dynamics of Proteins at Work. *Curr. Opin. Biomed. Eng.* **2019**, *12*, 8-17.
63. Tuukkanen, A. T.; Spilotros, A.; Svergun, D. I. Progress in Small-Angle Scattering from Biological Solutions at high-Brilliance Synchrotron. *IUCrJ.* **2017**, *4*, 518–528.
64. Skou, S.; Gillilan, R. E.; Ando, N. Synchrotron-Based Small-Angle X-Ray Scattering of Proteins in Solution. *Nat. Protoc.* **2014**, *9*, 1727-1739.
65. Lakowicz, J. R. Principles of Fluorescence Spectroscopy, 3rd Ed. Springer, 2006.
66. Birks, J. B.; Dyson, D. J.; Munro, I. H. 'Excimer' Fluorescence. II. Lifetime Studies of Pyrene Solutions. *Proc. R. Soc. A: Math. Phys. Eng. Sci.* **1963**, *275*, 575-588.
67. Wilemski, G.; Fixman, M. Diffusion-Controlled Intrachain Reactions of Polymers. I Theory. *J. Chem. Phys.* **1974**, *60*, 866–877.
68. Wilemski, G.; Fixman, M. Diffusion-Controlled Intrachain Reactions of Polymers. II Results for a Pair of Terminal Reactive Groups. *J. Chem. Phys.* **1974**, *60*, 878–890.
69. Winnik, M. A. End-to-End Cyclization of Polymer Chains. *Acc. Chem. Res.* **1985**, *18*, 73-79.
70. Bieri, O.; Wirz, J.; Hellrung, B.; Schutkowski, M.; Drewello, M.; Kiefhaber, T. The Speed Limit for Protein Folding Measured by Triplet–Triplet Energy Transfer. *Proc. Natl. Acad. Sci.* **1999**, *96*, 9597-9601.

71. Krieger, F.; Fierz, B.; Bieri, O.; Drewello, M.; Kiefhaber, T. Dynamics of Unfolded Polypeptide Chains as Model for the Earliest Steps in Protein Folding. *J. Mol. Biol.* **2003**, *332*, 265–274.
72. Hofmann, H.; Soranno, A.; Borgia, A.; Gast, K.; Nettels, D.; Schuler, B. Polymer Scaling Laws of Unfolded and Intrinsically Disordered Proteins Quantified with Single-Molecule Spectroscopy. *Proc. Natl. Acad. Sci.* **2012**, *109*, 16155-16160.
73. Jacob, M. H.; D'Souza, R. N.; Lazar, A. I.; Nau, W. M. Diffusion-Enhanced Förster Resonance Energy Transfer in Flexible Peptides: From the Haas-Steinberg Partial Differential Equation to a Closed Analytical Expression. *Polymers*, **2023**, *15*, 705.
74. McNelles, S. A.; Thoma, J. L.; Adronov, A.; Duhamel, J. Quantitative Characterization of the Molecular Dimensions of Flexible Dendritic Macromolecules in Solution by Pyrene Excimer Fluorescence. *Macromolecules* **2018**, *51*, 1586–1590.
75. Thoma, J.; McNelles, S. A.; Adronov, A.; Duhamel, J. Direct Measure of the Local Concentration of Pyrenyl Groups in Pyrene-Labeled Dendrons Derived from the Rate of Fluorescence Collisional Quenching. *Polymers* **2020**, *12*, 2919.
76. Siu, H.; Duhamel, J. Comparison of the Association Level of a Pyrene-Labeled Associative Polymer Obtained from an Analysis Based on Two Different Models. *J. Phys. Chem. B* **2005**, *109*, 1770–1780.
77. Chen, S.; Duhamel, J.; Bahun, G.; Adronov, A. Effect of Fluorescent Impurities in the Study of Pyrene-Labeled Macromolecules by Fluorescence. *J. Phys. Chem. B* **2011**, *115*, 9921-9929.

78. Bains, G.; Patel, A.; Narayanaswami, V. Pyrene: A Probe to Study Protein Conformation and Conformational Changes. *Macromolecules* **2011**, *16*, 7909-7935.
79. Cuichen, W.; Chunming, W.; Ling, Y.; James, C. Pyrene Excimer Nucleic Acid Probes for Biomolecular Signaling. *J. Biomed. Nanotech.* **2009**, *5*, 495-504.
80. Crawford, A.; Dyer, A.; Liu, Z.; Steffen, A.; Beeby, A.; Palsson, L-O.; Tozer, D.; Marder, T. Experimental and Theoretical Studies of the Photophysical Properties of 2- and 2,7-Functionalized Pyrene Derivatives. *J. Am. Chem. Soc.* **2011**, *133*, 13349-13362.
81. Nakajima, A. Fluorescence Spectra of Pyrene in Chlorinated Aromatic Solvents. *J. Lumin.* **1976**, *11*, 429-432.
82. Kalyanasundaram, K.; Thomas, J. Environmental Effects on Vibronic Band Intensities in Pyrene Monomer Fluorescence and their Application in Studies of Micellar Systems. *J. Am. Chem. Soc.* **1977**, *99*, 2039-2044.
83. Lianos, P.; Georghiou, S. Solute-solvent Interactions and its Effect on the Vibronic and Vibrational Structure of Pyrene Spectra. *Photochem. Photobiol.* **1979**, *30*, 355-362.
84. Dong, D.C.; Winnik, M.A. The Py Scale of Solvent Polarities. Solvent Effects on the Vibronic fine Structure of Pyrene Fluorescence and Empirical Correlation with ET and Y Values. *Photochem. Photobiol.* **1982**, *35*, 17-21.
85. Mathew, A.; Siu, H.; Duhamel, J. A Blob Model to Study Chain Folding by Fluorescence. *Macromolecules* **1999**, *32*, 7100-7108.
86. Duhamel, J. Polymer Chain Dynamics in Solution Probed with a Fluorescence Blob Model. *Acc. Chem. Res.* **2006**, *39*, 953-960.

87. Fowler, M.; Duhamel, J.; Bahun, G.; Adronov, A.; Zaragoza-Galan, G.; Rivera, E. Studying Pyrene-Labeled Macromolecules with the Model-Free Analysis. *J. Phys. Chem. B* **2012**, *116*, 14689-14699.
88. Duhamel, J. Global Analysis of Fluorescence Decays to Probe the Internal Dynamics of Fluorescently Labeled Macromolecules. *Langmuir* **2014**, *30*, 2307-2324.
89. Duhamel, J. New Insights in the Study of Pyrene Excimer Fluorescence to Characterize Macromolecules and their Supramolecular Assemblies in Solution. *Langmuir* **2012**, *28*, 6527-6538.
90. Duhamel, J. Internal Dynamics of Dendritic Molecules Probed by Pyrene Excimer Formation. *Polymers* **2012**, *4*, 211-239.
91. Cao, X.; Casier, R.; Little, H.; Duhamel, J. Characterization of the Distribution of Pyrene Molecules in Confined Geometries with the Model Free Analysis and its Applications. *J. Phys. Chem. B* **2017**, *121*, 11325-11332.
92. Ward, A. B.; Sali, A.; Wilson, I. A. Integrative Structural Biology. *Science* **2013**, *339*, 913-915.
93. Bonomi, M.; Camilloni, C. Integrative Structural and Dynamical Biology with PLUMED-ISBD. *Bioinformatics* **2017**, *33*, 3999-4000.
94. Li, L.; Duhamel, J. Conformation of Pyrene-Labeled Amylose in DMSO Characterized with the Fluorescence Blob Model. *Macromolecules* **2016**, *49*, 7965-7974.
95. Li, L.; Kim, D.; Zhai, X.; Duhamel, J. A Pyrene Excimer Fluorescence (PEF) Study of the Interior of Amylopectin in Dilute Solution. *Macromolecules* **2020**, *53*, 6850-6860.

96. Kim, D.; Duhamel, J. Cluster Size of Amylopectin and Nanosized Amylopectin Fragments Characterized by Pyrene Excimer Formation. *Polymers* **2022**, *14*, 3418-3437.
97. Ingratta, M.; Duhamel, J. Effect of Side-Chain Length on the Side-chain Dynamics of α -Helical Poly(L-glutamic acid) as Probed by a Fluorescence Blob Model. *J. Phys. Chem. B* **2008**, *112*, 9209-9218.
98. Casier, R.; Duhamel, J. Blob-Based Approach to Estimate the Folding Time of Proteins Supported by Pyrene Excimer Fluorescence Experiments. *Macromolecules* **2020**, *53*, 9823-9835.
99. Casier, R.; Duhamel, J. Pyrene Excimer Fluorescence as a Direct and Easy Experimental Means To Characterize the Length Scale and Internal Dynamics of Polypeptide Foldons. *Macromolecules* **2018**, *51*, 3450-3457.
100. Casier, R.; Duhamel, J. Effect of Like Charges on the Conformation and Internal Dynamics of Polypeptides Probed by Pyrene Excimer Fluorescence. *Macromolecules* **2020**, *53*, 5147-5157.
101. Casier, R.; Duhamel, J. Pyrene Excimer Formation (PEF) and its Application to the Study of Polypeptide Dynamics. *Langmuir* **2022**, *38*, 3623-3629.
102. Yip, J.; Duhamel, J.; Bahun, G.; Adronov, A. A Study of the Dynamics of the Branch Ends of a Series of Pyrene-Labeled Dendrimers Based on Pyrene Excimer Formation. *J. Phys. Chem. B* **2010**, *114*, 10254-10265.

103. Farhangi, S.; Casier, R.; Li, L.; Thoma, J.; Duhamel, J. Characterization of Long-Range Internal Dynamics of Pyrene-Labeled Macromolecules by Pyrene Excimer Fluorescence. *Macromolecules* **2016**, *49*, 9597-9604.
104. Farhangi, S.; Duhamel, J. Probing Side Chain Dynamics of Branched Macromolecules by Pyrene Excimer Fluorescence. *Macromolecules* **2016**, *49*, 353-361.
105. Little, H.; Thoma, J.; Yeung, R.; D'Sa, A.; Duhamel, J. Persistence Length and Encounter Frequency Determination from Fluorescence Studies of Pyrene-Labeled Poly(oligo(ethyleneglycol) methyl ether methacrylates)s. *Macromolecules* **2023**, *56*, 3562-3573.
106. Buhlieier, E.; Wehner, W.; Vögtle, F. "Cascade"- and "Nonskid-Chain-like" Syntheses of Molecular Cavity Topologies. *Synthesis* **1978**, *2*, 155-158.
107. Denkewalter, R.; Kolc, J.; Lukasavage, W. Preparation of Lysine based Macromolecular Highly Branched Homogeneous Compound. U.S. Patent US4360646A, November 23rd, 1982.
108. Denkewalter, R.; Kolc, J.; Lukasavage, W. Macromolecular Highly Branched Homogeneous Compound. U.S. Patent US4410688A, October 18th, 1983.
109. Denkewalter, R.; Kolc, J.; Lukasavage, W. Macromolecular Highly Branched Homogenous Compound Based on Lysine Units.
110. Newkome, G.; Yao, Z.; Baker, G.; Gupta, V. Micelles. Part 1. Cascade Molecules: A New Approach to Micelles. A [27]-Arborol. *J. Org. Chem.* **1985**, *50*, 2003-2004.

111. Tomalia, D.; Baker, H.; Hall, D.; Kallos, G.; Martin, S.; Roeck, J.; Ryder, J.; Smith, P. A New Class of Polymers: Starburst-Dendritic Macromolecules. *Polym. J.* **1985**, *17*, 117-132.
112. Tomalia, D.; Naylor, A.; Goddard III, W. Starburst Dendrimers: Molecular-Level Control of Size, Shape, Surface Chemistry, Topology, and Flexibility from Atoms to Macroscopic Matter. *Angew. Chem. Int. Ed. Engl.* **1990**, *29*, 138-175.
113. Roush, W.; Adam, M.; Harris, D. Cascade Molecules: A New Approach to Micelles. *Arborol. J. Org. Chem.* **1985**, *50*, 2003-2004.
114. Hawker, C.; Fréchet. Preparation of Polymers with Controlled Molecular Architecture. A New Convergent Approach to Dendritic Macromolecules. *J. Am. Chem. Soc.* **1990**, *112*, 7638-7647.
115. Miller, T.; Neenan, T. Convergent Synthesis of Monodisperse Dendrimers Based upon 1,2,5-Trisubstituted Benzenes. *Chem. Mater.* **1990**, *2*, 346-349.
116. Balzani, V.; Ceroni, P.; Maestri, M.; Vicinelli, V. Light-harvesting Dendrimers. *Curr. Opin. Chem. Biol.* **2003**, *7*, 657-665.
117. Zeng, Y.; Li, Y-Y.; Chen, J.; Yan, G.; Li, Y. Dendrimers: A Mimic Natural Light-Harvesting System. *Chem. Asian J.* **2010**, *5*, 992-1005.
118. Andrews, D. Light Harvesting in Dendrimer Materials: Designer Photophysics and Electrostatics. *J. Mater. Res.* **2012**, *27*, 627-638.
119. Kannan, R.; Nance, E.; Kanan, S.; Tomalia, D. Emerging Concepts in Dendrimer-based Nanomedicines: From Design Principles to Clinical Applications. *J. Intern. Med.* **2014**, *6*, 579-617.

120. Nikzamir, M.; Hanifehpour, Y.; Akbarzadeh, A.; Panahi, Y. Applications of Dendrimers in Nanomedicine and Drug Delivery: A Review *J. Inorg. Organomet. Polym.* **2021**, *31*, 2246-2261.
121. Navarro, G.; Tros de I Larduya, C. Activated and Non-activated PAMAM dendrimers for Gene Delivery in Vitro and in Vivo. *Nanomedicine* **2009**, *5*, 287-297.
122. Braun, C.; Vetro, J.; Tomalia, D.; Koe, G.; Koe, J.; Middaugh, C. Structure/Function Relationships of Polyamidoamine/DNA Dendrimers as Gene Delivery Vehicles. *J. Pharm. Sci.* **2005**, *94*, 423-436.
123. Astruc, D.; Chardac, F. Dendritic Catalysts and Dendrimers in Catalysis. *Chem. Rev.* **2001**, *101*, 2991-3023.
124. Twyman, L.; King, A.; Martin, I. Catalysis inside dendrimers. *Chem. Soc. Rev.* **2002**, *31*, 69-82.
125. Satija, J.; Sai, V.; Mukherji, S. Dendrimers in Biosensors: Concept and Applications. *J. Mater. Chem.* **2011**, *21*, 14367-14386.
126. Chandra, S.; Mayer, M.; Baeumner, A. PAMAM dendrimers: A Multifunctional Nanomaterial for ECL Biosensors. *Talanta*, **2017**, *168*, 126-129.
127. Yip, J.; Duhamel, J.; Bahun, G.; Adronov, A. A Study of the Dynamics of the Branch Ends of a Series of Pyrene-Labeled Dendrimers Based on Pyrene Excimer Formation. *J. Phys. Chem. B* **2010**, *114*, 10254-10265.

128. Zhang, Y.; Song, W.; Lu, Y.; Xu, Y.; Wang, C.; Yu, D-G.; Kim, Il. Recent Advances in Poly(α -L-glutamic acid)-Based Nanomaterials for Drug Delivery. *Biomacromolecules* **2022**, *12*, 636- 662.
129. Balogun-Agbaje, O.; Odeniyi, O.; Odeniyi, M. Drug Delivery Applications of Poly- γ -Glutamic Acid. *Futur. J. Pharam. Sci.* **2021**, *7*, 1-10.
130. Najar, I.; Das, S. Poly-Glutamic Acid (PGA)-Structure, Synthesis, Genomic Organization, and its Application: A Review. *IJPSR* **2015**, *2015*, 2258-2280.
131. Kidera, A.; Nakajuma, A. Light Scattering from Poly(L-glutamic acid) in Aqueous Solutions in the Helix-Coil Transition Region. *Macromolecules* **1984**, *17*, 659-663.
132. Higashi, N.; Shosu, T.; Koga, T.; Niwa, M.; Tanigawa, M. pH-Responsive, Self-Assembling Nanoparticle from a Fullerene-Tagged Poly(L-glutamic acid) and its Superoxide Dismutase Mimetic Property. *J. Colloid Interface Sci.* **2006**, *298*, 118-123.
133. Shibata, A.; Kai, T.; Yamashita, S.; Itoh, Y.; Yamashita, T. Conformation of Poly(L-glutamic acid) at the Air/Water Interface. *Biochim. Biophys. Acta. Biomembr.* **1985**, *812*, 587-590.
134. Donten, M.; Hamm, P. pH-Jump Induced α -Helix Folding of Poly-L-Glutamic Acid. *Chem. Phys.* **2013**, *422*, 124-130.
135. Bradbury, E.; Crane-Robinson, C.; Hartman, P. Effect of Polydispersity on the n.m.r. Spectra of Poly(g-benzyl-L-glutamate) through the Helix-Coil Transition. *Polymer* **1973**, *11*, 543-548.
136. Bradbury, E.; Cary, P. Crane-Robinson, C.; Hartman, P. Nuclear Magnetic Resonance of Synthetic Polypeptides. *Pure Appl. Chem.* **1973**, *36*, 53-92.

137. Matsumoto, M. Electric and Hydrodynamic Properties of Polypeptides in Solution. IV. A New conformational Change of Poly(L-glutamic Acid) in Dimethylsulfoxide-Methanol Mixtures. *Biopolymers* **1973**, *12*, 1729-1739.
138. Duhamel, J.; Kanagalingam, S.; O'Brien, T.; Ingratta, M. Side-Chain Dynamics of an α -Helical Polypeptide Monitored by Fluorescence. *J. Am. Chem. Soc.* **2003**, *125*, 12810-12822.
139. Blank, F.; Janiak, C. Metal Catalysts for the vinyl/addition Polymerization of Norbornene. *Coord. Chem. Rev.* **2009**, *253*, 827-861.
140. Kai, H.; Izumi, A.; Hayakawa, S.; Niemiec, J.; Ebner, C.; Schofield, M.; Skilskyji, D.; Rhodes, L. Interchain Ordering Structure and Main Chain Conformation analysis of Thermal Stability in Vinyl-Addition Polynorbornene. *Polymer* **2022**, *257*, 1-5.
141. Janiak, C.; Lassahn, P. Metal Catalysts for the Vinyl Polymerization of Norbornene. *J. Mol. Catal. A Chem.* **2001**, *166*, 193-209.
142. Patil, A.; Zushma, S.; Stibrany, R.; Rucker, S.; Wheeler, L. Vinyl-Type Polymerization of Norbornene by Nickel(II) Bisbenzimidazole Catalysts. *J. Polym. Sci. A Polym. Chem.* **2003**, *41*, 2095-2106.
143. Porri, L.; Scalera, V.; Bagatti, M.; Famulari, A.; Meille, S. Titanium-Catalyzed Norbornene Oligomerization Isolation of a Crystalline Heptamer with a 2,3-*exo*-Disyndiotactic Structure. *Macromol. Rapid Commun.* **2006**, *27*, 1937-1941.
144. Mi, X.; Ma, Z.; Cui, N.; Wang, L. Ke, Y. Hu, Y. Vinyl Polymerization of Norbornene with Dinuclear Diimine Nickel Dichloride/MAO. *J. Appl. Polym.* **2003**, *88*, 3273-3278.

145. Bykov, V.; Butenko, T. Composition and Microstructure of Norbornene-Ethylene Copolymers. *Polym. Sci. Ser. B* **2018**, *60*, 754-759.
146. Kaita, S.; Matsushita, K.; Tobita, M.; Maruyama, Y.; Wakatsuki, Y. Cyclopentadienyl Nickel and Palladium Complexes/Activator System for the Vinyl-Type Copolymerization of Norbornene with Norbornene Carboxylic acid Esters: Control of Polymer Solubility and Glass Transition Temperature. *Macromol. Rapid Commun.* **2006**, *27*, 1752-1756.
147. Wang, X.; Jeong, Y.; Love, C.; Stretz, H.; Stein, G.; Long, B. Design, Synthesis, and Characterization of Vinyl Addition Polynorbornenes with Tunable Thermal Properties. *Polym. Chem.* **2021**, *12*, 5831-5841.
148. Tritto, I.; Boggioni, L.; Ferro, D. Metallocene Catalyzed Ethene- and Propene co-Norbornene Polymerization: Mechanism from a Detailed Microstructural Analysis. *Coord. Chem. Rev.* **2006**, *250*, 212-241.
149. Boggioni, L.; Losio, S.; Tritto, I. Microstructure of Copolymers of Norbornene Based on Assignments of ¹³C NMR Spectra: Evolution of a Methodology. *Polymers* **2018**, *10*, 1-24.
150. Yilmaz, S. S.; Abbasoglu, R.; Hazer, B. A Molecular Mechanics and Semiempirical Molecular Orbital Study on the Conformation of Polynorbornene Chains. *J. Mol. Model* **2003**, *9*, 230-234.
151. Wang, X.; Wilson, T. J.; Alentiev, D.; Gringolts, M.; Finkelshtein, E.; Bermeshev, M.; Long, B. K. Substituted Polynorbornene Membranes: A Modular Template for Targeted Gas Separations. *Polym. Chem.* **2021**, *12*, 2947-2977.

152. Liaw, D.-J.; Wang, K.-L.; Chen, W.-H. Syntheses of Novel Polynorbornene Derivatives via Ring Opening Metathesis Polymerization. *Macromol. Symp.* **2006**, 245-246, 68-76.
153. One- and Two-Dimensional Nuclear Magnetic Resonance Characterization of Poly(aspartic acid) Prepared by Thermal Polymerization of L-Aspartic Acid. *Macromolecules* 1994, 27, 7613-7620.

Chapter 2

1. Wilemski, G.; Fixman, M. Diffusion-Controlled Intrachain Reactions of Polymers. I Theory. *J. Chem. Phys.* **1974**, *60*, 866–877.
2. Wilemski, G.; Fixman, M. Diffusion-Controlled Intrachain Reactions of Polymers. II Results for a Pair of Terminal Reactive Groups. *J. Chem. Phys.* **1974**, *60*, 878–890.
3. Winnik, M. A. End-to-End Cyclization of Polymer Chains. *Acc. Chem. Res.* **1985**, *18*, 73-79.
4. Bieri, O.; Wirz, J.; Hellrung, B.; Schutkowski, M.; Drewello, M.; Kiefhaber, T. The Speed Limit for Protein Folding Measured by Triplet–Triplet Energy Transfer. *Proc. Natl. Acad. Sci.* **1999**, *96*, 9597-9601.
5. Krieger, F.; Fierz, B.; Bieri, O.; Drewello, M.; Kiefhaber, T. Dynamics of Unfolded Polypeptide Chains as Model for the Earliest Steps in Protein Folding. *J. Mol. Biol.* **2003**, *332*, 265–274.
6. Hofmann, H.; Soranno, A.; Borgia, A.; Gast, K.; Nettels, D.; Schuler, B. Polymer Scaling Laws of Unfolded and Intrinsically Disordered Proteins Quantified with Single-Molecule Spectroscopy. *Proc. Natl. Acad. Sci.* **2012**, *109*, 16155-16160.
7. Jacob, M. H.; D’Souza, R. N.; Lazar, A. I.; Nau, W. M. Diffusion-Enhanced Förster Resonance Energy Transfer in Flexible Peptides: From the Haas-Steinberg Partial Differential Equation to a Closed Analytical Expression. *Polymers*, **2023**, *15*, 705.
8. Newkome, G.R.; Yao, Z.; Baker, G.R.; Gupta, V.K. Micelles. Part 1. Cascade molecules: A new approach to micelles. A [27]-arborol. *J. Org. Chem.* **1985**, *50*, 2003–2004.
9. Tomalia, D.A.; Baker, H.; Dewald, J.; Hall, M.; Kallos, G.; Martin, S.; Roeck, J.; Ryder, J.; Smith, P. A new class of polymers: Starburst-dendritic macromolecules. *Polym. J.* **1985**, *17*, 117–132.

10. Stals, P. J. M.; Li, Y.; Burdynska, J.; Nicolay, R.; Nese, A.; Palmans, A. R. A.; Meijer, E. W.; Matyjaszewski, K.; Sheiko, S. S. How Far Can We Push Polymer Architectures? *J. Am. Chem. Soc.* **2013**, *135*, 11421-11424.
11. Li, Z.; Tang, M.; Liang, S.; Zhang, M.; Biesold, G. M.; He, Y.; Hao, S.-M.; Choi, W.; Liu, Y.; Peng, J.; Lin, Z. Bottlebrush Polymers: From Controlled-Synthesis, Self-Assembly, Properties to Applications. *Prog. Polym. Sci.* **2021**, *116*, 101387.
12. Duhamel, J. New Insights in the Study of Pyrene Excimer Fluorescence to Characterize Macromolecules and their Supramolecular Assemblies in Solution. *Langmuir* **2012**, *28*, 6527-6538.
13. Cuniberti, C.; Perico, A. Intramolecular Excimer Formation in Polymers : Pyrene Labelled Polyvinylacetate. *Eur. Polym. J.* **1980**, *16*, 887-893.
14. Sato, T.; Matsuda, Y. Macromolecular Assemblies in Solution: Characterization by Light Scattering. *Polym. J.* **2009**, *41*, 241–251.
15. Hammel, M. Validation of Macromolecular Flexibility in Solution by Small-Angle X-Ray Scattering. *Eur. Biophys. J.* **2012**, *41*, 789-799.
16. Prosa, T. J.; Bauer, B. J. ; Amis, E. J. ; Tomalia, D. A. ; Scherrenberg, R. A SAXS Study of the Internal Structure of Dendritic Polymer Systems. *J. Polym. Sci. B, Part B: Polym. Phys.* **1997**, *35*, 2913-2924.
17. Venditti, V.; Egner, T. K.; Clore, G. M. Hybrid Approaches to Structural Characterization of Conformational Ensembles of Complex Macromolecular Systems Combining NMR Residual Dipolar Couplings and Solution X-ray Scattering. *Chem. Rev.* **2016**, *116*, 6305-6322.
18. Guinier, A.; Fournet, G. Small Angle X-Ray Scattering. Wiley, London, 1955, pp 25-28.

19. Tuukkanen, A. T.; Spilotros, A.; Svergun, D. I. Progress in Small-Angle Scattering from Biological Solutions at high-Brilliance Synchrotron. *IUCrJ.* **2017**, *4*, 518–528.
20. Maiti, P. K.; Çağın, T.; Wang, G.; Goddard, W. A. Structure of PAMAM Dendrimers: Generations 1 through 11. *Macromolecules* **2004**, *37*, 6236–6254.
21. McNelles, S. A.; Thoma, J. L.; Adronov, A.; Duhamel, J. Quantitative Characterization of the Molecular Dimensions of Flexible Dendritic Macromolecules in Solution by Pyrene Excimer Fluorescence. *Macromolecules* **2018**, *51*, 1586–1590.
22. Thoma, J.; McNelles, S. A.; Adronov, A.; Duhamel, J. Direct Measure of the Local Concentration of Pyrenyl Groups in Pyrene-Labeled Dendrons Derived from the Rate of Fluorescence Collisional Quenching. *Polymers* **2020**, *12*, 2919.
23. Thoma, J. L.; Duhamel, J. Characterization of the Local Volume Probed by the Side Chain Ends of Poly(oligo(ethylene glycol) 1-pyrenemethyl ether methacrylate) Bottle Brushes in Solution Using Pyrene Excimer Fluorescence. *Macromolecules* **2021**, *54*, 9341-9350.
24. Lau, G. C.; Sather, N. A.; Sai, H.; Waring, E. M.; Deiss-Yehiely, E.; Barreda, L.; Beeman, E. A.; Palmer, L. C.; Stupp, S. I. Oriented Multiwalled Organic–Co(OH)₂ Nanotubes for Energy Storage. *Adv. Funct. Mater.* **2018**, *28*.
25. Siu, H.; Duhamel, J. Comparison of the Association Level of a Pyrene-Labeled Associative Polymer Obtained from an Analysis Based on Two Different Models. *J. Phys. Chem. B* **2005**, *109*, 1770–1780.
26. Duhamel, J. Internal Dynamics of Dendritic Molecules Probed by Pyrene Excimer Formation. *Polymers* **2012**, *4*, 211-239.

27. Fowler, M. A.; Duhamel, J.; Bahun, G. J.; Adronov, A.; Zaragoza-Galán, G.; Rivera, E. Studying Pyrene-Labeled Macromolecules with the Model Free Analysis. *J. Phys. Chem. B* **2012**, *116*, 14689-14699.
28. Thoma, J. L.; Duhamel, J.; Li, M.-J.; Bertocchi, M. J.; Weiss, R. G. Long Range PolymerChain Dynamics of a Stiff Polymer. Fluorescence from Poly(isobutylene-*alt*-maleic anhydride) with N-(1-Pyrenylmethyl) Succinimide Groups. *Macromolecules* **2017**, *50*, 3396-3403.
29. Thoma, J. L.; Duhamel, J.; Bertocchi, M. J.; Weiss, R. G. Long Range Polymer Chain Dynamics of Highly Flexible Polysiloxane in Solution Probed by Pyrene Excimer Fluorescence. *Polymers* **2018**, *10*, 345/1-345/15.
30. Maiti, P.; Goddard, W. Solvent Quality Changes the Structure of G8 PAMAM Dendrimer, a Disagreement with Some Experimental Interpretations. *J. Phys. Chem. B* **2006**, *110*, 25628-25632.
31. Yip, J.; Duhamel, J.; Bahun, G.; Adronov, A. A Study of the Branch Ends of a Series of Pyrene-Labeled Dendrimers Based on Pyrene Excimer Formation. *J. Phys. Chem. B* **2010**, *114*, 10254-10265.
32. Chen, S.; Duhamel, J.; Bahun, G.; Adronov, A. Effect of Fluorescent Impurities in the Study of Pyrene-Labeled Macromolecules by Fluorescence. *J. Phys. Chem. B* **2011**, *115*, 9921-9929.
33. Lakowicz, J. R. in *Principles of Fluorescence Spectroscopy*, 3rd Ed. Springer, NY, 2006, pp 277-330.

Chapter 3

1. Nisato, G.; Ivkov, R.; Amis, A. J. Structure of Charged Dendrimer Solutions as Seen by Small Angle Neutron Scattering. *Macromolecules*, **1999**, *32*, 5895-5900.
2. Chen, W.-R.; Porcar, L.; Liu, Y. ; Buttler, P. D.; Magid, L. J. Small Angle Neutron Scattering Studies of the Counterion Effects on the Molecular Conformation and Structure of Charged G4 PAMAM Dendrimers in Aqueous Solutions. *Macromolecules* **2007**, *40*, 5887-5898.
3. Porcar, L.; Hong, K.; Butler, P. D.; Herwig, K. W.; Smith, G. S.; Liu, Y.; Chen, W.-R. Intramolecular Structural Change of PAMAM Dendrimers in Aqueous Solutions Revealed by Small-Angle Neutron Scattering. *J. Phys. Chem. B* **2010**, *114*, 1751-1756.
4. Liu, Y.; Chen, Y-C.; Chen, L-H.; Hong, K.; Shew, Y-C.; Li, X.; Liu, L.; Melnichenko, Y.; Smith, G.; Herwig, K.; Porcar, L.; Chen, R-W. Electrostatic Swelling and Conformational Variation Observed in High-Generation Polyelectrolyte Dendrimers. *J. Phys. Chem. Lett.* **2010**, *1*, 2020-2024.
5. Welch, P.; Muthukumar, M. Tuning the Density Profile of Dendritic Polyelectrolytes. *Macromolecules* **1998**, *31*, 5892-5897.
6. Maiti, P.; Goddard, W. Solvent Quality Changes the Structure of G8 PAMAM Dendrimer, a Disagreement with Some Experimental Interpretations. *J. Phys. Chem. B* **2006**, *110*, 25628-25632.
7. Maiti, P.; Cagin, T.; Lin, S-T.; Goddard, W. Effect of Solvent and pH on the Structure of PAMAM Dendrimers. *Macromolecules* **2005**, *38*, 979-991.
8. Opitz, A. W.; Wagner, N. J. Structural Investigations of Poly(amido amine) Dendrimers in Methanol Using Molecular Dynamics. *J. Polym. Sci. B Polym. Phys.* **2006**, *44*, 3062-3077.

9. Liu, Y. Bryantsev, V.; Diallo, M.; Goddard, W. PAMAM Dendrimers Undergo pH Reponsive Conformational Changes without Swelling. *J. Am. Chem. Soc.* **2009**, *131*, 2798-2799.
10. Maiti, P. K. PAMAM Dendrimer : A pH-Controlled Nanosponge. *Can. J. Chem.* **2017**, *95*, 991-998.
11. Patel, S., Duhamel, J. Macromolecular Conformation of Low Generation PAMAM Dendrimers Probed by Pyrene Excimer Formation. *Macromolecules* **2023**, *56*, 4012-4021.
12. Prosa, T. Y. J.; Bauer, B. J. ; Amis, E. J. ; Tomalia, D. A. ; Scherrenberg, R. A SAXS Study of the Internal Structure of Dendritic Polymer Systems. *J. Polym. Sci. B Polym. Phys.* **1997**, *35*, 2913-2924.
13. Rathgeber, S.; Monkenbush, M.; Kreitschmann, M.; Urban, V.; Brulet, A. Dynamics of Star-Burst Dendrimers in Solution in Relation to their Structural Properties. *J. Chem. Phys.* **2002**, *117*, 4047-4062.
14. Siu, H.; Duhamel, J. Comparison of the Association Level of a Pyrene-Labeled Associative Polymer Obtained from an Analysis Based on Two Different Models. *J. Phys. Chem. B* **2005**, *109*, 1770–1780.
15. Duhamel, J. New Insights in the Study of Pyrene Excimer Fluorescence to Characterize Macromolecules and Their Supramolecular Assemblies in Solution. *Langmuir* **2012**, *28*, 6527–6538.
16. Cuniberti, C.; Perico, A. Intramolecular Excimer Formation in Polymers : Pyrene Labelled Polyvinylacetate. *Eur. Polym. J.* **1980**, *16*, 887-893.
17. Duhamel, J. Internal Dynamics of Dendritic Molecules Probed by Pyrene Excimer Formation. *Polymers* **2012**, *4*, 211-239.

18. Yip, J.; Duhamel, J.; Bahun, G.; Adronov, A. A Study of the Branch Ends of a Series of Pyrene-Labeled Dendrimers Based on Pyrene Excimer Formation. *J. Phys. Chem. B* **2010**, *114*, 10254-10265.
19. Chen, S.; Duhamel, J.; Bahun, G.; Adronov, A. Effect of Fluorescent Impurities in the Study of Pyrene-Labeled Macromolecules by Fluorescence. *J. Phys. Chem. B* **2011**, *115*, 9921-9929.
20. Lakowicz, J. R. in *Principles of Fluorescence Spectroscopy*, 3rd Ed. Springer, NY, 2006, pp 277-330.
21. McNelles, S.; Thoma, J.; Adronov, A.; Duhamel, J. Quantitative Characterization of the Molecular Dimensions of Flexible Dendritic Macromolecules by Pyrene Excimer Fluorescence. *Macromolecules* **2018**, *51*, 1586-1590.
22. Thoma, J.; McNelles, S. A.; Adronov, A.; Duhamel, J. Direct Measure of the Local Concentration of Pyrenyl Groups in Pyrene-Labeled Dendrons Derived from the Rate of Fluorescence Collisional Quenching. *Polymers* **2020**, *12*, 2919.

Chapter 4

1. Song, Z.; Tan, Z.; Cheng, J. Recent Advances and Future Perspectives of Synthetic Polypeptides from N-Carboxyanhydrides. *Macromolecules* **2019**, *52*, 8521-8539.
2. Shimizu, S.; Nuroga, Y.; Hyono, T.; Kurita, K. Small-angle X-ray Scattering Study on the Conformation of Poly(sodium L-glutamate) in NaCl and NaF Aqueous Solutions. *J. Appl. Crystallogr.* **2007**, *40*, s553-s557.
3. Zagrovic, B.; Jayachandran, G.; Millet, I.; Doniach, S.; Pande, V. How Large is an α -Helix? Studies of the Radii of Gyration of Helical Peptides by Small-angle X-ray Scattering and Molecular Dynamics. *J. Mol. Biol.* **2005**, *353*, 232-241.
4. Kidera, A.; Nakajuma, A. Light Scattering from Poly(L-glutamic acid) in Aqueous Solutions in the Helix-Coil Transition Region. *Macromolecules* **1984**, *17*, 659-663.
5. Higashi, N.; Shosu, T.; Koga, T.; Niwa, M.; Tanigawa, M. pH-Responsive, Self-Assembling Nanoparticle from a Fullerene-Tagged Poly(L-glutamic acid) and its Superoxide Dismutase Mimetic Property. *J. Colloid Interface Sci.* **2006**, *298*, 118-123.
6. Myer, Y. The pH-Induced Helix-Coil Transition of Poly-L-lysine and Poly-L-Glutamic Acid and the 238-m μ Dichroic Band. *Macromolecules* **1969**, *2*, 624-628.
7. Shibata, A.; Kai, T.; Yamashita, S.; Itoh, Y.; Yamashita, T. Conformation of Poly(L-glutamic acid) at the Air/Water Interface. *Biochim. Biophys. Acta. Biomembr.* **1985**, *812*, 587-590.
8. Barbone, G.; Crescenzi, V.; Quadrifoglio, F. Conformational Transition of Poly(L-glutamic Acid) in Aqueous Solutions. *Biopolymers* **1966**, *4*, 529-538.
9. Donten, M.; Hamm, P. pH-Jump Induced α -Helix Folding of Poly-L-Glutamic Acid. *Chem. Phys.* **2013**, *422*, 124-130.

10. Bradbury, E.; Crane-Robinson, C.; Hartman, P. Effect of Polydispersity on the n.m.r. Spectra of Poly(γ -benzyl-L-glutamate) through the Helix-Coil Transition. *Polymer* **1973**, *11*, 543-548.
11. Doty, P.; Wada, A.; Yang, J. T.; Blout, E. Polypeptides. VIII. Molecular Configurations of Poly-L-Glutamic Acid in Water-Dioxane Solution. *J. Polym. Sci.* **1957** *23*, 851-861.
12. Bradbury, E.; Cary, P. Crane-Robinson, C.; Hartman, P. Nuclear Magnetic Resonance of Synthetic Polypeptides. *Pure Appl. Chem.* **1973**, *36*, 53-92.
13. Matsumoto, M.; Watanabe, H.; Yoshioka, K. Electric and Hydrodynamic Properties of Polypeptides in Solution. II. Conformational Change of Poly(L-glutamic Acid) in Various Organic Solvents. *Biopolymers* **1970**, *9*, 1307-317.
14. Matsumoto, M. Electric and Hydrodynamic Properties of Polypeptides in Solution. IV. A New conformational Change of Poly(L-glutamic Acid) in Dimethylsulfoxide-Methanol Mixtures. *Biopolymers* **1973**, *12*, 1729-1739.
15. Berbec, S.; Dec, R.; Molodenskiy, D.; Wielgus-Kutrowska, B.; Johannessen, C.; Hernik-Magon, A.; Tobias, F.; Bzowska, A.; Scibisz, G.; Keiderling, T.; Svergun, D.; Dzwolak, W. β -Type Amyloidlike Fibrils of Poly-L-glutamic Acid Convert into Long, Highly Ordered Helices upon Dissolution in Dimethyl Sulfoxide. *J. Phys. Chem. B* **2018**, *122*, 11895-11905.
16. Duhamel, J.; Kanagalingam, S.; O'Brien, T.; Ingratta, M. Side-Chain Dynamics of an α -Helical Polypeptide Monitored by Fluorescence. *J. Am. Chem. Soc.* **2003**, *125*, 12810-12822.
17. Casier, R.; Duhamel, J. Effect of Like Charges on the Conformation and Internal Dynamics of Polypeptides Probed by Pyrene Excimer Fluorescence. *Macromolecules* **2020**, *53*, 5147-5157.

18. Casier, R.; Duhamel, J. Pyrene Excimer Fluorescence as a Direct and Easy Experimental Means To Characterize the Length Scale and Internal Dynamics of Polypeptide Foldons. *Macromolecules* **2018**, *51*, 3450-3457.
19. Ingratta, M.; Duhamel, J. Effect of Side-Chain Length on the Side-chain Dynamics of α -Helical Poly(L-glutamic acid) as Probed by a Fluorescence Blob Model. *J. Phys. Chem. B* **2008**, *112*, 9209-9218.
20. Anderson, N.; Cao, B.; Chinpan, C. Peptide/Protein Structure Analysis Using the Chemical Shift Index Method: Upfield α -CH Values Reveal Dynamic Helices and α_L Sites. *Biochem. Biophys. Res. Commun.* **1992**, *184*, 1008-1014.
21. Giugliarelli, A. Paolantoni, M.; Morresi, A. Sassi, Paola. Denaturation and Preservation of Globular proteins: The Role of DMSO. *J. Phys. Chem. B* **2012**, *116*, 13361-13367.
22. Mandumpal, J. B.; Kreck, C. A.; Mancera, R. L. A Molecular Mechanism of Solvent Cryoprotection in Aqueous DMSO Solutions. *Phys. Chem. Chem. Phys.* **2011**, *13*, 3839-3842.
23. Arakawa, T.; Kita, Y.; Timasheff, S. Protein Precipitation and Denaturation by Dimethyl Sulfoxide. *Biophys. Chem.* **2007**, *131*, 62-70.
24. Lwase, H.; Hirai, M.; Arai, S.; Mitsuya, S.; Shimizu, S.; Otomo, T.; Furusaka, M. Comparison of DMSO-Induced Denaturation of Hen Egg-White Lysozyme and Bovine α -Lactalbumin. *J. Phys. Chem. Solids* **1999**, *60*, 1379-1381.
25. Chakraborty, S.; Hosur, R. NMR Insights into the Core of GED Assembly by H/D Exchange Coupled with DMSO Dissociation and Analysis of the Denatured State. *J. Mol. Biol.* **2011**, *405*, 1202-1214.
26. Jackson, M. Mantsch, H. Beware of Proteins in DMSO. *Biochim. Biophys. Acta.* **1991**, *1078*, 231-235.

27. Voets, I.; Cruz, W.; Moitzi, C.; Lindner, P.; Arêas, E.; Schurtenberger, P. DMSO-Induced Denaturation of Hen Egg White Lysozyme. *J. Phys. Chem. B* **2010**, *114*, 11875-11883.
28. Hirota-Nakaoka, N.; Hasegawa, K.; Naiki, H.; Goto, Y. Dissolution of β 2-Microglobulin Amyloid Fibrils by Dimethylsulfoxide. *J. Biochem.* **2003**, *134*, 159-164.
29. Bellanda, M.; Peggion, E.; Burgi, R.; Gunsteren, W.; Mammi, S. Conformational Study of an Aib-Rich Peptide in DMSO by NMR. *J. Pept. Res.* **2001**, *57*, 97-106.
30. Chakraborty, S.; Mohan, P.; Hosur, R. Residual Structure and Dynamics in DMSO-*d*₆ Denatured Dynein Light Chain Protein. *Biochimie.* **2012**, *94*, 231-241.
31. Srivastava, K.; Goyal, B.; Kkumar, A.; Durani, S. Scrutiny of Electrostatic-Driven Conformational Ordering of Polypeptide Chains in DMSO: A Study with a Model Oligopeptide. *RSC Adv.* **2017**, *45*, 27981-27991.
32. Bernado, P.; Blackledge, M. A Self-Consistent Description of the Conformational Behaviour of Chemically Denatured Proteins from NMR and Small Angle Scattering. *Biophys. J.* **2009**, *97*, 2839-2845.
33. Hiraoki, T.; Hikichi, K. ¹³C Nuclear Magnetic Relaxation of Poly(D-glutamic acid) in Aqueous Solution. *Polym. J.* **1979**, *11*, 299-306.
34. Rodger, A.; Marshal, D. Beginners Guide to Circular Dichroism. *Biochem. (Lond.)* **2021**, *43*, 58-64.
35. Ladokhin, A.; Fernandex-Vidal, M.; White, S. CD Spectroscopy of Peptides and Proteins Bound to Large Unilamellar Vesicles. *J. Membrane Biol.* **2010**, *236*, 247-253.
36. Greenfield, N. Methods to Estimate the Conformation of Proteins and Polypeptides from Circular Dichroism Data. *Anal. Biochem.* **1996**, *235*, 1-10.

37. Mensch, C.; Bultinck, P.; Johannessen, C. Conformational Disorder and Dynamics of Proteins Sensed by Raman Optical Activity. *ACS Omega* **2018**, *3*, 12944-12955.
38. Batista, A.; Batista, J.; Bolzani, V.; Furlan, M.; Blanch, E. Selective DMSO-Induced Conformational Changes in Proteins from Raman Optical Activity. *Phys. Chem. Chem. Phys.* **2013**, *15*, 20147-20152.
39. Furuta, M.; Fujisawa, T.; Urago, H.; Eguchi, T.; Shingae, T.; Takahashi, S.; Blanch, E.; Unno, M. Raman Optical Activity of Trea-alanine in the Poly(L-proline) II Type Peptide Conformation. *Phys. Chem. Chem. Phys.* **2017**, *19*, 2078-2086.
40. Haris, P.; Chapman, D. The Conformational Analysis of Peptides Using Fourier Transform IR Spectroscopy. *Biopolymers* **1995**, *37*, 251-263.
41. Fulara, A.; Dzwolak, W. Bifurcated Hydrogen Bonds Stabilize Fibrils of Poly(L-glutamic) Acid. *J. Phys. Chem. B* **2010**, *114*, 8278-8283.
42. Baginska, K.; Makowska, J.; Wiczak, W.; Kasprzykowski, F.; Chmurzynski, L. Conformational Studies of Alanine-rich Peptide using CD and FTIR Spectroscopy. *J. Pept. Sci.* **2008**, *14*, 283-289.
43. Skou, S.; Gillilan, R. E.; Ando, N. Synchrotron-Based Small-Angle X-Ray Scattering of Proteins in Solution. *Nat. Protoc.* **2014**, *9*, 1727-1739.
44. Tuukkanen, A. T.; Spilotros, A.; Svergun, D. I. Progress in Small-Angle Scattering from Biological Solutions at high-Brilliance Synchrotron. *IUCrJ.* **2017**, *4*, 518-528.
45. Boldon, L.; Laliberte, F.; Lie, Li. Review of the Fundamental Theories behind Small Angle X-ray Scattering, Molecular Dynamics Simulations, and Relevant Integrated Application. *Nano. Rev.* **2014**, *6*, 1-38.

46. Sato, T.; Matsuda, Y. Macromolecular Assemblies in Solution: Characterization by Light Scattering. *Polym. J.* **2009**, *41*, 241–251.
47. Yu. H. Extending the Size Limit of Protein Nuclear Magnetic Resonance. *Proc. Natl. Acad. Sci.* **1999**, *96*, 322-334.
48. One- and Two-Dimensional Nuclear Magnetic Resonance Characterization of Poly(aspartic acid) Prepared by Thermal Polymerization of L-Aspartic Acid. *Macromolecules* **1994**, *27*, 7613-7620.
49. Chen, Y.; Wallace, B.A. Secondary Solvent Effects on the Circular Dichroism Spectra of Polypeptides in Non-aqueous Environments: Influence of Polarisation Effects on the far Ultraviolet Spectra of Alamethicin. *Biophys. Chem.* **1997**, *65*, 65-74.
50. Mensch, C.; Bultinck, P.; Johannessen, C. Conformational Disorder and Dynamics of Proteins Sensed by Raman Optical Activity. *ACS Omega*, **2018**, *3*, 12944-12955.
51. Keiderling, T. Vibrational Circular Dichroism: Applications to Conformational Analysis of Biomolecules. In *Circular Dichroism and the Conformational Analysis of Biomolecules*; Fasman, G; Plenum Press: New York, 1996, pp 555-598.
52. Markley, J.; Meadows, D.; Jardetzky, O. Nuclear Resonance Studies of Helix-Coil Transitions in Polyamino Acids. *J. Mol. Biol.* **1967**, *27*, 25-40.
53. Bradbury, E.; Crane-Robinson, C.; Goldman, H.; Rattle, H. Proton Magnetic Resonance and Optical Spectroscopic Studies of Water-Soluble Polypeptides: Poly-L-Lysine HBr, Poly(L-Glutamic Acid), and Copoly(L-Glutamic Acid⁴², L-Lysine HBr²⁸, L-Alanine³⁰). *Biopolymers* **1968**, *6*, 851-862.
54. Lader, H.; Komoroski, R.; Mandelkern, L. A Nuclear Magnetic Resonance Study of the Helix-Coil Transition of Poly(L-Glutamic Acid). *Biopolymers* **1977**, *16*, 895-905.

55. Tsutsumi, A.; Parly, B.; Forchioni, A.; Chachaty, C. A Magnetic Resonance Study of the Segmental Motion and Local Conformations of Poly(L-Glutamic acid) in Aqueous Solution. *Macromolecules* **1978**, *11*, 977-986.
56. Lader, H.; Manderlkern, L. Origin of Multipeak Behavior in the NMR Spectra of Poly(L-Glutamic Acid). *Biopolymers* **1979**, *18*, 2607-2623.
57. Duhamel, J. New Insights in the Study of Pyrene Excimer Fluorescence to Characterize Macromolecules and their Supramolecular Assemblies in Solution. *Langmuir* **2012**, *28*, 6527-6538.
58. Stryer, L.; Haugland, R. P. Energy Transfer: A Spectroscopic Ruler. *Proc. Natl. Acad. Sci. USA* **1967**, *58*, 719-726.
59. Little, H.; Patel, S.; Duhamel, J. Probing the Inner Density of Complex Macromolecules by Pyrene Excimer Formation. *Phys. Chem. Chem. Phys.* **2023**, *25*, 26515.
60. Winnik, F. Fluorescence Studies of Aqueous Solutions of Poly(N-isopropylacrylamide) below and above their LCST. *Macromolecules* **1989**, *23*, 233-242.
61. Patel, S.; Duhamel, J. Macromolecular Conformation of Low-Generation PAMAM Dendrimers Probed by Pyrene Excimer Formation. *Macromolecules* **2023**, *56*, 4012-4021.
62. Mathew, A.; Siu, H.; Duhamel, J. A Blob Model to Study Chain Folding by Fluorescence. *Macromolecules* **1999**, *32*, 7100-7108.
63. Farhangi, S.; Duhamel, J. Probing Side Chain Dynamics of Branched Macromolecules by Pyrene Excimer Fluorescence. *Macromolecules* **2016**, *49*, 353-361.
64. CRC Handbook of Chemistry and Physics, 104th ed.; Rumble, J. R., Ed.; CRC Press: Boca Raton, FL, 2020; Section 12, p 5.

65. Pauling, L.; Corey, R.; Branson, H. The Structure of Proteins: Two Hydrogen-Bonded Helical Configuration of the Polypeptide Chain. *Proc. Natl. Acad. Sci. U.S.A* **1951**, *37*, 205-211.
66. Toniolo, C.; Benedetti, E. The Polypeptide 3_{10} Helix. *Trends Biochem.* **1991**, *16*, 350-353.
67. Chebrek, R.; Leonard, S.; Brevern, A.; Gelly, J-C. Polyproline: Polyproline Helix II and Secondary Structure Assignment Database. *Database* **2014**, *2014*, 1-8.
68. Ge.; Wen, Y.; Liu, H.; Lu, T.; Yu, Y.; Zhang, X.; Li, B.; Zhang, S-T.; Li, W.; Yang, B. A Key Stacking Factor for the Effective Formation of Pyrene Excimer in Crystals: Degree of π - π overlap. *J. Mater. Chem. C.* **2020**, *8*, 11830-11838.
69. Norisuye, T.; Teramoto, A.; Fujita, H. Solution properties of Synthetic Polypeptides. XIII. Dimensions of Interrupted Helices of Poly(γ -benzyl L-Glutamate). *Poly. J.* **1973**, *4*, 323-331.

Chapter 5

1. Kim, S-Y.; Zukoski, C. Molecular Weight Effects on Particle and Polymer Microstructure in Concentrated Polymer Solutions. *Macromolecules* **2013**, *46*, 6634-6643.
2. Capacchione, C.; De Carlo F.; Zannoni, C.; Okuda, J.; Proto, A. Propylene-Styrene Multiblock Copolymers: Evidence for Monomer Enchainment via opposite Insertion Regiochemistry by a Single-Site Catalyst. *Macromolecules* **2004**, *37*, 8918-8922.
3. Kumar, D.; Lidster, B.; Adams, R.; Turner, M. Understanding the Microstructure of Poly(*p*-phenylenevinylene)s Prepared by Ring-Opening Metathesis Polymerization Using ¹³C-Labeled Paracyclophanediene Monomers. *Macromolecules* **2018**, *51*, 4572-4577.
4. Worch, J.; Prydderch, H.; Jimaja, S.; Bexis, P.; Becker, M.; Dove, A. Stereochemical Enhancement of Polymer Properties. *Nat. Rev. Chem.* 2019, *3*, 514-535.
5. Urayama, H.; Moon, S-I; Kimura, Y. Microstructure and Thermal Properties of Polylactides with Different L- and D- Unit Sequences: Importance of the Helical Nature of the L-sequenced Segments. *Macromol. Mater. Eng.* **2003**, *288*, 137-143.
6. Hentschel, J.; Börner, H. Peptide-Directed Microstructure Formation of Polymers in Organic Media. *J. Am. Chem. Soc.* **2006**, *128*, 14142-14149.
7. Jian, Q.; Wong, S.; Klausen, R. Effect of Polycyclosilane microstructure on Thermal Properties. *Polym. Chem.* **2021**, *12*, 4785-4794.
8. Qu, L.; Shi, G.; Yuan, J.; Han, G.; Chen F. Preparation of Polypyrrole Microstructure by Direct Electrochemical Oxidation of Pyrrole in an Aqueous Solution of Camphorsulfonic Acid. *J. Electroanal. Chem.* **2004**, *561*, 149-156.
9. Yu. X.; Burnham, N.; Tao, M. Surface Microstructure of Bitumen Characterized by Atomic Force Microscopy. *Adv. Colloid Interface Sci.* **2015**, *218*, 17-33.

10. Gartner, T.; Jayaraman, A. Modeling and Simulations of Polymers: A Roadmap. *Macromolecules* **2019**, *52*, 755-786.
11. Peng, R.; Zhou, H.; Wang, H.; Mishnaevsky, L. Modeling of Nano-reinforced Polymer Composites: Microstructure Effect on Young's Modulus. *Comput. Mater. Sci.* **2012**, *60*, 19-31.
12. Bostanabad, R.; Zhang, Y.; Li, X.; Kearney, T.; Brinson, L.; Apley, D.; Liu, W.; Chen, W. Computation Microstructure Characterization and Reconstruction: Review of the state-of-the-art Techniques. *Prog. Mater. Sci.* **2018**, *95*, 1-41.
13. Gooneie, A.; Schuschnigg, S.; Holzer, C. A Review of Multiscale Computational Methods in Polymeric Materials. *Polymers* **2017**, *9*, 1-80.
14. Elliot, J. Novel Approaches to Multiscale Modelling in Materials Science. *Int. Mater. Rev.* **2013**, *56*, 207-225.
15. Soares, J. Polyolefins with Long Chain Branches Made with Single-Site Coordination Catalysts: A review of Mathematical Modeling Techniques for Polymer Microstructure. *Macromol. Mater. Eng.* **2004**, *289*, 70-87.
16. Ahmed, S.; Ludovice, P.; Kohl, P. Microstructure of 2,3 erythro di-isotactic Polynorbornene from Atomistic Simulations. *Comput. Theor. Polym. Sci.* **2000**, *10*, 221-233.
17. Ahmed, S.; Bidstrup, S-A.; Kohl, P.; Ludovice, P. Stereochemical Structure-Property Relationships in Polynorbornene from Simulation. *Macromol. Symp.* 1998, *133*, 1-10.
18. Ahmed, S.; Bidstrup, S-A.; Kohl, P.; Ludovice, P. Development of a New Force Field for Polynorbornene. *J. Phys. Chem. B* **1998**, *102*, 9783-9790.
19. Chung, W.; Henderson, C.; Ludovice, P. RIS Model of the Helix-Kink Conformation of Erythro Diisotactic Polynorbornene. *Macromol. Theory Simul.* **2010**, *19*, 421-431.

20. Xiang, M.; Lyu, D.; Qin, Y.; Chen, Ra.; Liu, L.; Men, Y. Microstructure of Bottlebrush poly(n-alkyl methacrylate)s beyond Side Chain Packing. *Polym.* **2020**, *210*, 1-6.
21. Mao, Y.; Shi, J.; Cai, L.; Hwang, W.; Shi, Y-C. Microstructures of Starch Granules with Different Amylose Contents and Allomorphs as Revealed by Scattering Techniques. *Biomacromolecules* **2023**, *24*, 1980-1993.
22. Rische, T.; Waddon, A.; Dickinson, L.; McKnight, W. Microstructure and Morphology of Cycloofin Copolymers. *Macromolecules* **1998**, *31*, 1871-1874.
23. Jackson, D.; Koberstein, T.; Weiss, R. Small-Angle X-ray Scattering Studies of Zinc Stearate-Filled Sulfonated Poly(ethylene-co-ethylidene norbornene) Ionomers. *J. Polym. Sci. B Polym. Phys.* **1999**, *37*, 3141-3150.
24. Mather, P.; Jeon, H.; Romo-Uribe, A. Mechanical Relaxation and Microstructure of Poly(norbornyl-POSS) Copolymers. *Macromolecules* **1999**, *32*, 1194-1203.
25. Skou, S.; Gillilan, R. E.; Ando, N. Synchrotron-Based Small-Angle X-Ray Scattering of Proteins in Solution. *Nat. Protoc.* **2014**, *9*, 1727-1739.
26. Tuukkanen, A. T.; Spilotros, A.; Svergun, D. I. Progress in Small-Angle Scattering from Biological Solutions at high-Brilliance Synchrotron. *IUCrJ.* **2017**, *4*, 518–528.
27. Boldon, L.; Laliberte, F.; Lie, Li. Review of the Fundamental Theories behind Small Angle X-ray Scattering, Molecular Dynamics Simulations, and Relevant Integrated Application. *Nano. Rev.* **2014**, *6*, 1-38.
28. Sato, T.; Matsuda, Y. Macromolecular Assemblies in Solution: Characterization by Light Scattering. *Polym. J.* **2009**, *41*, 241–251.

29. Kai, H.; Izumi, A.; Hayakawa, S. Niemiec, J.; Ebner, C.; Schofield, M.; Skilskyj, D.; Rhodes, L. Interchain Ordering Structure and Main Chain Conformation Analysis of Thermal Stability in Vinyl-Addition Polynorbornene.
30. Tritto, I.; Boggioni, L.; Ferro, D. Metallocene Catalyzed ethene- and propene co-norbornene Polymerizations: Mechanism from a detailed Microstructural Analysis. *Cord. Chem. Rev.* **2006**, *250*, 212-241.
31. Forsyth, J.; Pereña, J. Benavente, R.; Pérez, E.; Tritto, I., Baggionia, L.; Brintzinger, H-H. Influence of the Polymer Microstructure on the Thermal Properties of Cycloolefin Copolymers with High Norbornene Contents. *Macromol. Chem. Phys.* **2001**, *202*, 614-620.
32. Karafilidis, C.; Angermund, K.; Gabor, B.; Ruffńska, A.; Mynott, R.; Breitenburch, G.; Thiel, W.; Fink, G. Helical Microstructure of Polynorbornene. *Angew. Chem. Int. Ed.* **2007**, *46*, 3745-3749.
33. Basic, V.; Cipullo, R. Microstructure of Polypropylene. *Prog. Polym. Sci.* **2001**, *26*, 443-533.
34. Bergström, C.; Sperlich, B.; Ruotoistenmäki, J.; Sappälä, J. Investigation of the Microstructure of Metallocene-Catalyzed Norbornene-Ethylene Copolymers Using NMR Spectroscopy. *J. Polym. Sci. Part A: Polym. Chem.* **1998**, *36*, 1633-1638.
35. Nag, N.; Sasidharan, S.; Saudagar, P.; Tripathi, T. Chapter 1- Fundamentals of Spectroscopy for Biomolecular Structure and Dynamics. In *Advance Spectroscopic Methods to Study Biomolecular Structure and Dynamics*, 1st ed; Academic Press, 2022, 1-35.
36. Wolk, S.; Swift, G. Paik, Y.; Yocom, K.; Smith, R.; Simon, E. One- and Two-Dimensional Nuclear Magnetic Resonance Characterization of Poly(aspartic acid) Prepared by Thermal Polymerization of L-Aspartic Acid. *Macromolecules* **1994**, *27*, 7613-7620.

37. Boggioni, L.; Losio, S.; Tritto, I. Microstructure of Copolymers of Norbornene Based on Assignments of ^{13}C NMR Spectra: Evolution of a Methodology. *Polymers* **2018**, *10*, 1-24.
38. Patil, A.; Zushma, S.; Stibrany, R.; Rucker, S.; Wheeler, L. Vinyl-Type Polymerization of Norbornene by Nickel (II) Bisbenzimidazole Catalysts. *J. Polym. Sci., Part A: Polym. Chem.* **2003**, *41*, 2095-2106.
39. Frenkel, D. Simulations: The Dark Side. *Eur. Phys. J. Plus* **2013**, *128*, 1-21.
40. Arndt-Rosenau, M.; Beulich, I. Microstructure of Ethene/Norbornene Copolymers. *Macromolecules* **1999**, *32*, 7335-7343.
41. Wendt, R.; Mynott, R.; Hauschild, K.; Ruchatz, D.; Fink, G. ^{13}C NMR Studies of ethene-norbornene Copolymers: Assignment of Sequence Distributions using ^{13}C -enriched monomers and Determination of the Copolymerization Parameters. *Macromol. Chem. Phys.* **1999**, *200*, 1340-1350.
42. Arndt, M.; Engehausen, R.; Kaminsky, W.; Zoumis, K. Hydrooligomerization of Cycloolefins- A View of the Microstructure of Polynorbornene. *J. Mol. Catal. A. Chem.* **1995**, *101*, 171-178.
43. Ferro, D.; Ragazzi, M. Correlation Between ^{13}C NMR Chemical Shifts and Conformation of Polymers. 4. Solid-State Spectra of Poly(3-methyl-1-pentene). *Macromolecules* **1984**, *17*, 485-490.
44. Bergström, C.; Sperlich, B.; Ruotoistenmäki, J.; Seppälä, J. *J. Polym. Sci. A Polym. Chem.* **1998**, *36*, 1633-1638.
45. Randall, J. C. A Review of High Resolution Liquid ^{13}C Nuclear Magnetic Resonance Characterization of Ethylene Based Polymers. *J. Macromol. Sci. Rev. Macromol. Chem. Phys. C* **1989**, *C29*, 201-317.

46. Kieseewetter, J.; Arikan, B.; Kaminsky, W. Copolymerization of Ethene with Norbornene Using Palladium(II) α -diimide Catalysts: Influence of Feed Composition, Polymerization temperature, and Ligand Structure on Copolymer Properties and Microstructure *Polymer* **2006**, *47*, 3302-3314.
47. Carbone, P.; Ragazzi, M.; Tritto, I.; Boggioni, L.; Ferro, D. Ab Initio Molecular Modeling of ^{13}C NMR Chemical Shifts of Polymers. 2. Propene-Norbornene Copolymers. *Macromolecules* **2003**, *36*, 891-899.
48. Boggioni, K.; Bertini, F.; Zannoni, G.; Tritto, I.; Carbone, P.; Ragazzi, M.; Ferro, D. Propene-Norbornene Copolymers: Synthesis and Analysis of Polymer Structure by ^{13}C NMR Spectroscopy and ab Initio Chemical Shift Computations. *Macromolecules* **2003**, *36*, 882-890.
49. Provasoli, A.; Ferro, D.; Tritto, I.; Boggioni, L. The Conformational Characteristics of Ethylene-norbornene Copolymers and Their Influence on the ^{13}C NMR Spectra *Macromolecules* **1999**, *32*, 6697-6706.
50. Ward, A. B.; Sali, A.; Wilson, I. A. Integrative Structural Biology. *Science* **2013**, *339*, 913-915.
51. Bonomi, M.; Camilloni, C. Integrative Structural and Dynamical Biology with PLUMED-ISBD. *Bioinformatics* **2017**, *33*, 3999-4000.
52. Patel, S.; McNelles, S.; Adronov, A.; Duhamel, J. Intra-Macromolecular Conformational Changes in Low Generation PAMAM Dendrimers Probed by Pyrene Excimer Formation. *J. Phys. Chem.* **2023**, *37*, 8040-8048.
53. Little, H.; Patel, S.; Duhamel, J. Probing the Inner Local Density of Complex Macromolecules by Pyrene Excimer Formation. *Phys. Chem. Chem.* **2023**, *25*, 26515-26525.

54. Patel, S.; Duhamel, J. Macromolecular Conformation of Low-Generation PAMAM Dendrimers Probed by Pyrene Excimer Formation. *Macromolecules* **2023**, *56*, 4012-4021.
55. Thoma, J.; McNelles, S.; Adronov, A.; Duhamel, J. Direct Measure of the Local Concentration of Pyrenyl Groups in Pyrene-Labeled Dendrons Derived from the Rate of Florescence Collision Quenching. *Polymers* **2020**, *12*, 2919-2933.
56. Casier, R.; Duhamel, J. Blob-Based Predictions of Protein Folding Times from the Amino Acid Dependent Conformation of Polypeptides in Solution. *Macromolecules* **2021**, *54*, 919-929.
57. Thoma, J.; Little, H.; Duhamel, J.; Zhang, L.; Leung, T. Persistence Length of PEGMA Bottle Brushes Determined by Pyrene Excimer Fluorescence. *Accepted in Polymers* **2023**.
58. Mathew, A.; Siu, H.; Duhamel, J. A Blob Model to Study Chain Folding by Fluorescence. *Macromolecules* **1999**, *32*, 7100-7108.
59. Duhamel, J. Polymer Chain Dynamics in Solution Probed with a Fluorescence Blob Model. *Acc. Chem. Res.* **2006**, *39*, 953-960.
60. Ingratta, M.; Duhamel, J. Correlating Pyrene Excimer Formation with Polymer Chain Dynamics in Solution. Possibilities and Limitations. *Macromolecules* **2007**, *40*, 6647-6657.
61. Ingratta, M.; Hollinger, J.; Duhamel, J. A Case for Using Randomly Labeled Polymers to Study Long-Range Polymer Chain Dynamics by Fluorescence. *J. Am. Chem. Soc.* **2008**, *130*, 9420-9428.
62. Ingratta, M.; Duhamel, J. Effect of Side-Chain Length on the Side-Chain Dynamics of α -Helical Poly(L-Glutamic acid) as Probed by a Fluorescence Blob Model. *J. Phys. Chem. B* **2008**, *112*, 9209-9218.

63. Li, L.; Duhamel, J. Conformation of Pyrene-Labeled Amylose in DMSO Characterized with the Fluorescence Blob Model. *Macromolecules* **2016**, *49*, 7965-7974.
64. Farhangi, S.; Duhamel, J. Probing Side Chain Dynamics of Branched Macromolecules by Pyrene Excimer Fluorescence. *Macromolecules* **2016**, *49*, 353-361.
65. Li, L.; Kim, D.; Zhai, X.; Duhamel, J. A Pyrene Excimer Fluorescence (PEF) Study of the Interior of Amylopectin in Dilute Solution. *Macromolecules* **2020**, *53*, 6850-6860.
66. Casier, R.; Duhamel, J. Effect of Like Charges on the Conformation and Internal Dynamics of Polypeptides Probed by Pyrene Excimer Fluorescence. *Macromolecules* **2020**, *53*, 5147-5157.
67. Casier, R.; Duhamel, J. Effect of Structure on Polypeptide Blobs: A model Study Using Poly(L-lysine). *Langmuir* **2020**, *36*, 7980-7990.
68. Casier, R.; Duhamel, J. Pyrene Excimer Formation (PEF) and its Application to the Study of Polypeptide Dynamics. *Langmuir* **2022**, *38*, 3623-3629.
69. Kim, D.; Duhamel, J. Interior of Glycogen Probed by Pyrene Excimer Fluorescence. *Carbohydr. Polym.* **2023**, *299*, 1-7.
70. Patel, S.; Duhamel, J. Extending the Range of Distances Used to Characterize the Conformation of Macromolecules by Pyrene Excimer Formation: Application the Conformation of Poly(L-glutamic acid) in Dimethyl Sulfoxide. Unpublished results.
71. Blank, D.; Janiak, C. Metal Catalysts for the Vinyl/Addition Polymerization of Norbornene. *Coord. Chem. Rev.* **2009**, *253*, 827-861.
72. Janiak, C.; Lassahn, P. Metal Catalysts for the Vinyl Polymerization of Norbornene. *J. Mol. Catal. A Chem.* **2001**, *166*, 193-209.

73. Bykov, V.; Butenko, T. Composition and Microstructure of Norbornene-Ethylene Copolymers. *Polym. Sci. Ser. B* **2018**, *60*, 754-759.
74. Mi, X.; Ma, Z.; Cui, N.; Wang, L. Ke, Y. Hu, Y. Vinyl Polymerization of Norbornene with Dinuclear Diimine Nickel Dichloride/MAO. *J. Appl. Polym.* **2003**, *88*, 3273-3278.
75. Hassan, T.; Ikeda, T.; Shiono, T. Highly Efficient Ti-Based Catalyst Systems for Vinyl Addition Polymerization of Norbornene. *Macromolecules* **2004**, *37*, 7432-7436.
76. Wang, X.; Jeong, Y.; Love, C.; Stretz, H.; Stein, G.; Long, B. Design, synthesis, and Characterization of Vinyl Addition Polynorbornenes with Tunable Thermal Properties. *Poly. Chem.* **2021**, *12*, 5831-5841.
77. Porri, L.; Scalera, V.; Bagatti, M.; Famulari, A.; Meille, S. Titanium-Catalyzed Norbornene Oligomerization Isolation of a Crystalline Heptamer with a 2,3-*exo*-Disyndiotactic Structure. *Macromol. Rapid Commun.* **2006**, *27*, 1937-1941.
78. Kaita, S.; Matsushita, K.; Tobita, M.; Maruyama, Y. Wakatsuki, Y. Cyclopentadienyl Nickel and Palladium Complexes/Activator System for the Vinyl-Type Copolymerization of Norbornene with Norbornene Carboxylic acid Esters: Control of Polymer Solubility and Glass Transition Temperature. *Macromol. Rapid Commun.* **2006**, *27*, 1752-1756.
79. Yilmaz, S. S.; Abbasoglu, R.; Hazer, B. A Molecular Mechanics and Semiempirical Molecular Orbital Study on the Conformation of Polynorbornene Chains. *J. Mol. Model* **2003**, *9*, 230-234.
80. Wang, X.; Wilson, T. J.; Alentiev, D.; Gringolts, M.; Finkelshtein, E.; Bermeshev, M.; Long, B. K. Substituted Polynorbornene Membranes: A Modular Template for Targeted Gas Separations. *Polymer Chemistry* **2021**, *12*, 2947-2977.

81. Liaw, D.-J.; Wang, K.-L.; Chen, W.-H. Syntheses of Novel Polynorbornene Derivatives via Ring Opening Metathesis Polymerization. *Macromol. Symp.* **2006**, *245-246*, 68-76.
82. Commarieu, B.; Potier, J.; Compaore, M.; Boever, R.; Imbeault, R.; Claverie, J. A Simple and Efficient Protocol for the Catalytic Insertion Polymerization of Function Norbornenes. *J. Vis. Exp.* **2017**, *120*, 1-6.
83. Potier, J.; Commarieu, B.; Soldera, A.; Claverie, J. P. Thermodynamic Control in the Catalytic Insertion Polymerization of Norbornenes as Rationale for the Lack of Reactivity of Endo-Substituted Norbornenes. *ACS Catal.* **2018**, *8*, 6047–6054.
84. Buono, A.; Famulari, A.; Meille, S.; Ricci, G.; Porri, L. 2,3-exo-Diyndiotactic Polynorbornene: A Crystalline Polymer with Tubular Helical Molecular Structure. *Macromolecules* **2011**, *44*, 3681-3684.
85. Porri, L.; Scalera, V.; Bagatti, M.; Famulari, A.; Meille, S. Titanium-Catalyzed Norbornene Oligomerization. Isolation of a Crystalline Heptamer with a 2,3-exo-Disyndiotactic Structure. *Macromol. Rapid Commun.* **2006**, *27*, 1937-1941.
86. Ge, Y.; Wen, Y.; Liu, H.; Lu, T.; Yu, Y.; Zhang, X.; Li, B.; Zhang, S-T.; Li, W.; Yang, B. A Key Stacking Factor for the Effective Formation of Pyrene Excimer Crystals: Degree of π - π Overlap. *J. Mater. Chem. C.* **2020**, *8*, 11830-11838.

Chapter 6

1. McNelles, S. A.; Thoma, J. L.; Adronov, A.; Duhamel, J. Quantitative Characterization of the Molecular Dimensions of Flexible Dendritic Macromolecules in Solution by Pyrene Excimer Fluorescence. *Macromolecules* **2018**, *51*, 1586–1590.
2. Thoma, J.; McNelles, S. A.; Adronov, A.; Duhamel, J. Direct Measure of the Local Concentration of Pyrenyl Groups in Pyrene-Labeled Dendrons Derived from the Rate of Fluorescence Collisional Quenching. *Polymers* **2020**, *12*, 2919.
3. Maiti, P. K.; Çağın, T.; Wang, G.; Goddard, W. A. Structure of PAMAM Dendrimers: Generations 1 through 11. *Macromolecules* **2004**, *37*, 6236– 6254.
4. Prosa, T. J.; Bauer, B. J.; Amis, E. J.; Tomalia, D. A.; Scherrenberg, R. A SAXS Study of the Internal Structure of Dendritic Polymer Systems. *J. Polym. Sci., Part B: Polym. Phys.* **1997**, *35*, 2913– 2924.
5. Nisato, G.; Ivkov, R.; Amis, A. J. Structure of Charged Dendrimer Solutions as Seen by Small Angle Neutron Scattering. *Macromolecules* **1999**, *32*, 5895– 5900.
6. Chen, W.-R.; Porcar, L.; Liu, Y.; Butler, P. D.; Magid, L. J. Small Angle Neutron Scattering Studies of the Counterion Effects on the Molecular Conformation and Structure of Charged G4 PAMAM Dendrimers in Aqueous Solutions. *Macromolecules* **2007**, *40*, 5887– 5898.
7. Porcar, L.; Hong, K.; Butler, P. D.; Herwig, K. W.; Smith, G. S.; Liu, Y.; Chen, W.-R. Intramolecular Structural Change of PAMAM Dendrimers in Aqueous Solutions Revealed by Small-Angle Neutron Scattering. *J. Phys. Chem. B* **2010**, *114*, 1751-1756.
8. Liu, Y.; Chen, Y.-C.; Chen, L.-H.; Hong, K.; Shew, Y.-C.; Li, X.; Liu, L.; Melnichenko, Y.; Smith, G. Electrostatic Swelling and Conformational Variation Observed in High-Generation Polyelectrolyte Dendrimers. *J. Phys. Chem. Lett.* **2010**, *1*, 2020– 2024.

9. Maiti, P.; Cagin, T.; Lin, S.-T.; Goddard, W. Effect of Solvent and pH on the Structure of PAMAM Dendrimers. *Macromolecules* **2005**, *38*, 979–991.
10. Patel, S.; Duhamel, J. Macromolecular Conformation of Low-Generation PAMAM Dendrimers Probed by Pyrene Excimer Formation. *Macromolecules* **2023**, *56*, 4012-4021.
11. Intramacromolecular Conformational Changes in Low Generation PAMAM dendrimers Probed by Pyrene Excimer Formation. *J. Chem. B* **2023**, *127*, 8040-8048.

S2-References

1. So, H.; Lee, J.; Han, S. Y.; Oh, H. bin. MALDI In-Source Decay Mass Spectrometry of Polyamidoamine Dendrimers. *J. Am. Soc. Mass Spectrom.* **2012**, *23*, 1821–1825.
2. Subbi, J.; Agurauja, R., Tanner, R.; Allikmaa, V.; Lopp, M. Fragmentation of Poly(amidoamine) Dendrimers in Matrix-Assisted Laser Desorption. *Eur. Polym. J.* **2005**, *41*, 2552-2558.
3. Asakawa, D. General Mechanism of C α -C Peptide Backbone Bond Cleavage in Matrix-Assisted Laser Desorption/Ionization In-Source Decay Mediated by Hydrogen Abstraction. *J. Am. Soc. Mass Spectrom.* **2019**, *30*, 1491–1502.
4. Leipert, J.; Treitz, C.; Leippe, M.; Tholey, A. Identification and Quantification of N-Acyl Homoserine Lactones Involved in Bacterial Communication by Small-Scale Synthesis of Internal Standards and Matrix-Assisted Laser Desorption/Ionization Mass Spectrometry. *J. Am. Soc. Mass Spectrom.* **2017**, *28*, 2538–2547.
5. Hagan, N. A.; Smith, C. A.; Antoine, M. D.; Lin, J. S.; Feldman, A. B.; Demirev, P. A. Enhanced In-Source Fragmentation in MALDI-TOF-MS of Oligonucleotides Using 1,5-Diaminonaphthalene. *J. Am. Soc. Mass Spectrom.* **2012**, *23*, 773–777.

6. Demeure, K.; Gabelica, V.; de Pauw, E. A. New Advances in the Understanding of the In-Source Decay Fragmentation of Peptides in MALDI-TOF-MS. *J. Am. Soc. Mass Spectrom.* **2010**, *21*, 1906–1917.
7. Liu, Z.; Schey, K. L. Fragmentation of Multiply-Charged Intact Protein Ions Using MALDI TOF-TOF Mass Spectrometry. *J. Am. Soc. Mass Spectrom.* **2008**, *19*, 231–238.
8. Wang, B. B.; Zhang, X.; Jia, X. R.; Li, Z. C.; Ji, Y.; Yang, L.; Wei, Y. Fluorescence and Aggregation Behavior of Poly(Amidoamine) Dendrimers Peripherally Modified with Aromatic Chromophores: The Effect of Dendritic Architectures. *J. Am. Chem. Soc.* **2004**, *126*, 15180–15194.
9. Liu, Y.; Chiu, G. N. C. Dual-Functionalized PAMAM Dendrimers with Improved P-Glycoprotein Inhibition and Tight Junction Modulating Effect. *Biomacromolecules* **2013**, *14*, 4226–4235.
10. Sk, U. H.; Hira, S. K.; Rej, A.; Roymahapatra, D.; Manna, P. P. Development of a PAMAM Dendrimer for Sustained Release of Temozolomide against Experimental Murine Lymphoma: Assessment of Therapeutic Efficacy. *ACS Appl. Bio. Mater.* **2021**, *4*, 2628–2638.
11. Liu, H.; Tørring, T.; Dong, M.; Rosen, C. B.; Besenbacher, F.; Gothelf, K. v. DNA-Templated Covalent Coupling of G4 PAMAM Dendrimers. *J. Am. Chem. Soc.* **2010**, *132*, 18054–18056.
12. Svenningsen, S. W.; Janaszewska, A.; Ficker, M.; Petersen, J. F.; Klajnert-Maculewicz, B.; Christensen, J. B. Two for the Price of One: PAMAM-Dendrimers with Mixed Phosphoryl Choline and Oligomeric Poly(Caprolactone) Surfaces. *Bioconjug. Chem.* **2016**, *27*, 1547–1557.

13. Bono, N.; Pennetta, C.; Bellucci, M. C.; Sganappa, A.; Malloggi, C.; Tedeschi, G.; Candiani, G.; Volonterio, A. Role of Generation on Successful DNA Delivery of PAMAM-(Guanidino)Neomycin Conjugates. *ACS Omega* **2019**, *4*, 6796–6807.
14. Yamashita, S.; Katsumi, H.; Sakane, T.; Yamamoto, A. Phosphorylated Serine-Modified Polyamidoamine Dendrimer as an Osteoid Surface-Targeting Drug Carrier. *Mol. Pharm.* **2022**, *19*, 2573–2582.
15. Tosh, D. K.; Yoo, L. S.; Chinn, M.; Hong, K.; Kilbey, S. M.; Barrett, M. O.; Fricks, I. P.; Harden, T. K.; Gao, Z. G.; Jacobson, K. A. Polyamidoamine (PAMAM) Dendrimer Conjugates of “Clickable” Agonists of the A3 Adenosine Receptor and Coactivation of the P2Y14 Receptor by a Tethered Nucleotide. *Bioconjug. Chem.* **2010**, *21*, 372–384.
16. Waite, C. L.; Roth, C. M. PAMAM-RGD Conjugates Enhance SiRNA Delivery through a Multicellular Spheroid Model of Malignant Glioma. *Bioconjug. Chem.* **2009**, *20*, 1908–1916.
17. Sk, U. H.; Kambhampati, S. P.; Mishra, M. K.; Lesniak, W. G.; Zhang, F.; Kannan, R. M. Enhancing the Efficacy of Ara-C through Conjugation with PAMAM Dendrimer and Linear PEG: A Comparative Study. *Biomacromolecules* **2013**, *14*, 801–810.
18. Rodrigo, A. C.; Rivilla, I.; Perez-Martinez, F. C.; Monteagudo, S.; Ocana, V.; Guerra, J.; Garcia-Martinez, J. C.; Merino, S.; Sanchez-Verdu, P.; Cena, V.; Rodriguez-Lopez, J. Efficient, Non-Toxic Hybrid PPV-PAMAM Dendrimer as a Gene Carrier for Neuronal Cells. *Biomacromolecules* **2011**, *12*, 1205–1213.
19. Fischer-Durand, N.; Salmain, M.; Rudolf, B.; Jugé, L.; Guérineau, V.; Laprèvote, O.; Vessières, A.; Jaouen, G. Design of a New Multifunctionalized PAMAM Dendrimer with Hydrazide-Terminated Spacer Arm Suitable for Metal-Carbonyl Multilabeling of Aldehyde-Containing Molecules. *Macromolecules* **2007**, *40*, 8568–8575.

20. Zhang, X.; Zeng, Y.; Yu, T.; Chen, J.; Yang, G.; Li, Y. Tetrathiafulvalene Terminal-Decorated PAMAM Dendrimers for Triggered Release Synergistically Stimulated by Redox and CB[7]. *Langmuir* **2014**, *30*, 718–726.
21. Navath, R. S.; Kurtoglu, Y. E.; Wang, B.; Kannan, S.; Romero, R.; Kannan, R. M. Dendrimer-Drug Conjugates for Tailored Intracellular Drug Release Based on Glutathione Levels. *Bioconjug. Chem.* **2008**, *19*, 2446–2455.
22. Kim, Y.; Klutz, A. M.; Jacobson, K. A. Systematic Investigation of Polyamidoamine Dendrimers Surface-Modified with Poly(Ethylene Glycol) for Drug Delivery Applications: Synthesis, Characterization, and Evaluation of Cytotoxicity. *Bioconjug. Chem.* **2008**, *19*, 1660–1672.
23. Shi, X.; Lesniak, W.; Islam, M. T.; MuÑiz, M. C.; Balogh, L. P.; Baker, J. R. Comprehensive Characterization of Surface-Functionalized Poly(Amidoamine) Dendrimers with Acetamide, Hydroxyl, and Carboxyl Groups. *Colloids Surf. A Physicochem. Eng. Asp.* **2006**, *272*, 139–150.
24. Ghilardi, A.; Pezzoli, D.; Bellucci, M. C.; Malloggi, C.; Negri, A.; Sganappa, A.; Tedeschi, G.; Candiani, G.; Volonterio, A. Synthesis of Multifunctional PAMAM-Aminoglycoside Conjugates with Enhanced Transfection Efficiency. *Bioconjug. Chem.* **2013**, *24*, 1928–1936.
25. Kolhatkar, R. B.; Kitchens, K. M.; Swaan, P. W.; Ghandehari, H. Surface Acetylation of Polyamidoamine (PAMAM) Dendrimers Decreases Cytotoxicity While Maintaining Membrane Permeability. *Bioconjug. Chem.* **2007**, *18*, 2054–2060.
26. Stasko, N. A.; Fischer, T. H.; Schoenfisch, M. H. S-Nitrosothiol-Modified Dendrimers as Nitric Oxide Delivery Vehicles. *Biomacromolecules* **2008**, *9*, 834–841.

27. Dvornic, P. R.; Hartmann-Thompson, C.; Keinath, S. E.; Hill, E. J. Organic-Inorganic Polyamidoamine (PAMAM) Dendrimer-Polyhedral Oligosilsesquioxane (POSS) Nanohybrids. *Macromolecules* **2004**, *37*, 7818–7831.
28. Martin, H.; Kinns, H.; Mitchell, N.; Astier, Y.; Madathil, R.; Howorka, S. Nanoscale Protein Pores Modified with PAMAM Dendrimers. *J. Am. Chem. Soc.* **2007**, *129*, 9640–9649.
29. Press, W. H.; Flannery, B. P.; Teukolsky, S. A.; Vetterling, W. T. Numerical Recipes. The Art of Scientific Computing (Fortran Version); Cambridge University Press: Cambridge, p 82, 1992.

S3-References

1. Press, W. H.; Flannery, B. P.; Teukolsky, S. A.; Vetterling, W. T. Numerical Recipes. The Art of Scientific Computing (Fortran Version); Cambridge University Press: Cambridge, p 82, 1992.
2. Patel, S.; Duhamel, J. Macromolecular Conformation of Low Generation PAMAM Dendrimers Probed by Pyrene Excimer Formation. *Macromolecules*, **2023**, *56*, 4012-4021.

S4-References

1. Mathew, A.; Siu, H.; Duhamel, J. A Blob Model to Study Chain Folding by Fluorescence. *Macromolecules* **1999**, *32*, 7100-7108.
2. Ingratta, M.; Duhamel, J. Effect of Side-Chain Length on the Side-chain Dynamics of α -Helical Poly(L-glutamic acid) as Probed by a Fluorescence Blob Model. *J. Phys. Chem. B.* **2008**, *112*, 9209-9218.

3. Casier, R.; Duhamel, J. Pyrene Excimer Fluorescence as a Direct and Easy Experimental Means to Characterize the Length Scale and Internal Dynamics of Polypeptide Foldons. *Macromolecules* **2018**, *51*, 3450-3457.
4. Casier, R.; Duhamel, J. Effect of Like Charges on the Conformation and Internal Dynamics of Polypeptides Probed by Pyrene Excimer Fluorescence. *Macromolecules* **2020**, *53*, 5147-5157.
5. Ge.; Wen, Y.; Liu, H.; Lu, T.; Yu, Y.; Zhang, X.; Li, B.; Zhang, S-T.; Li, W.; Yang, B. A Key Stacking Factor for the Effective Formation of Pyrene Excimer in Crystals: Degree of π - π overlap. *J. Mater. Chem. C* **2020**, *8*, 11830-11838.

Appendix: Supporting Information (SI)

Appendix A: 2-SI for Chapter 2

A) Characterization of the pyrene derivatives by ^1H NMR and UV-Vis analysis

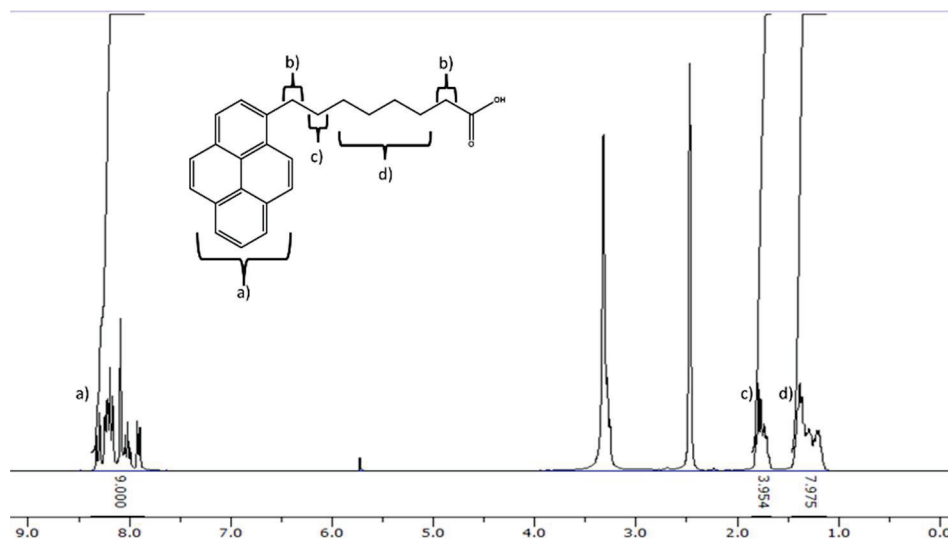


Figure S2.1. ^1H -NMR spectrum of 1-pyreneoctanoic acid in d_6 -DMSO (300 MHz): δ 1.47-1.13 (m, 8H), 1.85-1.67 (m, 4H), 8.38-7.86 (m, 9H). Protons b) are under the water peak (3.3 ppm).

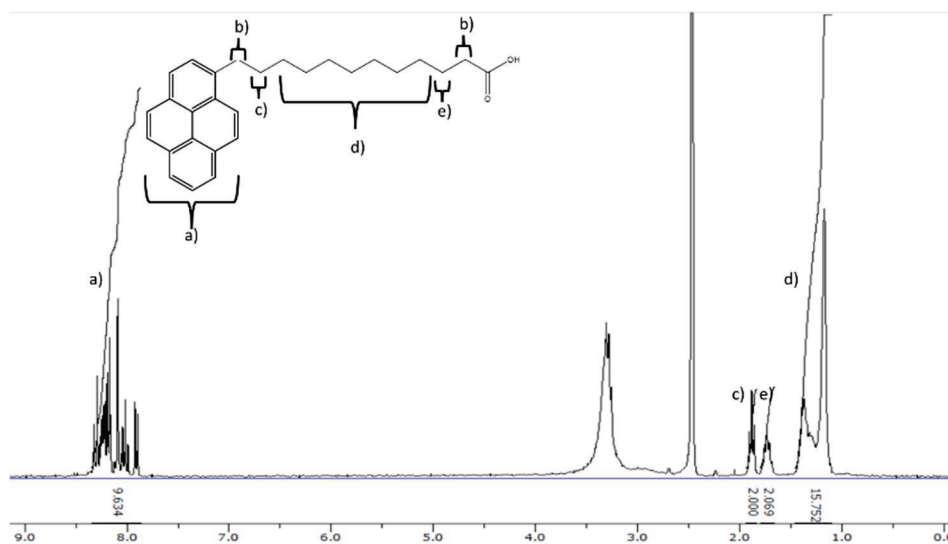


Figure S2.2. ^1H -NMR spectrum of 1-pyrenedodecanoic acid in $\text{DMSO-}d_6$: (300 MHz, DMSO): δ 1.47-1.09 (m, 16H), 1.80-1.67 (m, 2H), 1.84 – 1.94 (t, 2H), 8.35-7.87 (m, 9.6H). Protons b) are under the water peak (3.3 ppm).

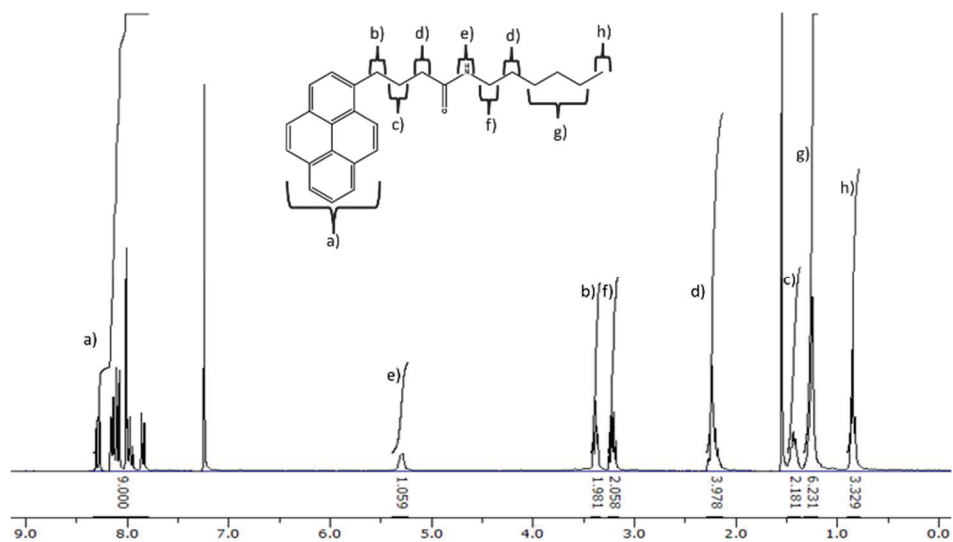


Figure S2.3. ¹H NMR spectrum of hexyl-1-pyrenebutyramide in CDCl₃ (300 MHz): δ 0.85 (t, 3H), 1.33-1.19 (m, 6H), 1.49-1.37 (, 2H), 2.29-2.13 (m, 4H), 3.26-3.16 (q, 2H), 3.43-3.34 (t, 2H), 5.39-5.24 (broad singlet, 1H), 8.33-7.80 (m, 9H).

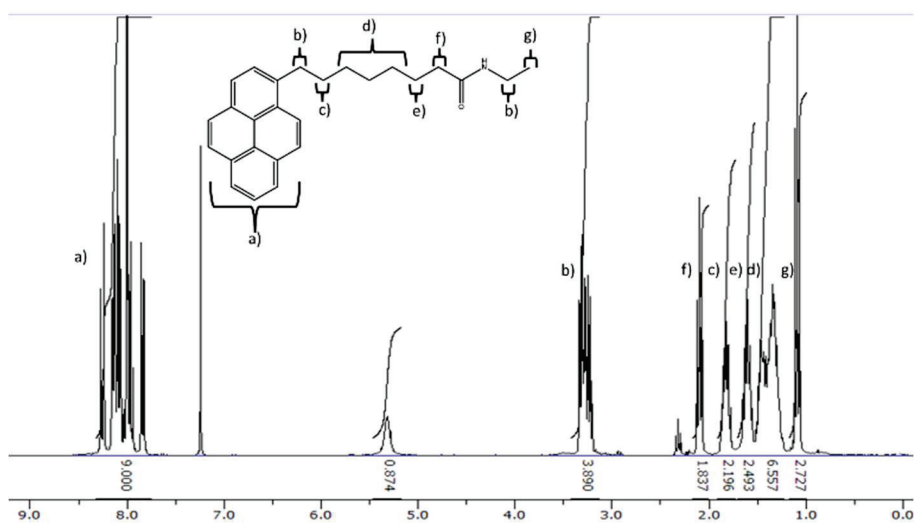


Figure S2.4. ¹H NMR spectrum of ethyl-1-pyreneoctanamide in CDCl₃ (300 MHz): δ 1.089 (t, 3H), 1.52-1.23 (m, 6.6H), 1.53 -1.71 (p, 2.5H), 1.91-1.73 (p, 5H), 2.17-2.01 (t, 2H), 3.42-3.13 (m, 4H), 5.47-5.18 (broad s, 1H), 8.32-7.75 (M, 9H)

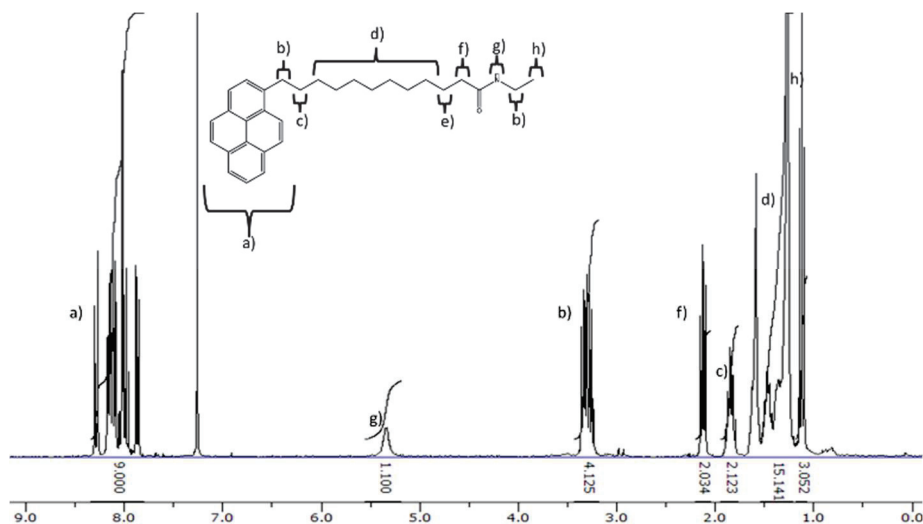


Figure S2.5. ^1H NMR spectrum of *n*-ethyl-1-pyrenedodecanamide in CDCl_3 (300 MHz): δ 1.08-1.16 (t, 3H), 1.19- 1.41 (m, 15), 1.78-2.18 (p, 2H), 2.07-2.18 (t, 2H), 3.21-3.39 (m, 4H), 5.24-5.44 (broad s, 1H), 7.83-8.33 (m, 9H). Protons e) are underneath the water peak in CDCl_3 .

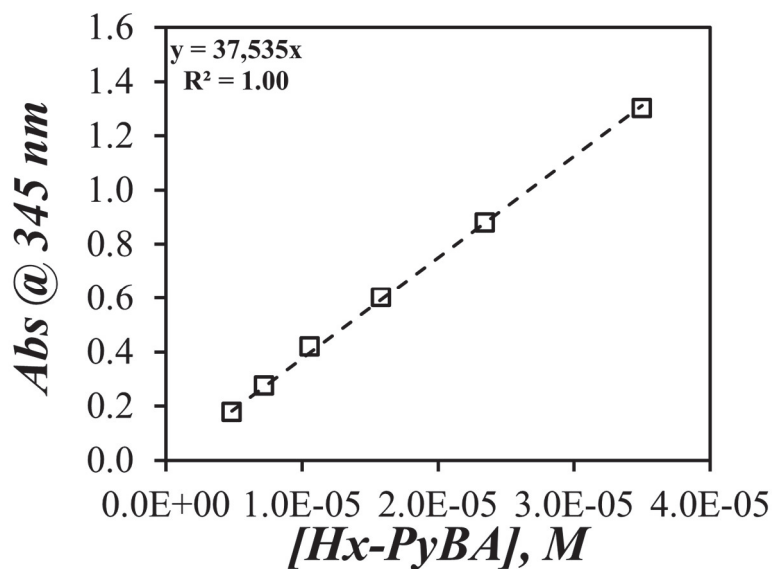


Figure S2.6. Plot of absorbance as a function of the concentration of hexyl-1-pyrenebutyramide (Hx-PyBA) in DMF.

B] ¹H NMR characterization of the PyCX-PAMAM-GY dendrimers

All ¹H NMR spectra were acquired on a Bruker 300 MHz NMR spectrometer. For each NMR spectrum, the number of pyrenes per dendrimer ($N_{\text{Py/Den}}$) was calculated with Equation S2.1 or Equation S2.2 for the PyC4-PAMAM-GY and PyC8-PAMAM-GY or PyC12-PAMAM-GY constructs, respectively. The difference between Equation S1 and S2 is due to the merging of the ¹H NMR signal in the 3.15 – 3.44 ppm region arising from the methylene protons adjacent to pyrene and the methylene protons adjacent to the nitrogen in the amide bonds for the spectra acquired in CDCl₃, which is the solvent used to acquire the ¹H NMR spectra of the PyC12-PAMAM-GY samples. In *d*₆-DMSO, the signals are separated and could be integrated separately. Also of note, the signal of the amide protons appeared together with the pyrene protons in the ¹H NMR spectra acquired in *d*₆-DMSO but not in CDCl₃. The calculation for a PyC4-PAMAM-G0 construct in DMSO using Equation S1 is presented as an example. The integral of the ¹H NMR signal between 7.73 and 8.52 ppm corresponding to the number of ($N_{\text{Py/Den}}$) pyrene and ($N_{\text{amide/Den}}$) amide protons per dendrimers multiplied by their respective number of protons was divided by the integral of the ¹H NMR signal between 3.06 and 3.20 ppm corresponding to the number ($N_{\text{CH}_2/\text{Den}}$) of methylene protons adjacent to the nitrogen of each amide bond multiplied by 2 as shown in Figure S7, to yield the ratio (R). Rearrangement of R yielded $N_{\text{Py/Den}}$ whose expression is given in Equation S1. An $N_{\text{Py/Den}}$ value of 4.0 pyrenes per dendrimer was obtained for the PyC4-PAMAM-G0 sample. The experimentally determined and expected $N_{\text{Py/Den}}$ values are listed in Table 1 and were found to agree within 5% error from each other suggesting that the PyCX-PAMAM-GY samples used in this study were fully labeled.

$$N_{\text{Py/Den}} = \frac{R \times N_{\text{CH}_2/\text{Den}} \times 2H - N_{\text{amide/Den}} \times 1H}{9H} \quad (\text{S2.1})$$

$$N_{Py/Den} = \frac{R \times (N_{CH_2/Den} + N_{CH_2-Py}) \times 2H}{9H} \quad (S2.2)$$

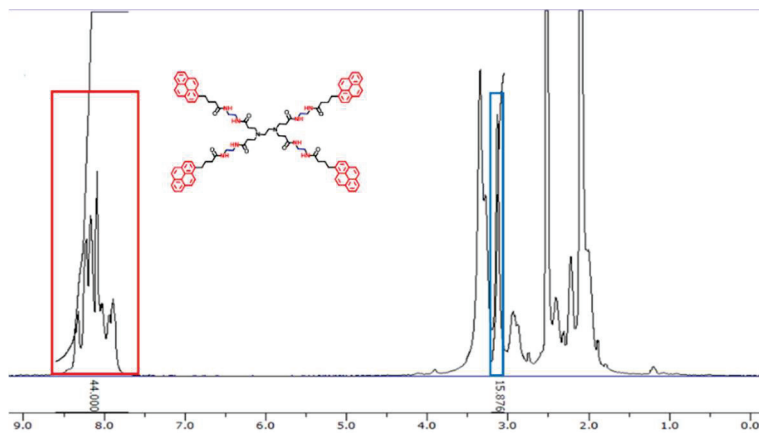


Figure S2.7. ^1H NMR spectrum of PAMAM-G0 labeled with 1-pyrene butyric acid in d_6 -DMSO.

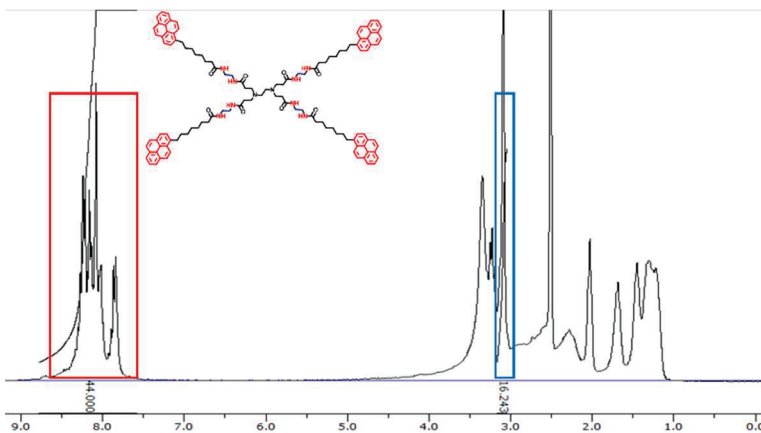


Figure S2.8. ^1H NMR spectrum of PAMAM-G0 labeled with 1-pyrene octanoic acid in d_6 -DMSO.

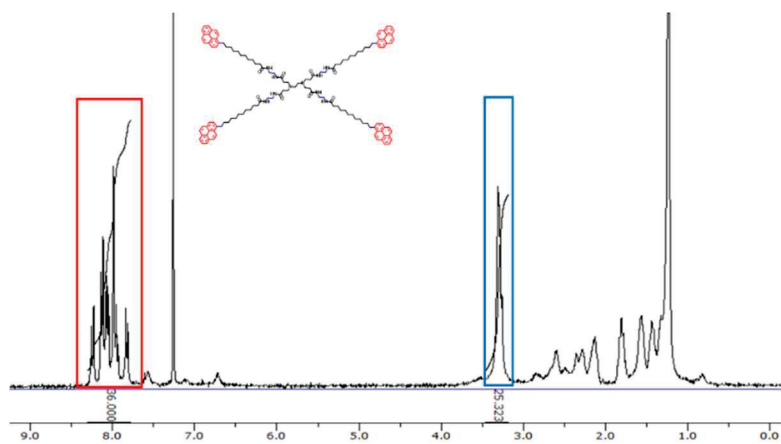


Figure S2.9. ^1H NMR spectrum of PAMAM-G0 labeled with 1-pyrene dodecanoic acid in CDCl_3 .

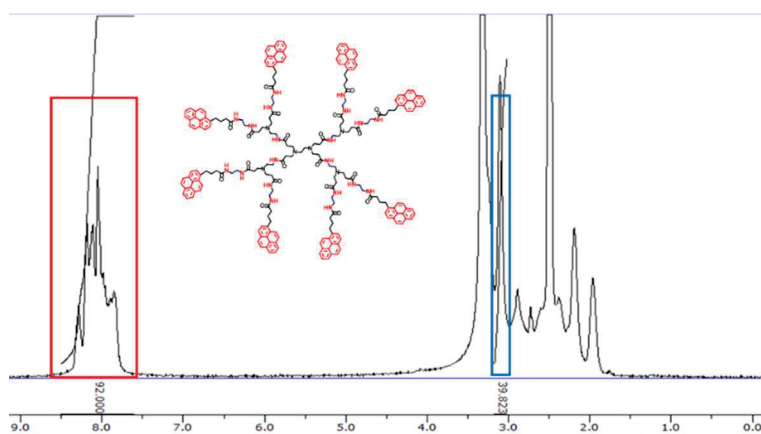


Figure S2.10. ^1H NMR spectrum of PAMAM-G1 labeled with 1-pyrene butyric acid in d_6 -DMSO.

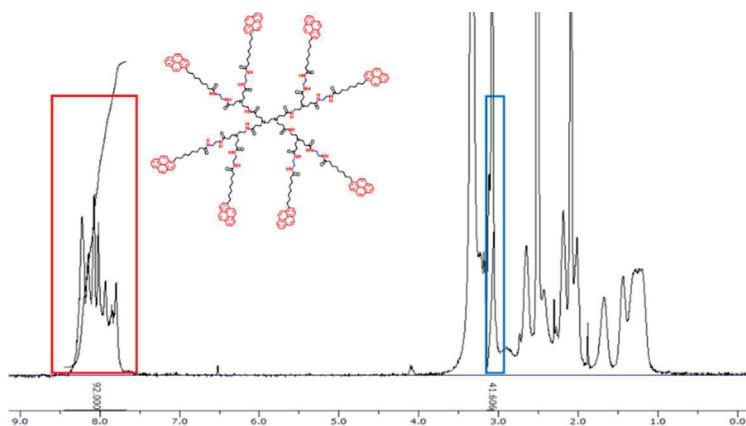


Figure S2.11. ^1H NMR spectrum of PAMAM-G1 labeled with 1-pyrene octanoic acid in d_6 -DMSO.

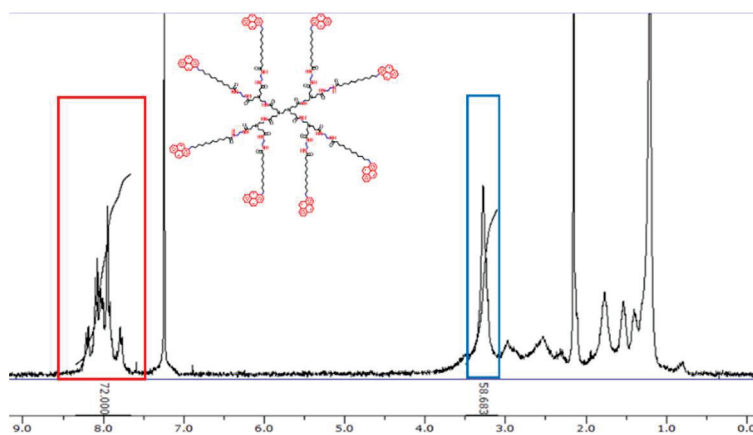


Figure S2.12. ^1H NMR spectrum of PAMAM-G1 labeled with 1-pyrene dodecanoic acid in CDCl_3 .

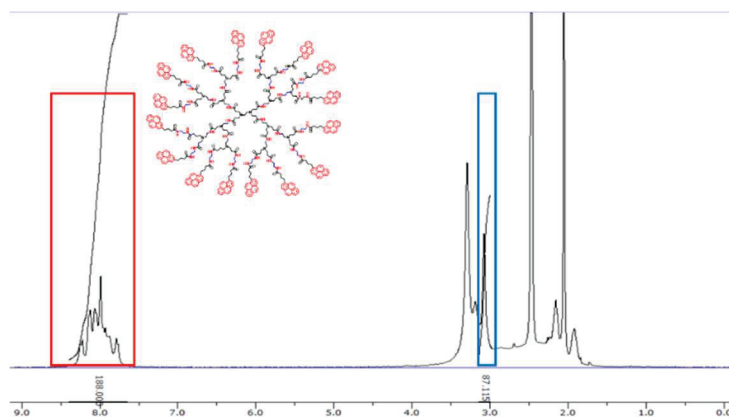


Figure S2.13. ^1H NMR spectrum of PAMAM-G2 labeled with 1-pyrene butyric acid in d_6 -DMSO.

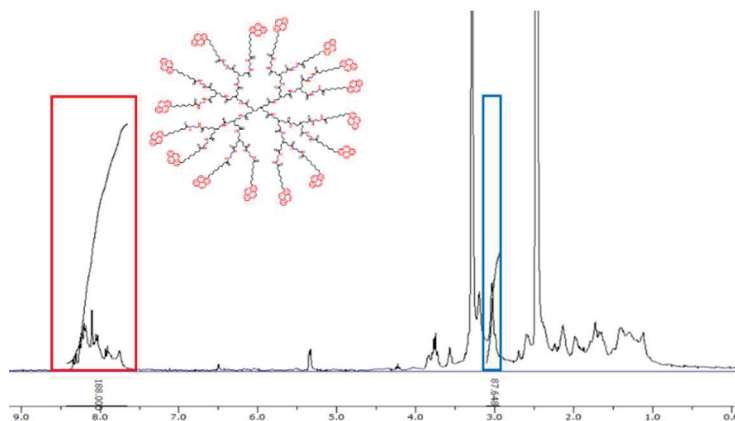


Figure S2.14. ^1H NMR spectrum of PAMAM-G2 labeled with 1-pyrene octanoic acid in d_6 -DMSO.

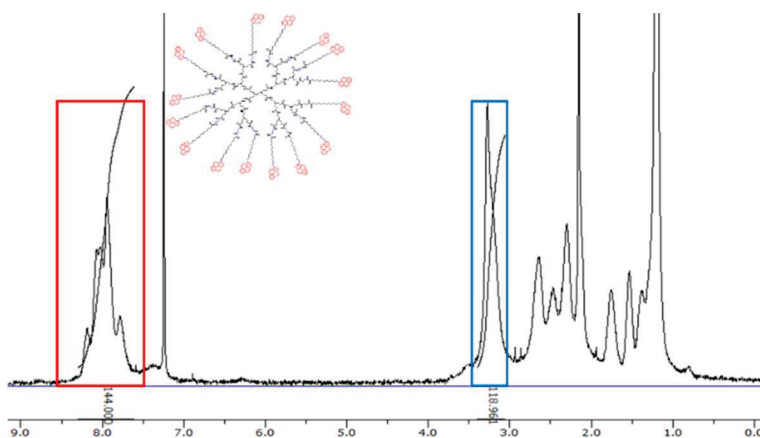


Figure S2.15. ^1H NMR of PAMAM-G2 labeled with 1-pyrene dodecanoic acid in CDCl_3 .

C] Characterization of the PyCX-PAMAM-GY dendrimers by Mass Spectrometry (MS)

The mass spectra for all PyCX-PAMAM samples were acquired on a Bruker Autoflex Speed MALDI in reflectron mode with the exception of PyC8-PAMAM-G2, whose mass spectrum was acquired in the linear mode. The mass spectrum of PyC12-PAMAM-G2 could not be acquired due to difficulties associated with desorption/ionization of the sample, despite numerous attempts made using higher concentrations and different matrices along with cationization agents. All other PyCX-PAMAM-GY samples were prepared at a concentration of 20 μM in tetrahydrofuran

containing 0.5 wt% DMSO. An aliquot (2 μ L) of the freshly prepared solution was diluted with 2 μ L of a saturated solution of 2,5-dihydroxybenzoic acid in a mixture of acetonitrile (50%), water (50%), and TFA (0.1 %). The mixture was vortexed for 30 seconds, followed by spotting 1 μ L, in duplicates, onto the grounded stainless-steel plate. For lower molecular weight samples (< 3 kg/mol), the MALDI-TOF spectra were calibrated using red phosphorous while higher molecular weight samples (> 3 kg/mol) were calibrated using protein standards ranging from 3 to 12 kg/mol. The MALDI-TOF spectra for the samples typically contained several peaks, which, at first glance, would suggest that the PAMAM dendrimers were partially labeled. However, similarly complex mass spectra have been reported for poly- or oligo-amides¹⁻⁷ and modified PAMAM dendrimers.⁸⁻²⁸ Consequently, a more detailed discussion of their analysis is presented hereafter to demonstrate that despite the apparently complex mass spectra, the constructs used in this study were likely to be fully labeled.

First, none of the characteristic peaks corresponding to a partially pyrene-labeled PyCX-PAMAM-GY sample was found in any of the mass spectra but all mass spectra yielded a peak corresponding to the fully labeled PyCX-PAMAM-GY sample. This observation suggested that the PyCX-PAMAM-GY samples were fully labeled and that the peaks with a smaller m/z ratio may have been the result of fragmentation. The spectra obtained for the PyC4-PAMAM-GY samples shown in Figures S16, S19, and S22 exhibited a higher intensity peak for the parent molecule relative to the peaks observed at lower m/z ratios. Second, the extent of additional peaks observed in each spectrum of the PyC4-PAMAM-GY samples was found to be significantly less compared to the PyC8-PAMAM-GY (Figure S17, S20, and S23) and PyC12-PAMAM-GY (Figure S18 and S21) samples. Although the signal intensity observed by MALDI-TOF is not indicative of the concentration of the respective species, the consistently larger number and

intensity of the additional peaks suggest that the longer linker used to attach the 1-pyrene-octanoyl and -dodecanoyl units to the PAMAM dendrimers may play a role in the sample fragmentation. The longer linkers may afford sufficient length for the pyrenyl groups to come near the amide bond. The ability of the pyrenyl groups to absorb the 355 nm photon emitted by the laser used in the MALDI-TOF experiments might be related to the occurrence of a fragmentation event. In most samples, the fragments observed were consistent with the cleavage between the $-CH_2-$ and $C=O$ adjacent to the amide bond of the linker connecting the pyrenyl label to the PAMAM dendrimers. An example of the fragmentation and the associated molecular weights for the different PyCX-PAMAM-G0 dendrimers is given in Figure S16. This cleavage pattern suggested that the pyrenyl groups were covalently attached onto the PAMAM-GY samples prior to fragmentation, thereby further suggesting that the PyCX-PAMAM-GY samples used in this study were fully labeled. The cleavage between $-CH_2-$ and the carbonyl group adjacent to an amide bond would yield an acylium ion, which has been reported in other MALDI-TOF spectra⁴ as well as for pyrene-labeled PAMAM dendrimers.⁸ All MALDI-TOF spectra along with the identified fragment peaks are provided as Figures S17 – S24. Given the absence of peaks corresponding to partially labeled PyCX-PAMAM-GY samples in the MALDI-TOF spectra and with support of the number of pyrenes per dendrimer determined from the ¹H NMR spectra, it was concluded that the PyCX-PAMAM-GY samples studied in this work were likely to be fully labeled.

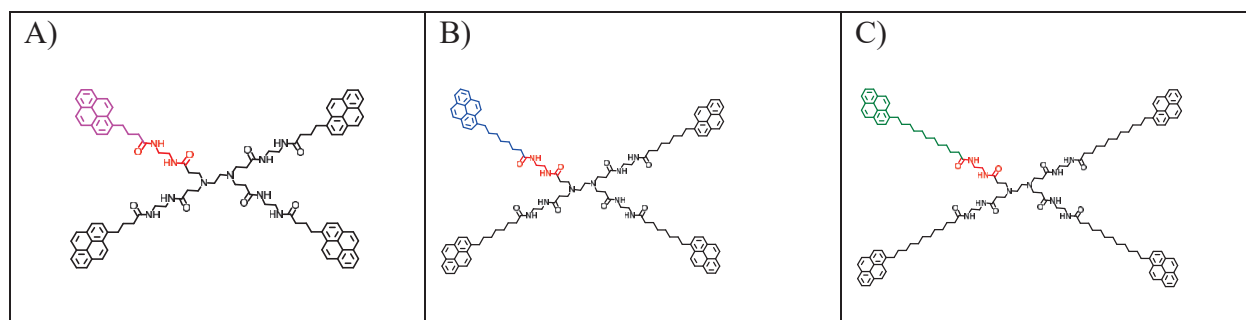


Figure S2.16. An example of the typical fragmentation pattern observed for PAMAM-G0 dendrimers labeled with A) 1-pyrenebutyric, B) 1-pyreneoctanoic and C) 1-pyrenedodecanoic acid. The fragments shown in purple, blue, and green have molecular weights of 244.3, 300.5, and 356.6 g/mol, respectively, which are associated with the fragmentation involved in the removal of a pyrenyl label, whereas the fragment shown in red corresponds to a molecular weight of 116.1 g/mol and is associated with the fragmentation event within the dendrimer.

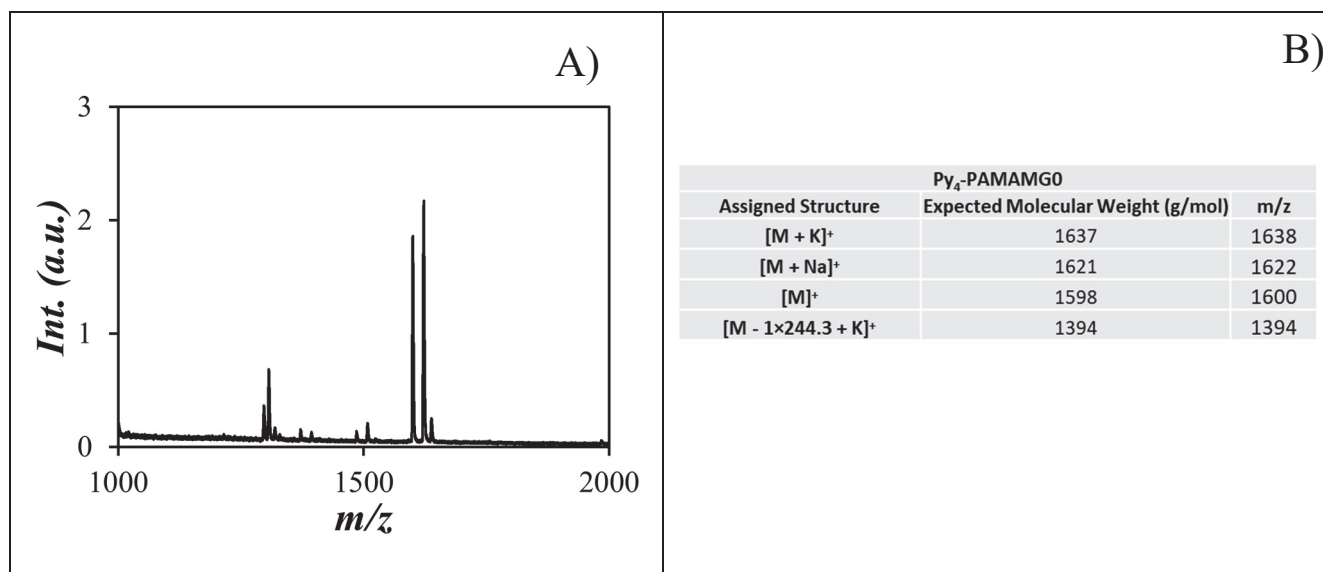


Figure S2.17. A) Mass spectrum of PAMAM-G0 labeled with 1-pyrenebutyric acid and B) table of m/z ratios for the main species found in the mass spectrum. No m/z peak was observed at 1328 and 1057 g/mol corresponding to PAMAM-G0 labeled with 3 and 2 1-pyrenebutyryl groups.

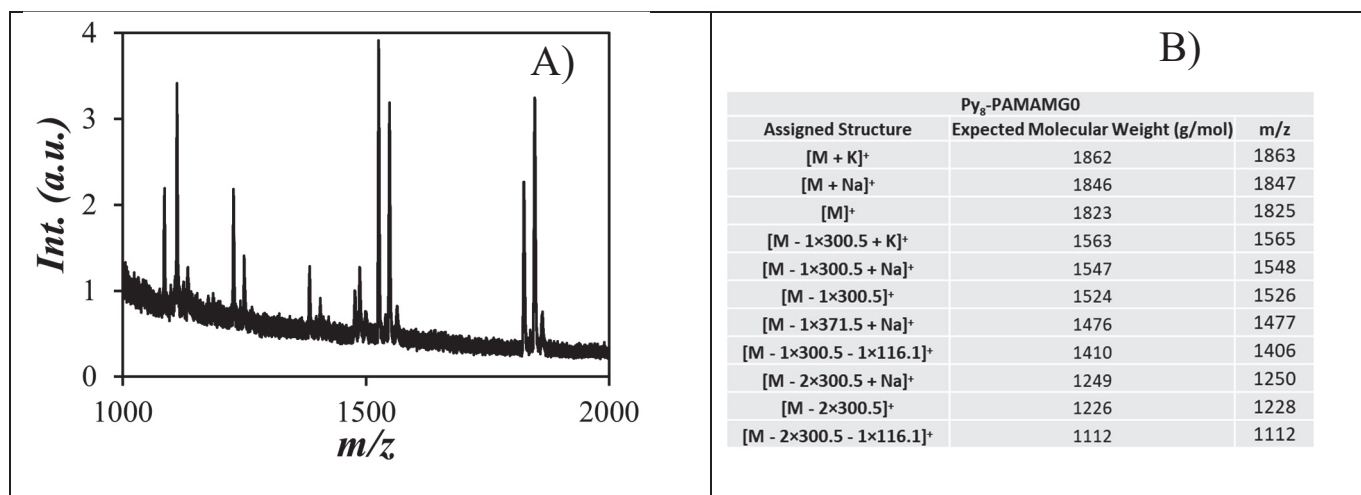


Figure S2.18. A) Mass spectrum of PAMAM-G0 labeled with 1-pyreneoctanoic acid and B) table of the m/z ratios of the main species found in the mass spectrum. No m/z peak was observed at 1496 and 1170 g/mol corresponding to PAMAM-G0 labeled with 3 and 2 1-pyreneoctanoyl groups.

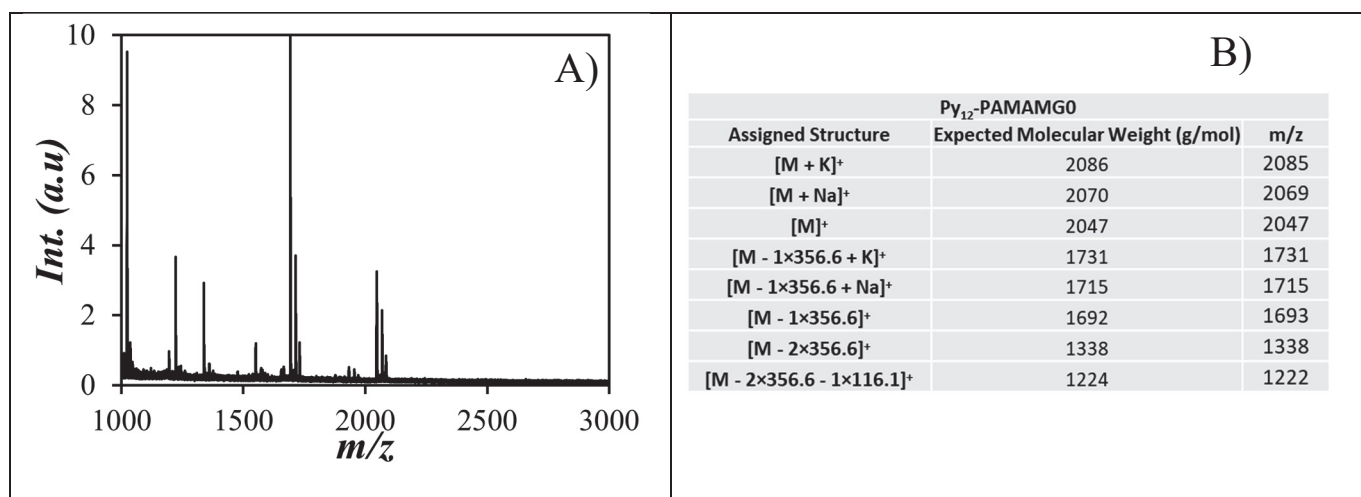


Figure S2.19. A) Mass spectrum of PAMAM-G0 labeled with 1-pyrenedodecanoic acid and B) table of the m/z ratios for the main species found in the mass spectrum. No m/z peak was observed at 1664 and 1282 g/mol corresponding to PAMAM-G0 labeled with 3 and 2 1-pyrenedodecanoyl groups.

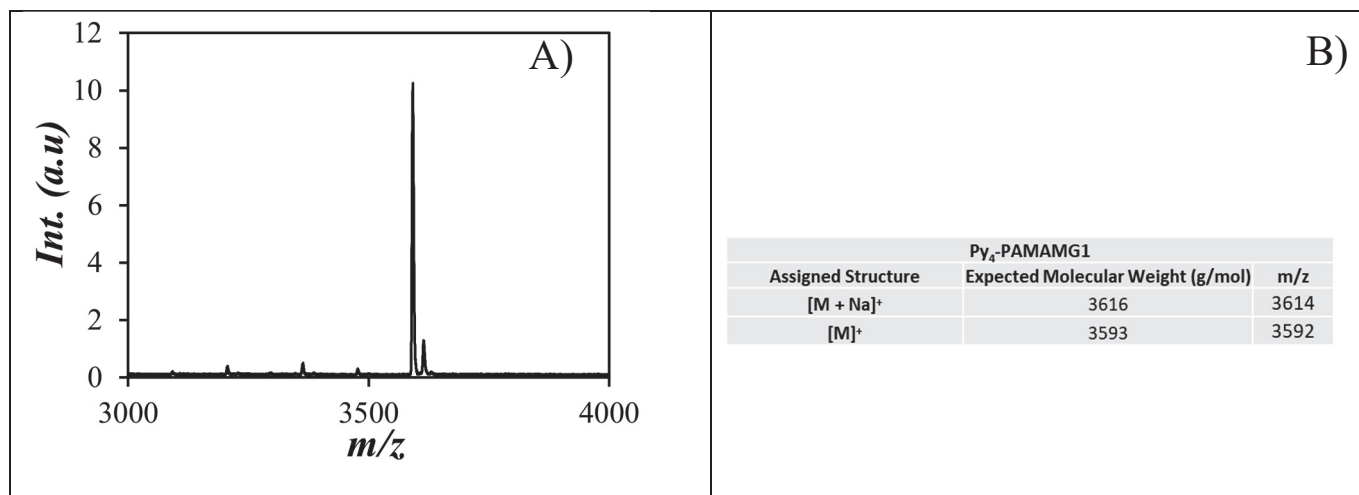


Figure S2.20. A) Mass spectrum of PAMAM-G1 labeled with 1-pyrenebutyric acid and B) table of the m/z ratios of the main species found in the mass spectrum. No m/z peak was observed at 3322 and 3052 g/mol corresponding to PAMAM-G1 labeled with 3 and 2 pyrenyl groups.

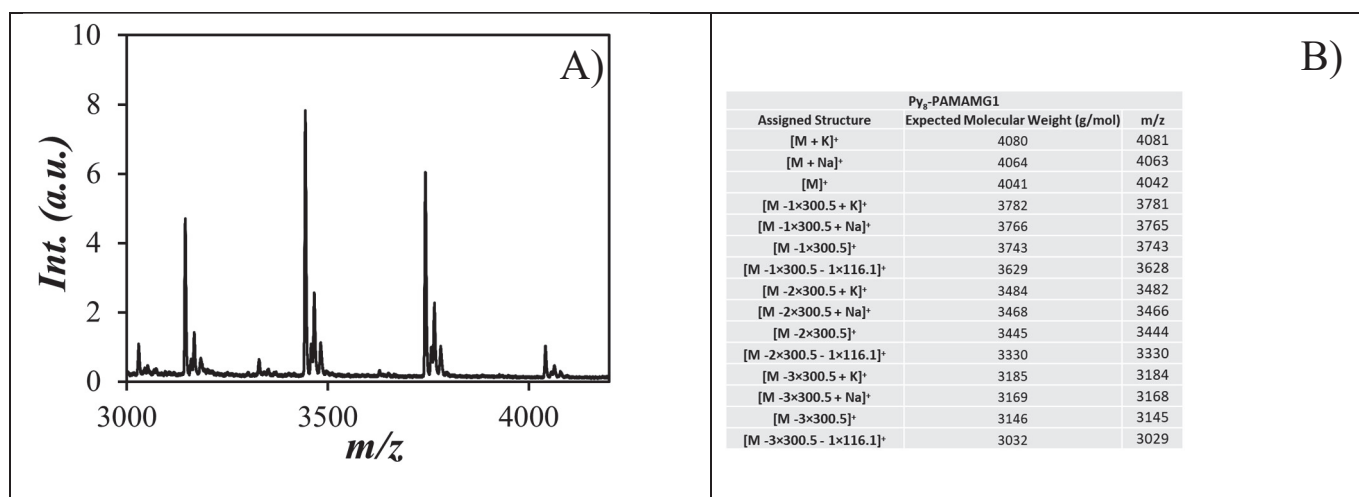


Figure S2.21. A) Mass spectrum for PAMAM-G1 labeled with 1-pyreneoctanoic acid and B) table of the m/z ratio for the main species found in the mass spectrum. No m/z peak was observed at 3714.95, 3388.5, and 3062.07 g/mol corresponding to PAMAM-G1 labeled with 7, 6, and 5 1-pyreneoctanoyl groups.

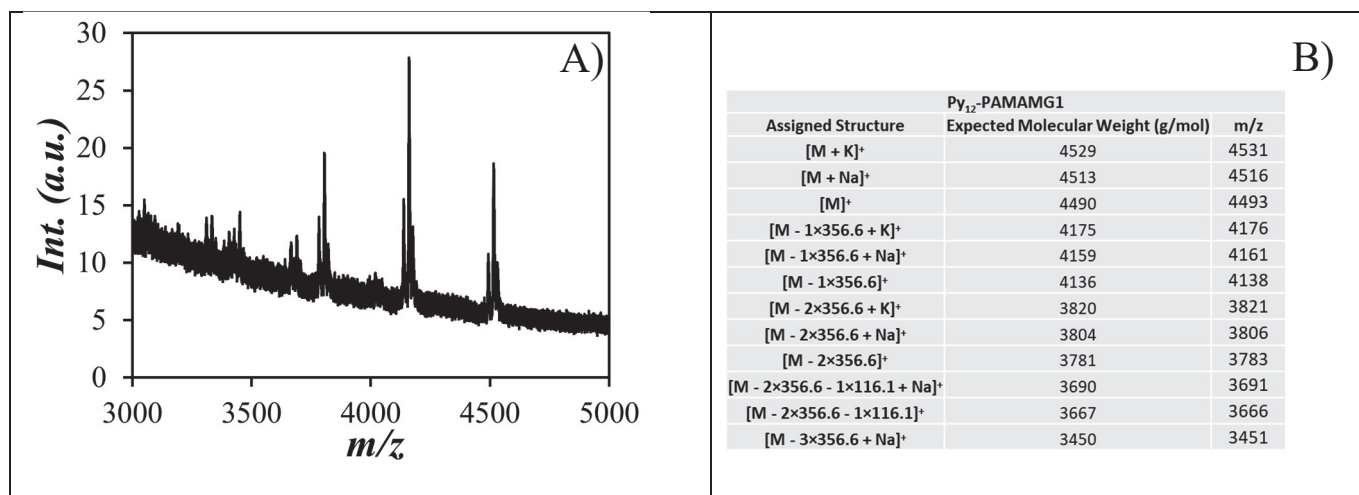


Figure S2.22. A) Mass spectrum for PAMAM-G1 labeled with 1-pyrenedodecanoic acid and B) table of the m/z ratios for the species found in the mass spectrum. No m/z peak was observed at 4108, 3725, and 3343 g/mol corresponding to PAMAM-G1 labeled with 7, 6, and 5 1-pyrenedodecanoyl groups.

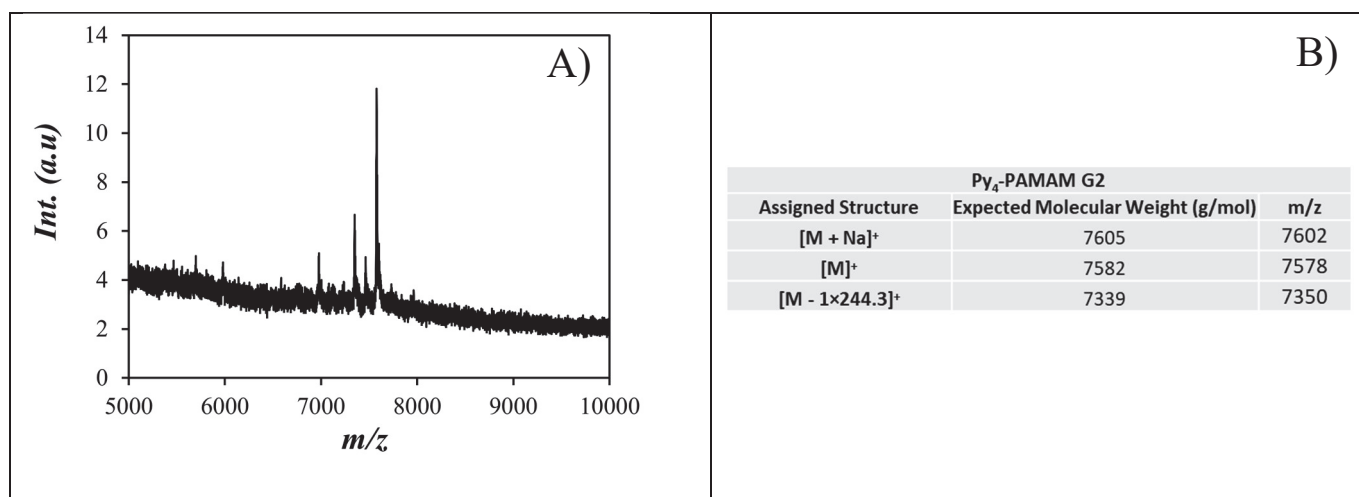


Figure S2.23. A) Mass spectrum for PAMAM-G2 labeled with 1-pyrenebutyric acid and B) table of the m/z ratios of the main species found in the mass spectrum. No m/z peak was observed at 7311, 7041, 6771, 6500, 6230, 5960, 5689, 5419, and 5149 g/mol corresponding to PAMAM-G2 labeled with 15, 14, 13, 12, 11, 10, 9, 8, and 7 1-pyrenebutyryl groups.

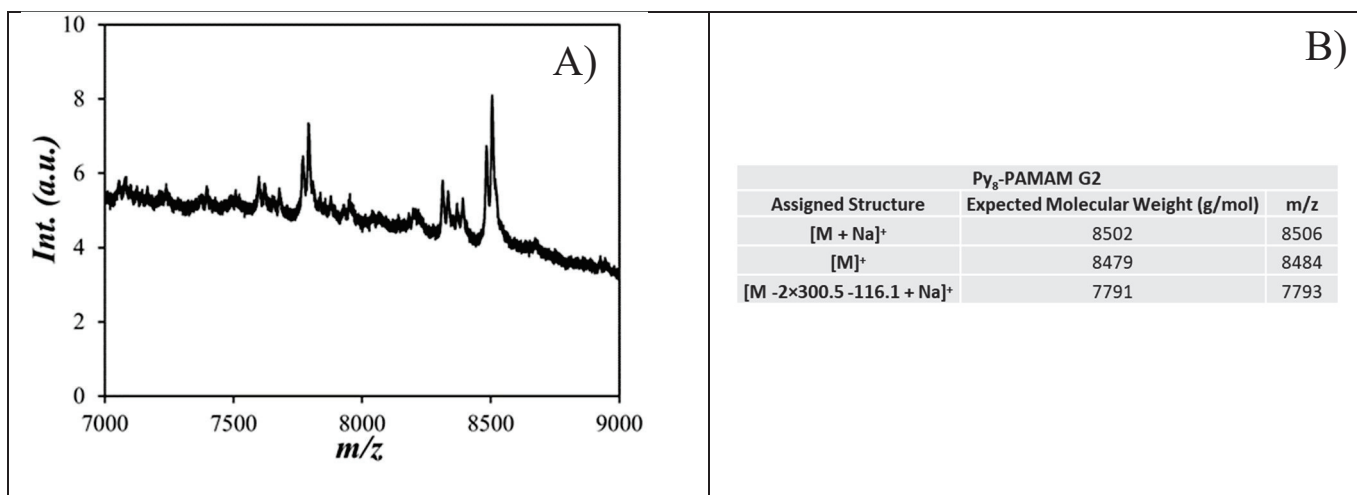


Figure S2.24. A) Mass spectrum for PAMAM-G2 labeled with 1-pyreneoctanoic acid and B) table of the m/z ratio of the main species found in the mass spectrum. No m/z peak was observed at 8161, 7835, 7508, 7182, 6853, 6527, 6198, 5870, 5543, and 5217 g/mol corresponding to PAMAM-G2 labeled with 15, 14, 13, 12, 11, 10, 9, 8, 7, and 6 1-pyreneoctanoyl groups.

D) Global Analysis of Monomer and Excimer Decays using the Model-Free Analysis (MFA)

All fluorescence decays were globally fitted with the model-free analysis (MFA). Equations S2.1 and S2.2 were used to fit the monomer and excimer fluorescence decays, respectively, and the parameters used in Equations S2.1 and S2.2 were optimized according to the Marquardt-Levenberg algorithm.²⁹ The MFA retrieved the parameters f_{diff} ($= f_{diffE0} + f_{diffEL}$), f_{free} , and f_{agg} ($= f_{E0} + f_{EL}$) which represent the molar fractions of the pyrene species, which form excimer by diffusion, unreacted pyrene in the solution, and aggregated pyrenes forming excimer by direct excitation.

$$[Py^*]_{(t)} = k_{M,mic}^{rad} \epsilon_{M,mic} [Py_{diff}^*]_{(t=0)} \times \sum_{i=1}^n a_i \times \exp(-t / \tau_i) + k_{M,wat}^{rad} \epsilon_{M,wat} [Py_{free}^*]_{(t=0)} \times \exp(-t / \tau_M) \quad (S2.3)$$

$$\begin{aligned}
[E^*]_{(t)} = & -[Py_{diff}^*]_{(t=0)} \times \sum_{i=1}^n a_i \frac{\frac{1}{\tau_i} - \frac{1}{\tau_M}}{\frac{1}{\tau_i} - \frac{1}{\tau_{E0}}} \exp(-t / \tau_i) \\
& + \left([E0^*]_{(t=0)} + [Py_{diff}^*]_{(t=0)} \times \sum_{i=1}^n a_i \frac{\frac{1}{\tau_i} - \frac{1}{\tau_M}}{\frac{1}{\tau_i} - \frac{1}{\tau_{E0}}} \right) \times \exp(-t / \tau_{E0}) \\
& - k_{E0,mic}^{rad} \varepsilon_{M,mic} [Py_{diff}^*]_{(t=0)} \times \sum_{i=1}^n a_i \frac{\frac{1}{\tau_i} - \frac{1}{\tau_M}}{\frac{1}{\tau_i} - \frac{1}{\tau_D}} \exp(-t / \tau_i) \\
& + \left([D^*]_{(t=0)} + [Py_{diff}^*]_{(t=0)} \times \sum_{i=1}^n a_i \frac{\frac{1}{\tau_i} - \frac{1}{\tau_M}}{\frac{1}{\tau_i} - \frac{1}{\tau_D}} \right) \times \exp(-t / \tau_D) \\
& + [ES^*]_{(t=0)} \times \exp(-t / \tau_{ES})
\end{aligned} \tag{S2.4}$$

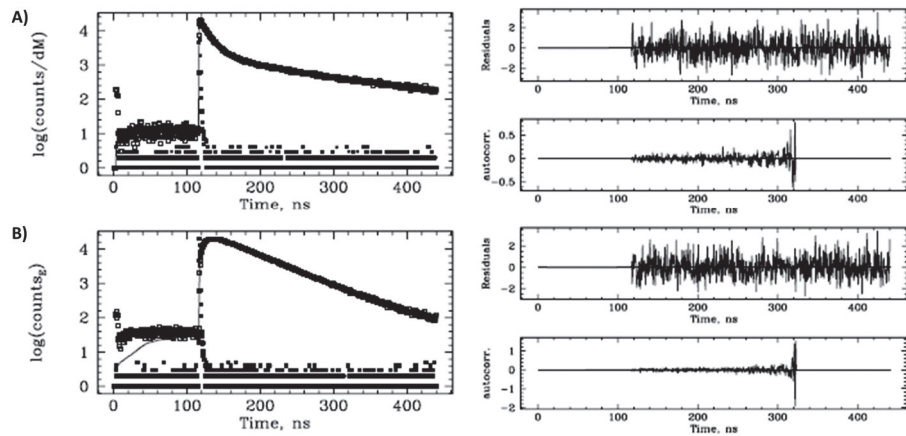


Figure S2.25. Global MFA of the fluorescence decays of the A) monomer and B) excimer acquired at 379 nm and 510 nm, respectively, for a PyC8-PAMAM-G0 construct.

E] Parameters obtained from the MFA of the PyCX-PAMAM-GY dendrimers:

Table S2.1. Parameters retrieved from the MFA of the monomer decays of PyCX-PAMAM-GY dendrimers in degassed *N,N*-dimethylformamide (DMF).

PAMAM Generation	Derivative	a_1	τ_1 (ns)	a_2	τ_2 (ns)	a_3	τ_3 (ns)	f_{Mfree}	τ_M	χ^2
G0	PBA	0.28	3.33	0.67	6.08	0.01	38.3	0.04	173	1.18
	POA	0.40	4.02	0.55	9.54	0.03	47.7	0.02	161	1.03
	PDA	0.21	4.79	0.67	12.00	0.06	45.8	0.05	161	1.00
G1	PBA	0.52	3.12	0.46	5.11	0.01	85.8	0.00	173	1.15
	POA	0.38	4.01	0.57	8.37	0.03	32.3	0.02	161	1.20
	PDA	0.53	4.52	0.35	10.91	0.04	70.5	0.07	161	1.08
G2	PBA	0.42	2.59	0.57	4.22	0.00	34.9	0.00	173	1.25
	POA	0.44	1.70	0.49	4.28	0.03	87.3	0.04	161	1.10
	PDA	0.26	2.36	0.64	6.22	0.08	21.4	0.02	161	1.26

Table S2.2. Parameters retrieved from the MFA of the excimer decays of PyCX-PAMAM-GY dendrimers in degassed DMF.

PAMAM Generation	Derivative	f_{diff}^{E0}	f_{Ediff}^D	τ_{E0} (ns)	τ_D (ns)	τ_S (ns)	f_{EE0}	f_{ED}	f_{ES}	χ^2
G0	PBA	0.26	0.30	27.11	53.61	3.5	0.00	0.22	0.22	1.18
	POA	-	0.97	-	49.99	-	-	0.03	-	1.03
	PDA	0.36	0.59	34.65	51.25	-	0.02	0.03	-	1.00
G1	PBA	0.22	0.36	44.73	53.77	3.5	0.03	0.04	0.36	1.15
	POA	0.7	0.24	44.26	61.22	-	0.00	0.06	-	1.20
	PDA	0.61	0.32	42.87	55.63	-	0.03	0.04	-	1.08
G2	PBA	0.04	0.27	36.42	54.45	3.5	0.15	0.32	0.37	1.25
	POA	0.61	0.34	43.83	55.89	-	0.00	0.04	-	1.10
	PDA	0.58	0.26	39.79	58.26	-	0.12	0.05	-	1.26

Table S2.3. Parameters calculated from the MFA analysis of the monomer and excimer decays for PyCX-PAMAM-GY dendrimers in degassed DMF.

<i>PAMAM Generation</i>	<i>Derivative</i>	f_{diff}	f_{free}	f_{agg}	f_{diffE}	f_{diffD}	f_{E0}	f_D
G0	PBA	0.68	0.03	0.30	0.40	0.28	0.30	0.00
	POA	0.95	0.02	0.03	0.00	0.95	0.00	0.03
	PDA	0.90	0.05	0.05	0.34	0.56	0.02	0.03
G1	PBA	0.90	0.00	0.10	0.35	0.55	0.04	0.05
	POA	0.92	0.02	0.06	0.69	0.23	0.00	0.06
	PDA	0.86	0.07	0.07	0.57	0.30	0.03	0.04
G2	PBA	0.73	0.00	0.27	0.50	0.23	0.15	0.13
	POA	0.92	0.04	0.04	0.59	0.33	0.00	0.04
	PDA	0.82	0.02	0.16	0.57	0.25	0.11	0.05

Table S2.4. Parameters retrieved from the MFA of the monomer decays of PyCX-PAMAM-GY dendrimers in degassed dimethyl sulfoxide (DMSO).

<i>PAMAM Generation</i>	<i>Derivative</i>	a_1	$\tau_1 (ns)$	a_2	$\tau_2 (ns)$	a_3	$\tau_3 (ns)$	f_{Mfree}	τ_M	χ^2
G0	PBA	0.53	7.47	0.42	12.4	0	48.76	0.05	138	1.06
	POA	0.33	6.57	0.61	15.14	0.04	39.95	0.02	130	1.18
	PDA	0.14	4.18	0.74	14.86	0.09	38.55	0.03	130	1.05
G1	PBA	0.65	6.02	0.34	10.16	0	72.35	0.07	138	1.21
	POA	0.25	2.8	0.62	10.38	0.09	19.68	0.04	130	1.13
	PDA	0.14	4.18	0.74	14.86	0.09	38.55	0.03	130	1.05
G2	PBA	0.33	3.08	0.65	6.92	0.01	27.41	0.01	138	1.24
	POA	0.25	2.03	0.67	7.21	0.02	29.02	0.06	130	1.05
	PDA	0.36	5.49	0.47	15.1	-	-	0.17	130	1.26

Table S2.5. Parameters retrieved from the MFA of the excimer decays of PyCX-PAMAM-GY dendrimers in DMSO.

PAMAM Generation	Derivative	f_{diff}^{EO}	f_{Ediff}^D	τ_{EO} (ns)	τ_D (ns)	τ_S (ns)	f_{EE0}	f_{ED}	f_{ES}^*	χ^2
G0	PBA	0.23	0.42	36.52	51.84	3.5	0	0.04	0.31	1.06
	POA	0.08	0.82	58.75	46.63	-	0.04	0.05	-	1.18
	PDA	-	0.93	-	46.99	-	-	0.07	-	1.05
G1	PBA	0.34	0.21	41.43	53.39	3.5	0.01	0.11	0.33	1.21
	POA	0.72	0.24	43.16	55.06	-	0	0.04	-	1.13
	PDA	0.65	0.17	44.21	52.3	-	0.04	0.14	-	1.05
G2	PBA	0.28	0.21	40.5	54.1	3.5	0	0.06	0.45	1.24
	POA	0.59	0.36	42.36	53.93	-	0	0.04	-	1.05
	PDA	0.52	0.31	38.27	52.27	-	0	0.16	-	1.26

Table S2.6. Parameters calculated from the MFA analysis of the monomer and excimer decays for PyCX-PAMAM-GY dendrimers in degassed DMSO.

PAMAM Generation	Derivative	f_{diff}	f_{free}	f_{agg}	f_{diffE}	f_{diffD}	f_{EO}	f_D
G0	PBA	0.90	0.05	0.06	0.32	0.58	0.00	0.06
	POA	0.89	0.02	0.09	0.08	0.81	0.04	0.05
	PDA	0.90	0.03	0.07	0.00	0.90	0.00	0.07
G1	PBA	0.82	0.01	0.18	0.50	0.31	0.01	0.16
	POA	0.92	0.04	0.04	0.69	0.23	0.00	0.04
	PDA	0.70	0.15	0.15	0.56	0.15	0.03	0.12
G2	PBA	0.88	0.01	0.11	0.50	0.38	0.00	0.11
	POA	0.90	0.06	0.04	0.56	0.34	0.00	0.04
	PDA	0.81	0.04	0.16	0.50	0.30	0.00	0.16

Table S2.7. Parameters retrieved from the MFA of the monomer decays of hexyl-1-pyrenebutyramide in degassed DMF.

<i>[PBA-hexyl], mM</i>	a_1	τ_1 (ns)	a_2	τ_2 (ns)	f_{Mfree}	τ_M	χ^2
11	0.24	36.53	0.76	67.73	0	173	0.97
14	0.38	34.31	0.62	58.98	0	173	1.15
16	0.53	31.70	0.47	54.71	0	173	1.10
19	0.65	30.85	0.35	53.49	0	173	1.06
22	0.72	28.07	0.28	50.25	0	173	1.07

Table S2.8. Parameters retrieved from the MFA of the excimer decays of hexyl-1-pyrenebutyramide in degassed DMF.

<i>[PBA-hexyl], mM</i>	f_{diff}^{E0}	τ_D (ns)	f_{ED}	χ^2
11	0.99	54.75	0.01	0.97
14	0.98	54.39	0.02	1.15
16	0.99	53.35	0.01	1.10
19	0.97	53.05	0.03	1.06
22	0.98	52.46	0.02	1.07

Table S2.9. Parameters retrieved from the MFA of the monomer decays of hexyl-1-pyrenebutyramide in degassed dimethyl sulfoxide (DMSO).

<i>[PBA-hexyl], mM</i>	a_1	τ_1 (ns)	a_2	τ_2 (ns)	f_{Mfree}	τ_M	χ^2
12	0.10	30.80	0.90	67.46	0	138	1.11
15	0.10	26.54	0.90	60.43	0	138	1.05
20	0.13	24.98	0.87	51.16	0	138	1.09
23	0.24	27.91	0.76	46.75	0	138	1.07
26	0.18	24.10	0.82	42.59	0	138	1.11

Table S2.10. Parameters retrieved from the MFA of the monomer decays of hexyl-1-pyrenebutyramide in degassed DMSO.

<i>[PBA-hexyl], mM</i>	f_{diff}^{E0}	τ_D (ns)	f_{ED}	χ^2
12	0.99	51.99	0.01	1.11
15	0.98	51.52	0.02	1.05
20	0.98	49.02	0.02	1.09
23	0.97	49.65	0.03	1.07
26	0.97	48.78	0.03	1.11

F] Determination of k_{diff} from plots of $\langle k \rangle$ as a function of [H-PyBA] in DMF and DMSO

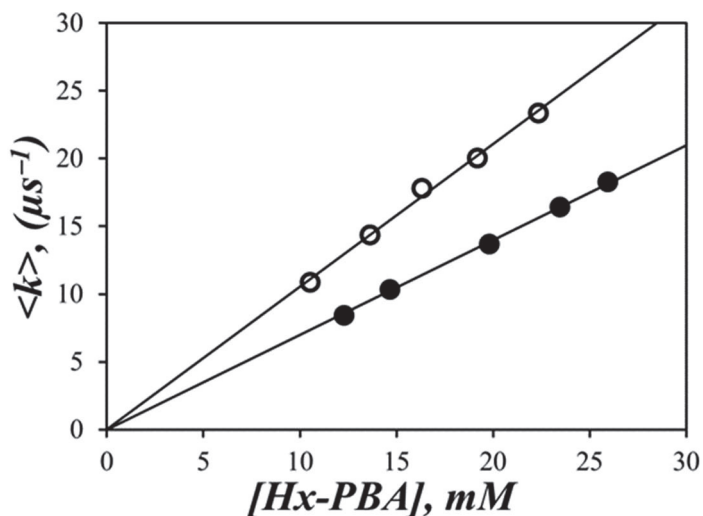


Figure S2.26. Plot of $\langle k \rangle$ as a function of the concentration of hexyl-1-pyrenebutyramide in (○) DMF and (●) DMSO.

G] Equations used for the radius of gyration and the end-to-end distance of the dendrimers

Table S2.9. Equations for R_G and r_{EE} of the PAMAM and HMPA dendrimers

	Equations for R_G and r_{EE}	Parameters used in the equations ($l = 0.24$ nm)
PAMAM	$R_g(N) = \frac{2 \times \left[2^{N+1} \sum_{i=1}^{c/2+(N+1) \times b} \sqrt{i} - \sum_{k=0}^N 2^k \sum_{i=1}^{c/2+k \times b} \sqrt{i} \right]}{c + b \times (2^{N+1} - 1)} \times l$	$b = 7$ $c = 4$
	$r_{EE}(N) = l \times \left(\frac{\left[2 - 2^{N+2} + (N+1) \times 2^{N+3} \right] b + 2^{N+1} c + 2^{N+1} - 1}{2^{N+2} - 1} \right)^{1/2}$	$b = 7$ $c = 4$
HMPA	$R_g(N) = \frac{2^N \sum_{i=1}^{4 \times (N-1) + 2} \sqrt{i} - \sum_{k=1}^{N-1} 2^k \sum_{j=1}^{4k} \sqrt{j}}{6 \times (2^N - 1)} \times l$	
	$r_{EE}(N) = l \times \left(1 + 2a + b \frac{N \times 2^N - 2^{N+1} + 2}{2^N - 1} \right)^{1/2}$	$a = 2$ $b = 8$

Appendix B: S3-SI for Chapter 3

A) Global Analysis of Monomer and Excimer Decays Using the Model-Free Analysis

All fluorescence decays were globally fitted with the model-free analysis (MFA). Equations S3.1 and S3.2 were used to fit the monomer and excimer fluorescence decays, respectively, and the parameters used in Equations S3.1 and S3.2 were optimized according to the Marquardt-Levenberg algorithm.¹ The MFA retrieved the parameters f_{diff} ($= f_{diffE0} + f_{diffEL}$), f_{free} , and f_{agg} ($= f_{E0} + f_{EL}$) which represent the molar fractions of the pyrene species, which form excimer by diffusion, are unreacted pyrene in the solution, and are aggregated pyrenes forming excimer by direct excitation. An example of the global analysis fit according to the MFA is provided in Figure S1.

$$[Py^*]_{(t)} = k_{M,mic}^{rad} \varepsilon_{M,mic} [Py_{diff}^*]_{(t=0)} \times \sum_{i=1}^n a_i \times \exp(-t / \tau_i) + k_{M,wat}^{rad} \varepsilon_{M,wat} [Py_{free}^*]_{(t=0)} \times \exp(-t / \tau_M) \quad (S3.1)$$

$$[E^*]_{(t)} = -[Py_{diff}^*]_{(t=0)} \times \sum_{i=1}^n a_i \frac{\frac{1}{\tau_i} - \frac{1}{\tau_M}}{\frac{1}{\tau_i} - \frac{1}{\tau_{E0}}} \exp(-t / \tau_i) + \left([E0^*]_{(t=0)} + [Py_{diff}^*]_{(t=0)} \times \sum_{i=1}^n a_i \frac{\frac{1}{\tau_i} - \frac{1}{\tau_M}}{\frac{1}{\tau_i} - \frac{1}{\tau_{E0}}} \right) \times \exp(-t / \tau_{E0}) - k_{E0,mic}^{rad} \varepsilon_{M,mic} [Py_{diff}^*]_{(t=0)} \times \sum_{i=1}^n a_i \frac{\frac{1}{\tau_i} - \frac{1}{\tau_D}}{\frac{1}{\tau_i} - \frac{1}{\tau_D}} \exp(-t / \tau_i)$$

$$\begin{aligned}
& + \left([D^*]_{(t=0)} + [Py_{diff}^*]_{(t=0)} \times \sum_{i=1}^n a_i \frac{1}{\tau_i} - \frac{1}{\tau_M} \right) \times \exp(-t / \tau_D) \\
& + [ES^*]_{(t=0)} \times \exp(-t / \tau_{ES})
\end{aligned} \tag{S3.2}$$

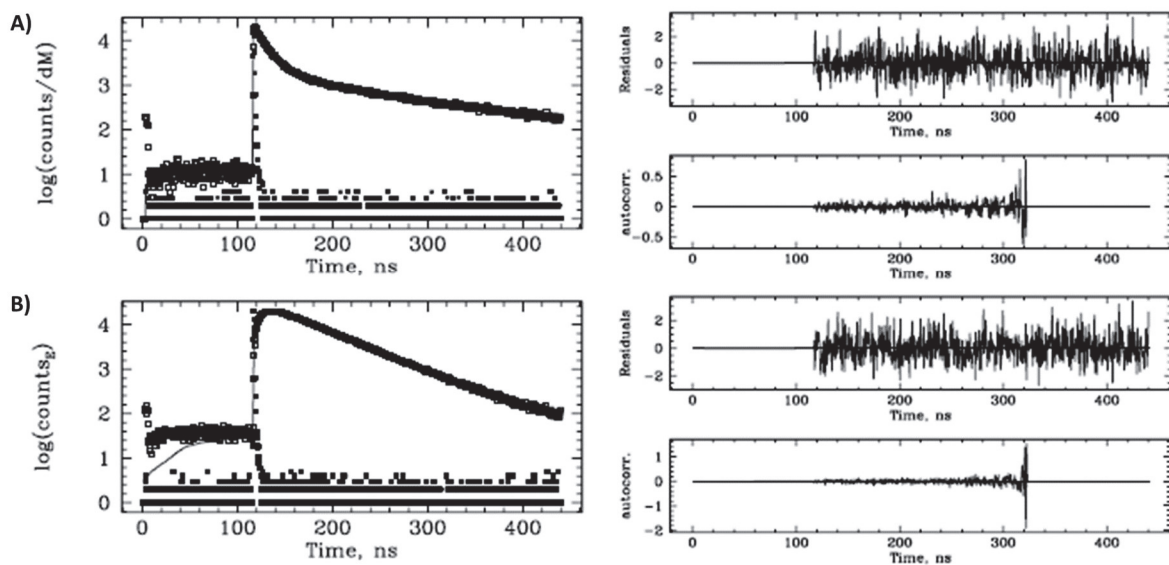


Figure S3.1. Global MFA of the fluorescence decays of the A) monomer and B) excimer acquired at 379 nm and 510 nm, respectively, for a PyC8-PAMAM-G0 construct in DMSO.

B] Parameters retrieved from the MFA of the florescence decays:

Table S3.1. Parameters retrieved from the MFA of the monomer decays for the PyCX-PAMAM-GY samples in degassed DMF.²

<i>PAMAM Generation</i>	<i>Derivative</i>	a_1	τ_1 (ns)	a_2	τ_2 (ns)	a_3	τ_3 (ns)	f_{Mfree}	τ_M	χ^2
G0	PyBA	0.89	5.0	0.07	12.0	0.01	93.8	0.04	173	1.13
	PyOA	0.40	4.0	0.55	9.5	0.03	47.7	0.02	161	1.03
	PyDA	0.21	4.8	0.67	12.0	0.06	45.8	0.05	161	1.00
G1	PyBA	0.52	3.1	0.46	5.1	0.01	85.8	0.00	173	1.15
	PyOA	0.38	4.0	0.57	8.4	0.03	32.3	0.02	161	1.20
	PyDA	0.53	4.5	0.35	10.9	0.04	70.5	0.07	161	1.08
G2	PyBA	0.62	2.9	0.37	4.6	0.01	35.8	0.00	173	1.24
	PyOA	0.49	4.3	0.44	1.7	0.03	87.3	0.04	161	1.10
	PyDA	0.64	6.2	0.26	2.4	0	21.4	0.02	161	1.26

Table S3.2. Parameters retrieved from the MFA of the excimer decays for the PyCX-PAMAM-GY samples in degassed DMF.²

<i>PAMAM Generation</i>	<i>Derivative</i>	f_{diff}^{EO}	f_{Ediff}^D	τ_{EO} (ns)	τ_D (ns)	τ_S (ns)	f_{EEO}	f_{ED}	f_{ES}^*	χ^2
G0	PyBA	0.30	0.21	52.3	23.5	3.5	0.22	0.00	0.22	1.13
	PyOA	-	0.97	-	50.0	-	-	0.03	-	1.03
	PyDA	0.36	0.59	34.6	51.3	-	0.02	0.03	-	1.00
G1	PyBA	0.22	0.36	44.7	53.8	3.5	0.03	0.04	0.36	1.15
	PyOA	0.24	0.70	61.2	44.3	-	0.06	0.00	-	1.20
	PyDA	0.32	0.61	55.6	42.9	-	0.04	0.03	-	1.08
G2	PyBA	0.14	0.30	60.5	44.9	3.5	0.08	0.09	0.39	1.24
	PyOA	0.34	0.61	55.9	43.8	-	0.04	0	-	1.10
	PyDA	0.26	0.58	58.3	39.8	-	0.05	0.12	-	1.26

Table S3.3. Molar fractions calculated from the parameters obtained with the MFA of the monomer and excimer decays of the PyCX-PAMAM-GY constructs acquired in DMF.²

<i>PAMAM Generation</i>	<i>Derivative</i>	f_{diff}	f_{free}	f_{agg}	f_{diffE}	f_{diffD}	f_{E0}	f_D
G0	PyBA	0.68	0.03	0.30	0.40	0.28	0.30	0.00
	PyOA	0.95	0.02	0.03	0.00	0.95	0.00	0.03
	PDA	0.90	0.05	0.05	0.34	0.56	0.02	0.03
G1	PyBA	0.90	0.00	0.10	0.35	0.55	0.04	0.05
	PyOA	0.92	0.02	0.06	0.23	0.69	0.06	0.00
	PyDA	0.86	0.07	0.07	0.30	0.57	0.04	0.03
G2	PyBA	0.73	0.00	0.27	0.23	0.50	0.13	0.15
	PyOA	0.92	0.04	0.04	0.33	0.59	0.04	0.00
	PyDA	0.82	0.02	0.16	0.25	0.57	0.05	0.11

Table S3.4. Parameters retrieved from the MFA of the monomer decays for the PyCX-PAMAM-GY samples acquired in degassed DMF with 5 mM HCl.

<i>PAMAM Generation</i>	<i>Derivative</i>	a_1	τ_1 (ns)	a_2	τ_2 (ns)	a_3	τ_3 (ns)	f_{Mfree}	τ_M	χ^2
G0	PyBA	0.75	6.5	0.19	14.4	-	-	0.06	165	1.15
	PyOA	0.41	6.5	0.53	14.0	0.05	57.3	0.02	161	1.10
	PyDA	0.15	4.7	0.69	13.8	0.10	43.6	0.06	161	1.06
G1	PyBA	0.69	5.3	0.29	8.7	0.01	59.4	0.01	165	1.15
	PyOA	0.26	4.2	0.64	10.2	0.07	32.4	0.03	161	1.09
	PyDA	0.19	3.5	0.60	10.9	0.09	42.5	0.11	161	1.08
G2	PyBA	0.58	3.6	0.40	6.8	0.01	46.7	0.01	165	1.18
	PyOA	0.53	6.4	0.39	2.8	0.03	70.4	0.06	161	1.14
	PyDA	0.41	3.0	0.51	8.9	0	29.8	0.02	161	1.06

Table S3.5. Parameters retrieved from the MFA of the excimer decays for the PyCX-PAMAM-GY samples acquired in degassed DMF with 5 mM HCl.

<i>PAMAM Generation</i>	<i>Derivative</i>	f_{diff}^{E0}	f_{Ediff}^D	τ_{E0} (ns)	τ_D (ns)	τ_S (ns)	f_{EE0}	f_{ED}	f_{ES}^*	χ^2
G0	PyBA	0.28	0.36	56.8	44.7	3.5	0.03	0.01	0.31	1.15
	PyOA	-	0.99	-	49.7	-	-	0.01	-	1.10
	PyDA	-	0.97	-	50.5	-	-	0.03	-	1.06
G1	PyBA	0.17	0.43	60.1	45.2	3.5	0.04	0.00	0.36	1.15
	PyOA	0.32	0.64	58.9	44.8	-	0.04	0.00	-	1.09
	PyDA	0.23	0.74	39.5	51.1	-	0.00	0.04	-	1.08
G2	PyBA	0.17	0.32	60.2	44.8	3.5	0.00	0.15	0.29	1.18
	PyOA	0.40	0.55	53.5	43.8	-	0.03	0.00	-	1.14
	PyDA	0.33	0.60	37.7	52.2	-	0.0	0.06	-	1.06

Table S3.6. Molar fractions calculated from the parameters obtained with the MFA of the monomer and excimer decays of the PyCX-PAMAM-GY constructs acquired in DMF with 5 mM HCl.

<i>PAMAM Generation</i>	<i>Derivative</i>	f_{diff}	f_{free}	f_{agg}	f_{diffE}	f_{diffD}	f_{E0}	f_D
G0	PyBA	0.88	0.06	0.06	0.39	0.49	0.05	0.02
	PyOA	0.97	0.02	0.01	0.00	0.97	0.00	0.01
	PyDA	0.92	0.05	0.03	0.00	0.92	0.00	0.03
G1	PyBA	0.93	0.01	0.06	0.26	0.67	0.06	0.00
	PyOA	0.94	0.02	0.04	0.31	0.63	0.04	0.00
	PyDA	0.86	0.11	0.03	0.20	0.66	0.00	0.03
G2	PyBA	0.76	0.01	0.23	0.26	0.50	0.00	0.23
	PyOA	0.90	0.05	0.05	0.38	0.52	0.03	0.02
	PyDA	0.92	0.01	0.06	0.33	0.59	0.00	0.06

Table S3.7. Parameters retrieved from the MFA of the monomer decays for the PyCX-PAMAM-GY samples acquired in degassed DMF with 5 mM NaOH.

<i>PAMAM Generation</i>	<i>Derivative</i>	a_1	τ_1 (ns)	a_2	τ_2 (ns)	a_3	τ_3 (ns)	f_{Mfree}	τ_M	χ^2
G0	PyBA	0.67	4.0	0.25	7.1	0.03	77.7	0.05	165	1.13
	PyOA	0.26	4.2	0.67	8.8	0.05	33.6	0.02	161	1.09
	PyDA	0.50	7.0	0.39	14.2	0.05	62.5	0.06	161	1.16
G1	PyBA	0.39	2.8	0.59	4.7	0.01	65.1	0.01	165	1.19
	PyOA	0.53	3.8	0.43	8.0	0.02	54.0	0.03	161	1.24
	PyDA	0.30	3.1	0.57	7.7	0.04	37.3	0.08	161	1.07
G2	PyBA	0.20	1.9	0.77	3.9	0.01	36.4	0.01	165	1.10
	PyOA	0.50	4.3	0.43	2.2	0.02	53.6	0.05	161	1.12
	PyDA	0.40	2.4	0.51	7.0	0.07	19.9	0.02	161	1.16

Table S3.8. Parameters retrieved from the MFA of the excimer decays for the PyCX-PAMAM-GY samples acquired in degassed DMF with 5 mM NaOH.

<i>PAMAM Generation</i>	<i>Derivative</i>	f_{diff}^{E0}	f_{Ediff}^D	τ_{E0} (ns)	τ_D (ns)	τ_S (ns)	f_{EE0}	f_{ED}	f_{ES}^*	χ^2
G0	PyBA	0.29	0.37	53.4	43.2	3.5	0.07	0.00	0.28	1.13
	PyOA	0.21	0.72	43.9	50.2	-	-	0.07	-	1.09
	PyDA	-	0.92	-	50.3	-	-	0.08	-	1.16
G1	PyBA	0.24	0.36	56.0	42.7	3.5	0.06	0.00	0.33	1.19
	PyOA	0.40	0.49	55.3	41.9	-	0.11	0.00	-	1.24
	PyDA	0.22	0.66	56.3	44.3	-	0	0.09	-	1.07
G2	PyBA	0.14	0.34	59.0	45.1	3.5	0.09	0.13	0.31	1.10
	PyOA	0.31	0.60	56.8	43.7	-	0.05	0.04	-	1.12
	PyDA	0.35	0.57	56.3	39.1	-	0.06	0.03	-	1.16

Table S3.9. Molar fractions calculated from the parameters obtained with the MFA of the monomer and excimer decays of the PyCX-PAMAM-GY constructs acquired in DMF with 5 mM NaOH.

<i>PAMAM Generation</i>	<i>Derivative</i>	f_{diff}	f_{free}	f_{agg}	f_{diffE}	f_{diffD}	f_{E0}	f_D
G0	PyBA	0.86	0.04	0.09	0.38	0.48	0.09	0.00
	PyOA	0.91	0.02	0.07	0.21	0.70	0.00	0.07
	PyDA	0.87	0.05	0.08	-	0.87	-	0.08
G1	PyBA	0.90	0.01	0.09	0.36	0.54	0.09	0.00
	PyOA	0.87	0.02	0.11	0.39	0.48	0.11	0.00
	PyDA	0.82	0.07	0.11	0.21	0.61	0.03	0.08
G2	PyBA	0.69	0.01	0.30	0.20	0.49	0.12	0.18
	PyOA	0.87	0.05	0.09	0.30	0.57	0.05	0.04
	PyDA	0.90	0.01	0.09	0.34	0.56	0.06	0.03

Table S3.10. Parameters retrieved from the MFA of the monomer decays for the PyCX-PAMAM-GY samples acquired in degassed DMSO.²

<i>PAMAM Generation</i>	<i>Derivative</i>	a_1	τ_1 (ns)	a_2	τ_2 (ns)	a_3	τ_3 (ns)	f_{Mfree}	τ_M	χ^2
G0	PyBA	0.53	7.5	0.42	12.4	0.00	48.8	0.05	138	1.06
	PyOA	0.61	15.1	0.33	6.6	0.04	40.0	0.02	130	1.18
	PyDA	0.14	4.2	0.74	14.9	0.09	38.6	0.03	130	1.05
G1	PyBA	0.65	6.0	0.34	10.2	0.00	72.4	0.01	138	1.21
	PyOA	0.62	10.4	0.25	2.8	0.09	19.7	0.04	130	1.13
	PyDA	0.36	5.5	0.47	15.1	-	-	0.17	130	1.26
G2	PyBA	0.33	3.1	0.65	6.9	0.01	27.4	0.01	138	1.24
	PyOA	0.67	7.2	0.25	2.0	0.02	29.0	0.06	130	1.05
	PyDA	0.49	3.8	0.46	13.2	-	-	0.05	130	1.26

Table S3.11. Parameters retrieved from the MFA of the excimer decays for the PyCX-PAMAM-GY samples acquired in degassed DMSO.²

<i>PAMAM Generation</i>	<i>Derivative</i>	f_{diff}^{E0}	f_{Ediff}^D	τ_{E0} (ns)	τ_D (ns)	τ_S (ns)	f_{EE0}	f_{ED}	f_{ES}^*	χ^2
G0	PyBA	0.23	0.42	36.5	51.8	3.5	0.00	0.04	0.31	1.06
	PyOA	0.08	0.82	58.8	46.6	-	0.04	0.05	-	1.18
	PyDA	-	0.93	-	47.0	-	-	0.07	-	1.05
G1	PyBA	0.21	0.34	53.4	41.4	3.5	0.11	0.01	0.33	1.21
	PyOA	0.24	0.72	55.1	43.2	-	0.04	0.00	-	1.13
	PyDA	0.17	0.65	52.3	44.2	-	0.14	0.04	-	1.26
G2	PyBA	0.21	0.28	54.1	40.5	3.5	0.06	0.00	0.45	1.24
	PyOA	0.36	0.59	53.9	42.4	-	0.04	0.00	-	1.05
	PyDA	0.31	0.52	52.3	38.3	-	0.16	0.00	-	1.26

Table S3.12. Molar fractions calculated from the parameters obtained with the MFA of the monomer and excimer decays of the PyCX-PAMAM-GY constructs acquired in degassed DMSO.²

<i>PAMAM Generation</i>	<i>Derivative</i>	f_{diff}	f_{free}	f_{agg}	f_{diffE}	f_{diffD}	f_{E0}	f_D
G0	PyBA	0.90	0.05	0.06	0.32	0.58	0.00	0.06
	PyOA	0.89	0.02	0.09	0.08	0.81	0.04	0.05
	PyDA	0.90	0.03	0.07	-	0.90	-	0.07
G1	PyBA	0.82	0.01	0.18	0.31	0.50	0.16	0.01
	PyOA	0.92	0.04	0.04	0.23	0.69	0.04	0.00
	PyDA	0.70	0.15	0.15	0.15	0.56	0.12	0.03
G2	PyBA	0.88	0.01	0.11	0.38	0.50	0.11	0.00
	PyOA	0.90	0.06	0.04	0.34	0.56	0.04	0.00
	PyDA	0.81	0.04	0.16	0.30	0.50	0.16	0.00

Table S3.13. Parameters retrieved from the MFA of the monomer decays for the PyCX-PAMAM-GY samples acquired in degassed DMSO with 5 mM HCl.

<i>PAMAM Generation</i>	<i>Derivative</i>	a_1	τ_1 (ns)	a_2	τ_2 (ns)	a_3	τ_3 (ns)	f_{Mfree}	τ_M	χ^2
G0	PyBA	0.38	8.6	0.45	16.7	0.12	21.7	0.06	136	1.05
	PyOA	0.56	22.3	0.30	11.2	0.10	52.0	0.04	130	1.20
	PyDA	0.11	4.1	0.69	15.7	0.18	33.0	0.03	130	1.16
G1	PyBA	0.38	8.0	0.61	13.8	0.01	26.8	0.01	136	1.19
	PyOA	0.47	11.4	0.11	3.4	0.34	22.3	0.08	130	1.11
	PyDA	0.45	9.7	0.27	18.6	0.14	32.9	0.14	130	1.20
G2	PyBA	0.22	3.5	0.74	10.6	0.02	27.8	0.01	136	1.11
	PyOA	0.67	9.8	0.23	3.0	0.03	35.9	0.07	130	1.01
	PyDA	0.24	2.4	0.47	10.1	0.24	24.2	0.05	130	1.14

Table S3.14. Parameters retrieved from the MFA of the excimer decays for the PyCX-PAMAM-GY samples acquired in degassed DMSO with 5 mM HCl.

<i>PAMAM Generation</i>	<i>Derivative</i>	f_{diff}^{E0}	f_{Ediff}^D	τ_{E0} (ns)	τ_D (ns)	τ_S (ns)	f_{EE0}	f_{ED}	f_{ES}^*	χ^2
G0	PyBA	0.40	0.31	42.7	54.1	3.5	0.00	0.02	0.27	1.05
	PyOA	-	0.92	-	47.9	-	-	0.08	-	1.20
	PyDA	-	0.95	-	47.3	-	-	0.05	-	1.16
G1	PyBA	0.31	0.34	42.5	52.1	3.5	0.01	0.06	0.28	1.19
	PyOA	-	0.94	-	47.8	-	-	0.06	-	1.11
	PyDA	-	0.83	-	47.3	-	-	0.17	-	1.20
G2	PyBA	0.17	0.42	36.1	51.6	3.5	0.00	0.01	0.39	1.11
	PyOA	0.34	0.34	53.6	42.6	-	0.04	0.01	-	1.01
	PyDA	0.00	0.92	-	46.7	-	-	0.08	-	1.14

Table S3.15. Molar fractions calculated from the parameters obtained with the MFA of the monomer and excimer decays of the PyCX-PAMAM-GY constructs acquired in degassed DMSO with 5 mM HCl.

<i>PAMAM Generation</i>	<i>Derivative</i>	f_{diff}	f_{free}	f_{agg}	f_{diffE}	f_{diffD}	f_{E0}	f_D
G0	PyBA	0.91	0.05	0.03	0.52	0.40	0.01	0.02
	PyOA	0.89	0.03	0.08	0.00	0.89	-	0.08
	PyDA	0.92	0.02	0.05	0.00	0.92	-	0.05
G1	PyBA	0.90	0.01	0.09	0.43	0.47	0.01	0.09
	PyOA	0.87	0.08	0.06	0.00	0.87	-	0.06
	PyDA	0.73	0.12	0.15	0.00	0.73	-	0.15
G2	PyBA	0.97	0.01	0.02	0.28	0.69	0.00	0.02
	PyOA	0.87	0.07	0.06	0.44	0.44	0.06	0.01
	PyDA	0.88	0.04	0.08	0.00	0.88	-	0.08

Table S3.16. Parameters retrieved from the MFA of the monomer decays for the PyCX-PAMAM-GY samples acquired in degassed DMF.

<i>PAMAM Generation</i>	<i>Derivative</i>	a_1	τ_1 (ns)	a_2	τ_2 (ns)	a_3	τ_3 (ns)	f_{Mfree}	τ_M	χ^2
G0	PyBA	0.29	3.2	0.66	6.2	0	57.1	0.03	173	1.14
	PyOA	0.34	4.4	0.61	9.6	0.04	42.8	0.01	161	1.10
	PyDA	0.24	4.2	0.71	10.4	0.04	46.9	0.01	161	1.14
G1	PyBA	0.22	1.8	0.76	4.5	0.01	25.7	0.01	173	1.18
	PyOA	0.29	2.8	0.66	7.5	0.03	34.8	0.02	161	1.14
	PyDA	0.30	3.0	0.61	7.8	0.03	36.4	0.05	161	1.02
G2	PyBA	0.59	3.0	0.40	4.8	0.00	44.8	0.00	173	1.10
	PyOA	0.37	2.8	0.55	5.1	0.02	45.2	0.06	161	1.08
	PyDA	0.37	2.5	0.56	7.3	0	26.0	0.02	161	1.11

Table S3.17. Parameters retrieved from the MFA of the excimer decays for the PyCX-PAMAM-GY samples acquired in degassed DMF.

<i>PAMAM Generation</i>	<i>Derivative</i>	f_{diff}^{E0}	f_{Ediff}^D	τ_{E0} (ns)	τ_D (ns)	τ_S (ns)	f_{EE0}	f_{ED}	f_{ES}^*	χ^2
G0	PyBA	0.22	0.44	54.6	49.0	3.5	0.00	0.02	0.32	1.14
	PyOA	0	0.72	51.5	49.2	-	0	0.03	-	1.10
	PyDA	0	0.80	53.3	48.8	-	0	0.00	-	1.14
G1	PyBA	0.21	0.29	56.4	48.0	3.5	0.07	0.06	0.38	1.18
	PyOA	0.45	0.52	54.9	43.3	-	0.04	0.00	-	1.14
	PyDA	0.43	0.52	55.3	42.7	-	0	0.00	-	1.02
G2	PyBA	0.11	0.06	58.0	46.3	3.5	0.31	0.41	0.10	1.10
	PyOA	0.41	0.53	56.5	44.0	-	0.06	0	-	1.08
	PyDA	0.39	0.55	56.3	39.6	-	0	0.02	-	1.11

Table S3.18. Molar fractions calculated from the parameters obtained with the MFA of the monomer and excimer decays of the PyCX-PAMAM-GY constructs acquired in degassed DMF.

<i>PAMAM Generation</i>	<i>Derivative</i>	f_{diff}	f_{free}	f_{agg}	f_{diffE}	f_{diffD}	f_{E0}	f_D
G0	PyBA	0.94	0.03	0.03	0.31	0.62	0.00	0.03
	PyOA	0.97	0.01	0.02	0.00	0.72	0.00	0.02
	PyDA	0.97	0.01	0.02	0.00	0.79	0.00	0.00
G1	PyBA	0.78	0.01	0.21	0.33	0.46	0.11	0.00
	PyOA	0.94	0.02	0.04	0.44	0.51	0.04	0.00
	PyDA	0.91	0.05	0.04	0.41	0.49	0.00	0.00
G2	PyBA	0.19	0.00	0.81	0.13	0.07	0.00	0.46
	PyOA	0.89	0.05	0.06	0.39	0.50	0.06	0.00
	PyDA	0.92	0.02	0.06	0.38	0.54	0.04	0.02

Table S3.19. Parameters retrieved from the MFA of the monomer decays for the PyCX-PAMAM-GY samples acquired in degassed DMF with 5 mM HCl.

<i>PAMAM Generation</i>	<i>Derivative</i>	a_1	τ_1 (ns)	a_2	τ_2 (ns)	a_3	τ_3 (ns)	f_{Mfree}	τ_M	χ^2
G0	PyBA	0.62	7.1	0.31	11.8	0	50.8	0.04	173	1.10
	PyOA	0.24	5.4	0.67	12.2	0.07	43.4	0.02	161	1.12
	PyDA	0.54	8.7	0.39	16.3	0.05	51.5	0.02	161	1.18
G1	PyBA	0.67	5.7	0.28	8.3	0.03	18.6	0.01	173	1.24
	PyOA	0.32	4.1	0.60	10.5	0.05	38.2	0.03	161	1.05
	PyDA	0.23	3.4	0.64	9.8	0.07	40.2	0.06	161	1.08
G2	PyBA	0.24	3.5	0.71	5.7	0.05	15.0	0.01	173	1.20
	PyOA	0.33	3.1	0.57	6.4	0.03	42.2	0.07	161	1.08
	PyDA	0.37	3.1	0.52	9.0	0	29.4	0.02	161	1.14

Table S3.20. Parameters retrieved from the MFA of the excimer decays for the PyCX-PAMAM-GY samples acquired in degassed DMF with 5 mM HCl.

<i>PAMAM Generation</i>	<i>Derivative</i>	f_{diff}^{E0}	f_{Ediff}^D	τ_{E0} (ns)	τ_D (ns)	τ_S (ns)	f_{EE0}	f_{ED}	f_{ES}^*	χ^2
G0	PyBA	0.28	0.37	56.2	46.4	3.5	0.00	0.37	0.33	1.10
	PyOA	0	0.71	49.8	49.8	-	0.00	0.02	-	1.12
	PyDA	0	0.54	53.8	45.9	-	0.02	0.02	-	1.18
G1	PyBA	0.23	0.33	58.4	46.1	3.5	0.03	0.01	0.39	1.24
	PyOA	0.34	0.64	54.2	46.9	-	0.02	0.00	-	1.05
	PyDA	0.21	0.74	58.3	45.9	-	0.00	0.05	-	1.08
G2	PyBA	0.21	0.30	59.3	45.4	3.5	0.09	0.10	0.31	1.20
	PyOA	0.38	0.56	54.4	44.8	-	0.06	0	-	1.08
	PyDA	0.46	0.41	53.7	38.3	-	0.12	0.00	-	1.14

Table S3.21. Molar fractions calculated from the parameters obtained with the MFA of the monomer and excimer decays of the PyCX-PAMAM-GY constructs acquired in degassed DMF with 5 mM HCl.

<i>PAMAM Generation</i>	<i>Derivative</i>	f_{diff}	f_{free}	f_{agg}	f_{diffE}	f_{diffD}	f_{E0}	f_D
G0	PyBA	0.62	0.03	0.35	0.27	0.35	0.00	0.35
	PyOA	0.96	0.02	0.02	0.00	0.70	0.00	0.02
	PyDA	0.94	0.02	0.04	0.00	0.53	0.00	0.02
G1	PyBA	0.93	0.01	0.06	0.38	0.54	0.04	0.00
	PyOA	0.95	0.03	0.02	0.33	0.62	0.02	0.00
	PyDA	0.89	0.06	0.05	0.20	0.70	0.00	0.05
G2	PyBA	0.73	0.00	0.27	0.30	0.43	0.00	0.14
	PyOA	0.87	0.07	0.06	0.35	0.52	0.06	0.00
	PyDA	0.86	0.02	0.12	0.45	0.41	0.12	0.00

Table S3.22. Parameters retrieved from the MFA of the monomer decays for the PyCX-PAMAM-GY samples acquired in degassed DMF with 5 mM HCl and 10 mM NaOH.

<i>PAMAM Generation</i>	<i>Derivative</i>	a_1	τ_1 (ns)	a_2	τ_2 (ns)	a_3	τ_3 (ns)	f_{Mfree}	τ_M	χ^2
G0	PyBA	0.27	3.3	0.67	5.8	0.02	31.0	0.04	173	1.16
	PyOA	0.57	5.1	0.39	11.0	0.03	54.4	0.01	161	1.13
	PyDA	0.20	2.9	0.74	8.8	0.05	34.2	0.02	161	1.09
G1	PyBA	0.24	1.4	0.72	4.3	0.02	17.1	0.02	173	1.15
	PyOA	0.48	4.0	0.48	8.8	0.02	41.4	0.03	161	1.13
	PyDA	0.26	2.9	0.63	7.6	0.04	35.4	0.07	161	1.21
G2	PyBA	0.34	2.4	0.65	4.3	0.01	29.5	0.01	173	1.12
	PyOA	0.36	2.7	0.55	5.3	0.02	41.7	0.07	161	1.13
	PyDA	0.31	2.1	0.63	6.5	0.05	30.5	0.02	161	1.15

Table S3.23. Parameters retrieved from the MFA of the excimer decays for the PyCX-PAMAM-GY samples acquired in degassed DMF with 5 mM HCl and 10 mM NaOH.

<i>PAMAM Generation</i>	<i>Derivative</i>	f_{diff}^{E0}	f_{Ediff}^D	τ_{E0} (ns)	τ_D (ns)	τ_S (ns)	f_{EE0}	f_{ED}	f_{ES}^*	χ^2
G0	PBA	0.25	0.26	54.5	26.9	3.5	0.13	0.00	0.36	1.16
	POA	0.20	0.76	58.4	46.7	-	0.00	0.05	-	1.13
	PDA	0.23	0.76	50.1	48.9	-	0.00	0.01	-	1.09
G1	PBA	0.25	0.36	56.7	45.1	3.5	0.03	0.00	0.04	1.15
	POA	0.31	0.60	50.7	32.8	-	0.08	0.01	-	1.13
	PDA	0.36	0.53	56.6	39.4	-	0.11	0.00	-	1.21
G2	PBA	0.23	0.23	47.2	32.1	3.5	0.15	0.00	0.39	1.12
	POA	0.31	0.60	57.9	42.8	-	0.09	0.00	-	1.13
	PDA	0.40	0.35	51.3	32.5	-	0.25	0.00	-	1.15

Table S3.24. Molar fractions calculated from the parameters obtained with the MFA of the monomer and excimer decays of the PyCX-PAMAM-GY constructs acquired in degassed DMF with 5 mM HCl and 10 mM NaOH.

<i>PAMAM Generation</i>	<i>Derivative</i>	f_{diff}	f_{free}	f_{agg}	f_{diffE}	f_{diffD}	f_{E0}	f_D
G0	PBA	0.77	0.03	0.20	0.38	0.39	0.20	0.00
	POA	0.94	0.01	0.05	0.00	0.75	0.00	0.04
	PDA	0.97	0.02	0.01	0.00	0.75	0.00	0.01
G1	PBA	0.94	0.02	0.05	0.39	0.55	0.05	0.00
	POA	0.89	0.02	0.08	0.31	0.59	0.08	0.00
	PDA	0.84	0.06	0.10	0.33	0.50	0.00	0.00
G2	PBA	0.75	0.00	0.25	0.38	0.37	0.00	0.00
	POA	0.85	0.07	0.09	0.29	0.56	0.09	0.00
	PDA	0.74	0.01	0.25	0.39	0.34	0.25	0.00

Table S3.25. Parameters retrieved from the MFA of the monomer decays for the PyC4-HMPA-GY dendrimers acquired in degassed DMF with 5 mM HCl.

<i>PyC4-HMPA-GY</i>	α_1	τ_1 (ns)	α_2	τ_2 (ns)	α_3	τ_3 (ns)	f_{Mfree}	τ_M	χ^2
1	0.24	1.4	0.73	10.0	0.03	32.5	0.01	180	1.12
2	0.68	4.8	0.31	2.6	0.01	43.6	0.00	180	1.16
3	0.75	2.2	0.24	3.7	0.01	30.7	0.00	180	1.15
4	0.73	1.5	0.25	2.7	0.01	26.6	0.01	180	1.15
5	0.61	1.0	0.37	1.8	0.01	13.2	0.01	180	1.20

Table S3.26. Parameters retrieved from the MFA of the excimer decays for the PyC4-HMPA-GY dendrimers acquired in degassed DMF with 5 mM HCl.

<i>PyC4-HMPA-GY</i>	f_{diff}^{EO}	f_{Ediff}^D	τ_{EO} (ns)	τ_D (ns)	τ_S (ns)	f_{EEO}	f_{ED}	f_{ES}^*	χ^2
1	-	0.85	-	50.9	-	-	0.15	-	1.12
2	-	0.95	-	50.5	-	-	0.05	-	1.16
3	-	0.69	-	49.7	-	-	0.31	-	1.15
4	0.27	0.53	57.4	47.7	4	-	0.00	0.20	1.15
5	0.25	0.34	57.9	43.8	4	0.08	0.06	0.27	1.20

Table S3.27. Parameters retrieved from the MFA of the monomer decays for the PyC4-HMPA-GY dendrimers acquired in degassed DMSO with 5 mM HCl.

<i>PyC4-HMPA-GY</i>	α_1	τ_1 (ns)	α_2	τ_2 (ns)	α_3	τ_3 (ns)	f_{Mfree}	τ_M	χ^2
1	0.47	10.0	0.51	16.9	0.01	44.6	0.01	145	1.27
2	0.75	6.7	0.24	2.6	0.01	34.0	0.01	145	1.11
3	0.31	1.5	0.01	25.4	0.68	4.1	0.00	145	1.09
4	0.60	2.8	0.38	1.0	0.01	15.6	0.00	145	1.01
5	0.69	1.2	0.30	2.5	0.01	20.1	0.00	145	1.10

Table S3.28. Parameters retrieved from the MFA of the excimer decays for the PyC4-HMPA-GY dendrimers acquired in degassed DMSO with 5 mM HCl.

<i>PyC4-HMPA-GY</i>	f_{diff}^{E0}	f_{Ediff}^D	τ_{E0} (ns)	τ_D (ns)	τ_S (ns)	f_{EE0}	f_{ED}	f_{ES}^*	χ^2
1	-	0.93	-	46.2	-	-	0.07	-	1.27
2	-	0.91	-	46.4	-	-	0.09	-	1.11
3	-	0.74	-	46.8	-	-	0.26	-	1.09
4	0.74	0.00	47.9	9.2	-	0.15	0.11	-	1.01
5	0.25	0.42	56.9	41.7	4	0.04	0.00	0.30	1.10

Table S3.29. Parameters retrieved from the MFA of the monomer decays for Hx-PyBA acquired in degassed DMF.²

<i>[Hx-PyBA], mM</i>	a_1	τ_1 (ns)	a_2	τ_2 (ns)	f_{Mfree}	τ_M	χ^2
11	0.24	36.5	0.76	67.7	0	173	0.97
14	0.38	34.3	0.62	59.0	0	173	1.15
16	0.53	31.7	0.47	54.7	0	173	1.10
19	0.65	30.8	0.35	53.5	0	173	1.06
22	0.72	28.1	0.28	50.3	0	173	1.07

Table S3.30. Parameters retrieved from the MFA of the excimer decays for Hx-PyBA acquired in degassed DMF.²

<i>[Hx-PyBA], mM</i>	f_{diff}^{E0}	τ_D (ns)	f_{ED}	χ^2
11	0.99	54.8	0.01	0.97
14	0.98	54.4	0.02	1.15
16	0.99	53.4	0.01	1.10
19	0.97	53.1	0.03	1.06
22	0.98	52.5	0.02	1.07

Table S3.31. Parameters retrieved from the MFA of the monomer decay for Hx-PyBA acquired in degassed DMF with 5 mM HCl.

<i>[Hx-PyBA], mM</i>	<i>a₁</i>	<i>τ₁ (ns)</i>	<i>a₂</i>	<i>τ₂ (ns)</i>	<i>f_{Mfree}</i>	<i>τ_M</i>	<i>χ²</i>
11	0.32	38.4	0.68	68.0	0.00	165	1.08
14	0.32	31.5	0.68	56.4	0.00	165	1.09
16	0.62	33.2	0.38	56.2	0.00	165	1.21
19	0.47	27.6	0.53	47.5	0.00	165	1.03
22	0.72	27.9	0.28	50.9	0.00	165	1.06

Table S3.32. Parameters retrieved from the MFA of the excimer decay for Hx-PyBA in degassed DMF with 5 mM HCl.

<i>[Hx-PyBA], mM</i>	<i>f_{Ediff}^p</i>	<i>τ_D (ns)</i>	<i>f_{ED}</i>	<i>χ²</i>
11	0.99	54.9	0.01	1.08
14	0.98	53.5	0.02	1.09
16	0.98	53.2	0.02	1.21
19	0.97	53.1	0.03	1.03
22	0.98	52.4	0.02	1.06

Table S3.33. Parameters retrieved from the MFA of the monomer decay for Hx-PyBA in degassed DMSO.²

<i>[Hx-PyBA], mM</i>	<i>a₁</i>	<i>τ₁ (ns)</i>	<i>a₂</i>	<i>τ₂ (ns)</i>	<i>f_{Mfree}</i>	<i>τ_M</i>	<i>χ²</i>
12	0.10	30.8	0.90	67.5	0.00	138	1.11
15	0.10	26.5	0.90	60.4	0.00	138	1.05
20	0.13	25.0	0.87	51.2	0.00	138	1.09
23	0.24	27.9	0.76	46.7	0.01	138	1.07
26	0.18	24.1	0.82	42.6	0.00	138	1.11

Table S3.34. Parameters retrieved from the MFA of the excimer decay for Hx-PyBA in degassed DMSO.²

<i>Hx-PyBA</i> , mM	f_{Ediff}^D	τ_D (ns)	f_{ED}	χ^2
12	0.99	52.0	0.01	1.11
15	0.98	51.5	0.02	1.05
20	0.98	49.0	0.02	1.09
23	0.97	49.7	0.03	1.07
26	0.97	48.8	0.03	1.11

Table S3.35. Parameters retrieved from the MFA of the monomer decay for Hx-PyBA in degassed DMSO with 5 mM HCl.

<i>[Hx-PyBA]</i> , mM	a_1	τ_1 (ns)	a_2	τ_2 (ns)	f_{Mfree}	τ_M	χ^2
12	0.09	28.4	0.91	67.9	0.00	136	1.04
15	0.09	24.8	0.91	59.4	0.00	136	1.11
20	0.11	23.3	0.89	50.2	0.00	136	1.10
23	0.11	19.4	0.89	44.4	0.00	136	1.06
26	0.17	22.8	0.83	42.0	0.00	136	1.14

Table S3.36. Parameters retrieved from the MFA of the excimer decay for Hx-PyBA in degassed DMSO with 5 mM HCl.

<i>[Hx-PyBA]</i> , mM	f_{Ediff}^D	τ_D (ns)	f_{ED}	χ^2
12	0.99	51.7	0.01	1.04
15	0.98	51.1	0.02	1.11
20	0.98	49.8	0.02	1.10
23	0.98	49.0	0.02	1.06
26	0.97	49.4	0.03	1.14

C) Determination of k_{diff} from plots of $\langle k \rangle$ as a function of [Hx-PyBA] in DMF and DMSO

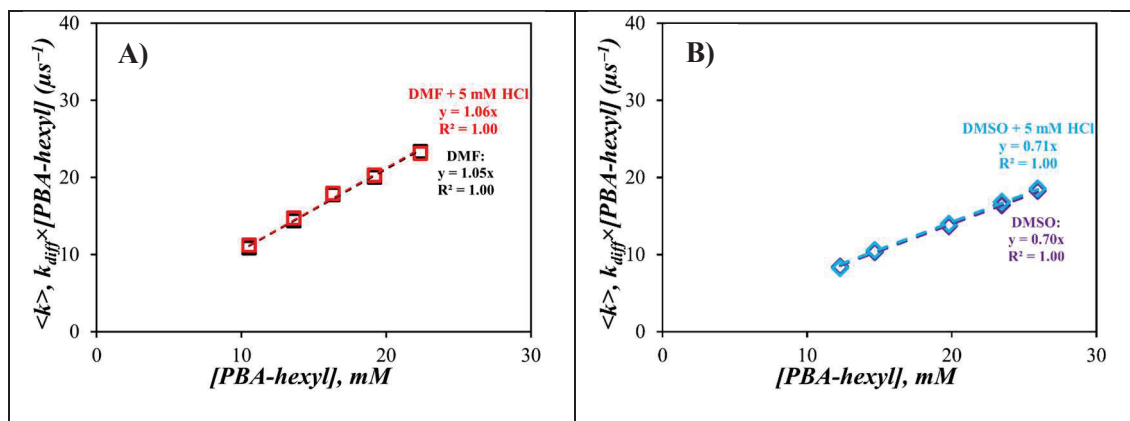


Figure S3.2. Plot of $\langle k \rangle$ as a function of the n-hexyl-1-pyrenebutyramide concentration in A) DMF (■, □) and B) DMSO (◇, ◆) with (■, ◇) and without (□, ◆) of 5 mM HCl, respectively.

Appendix C: S4- SI for Chapter 4

A) ^1H NMR and UV-Vis characterization

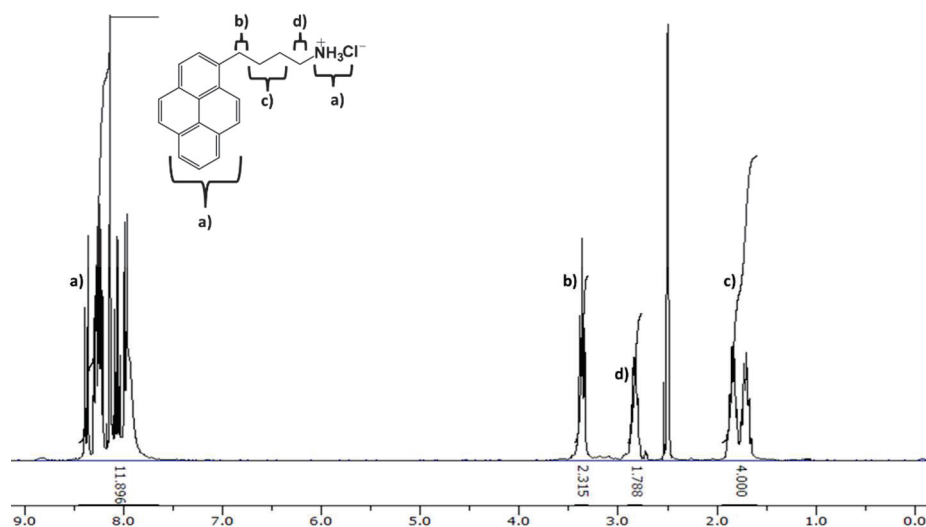


Figure S4.1. ^1H NMR spectrum of 1-pyrenebutylamine hydrochloride acquired in d_6 -DMSO (300 MHz): 1.60-1.95 (m, 4H), 2.77-2.91 (m, 2H), 3.31-3.44 (t, 2H), 7.65-8.45 (m, 12H)

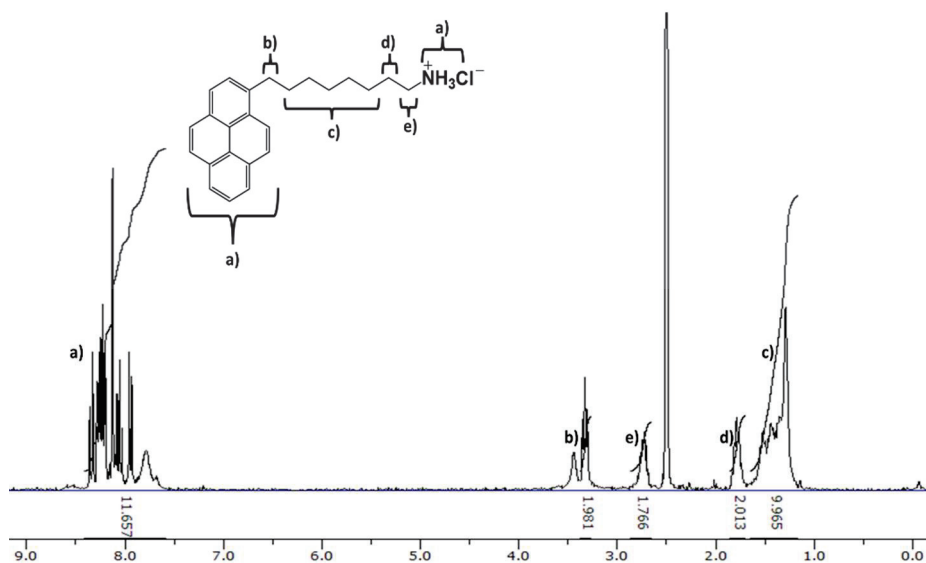


Figure S4.2. ^1H NMR spectrum of 1-pyreneoctylamine hydrochloride acquired in d_6 -DMSO (300 MHz): δ 1.16-1.64 (m, 10H), 1.70-1.86 (p, 2H), 2.66- 2.85 (m, 2H), 3.27-3.38 (t, 2H), 7.59-8.41 (m, 12H). The peak observed at 3.42 ppm near protons *b* was attributed to the water peak which had shifted due to the acidic environment.

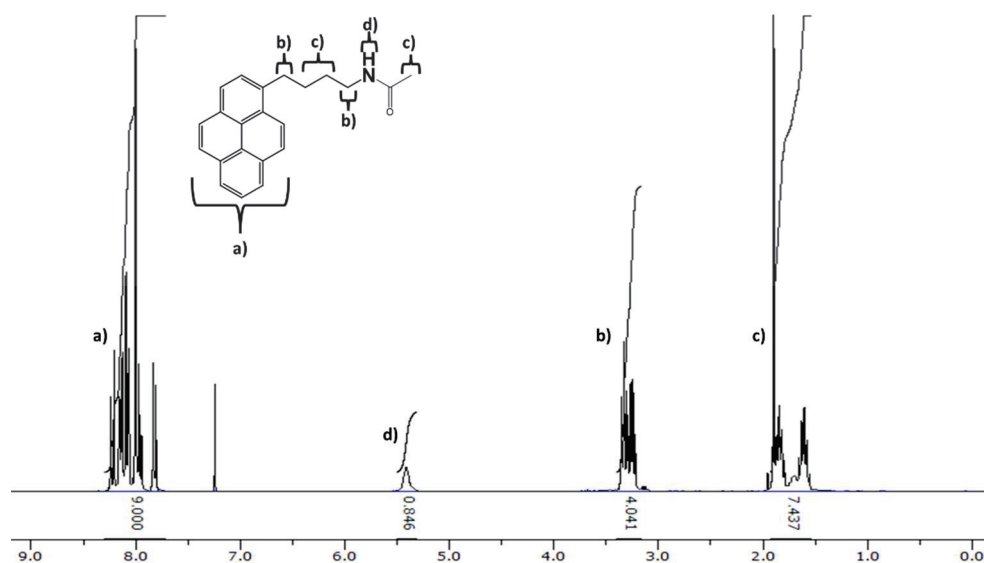


Figure S4.3. ¹H NMR spectrum of 1-pyrenebutylacetamide acquired in CDCl₃ (300 MHz): δ 1.54-1.95 (m, 7H), 3.18-3.41 (m, 4H), 5.29-5.48 (s, 1H), 7.79- 8.28 (m, 9H).

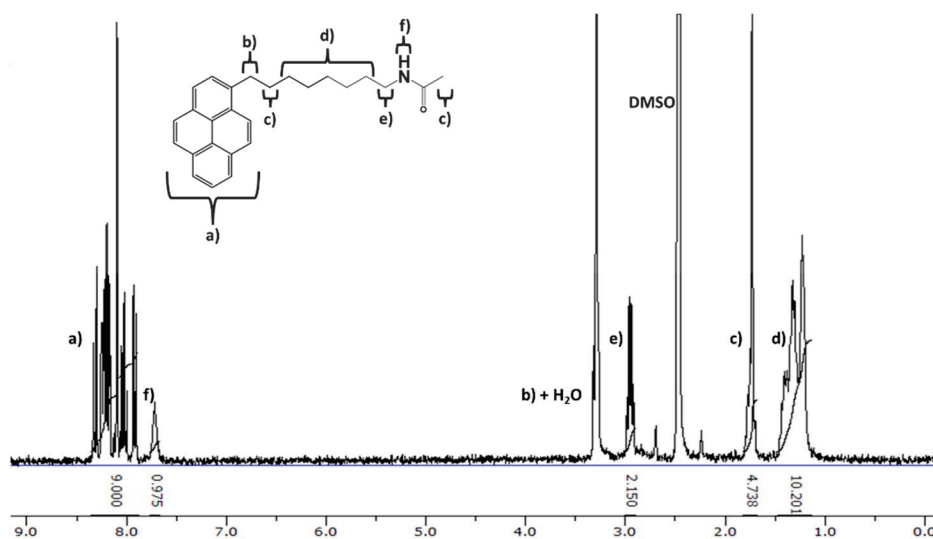


Figure S4.4. ¹H NMR spectrum of 1-pyreneoctylacetamide acquired in *d*₆-DMSO (300 MHz): 1.13-1.48 (m, 10H), 1.68-1.82 (m, 5H), 2.90-3.00 (q, 2H), 7.67-7.77 (broad s, 1H), 7.89-8.36 (m, 9H). Protons *b* were underneath the water peak at 3.32 ppm.

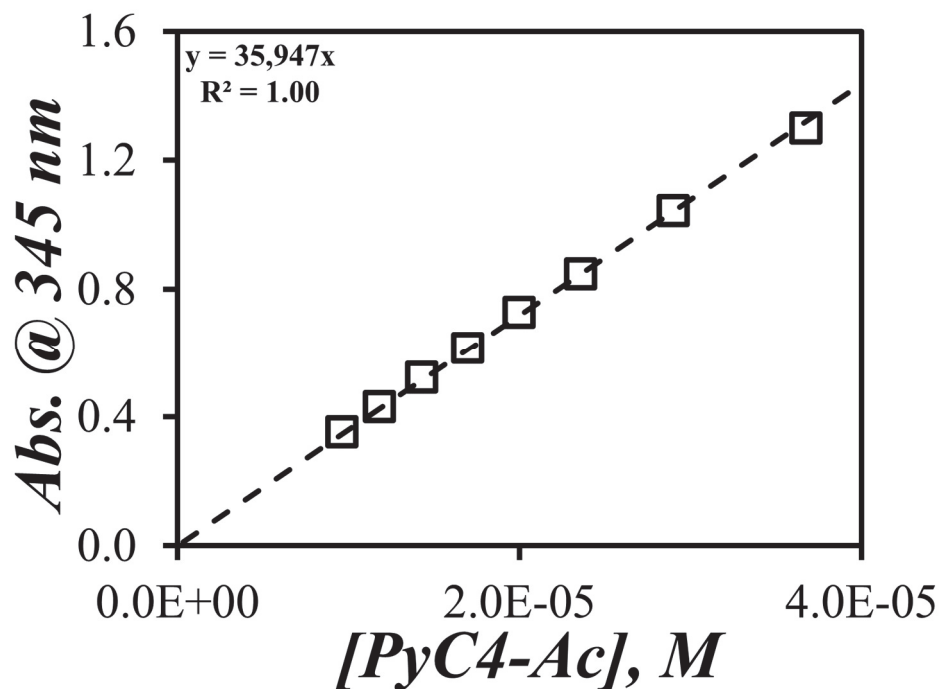


Figure S4.5. Plot of absorbance as a function of 1-pyrenebutylacetamide concentration in DMF.

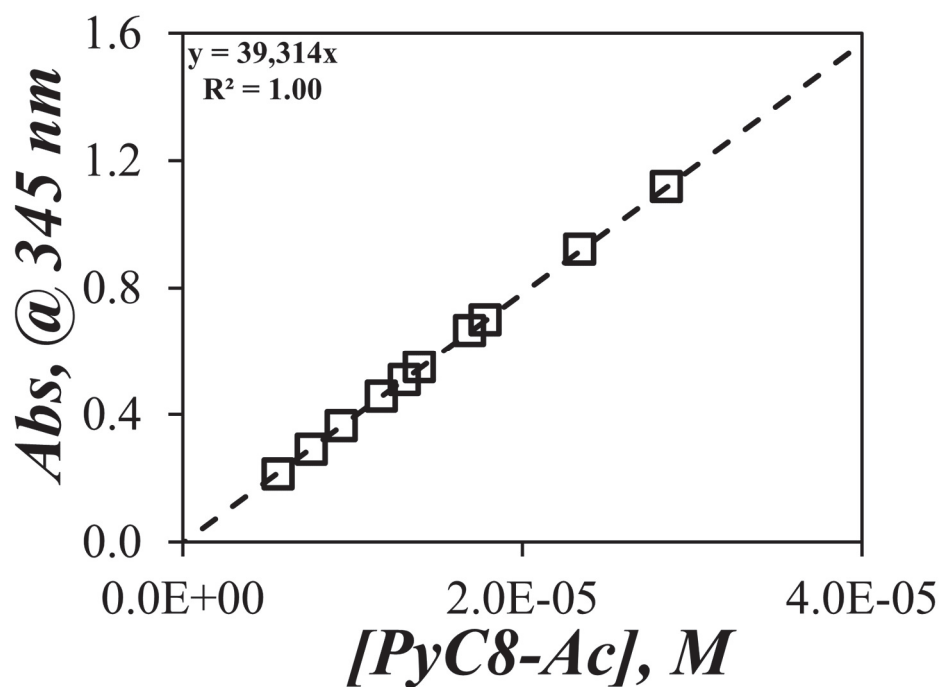


Figure S4.6. Plot of absorbance as a function of 1-pyreneoctylacetamide concentration in DMF.

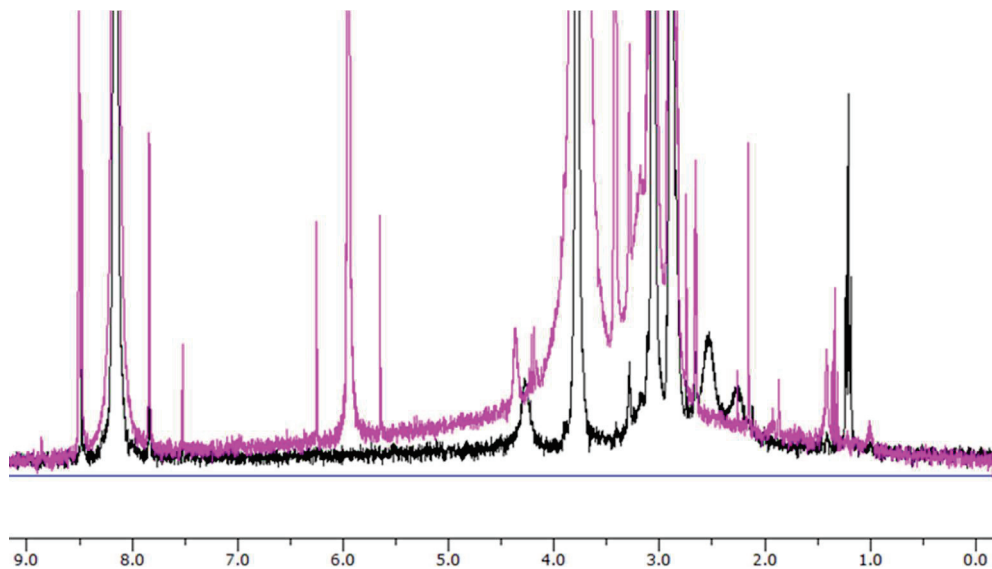


Figure S4.7. ¹H NMR spectra of (black) PLGA and (purple) PDLGA in *d*₇-DMF.

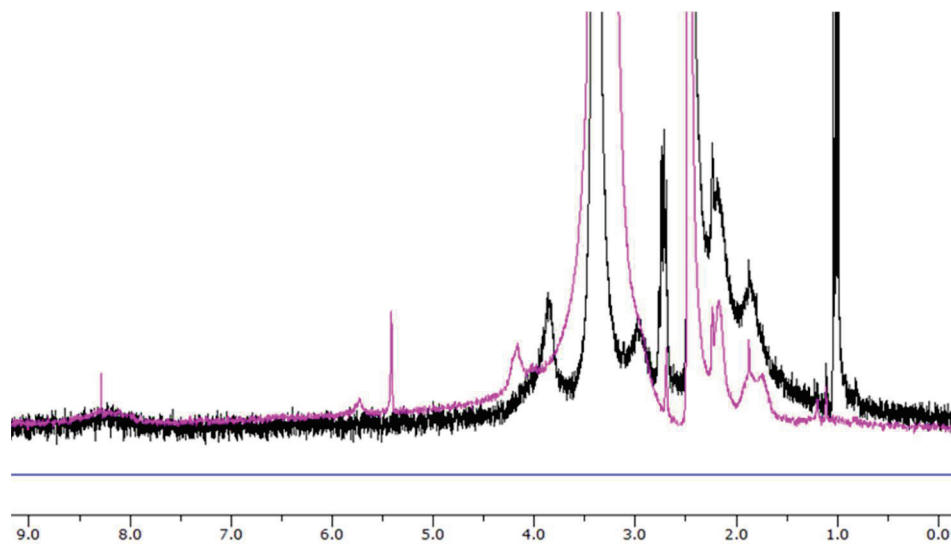


Figure S4.8. ¹H NMR spectra of (black) PLGA and (purple) PDLGA in *d*₆-DMSO.

B] Fluorescence Blob Model (FBM) Analysis

Equations S1 and S2 were used to fit the pyrene monomer and excimer fluorescence decays according to the fluorescence *blob* model.

$$\begin{aligned}
 [Py^*]_{(t)} = & [Py_{diff}^*]_{(t)} + [Py_{k_2}^*]_{(t)} + [Py_{free}^*]_{(t)} = [Py_{diff}]_o \exp\left(-\left(A_2 + \frac{1}{\tau_M}\right)t - A_3(1 - \exp(-A_4 t))\right) \\
 & + \left([Py_{k_2}]_o + [Py_{diff}]_o e^{-A_3} \sum_{i=0}^{\infty} \frac{A_3^i}{i!} \frac{A_2 + iA_4}{A_2 + iA_4 - k_2}\right) \exp\left(-\left(k_2 + \frac{1}{\tau_M}\right)t\right) \\
 & - [Py_{diff}]_o e^{-A_3} \sum_{i=0}^{\infty} \frac{A_3^i}{i!} \frac{A_2 + iA_4}{A_2 + iA_4 - k_2} \exp\left(-\left(A_2 + iA_4 + \frac{1}{\tau_M}\right)t\right) \\
 & + [Py_{free}]_o \exp\left(-\frac{t}{\tau_M}\right) \quad (S1)
 \end{aligned}$$

$$\begin{aligned}
 [E^*]_{(t)} = & [E0^*]_{(t)} + [D^*]_{(t)} = \\
 = & k_2 \left(\left([Py_{k_2}(E0)]_o + [Py_{diff}(E0)]_o e^{-A_3} \sum_{i=0}^{\infty} \frac{A_3^i}{i!} \frac{A_2 + iA_4}{A_2 + iA_4 - k_2} \right) \times \frac{\exp\left(-\frac{t}{\tau_{E0}}\right) - \exp\left(-\left(k_2 + \frac{1}{\tau_M}\right)t\right)}{k_2 + \frac{1}{\tau_M} - \frac{1}{\tau_{E0}}} \right. \\
 & \left. + [Py_{diff}(E0)]_o e^{-A_3} \sum_{i=0}^{\infty} \frac{A_3^i}{i!} \frac{A_2 + iA_4}{A_2 + iA_4 - k_2} \frac{\exp\left(-\left(A_2 + iA_4 + \frac{1}{\tau_M}\right)t\right) - \exp\left(-\frac{t}{\tau_{E0}}\right)}{A_2 + iA_4 + \frac{1}{\tau_M} - \frac{1}{\tau_{E0}}} \right) \\
 + & k_2 \left(\left([Py_{k_2}(D)]_o + [Py_{diff}(D)]_o e^{-A_3} \sum_{i=0}^{\infty} \frac{A_3^i}{i!} \frac{A_2 + iA_4}{A_2 + iA_4 - k_2} \right) \times \frac{\exp\left(-\frac{t}{\tau_D}\right) - \exp\left(-\left(k_2 + \frac{1}{\tau_M}\right)t\right)}{k_2 + \frac{1}{\tau_M} - \frac{1}{\tau_D}} \right. \\
 & \left. + [Py_{diff}(D)]_o e^{-A_3} \sum_{i=0}^{\infty} \frac{A_3^i}{i!} \frac{A_2 + iA_4}{A_2 + iA_4 - k_2} \frac{\exp\left(-\left(A_2 + iA_4 + \frac{1}{\tau_M}\right)t\right) - \exp\left(-\frac{t}{\tau_D}\right)}{A_2 + iA_4 + \frac{1}{\tau_M} - \frac{1}{\tau_D}} \right) \\
 + & [E0]_o \times \exp\left(-\frac{t}{\tau_{E0}}\right) + [D]_o \times \exp\left(-\frac{t}{\tau_D}\right) \quad (S2)
 \end{aligned}$$

The expression of A_2 , A_3 , and A_4 used in Equations S1 and S2 are given in Equation S3.a-c as a function of the parameters $\langle n \rangle$, k_{blob} , and $k_e \times [blob]$.

$$A_2 = \langle n \rangle \times \frac{k_{blob} k_e [blob]}{k_{blob} + k_e [blob]} \quad (S3.a)$$

$$A_3 = \langle n \rangle \times \left(\frac{k_{blob}}{k_{blob} + k_e [blob]} \right)^2 \quad (S3.b)$$

$$A_4 = k_{blob} + k_e [blob] \quad (S3.c)$$

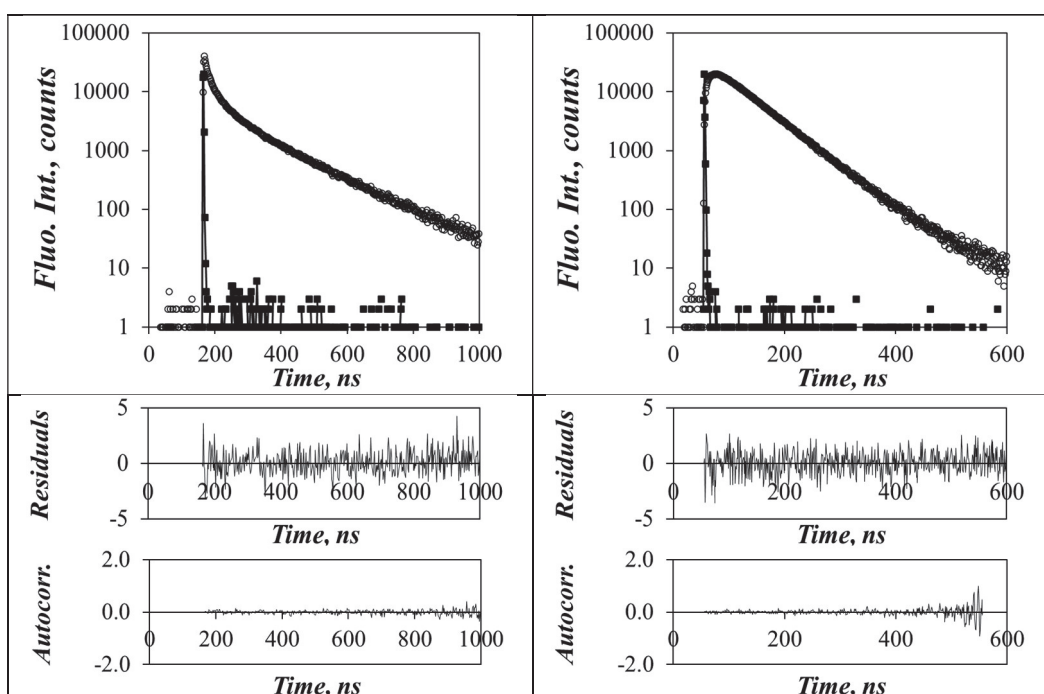


Figure S4.9. Global analysis using the fluorescence blob model (FBM) for the fluorescence decays of the A) monomer and B) excimer acquired at 379 nm and 510 nm, respectively, for the PyC4(15)-PDLGA sample in DMF excited at 345 nm.

C) Parameters retrieved from the FBM analysis

Table S4.1. Parameters retrieved from the FBM analysis of the monomer decays for the PyC4(x)-PLGA samples in DMF.

f_{Py} mol%	k_2 (ns^{-1})	f_{Mk2}	$k_e[\text{blob}]$ (μs^{-1})	f_{Mdiff}	k_{blob} (μs^{-1})	$\langle n \rangle$	τ_M	f_{Mfree}	χ^2
3.0	0.09	0.26	3.5	0.41	10	1.4	162	0.32	1.07
3.1	0.09	0.31	3.1	0.36	9	1.5	162	0.33	1.03
4.1	0.09	0.34	3.3	0.41	10	1.4	162	0.25	1.07
6.1	0.09	0.49	1.9	0.34	8	1.9	162	0.17	1.17
7.6	0.09	0.44	1.8	0.31	5	3.3	162	0.24	1.30
9.4	0.09	0.53	2.2	0.46	8	2.9	162	0.00	1.26

Table S4.2. Parameters retrieved from the FBM analysis of excimer decays for the PyC4(x)-PLGA samples in DMF.

f_{Py} mol%	f_{Ek2}	τ_{E0} (ns^{-1})	$f_{EdiffE0}$	f_{EE0}	τ_D (ns^{-1})	f_{EdiffD}	f_{ED}	χ^2
3.0	0.36	57	0.38	0.04	34	0.19	0.03	1.07
3.1	0.42	48	0.43	0.10	82	0.05	0.00	1.03
4.1	0.41	47	0.37	0.09	69	0.13	0.01	1.07
6.1	0.52	50	0.32	0.13	79	0.03	0.00	1.17
7.6	0.54	43	0.30	0.08	77	0.08	0.00	1.30
9.4	0.46	45	0.28	0.00	56	0.12	0.14	1.26

Table S4.3. Calculated molar fractions of pyrene species from the analysis of the monomer and excimer decays for the PyC4(x)-PLGA samples in DMF.

f_{Py} mol%	f_{k2}	f_{diffE}	f_{diffD}	f_{diff}	f_{E}	f_{D}	f_{agg}	f_{free}	χ^2
3.0	0.29	0.30	0.15	0.45	0.03	0.02	0.05	0.21	1.07
3.1	0.34	0.35	0.04	0.39	0.08	0.00	0.08	0.19	1.03
4.1	0.35	0.31	0.11	0.42	0.08	0.01	0.09	0.14	1.07
6.1	0.48	0.30	0.03	0.33	0.12	0.00	0.12	0.07	1.17
7.6	0.48	0.26	0.07	0.34	0.07	0.00	0.07	0.11	1.30
9.4	0.46	0.28	0.12	0.40	0.00	0.14	0.14	0.00	1.26

Table S4.4. Parameters retrieved from the FBM analysis of the monomer decays for the PyC8(X)-PLGA samples in DMF.

f_{Py} mol%	k_2 (ns^{-1})	$f_{\text{M}k2}$	$k_e[\text{blob}]$ (μs^{-1})	f_{Mdiff}	k_{blob} (μs^{-1})	$\langle n \rangle$	τ_{M}	f_{Mfree}	χ^2
1.7	0.16	0.15	1	0.40	13	1.4	155	0.45	1.13
2.2	0.16	0.21	5	0.31	17	1.7	155	0.48	1.22
3.0	0.16	0.37	4	0.34	16	1.8	155	0.29	1.06
4.6	0.16	0.60	3	0.33	14	2.1	155	0.07	1.22
4.7	0.16	0.55	4	0.33	16	2.0	155	0.12	1.15

Table S4.5. Parameters retrieved from the FBM analysis of excimer decays for the PyC8(*X*)-PLGA samples in DMF.

f_{Py} mol%	f_{Ek2}	τ_{E0} (ns ⁻¹)	f_{EdiffE0}	f_{EE0}	τ_{D} (ns ⁻¹)	f_{EdiffD}	f_{ED}	χ^2
1.7	0.26	38	0.46	0.02	76	0.25	0.00	1.13
2.2	0.37	47	0.47	0.08	90	0.72	0.01	1.22
3.0	0.49	45	0.38	0.01	68	0.06	0.05	1.06
4.6	0.61	46	0.29	0.04	67	0.04	0.02	1.22
4.7	0.59	49	0.33	0.04	69	0.02	0.01	1.15

Table S4.6. Calculated molar fractions of pyrene species from the analysis of the monomer and excimer decays for the PyC8(*X*)-PLGA samples in DMF.

f_{py} mol%	f_{k2}	f_{diffE}	f_{diffD}	f_{diff}	f_{E}	f_{D}	f_{agg}	f_{free}	χ^2
1.7	0.16	0.29	0.16	0.45	0.02	0.00	0.02	0.37	1.13
2.2	0.13	0.17	0.26	0.43	0.03	0.00	0.03	0.40	1.22
3.0	0.42	0.32	0.06	0.37	0.01	0.05	0.06	0.15	1.06
4.6	0.60	0.29	0.04	0.32	0.04	0.02	0.06	0.02	1.22
4.7	0.57	0.32	0.02	0.34	0.04	0.01	0.05	0.04	1.15

Table S4.7. Parameters retrieved from the FBM analysis of the monomer decays for the PyC4(X)-PLGA samples in DMSO.

f_{Py} mol%	k_2 (ns^{-1})	f_{Mk2}	$k_e[\text{blob}]$ (μs^{-1})	f_{Mdiff}	k_{blob} (μs^{-1})	$\langle n \rangle$	τ_M	f_{Mfree}	χ^2
3.0	-	-	-	-	-	-	-	-	-
3.1	0.08	0.22	5	0.51	11	1.2	137	0.27	1.19
4.1	0.08	0.24	5	0.55	12	1.1	137	0.21	1.07
6.1	0.08	0.37	4	0.52	8	1.7	137	0.12	1.06
7.6	0.08	0.32	3	0.50	7	2.1	137	0.19	1.12
9.4	0.08	0.56	5	0.41	14	2.5	137	0.04	1.10

Table S4.8. Parameters retrieved from the FBM analysis of excimer decays for the PyC4(X)-PLGA samples in DMSO.

f_{Py} mol%	f_{Ek2}	τ_{E0} (ns^{-1})	$f_{EdiffE0}$	f_{EE0}	τ_D (ns^{-1})	f_{EdiffD}	f_{ED}	χ^2
3.0	-	-	-	-	-	-	-	-
3.1	0.27	49	0.57	0.10	45	0.06	0.00	1.19
4.1	0.28	51	0.50	0.07	48	0.13	0.02	1.07
6.1	0.37	47	0.46	0.10	63	0.06	0.01	1.06
7.6	0.36	45	0.52	0.06	84	0.05	0.00	1.12
9.4	0.50	80	0.01	0.08	50	0.36	0.06	1.10

Table S4.9. Calculated molar fractions of pyrene species from the analysis of the monomer and excimer decays for the PyC4(*X*)-PLGA samples in DMSO.

f_{py} mol%	f_{k2}	f_{diffE}	f_{diffD}	f_{diff}	f_{E}	f_{D}	f_{agg}	f_{free}	χ^2
3.0	-	-	-	-	-	-	-	-	-
3.1	0.22	0.46	0.05	0.51	0.08	0.00	0.08	0.19	1.19
4.1	0.24	0.43	0.11	0.54	0.06	0.01	0.08	0.14	1.07
6.1	0.35	0.43	0.06	0.49	0.09	0.01	0.10	0.07	1.06
7.6	0.32	0.46	0.05	0.51	0.05	0.00	0.05	0.12	1.12
9.4	0.49	0.01	0.35	0.36	0.08	0.06	0.14	0.01	1.10

Table S4.10. Parameters retrieved from the FBM analysis of the monomer decays for the PyC8(*X*)-PLGA samples in DMSO.

f_{Py} mol%	k_2 (ns^{-1})	$f_{\text{M}k2}$	$k_e[\text{blob}]$ (μs^{-1})	f_{Mdiff}	k_{blob} (μs^{-1})	$\langle n \rangle$	τ_{M}	f_{Mfree}	χ^2
1.7	0.15	0.10	1	0.52	13	0.8	128	0.39	1.17
2.2	0.15	0.17	4	0.35	15	1.4	128	0.48	1.06
3.0	0.15	0.19	5	0.55	12	1.5	128	0.25	1.04
4.6	0.15	0.35	6	0.45	14	1.8	128	0.20	1.03
4.7	0.15	0.37	4	0.55	13	1.9	128	0.08	1.14

Table S4.11. Parameters retrieved from the FBM analysis of excimer decays for the PyC8(*X*)-PLGA samples in DMSO.

f_{Py} mol%	f_{Ek2}	τ_{E0} (ns ⁻¹)	f_{EdiffE0}	f_{EE0}	τ_{D} (ns ⁻¹)	f_{EdiffD}	f_{ED}	χ^2
1.7	0.15	34	0.56	0.00	73	0.24	0.04	1.17
2.2	0.28	45	0.52	0.08	77	0.07	0.04	1.06
3.0	0.24	45	0.57	0.06	66	0.13	0.00	1.04
4.6	0.39	46	0.47	0.11	77	0.03	0.00	1.03
4.7	0.47	44	0.47	0.02	61	0.10	0.02	1.14

Table S4.12. Calculated molar fractions of pyrene species from the analysis of the monomer and excimer decays for the PyC8(*X*)-PLGA samples in DMSO.

f_{py} mol%	f_{k2}	f_{diffE}	f_{diffD}	f_{diff}	f_{E}	f_{D}	f_{agg}	f_{free}	χ^2
1.7	0.10	0.37	0.16	0.53	0.00	0.03	0.03	0.34	1.17
2.2	0.18	0.34	0.04	0.38	0.05	0.03	0.08	0.35	1.06
3.0	0.20	0.46	0.10	0.56	0.05	0.00	0.05	0.19	1.04
4.6	0.35	0.41	0.03	0.44	0.10	0.00	0.10	0.11	1.03
4.7	0.42	0.42	0.09	0.51	0.01	0.01	0.03	0.04	1.14

Table S4.13. Parameters retrieved from the FBM analysis of the monomer decays for the PyC4(X)-PDLGA samples in DMF.

f_{Py} mol%	k_2 (ns^{-1})	$f_{\text{Mk}2}$	$k_e[\text{blob}]$ (μs^{-1})	f_{Mdiff}	k_{blob} (μs^{-1})	$\langle n \rangle$	τ_{M}	f_{Mfree}	χ^2
6.9	0.09	0.27	4	0.45	10	1.6	162	0.27	1.17
7.8	0.09	0.28	2	0.44	10	1.9	162	0.28	1.13
9.3	0.09	0.38	4	0.41	10	2.0	162	0.20	1.16
12.0	0.09	0.45	4	0.40	10	2.2	162	0.16	1.19
15.3	0.09	0.58	5	0.33	11	2.8	162	0.09	1.12

Table S4.14. Parameters retrieved from the FBM analysis of excimer decays for the PyC4(X)-PDLGA samples in DMF.

f_{Py} mol%	$f_{\text{Ek}2}$	$\tau_{\text{E}0}$ (ns^{-1})	$f_{\text{EdiffE}0}$	$f_{\text{EE}0}$	τ_{D} (ns^{-1})	f_{EdiffD}	f_{ED}	χ^2
6.9	0.33	47	0.43	0.12	72	0.11	0.01	1.17
7.8	0.34	58	0.36	0.10	40	0.17	0.02	1.13
9.3	0.41	50	0.36	0.06	63	0.09	0.08	1.16
12.0	0.46	49	0.32	0.04	63	0.09	0.09	1.19
15.3	0.55	50	0.30	0.11	78	0.01	0.03	1.12

Table S4.15. Calculated molar fractions of pyrene species from the analysis of the monomer and excimer decays for the PyC4(X)-PDLGA samples in DMF.

f_{py} mol%	f_{k2}	f_{diffE}	f_{diffD}	f_{diff}	f_{E}	f_{D}	f_{agg}	f_{free}	χ^2
6.9	0.28	0.36	0.09	0.45	0.10	0.01	0.11	0.17	1.17
7.8	0.29	0.30	0.14	0.44	0.08	0.02	0.10	0.17	1.13
9.3	0.37	0.32	0.08	0.40	0.05	0.07	0.13	0.10	1.16
12.0	0.42	0.30	0.08	0.38	0.04	0.09	0.13	0.07	1.19
15.3	0.53	0.29	0.01	0.30	0.11	0.03	0.14	0.03	1.12

Table S4.16. Parameters retrieved from the FBM analysis of the monomer decays for the PyC4(X)-PDLGA samples in DMSO.

f_{Py} mol%	k_2 (ns^{-1})	f_{Mk2}	$k_e[\text{blob}]$ (μs^{-1})	f_{Mdiff}	k_{blob} (μs^{-1})	$\langle n \rangle$	τ_{M}	f_{Mfree}	χ^2
6.9	0.06	0.27	8	0.49	12	1.0	137	0.24	1.22
7.8	0.06	0.24	6	0.45	9	1.6	137	0.30	1.13
9.3	0.06	0.33	6	0.46	8	1.8	137	0.21	1.06
12.0	0.06	0.39	5	0.46	7	1.9	137	0.14	1.24
15.3	0.06	0.47	7	0.42	9	2.5	137	0.10	1.17

Table S4.17. Parameters retrieved from the FBM analysis of excimer decays for the PyC4(X)-PDLGA samples in DMSO.

f_{Py} mol%	f_{Ek2}	τ_{E0} (ns ⁻¹)	f_{EdiffE0}	f_{EE0}	τ_{D} (ns ⁻¹)	f_{EdiffD}	f_{ED}	χ^2
6.9	0.31	51	0.36	0.07	51	0.21	0.06	1.22
7.8	0.31	55	0.31	0.02	42	0.27	0.08	1.13
9.3	0.37	55	0.19	0.08	47	0.33	0.04	1.06
12.0	0.40	50	0.19	0.08	49	0.29	0.03	1.24
15.3	0.46	49	0.41	0.12	105	0.00	0.00	1.17

Table S4.18. Calculated molar fractions of pyrene species from the analysis of the monomer and excimer decays for the PyC4(X)-PDLGA samples in DMSO.

f_{py} mol%	f_{k2}	f_{diffE}	f_{diffD}	f_{diff}	f_{E}	f_{D}	f_{agg}	f_{free}	χ^2
6.9	0.26	0.30	0.18	0.48	0.06	0.05	0.11	0.15	1.22
7.8	0.25	0.25	0.21	0.46	0.02	0.07	0.09	0.20	1.13
9.3	0.33	0.17	0.29	0.45	0.07	0.03	0.10	0.12	1.06
12.0	0.37	0.17	0.27	0.44	0.08	0.03	0.11	0.07	1.24
15.3	0.44	0.39	0.00	0.40	0.12	0.00	0.12	0.04	1.17

Table S4.19. Parameters retrieved from the FBM analysis of the monomer decays for the PyC8(X)-PDLGA samples in DMF.

f_{Py} mol%	k_2 (ns^{-1})	$f_{\text{Mk}2}$	$k_e[\text{blob}]$ (μs^{-1})	f_{Mdiff}	k_{blob} (μs^{-1})	$\langle n \rangle$	τ_{M}	f_{Mfree}	χ^2
2.6	0.16	0.15	0.2	0.40	19	1.0	155	0.44	1.14
2.7	0.16	0.08	0.3	0.47	16	0.8	155	0.45	1.13
4.0	0.16	0.15	0.3	0.42	13	1.6	155	0.43	1.22
5.0	0.16	0.22	3.9	0.50	17	1.6	155	0.28	1.16
7.6	0.16	0.26	7.2	0.40	13	2.3	155	0.33	1.12

Table S4.20. Parameters retrieved from the FBM analysis of excimer decays for the PyC8(X)-PDLGA samples in DMF.

f_{Py} mol%	$f_{\text{Ek}2}$	$\tau_{\text{E}0}$ (ns^{-1})	$f_{\text{EdiffE}0}$	$f_{\text{EE}0}$	τ_{D} (ns^{-1})	f_{EdiffD}	f_{ED}	χ^2
2.6	0.26	63	0.33	0.00	38	0.38	0.04	1.14
2.7	0.14	63	0.39	0.04	30	0.43	0.00	1.13
4.0	0.26	39	0.50	0.01	73	0.23	0.00	1.22
5.0	0.29	56	0.41	0.02	54	0.26	0.02	1.16
7.6	0.38	47	0.44	0.04	70	0.14	0.00	1.12

Table S4.21. Calculated molar fractions of pyrene species from the analysis of the monomer and excimer decays for the PyC8(*X*)-PDLGA samples in DMF.

f_{py} mol%	f_{k2}	f_{diffE}	f_{diffD}	f_{diff}	f_{E}	f_{D}	f_{agg}	f_{free}	χ^2
2.6	0.17	0.21	0.24	0.45	0.00	0.02	0.02	0.36	1.14
2.7	0.08	0.23	0.26	0.49	0.03	0.00	0.03	0.40	1.13
4.0	0.17	0.32	0.15	0.47	0.00	0.01	0.01	0.35	1.22
5.0	0.23	0.33	0.20	0.53	0.02	0.02	0.03	0.21	1.16
7.6	0.30	0.34	0.11	0.45	0.03	0.00	0.03	0.22	1.12

Table S4.22. Parameters retrieved from the FBM analysis of the monomer decays for the PyC8(*X*)-PDLGA samples in DMSO.

f_{Py} mol%	k_2 (ns^{-1})	$f_{\text{MK}2}$	$k_e[\text{blob}]$ (μs^{-1})	f_{Mdiff}	k_{blob} (μs^{-1})	$\langle n \rangle$	τ_{M}	f_{Mfree}	χ^2
2.6	-	-	-	-	-	-	-	-	-
2.7	0.15	0.07	1	0.29	11	1.7	128	0.64	1.07
4.0	0.15	0.11	4	0.42	10	1.7	128	0.47	1.06
5.0	0.15	0.17	4	0.54	14	1.4	128	0.29	1.32
7.6	0.15	0.21	4	0.42	11	2.2	128	0.37	1.30

Table S4.23. Parameters retrieved from the FBM analysis of excimer decays for the PyC8(*X*)-PDLGA samples in DMSO.

f_{Py} mol%	f_{Ek2}	τ_{E0} (ns ⁻¹)	f_{EdiffE0}	f_{EE0}	τ_{D} (ns ⁻¹)	f_{EdiffD}	f_{ED}	χ^2
2.6	-	-	-	-	-	-	-	-
2.7	0.19	61	0.43	0.04	39	0.30	0.04	1.07
4.0	0.20	44	0.45	0.05	60	0.30	0.00	1.06
5.0	0.22	52	0.46	0.05	54	0.26	0.00	1.32
7.6	0.31	47	0.47	0.05	61	0.15	0.01	1.30

Table S4.24. Calculated molar fractions of pyrene species from the analysis of the monomer and excimer decays for the PyC8(*X*)-PDLGA samples in DMSO.

f_{py} mol%	f_{k2}	f_{diffE}	f_{diffD}	f_{diff}	f_{E}	f_{D}	f_{agg}	f_{free}	χ^2
2.6	-	-	-	-	-	-	-	-	-
2.7	0.08	0.19	0.13	0.32	0.02	0.02	0.03	0.57	1.07
4.0	0.12	0.27	0.18	0.45	0.03	0.00	0.03	0.40	1.06
5.0	0.17	0.36	0.20	0.56	0.04	0.00	0.04	0.23	1.32
7.6	0.23	0.34	0.11	0.46	0.04	0.01	0.05	0.27	1.30

D] Molecular Mechanic Optimization:

Determination of the reach of a pyrenyl label inside a blob: Since the reach of a given pyrenyl label inside a *blob* is directly related to the length of the linker connecting the pyrene moiety to the macromolecule, the distance corresponding to the reach of a pyrenyl label inside a *blob* can be estimated using HyperChem simulations. A brief description of the process is provided for an L-glutamic acid residue labeled with 1-pyrenemethylamine. A restraint of 99 Å was placed between the α -C and P15, shown in Figure S4.10, and the construct was fully stretched via geometry optimization using a Fletcher-Reeves algorithm with RMS gradient of 0.1 kcal/(Å mol). Once completed the restraint was removed and the construct was re-optimized with no restraints. The coordinates of P15 and P16 were used to determine the coordinates for the center of mass (CoM) of the pyrene dye and the distance between the CoM for the pyrenyl dye and the α -C was calculated and found to equal 9.9 Å. Since the pyrenyl moiety can encounter the center of another pyrenyl dye 9.9 Å away, the reach for a pyrene dye is equal to $9.9 \text{ Å} \times 2 = 19.8 \text{ Å}$. Consequently, the α -C linked to the pyrenyl label can be viewed as being at the center of a *blob* with a diameter equal to 39.6 Å ($=2 \times 19.8 \text{ Å}$).

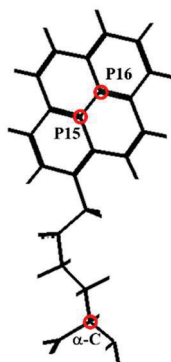


Figure S4.10. Structure of 1-pyrene methylamine labeled onto a L-glutamic acid residue.

Table S4.14. Coordinates used to calculate the distance corresponding to the maximum reach of a pyrenyl label covalently attached onto an L-glutamic acid residue.

Pyrene Derivative	Blob Diameter (nm)	Position	x	y	z
1-pyrene methylamine	4.0	P16	0.07	11.91	2.49
		P15	0.17	10.44	2.45
		CoM of pyrene	0.12	11.18	2.47
		α -C	-0.63	1.40	1.19
1-pyrene butylamine	5.7	P16	-1.68	13.93	3.22
		P15	-1.13	12.61	2.91
		CoM of pyrene	-1.41	13.27	3.06
		α -C	-2.96	-0.97	1.93
1-pyrene octylamine	7.7	P16	-0.81	16.31	3.27
		P15	-0.04	15.06	3.26
		CoM of pyrene	-0.43	15.69	3.26
		α -C	-0.76	-3.46	0.83

Determination of $N_{\text{blob}}^{\text{MMO}}$: As mentioned in the main text, $N_{\text{blob}}^{\text{MMO}}$ was determined in the same manner as in previous publications¹⁻⁴ for 4 different backbone conformations labeled with either 1-pyrenebutylamine or 1-pyreneoctylamine. To ensure accurate $N_{\text{blob}}^{\text{MMO}}$ values, positions at 5 carbons belonging to a pyrene moiety (P4, P7, P11, P14, and P17 in Figure S4.11A) were considered to set restraints requiring two specific positions to be within 3.4 Å from each other. Molecular mechanics optimizations (MMO) were conducted such that restraints between the reference pyrene (red) and adjacent pyrene (black) label would result in either a head-to-head or head-to-tail contact as illustrated in Figure S4.11B and C, respectively. As long as one of the two simulations yielded seven or more C-C overlap between the frames of the two pyrene dyes, which had to remain planar, this spatial arrangement was expected to be conducive of pyrene excimer formation (PEF) and the Glu residue bearing the secondary pyrenyl label was tallied to yield N_o , the number of Glu separating two pyrene-labeled Glu while still allowing good overlap. A good

overlap was defined when the number (n_c) of carbons in the frame of one pyrene overlapping the frame of the other pyrene was larger than 7.⁵ The procedure was repeated by moving the secondary pyrenyl label one Glu residue at a time until the primary and secondary pyrenyl labels could no longer overlap. The N_o value represented the number of Glu on one side of the reference pyrenyl label that could be labeled with a secondary pyrene and yield a good overlap that was expected to result in PEF. Accounting for the fact that a secondary pyrenyl label located on the other side of the reference pyrene could also form an excimer, $N_{\text{blob}}^{\text{theo}}$ was obtained as $2 \times N_o + 1$, where “1” was added to account for the reference pyrene.

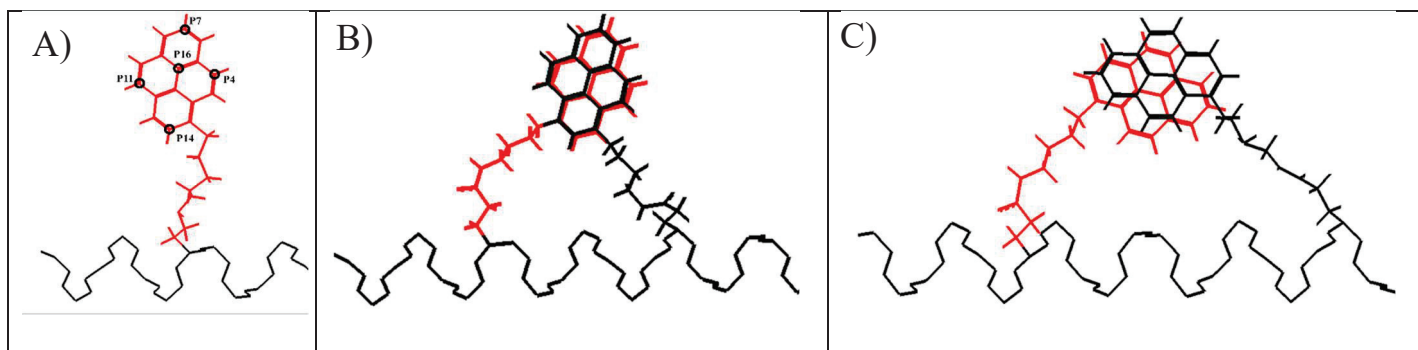


Figure S4.11. HyperChem renderings of PLGA with an α -helical conformation where the reference pyrene dye (red) has been labeled on the 7th glutamic acid residue. Figure A) represents the carbons used to impose restraints to result in either a B) head-*to*-head or C) head-*to*-tail encounter between the reference pyrene and the secondary pyrene dye (black). Note: The side chains of non-pyrene labeled glutamic acid residues were hidden.

Appendix D: S5- SI for Chapter 5

A) ^1H NMR and UV-vis characterization of the pyrenyl derivatives

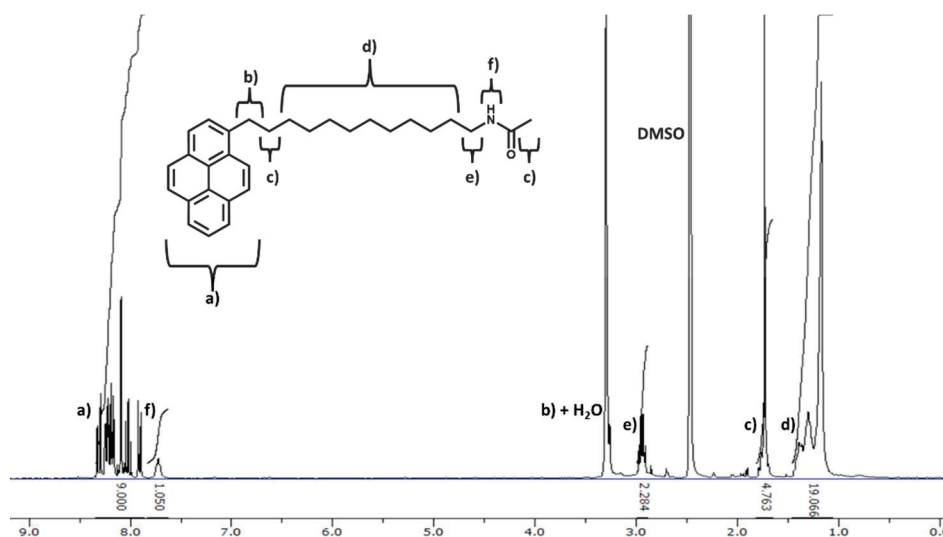


Figure S5.1. ^1H NMR spectrum of 1-pyrenedodecylacetamide acquired in d_6 -DMSO (300 MHz): δ 1.03-1.50 (m, 19H), 1.64-1.84 (m, 5H), 2.89-2.99 (q, 2H), 7.63-7.82 (s, 1H), 7.85-8.37 (m, 9H). Protons b) are under the water peak (3.3 ppm).

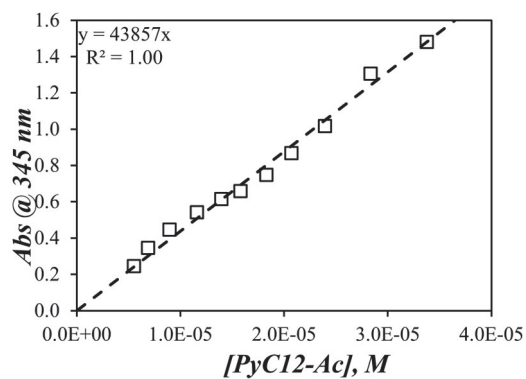


Figure S5.2. Plot of the absorbance at 345 nm as a function of 1-pyrenedodecylacetamide concentration in DMF.

B] Fluorescence Blob Model (FBM) analysis

Equations S5.1 and S5.2 were used to globally fit the monomer and excimer fluorescence decays according to the fluorescence *blob* model.

$$\begin{aligned}
 [Py^*] = & [Py_{diff}^*]_{t=0} \exp\left(-\left(A_2 + \frac{1}{\tau_M}\right)t - A_3(1 - \exp(-A_4 t))\right) + \\
 & \left([Py_{diff}^*]_{t=0} + [Py_{diff}^*]_{t=0} \exp(A_3) \sum_{i=0}^{\infty} \frac{A_3^i}{i!} \frac{A_2 + iA_4}{A_2 + iA_4 - k_2}\right) \exp\left(-\left(k_2 + \frac{1}{\tau_M}\right)t\right) \\
 & - [Py_{diff}^*]_{t=0} \exp(A_3) \sum_{i=0}^{\infty} \frac{A_3^i}{i!} \frac{A_2 + iA_4}{A_2 + iA_4 - k_2} \exp\left(-\left(A_2 + iA_4 + \frac{1}{\tau_M}\right)t\right) \\
 & + [Py_{free}^*]_{t=0} \exp\left(-\frac{t}{\tau_M}\right)
 \end{aligned} \tag{S5.1}$$

$$\begin{aligned}
 [E^*] = & k_2 \left([Py_{k_2}^*]_{t=0} + [Py_{diff}^*]_{t=0} \exp(-A_3) \sum_{i=0}^{\infty} \frac{A_3^i}{i!} \frac{A_2 + iA_4}{A_2 + iA_4 - k_2} \right) \\
 & \times \frac{\exp\left(-\frac{t}{\tau_{E0}}\right) - \exp\left(-\left(k_2 + \frac{1}{\tau_M}\right)t\right)}{k_2 + \frac{1}{\tau_M} - \frac{t}{\tau_{E0}}} + [Py_{diff}^*]_{t=0} \exp(-A_3) \\
 & \times \sum_{i=0}^{\infty} \frac{A_3^i}{i!} \frac{A_2 + iA_4}{A_2 + iA_4 - k_2} \frac{\exp\left(-\left(A_2 + iA_4 + \frac{1}{\tau_M}\right)t\right) - \exp\left(-\frac{t}{\tau_{E0}}\right)}{A_2 + iA_4 + \frac{1}{\tau_M} - \frac{1}{\tau_{E0}}} \\
 & + [E0^*]_{t=0} \times \exp\left(-\frac{t}{\tau_{E0}}\right) + [EL^*]_{t=0} \times \exp\left(-\frac{t}{\tau_{EL}}\right) + [ES^*]_{t=0} \times \exp\left(-\frac{t}{\tau_{ES}}\right)
 \end{aligned} \tag{S5.2}$$

The expressions of A_2 , A_3 and A_4 uses in Equations S5.1 and S5.2 are given in Equations S5.3a-c as a function of the parameters $\langle n \rangle$, k_{blob} , and $k_e \times [blob]$.

$$A_2 = \langle n \rangle \frac{k_{blob} k_e [blob]}{k_{blob} + k_e [blob]} \quad (S5.3a)$$

$$A_3 = \langle n \rangle \left(\frac{k_{blob}}{k_{blob} + k_e [blob]} \right)^2 \quad (S5.3b)$$

$$A_4 = k_{blob} + k_e [blob] \quad (S5.3c)$$

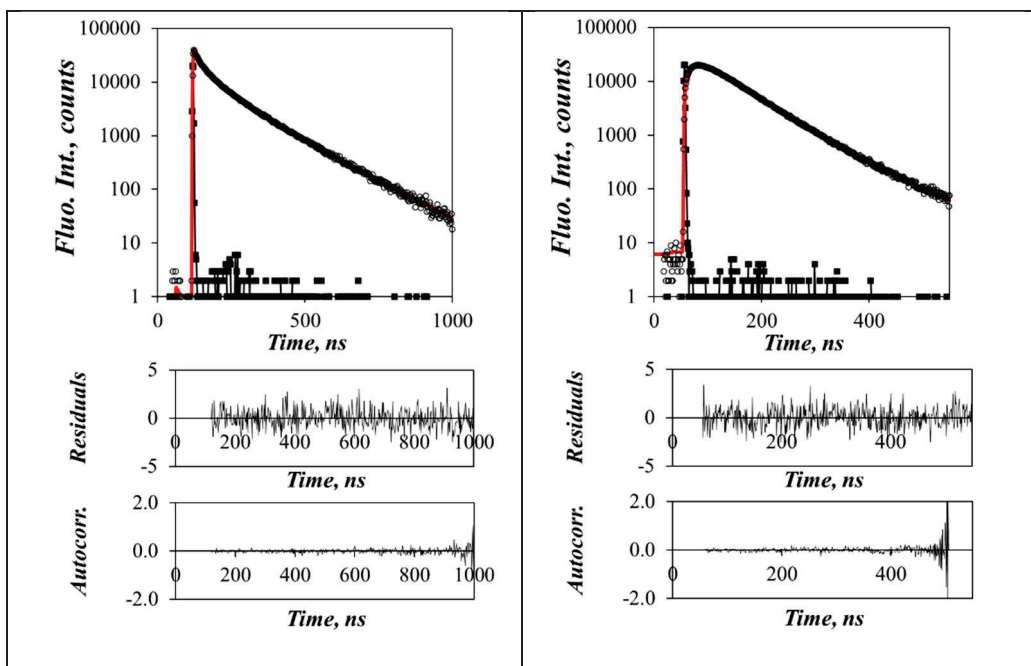


Figure S5.3. Representative fits with the global fluorescence blob model (FBM) analysis of the fluorescence decays of the pyrene A) monomer and B) excimer acquired at 379 nm and 510 nm, respectively, for the PyC12N(2.3)-PNb-Ac sample in DMSO excited at 345 nm.

C] Global analysis of the monomer and excimer fluorescence decays with the FBM

Table S5.1. Parameters retrieved from the FBM analysis of the monomer fluorescence decays of the PyC1N(x)-PNb samples in DMF.

F_{py} (mol%)	k_2 (ns ⁻¹)	f_{Mk2}	$k_e[\text{blob}]$ (μs^{-1})	f_{Mdiff}	k_{blob} (μs^{-1})	$\langle n \rangle$	τ_M (ns)	f_{Mfree}	χ^2
5.6	0.13	0.14	3	0.61	10	0.9	215	0.25	1.14
7.8	0.13	0.29	3	0.64	9	1.5	215	0.07	1.13
9.0	0.13	0.21	3	0.72	9	1.3	215	0.07	1.12
11.0	0.13	0.30	3	0.65	8	1.8	215	0.05	1.10
15.0	0.13	0.37	3	0.62	10	2.3	215	0.02	1.15

Table S5.2. Parameters retrieved from the FBM analysis of the excimer fluorescence decays of the PyC1N(x)-PNb samples in DMF.

f_{py} (mol%)	f_{Ek2}	τ_{E0} (ns)	$f_{EdiffE0}$	f_{EE0}	τ_D (ns)	f_{ED}	χ^2
5.6	0.17	36	0.59	0.03	91	0.03	1.14
7.8	0.28	45	0.51	0.10	88	0.00	1.13
9.0	0.21	28	0.39	0.05	64	0.00	1.12
11.0	0.29	42	0.50	0.07	81	0.00	1.10
15.0	0.34	40	0.41	0.06	73	0.03	1.15

Table S5.3. Molar fractions of the pyrene species obtained from the FBM analysis of the monomer and excimer fluorescence decays of the PyC1N(x)-PNb samples in DMF.

f_{py} (mol%)	f_{k2}	f_{diff}	f_E	f_D	f_{agg}	f_{free}	χ^2
5.6	0.17	0.58	0.03	0.03	0.05	0.19	1.14
7.8	0.30	0.55	0.11	0.00	0.11	0.04	1.13
9.0	0.31	0.57	0.07	0.00	0.07	0.05	1.12
11.0	0.33	0.57	0.08	0.00	0.08	0.03	1.10
15.0	0.40	0.48	0.08	0.04	0.11	0.01	1.15

Table S5.4. Parameters retrieved from the FBM analysis of the monomer fluorescence decays of the PyC4N(x)-PNb samples in DMF.

f_{py} (mol%)	k_2 (ns ⁻¹)	f_{Mk2}	$k_c[\text{blob}]$ (μs^{-1})	f_{Mdiff}	k_{blob} (μs^{-1})	$\langle n \rangle$	τ_{M} (ns)	f_{Mfree}	χ^2
6.8	0.08	0.25	7	0.59	11	1.21	155	0.16	1.03
8.2	0.08	0.37	4	0.56	7	2.14	155	0.07	1.10
10.3	0.08	0.44	3	0.53	7	2.45	155	0.03	1.10
10.5	0.08	0.62	1	0.37	6	3.19	155	0.02	1.21
11.5	0.08	0.49	3	0.46	6	2.52	155	0.05	1.11
12.4	0.08	0.65	0	0.35	7	2.88	155	0.00	1.29

Table S5.5. Parameters retrieved from the FBM analysis of the excimer fluorescence decays of the PyC4N(x)-PNb samples in DMF.

f_{py} (mol%)	f_{Ek2}	τ_{E0} (ns)	f_{EdiffE0}	f_{EE0}	τ_{D} (ns)	f_{ED}	χ^2
6.8	0.27	54	0.62	0.06	112	0.05	1.03
8.2	0.34	53	0.52	0.07	96	0.07	1.10
10.3	0.39	51	0.46	0.00	82	0.14	1.10
10.5	0.50	47	0.30	0.00	74	0.20	1.21
11.5	0.44	50	0.41	0.06	89	0.10	1.11
12.4	0.51	49	0.28	0.07	79	0.15	1.29

Table S5.6. Molar fractions of the pyrene species obtained from the analysis of the monomer and excimer fluorescence decays of the PyC4N(x)-PNb samples in DMF.

f_{py} (mol%)	f_{k2}	f_{diff}	f_{E}	f_{D}	f_{agg}	f_{free}	χ^2
6.8	0.24	0.55	0.06	0.04	0.10	0.11	1.03
8.2	0.33	0.50	0.06	0.06	0.13	0.04	1.10
10.3	0.39	0.46	0.00	0.14	0.14	0.01	1.10
10.5	0.50	0.30	0.00	0.20	0.20	0.01	1.21
11.5	0.43	0.40	0.06	0.09	0.15	0.02	1.11
12.4	0.51	0.27	0.07	0.15	0.22	0.00	1.29

Table S5.7. Parameters retrieved from the FBM analysis of the monomer fluorescence decays of the PyC8N(x)-PNb samples in DMF.

f_{PY} (mol%)	k_2 (ns ⁻¹)	f_{Mk2}	$k_e[\text{blob}]$ (μs^{-1})	f_{Mdiff}	k_{blob} (μs^{-1})	$\langle n \rangle$ (ns)	τ_{M}	f_{Mfree}	χ^2
0.9	0.13	0.08	8	0.38	19	0.71	152	0.54	1.19
2.0	0.13	0.14	7	0.48	15	1.05	152	0.38	1.01
2.7	0.13	0.18	6	0.55	13	1.12	152	0.28	1.05
3.3	0.13	0.22	6	0.60	14	1.22	152	0.17	1.02
4.9	0.13	0.36	4	0.58	12	1.90	152	0.06	1.12
8.6	0.13	0.48	5	0.48	14	2.12	152	0.03	1.17
11.0	0.13	0.58	4	0.41	12	3.18	152	0.01	1.25

Table S5.8. Parameters retrieved from the FBM analysis of the excimer fluorescence decays of the PyC8N(x)-PNb samples in DMF.

f_{PY} (mol%)	f_{EK2}	τ_{E0} (ns)	f_{EdiffE0}	f_{EE0}	τ_{D} (ns)	f_{ED}	χ^2
0.9	0.16	54	0.79	0.04	230	0.00	1.19
2.0	0.22	53	0.75	0.00	144	0.03	1.01
2.7	0.24	53	0.75	0.00	154	0.02	1.05
3.3	0.26	52	0.71	0.01	133	0.02	1.02
4.9	0.37	51	0.60	0.00	101	0.03	1.12
8.6	0.49	50	0.47	0.00	84	0.04	1.17
11.0	0.55	48	0.39	0.00	82	0.06	1.25

Table S5.9. Molar fractions of the pyrene species obtained from the analysis of the monomer and excimer fluorescence decays of the PyC8N(x)-PNb samples in DMF.

f_{py} (mol%)	f_{k2}	f_{diff}	f_{E}	f_{D}	f_{agg}	f_{free}	χ^2
0.9	0.08	0.41	0.02	0.00	0.02	0.48	1.19
2.0	0.15	0.51	0.00	0.02	0.02	0.32	1.01
2.7	0.19	0.58	0.00	0.01	0.01	0.22	1.05
3.3	0.23	0.62	0.01	0.01	0.02	0.13	1.02
4.9	0.36	0.58	0.00	0.02	0.02	0.04	1.12
8.6	0.48	0.46	0.00	0.04	0.04	0.02	1.17
11.0	0.55	0.39	0.00	0.06	0.06	0.01	1.25

Table S5.10. Parameters retrieved from the FBM analysis of the monomer fluorescence decays of the PyC12N(x)-PNb samples in DMF.

f_{py} (mol%)	k_2 (ns ⁻¹)	$f_{\text{M}k2}$	$k_c[\text{blob}]$ (μs^{-1})	f_{Mdiff}	k_{blob} (μs^{-1})	$\langle n \rangle$	τ_{M} (ns)	f_{Mfree}	χ^2
2.3	0.11	0.30	6	0.50	14	1.40	155	0.19	1.16
2.9	0.11	0.34	5	0.53	12	1.66	155	0.13	1.03
3.4	0.11	0.37	5	0.52	13	1.67	155	0.10	1.06
3.4	0.11	0.38	6	0.51	13	1.64	155	0.11	1.28
4.5	0.11	0.49	2	0.48	10	2.43	155	0.03	1.10
4.6	0.11	0.51	4	0.46	11	2.55	155	0.03	1.10

Table S5.11. Parameters retrieved from the FBM analysis of the excimer fluorescence decays of the PyC12N(x)-PNb samples in DMF.

f_{py} (mol%)	$f_{\text{E}k2}$	$\tau_{\text{E}0}$ (ns)	$f_{\text{E}diff\text{E}0}$	$f_{\text{E}E0}$	τ_{D} (ns)	$f_{\text{E}D}$	χ^2
2.3	0.57	50	0.35	0.04	108	0.037	1.16
2.9	0.56	48	0.36	0.02	96	0.052	1.03
3.4	0.54	48	0.38	0.00	85	0.082	1.06
3.4	0.53	49	0.40	0.04	108	0.030	1.28
4.5	0.45	48	0.46	0.00	81	0.091	1.10
4.6	0.42	47	0.46	0.00	77	0.122	1.10

Table S5.12. Molar fractions of the pyrene species obtained from the analysis of the monomer and excimer fluorescence decays of the PyC12N(x)-PNb samples in DMF.

f_{py} (mol%)	f_{k2}	f_{diff}	f_E	f_D	f_{agg}	f_{free}	χ^2
2.3	0.53	0.32	0.04	0.03	0.07	0.08	1.16
2.9	0.54	0.34	0.02	0.05	0.07	0.05	1.03
3.4	0.51	0.36	0.00	0.08	0.08	0.04	1.06
3.4	0.50	0.38	0.04	0.03	0.07	0.05	1.28
4.5	0.44	0.45	0.00	0.09	0.09	0.01	1.10
4.6	0.41	0.46	0.00	0.12	0.12	0.01	1.10

Table S5.13. Parameters retrieved from the FBM analysis of the monomer fluorescence decays of the PyC1N(x)-PNb samples in DMSO.

f_{py} (mol%)	k_2 (ns ⁻¹)	f_{Mk2}	$k_e[\text{blob}]$ (μs^{-1})	f_{Mdiff}	k_{blob} (μs^{-1})	$\langle n \rangle$	τ_M (ns)	f_{Mfree}	χ^2
5.6	0.11	0.15	6	0.55	10	0.78	179	0.31	1.08
7.8	0.11	0.24	4	0.67	9	1.29	179	0.09	1.09
9.0	0.11	0.22	4	0.69	7	1.34	179	0.09	1.12
11.0	0.11	0.27	3	0.69	7	1.58	179	0.05	1.04
15.0	0.11	0.36	3	0.62	7	2.25	179	0.02	1.12

Table S5.14. Parameters retrieved from the FBM analysis of the excimer fluorescence decays of the PyC1N(x)-PNb samples in DMSO.

f_{Py} (mol%)	f_{EK2}	τ_{E0} (ns ⁻¹)	$f_{EdiffE0}$	f_{EE0}	τ_D (ns ⁻¹)	f_{ED}	χ^2
5.6	0.19	50	0.72	0.02	133	0.08	1.08
7.8	0.23	49	0.62	0.07	116	0.09	1.09
9.0	0.22	45	0.70	0.00	114	0.08	1.12
11.0	0.25	45	0.65	0.00	107	0.10	1.04
15.0	0.32	44	0.55	0.00	96	0.13	1.12

Table S5.15. Molar fractions of the pyrene species obtained from the analysis of the monomer and excimer fluorescence decays of the PyC1N(x)-PNb samples in DMSO.

f_{Py} (mol%)	f_{k2}	f_{diffE}	f_{diff}	f_{E}	f_{D}	f_{agg}	f_{free}	χ^2
5.6	0.15	0.54	0.54	0.01	0.06	0.07	0.24	1.08
7.8	0.21	0.58	0.58	0.06	0.08	0.15	0.06	1.09
9.0	0.21	0.66	0.66	0.00	0.08	0.08	0.06	1.12
11.0	0.25	0.63	0.63	0.00	0.09	0.09	0.03	1.04
15.0	0.32	0.55	0.55	0.00	0.13	0.13	0.01	1.12

Table S5.16. Parameters retrieved from the FBM analysis of the monomer fluorescence decays of the PyC4N(x)-PNb samples in DMSO.

f_{py} (mol%)	k_2 (ns ⁻¹)	$f_{\text{M}k2}$	$k_{\text{e}}[\text{blob}]$ (μs^{-1})	f_{Mdiff}	k_{blob} (μs^{-1})	$\langle n \rangle$	τ_{M} (ns)	f_{Mfree}	χ^2
6.8	0.06	0.02	8	0.59	10	1.00	129	0.21	1.15
8.2	0.06	0.30	6	0.61	7	1.61	129	0.09	1.20
10.3	0.06	0.37	2	0.61	5	2.25	129	0.02	1.19
10.5	0.06	0.37	1	0.61	5	2.16	129	0.01	1.18
11.5	0.06	0.46	1	0.54	6	1.87	129	0.00	1.17
12.4	0.06	0.60	1	0.39	4	3.63	129	0.01	1.27

Table S5.17. Parameters retrieved from the FBM analysis of the excimer fluorescence decays of the PyC4N(x)-PNb samples in DMSO.

f_{Py} (mol%)	$f_{\text{E}k2}$	$\tau_{\text{E}0}$ (ns ⁻¹)	$f_{\text{EdiffE}0}$	$f_{\text{EE}0}$	τ_{D} (ns ⁻¹)	f_{ED}	χ^2
6.8	0.22	54	0.66	0.10	123	0.02	1.15
8.2	0.28	54	0.57	0.12	101	0.03	1.20
10.3	0.32	48	0.53	0.00	80	0.15	1.19
10.5	0.33	50	0.54	0.07	87	0.07	1.18
11.5	0.39	49	0.46	0.07	84	0.08	1.17
12.4	0.47	49	0.31	0.14	80	0.08	1.27

Table S5.18. Molar fractions of the pyrene species obtained from the analysis of the monomer and excimer fluorescence decays of the PyC4N(*x*)-PNb samples in DMSO.

f_{Py} (mol%)	f_{k2}	f_{diff}	f_{E}	f_{D}	f_{agg}	f_{free}	χ^2
6.8	0.19	0.56	0.08	0.02	0.10	0.15	1.15
8.2	0.27	0.54	0.11	0.03	0.14	0.05	1.20
10.3	0.32	0.52	0.00	0.14	0.14	0.01	1.19
10.5	0.32	0.53	0.07	0.07	0.14	0.01	1.18
11.5	0.39	0.46	0.07	0.08	0.15	0.00	1.17
12.4	0.47	0.31	0.14	0.08	0.21	0.00	1.27

Table S5.19. Parameters retrieved from the FBM analysis of the monomer fluorescence decays of the PyC8N(*x*)-PNb samples in DMSO.

f_{py} (mol%)	k_2 (ns ⁻¹)	$f_{\text{M}k2}$	$k_e[\text{blob}]$ (μs^{-1})	f_{Mdiff}	k_{blob} (μs^{-1})	$\langle n \rangle$	τ_{M} (ns)	f_{Mfree}	χ^2
0.9	0.13	0.05	7	0.20	14	1.26	127	0.75	1.15
2.0	0.13	0.10	6	0.45	13	1.00	127	0.45	1.16
2.7	0.13	0.12	7	0.54	13	0.95	127	0.33	1.10
3.3	0.13	0.16	7	0.61	12	1.17	127	0.23	1.10
5.0	0.13	0.26	6	0.66	11	1.67	127	0.09	1.14
8.6	0.13	0.45	0	0.52	5	2.91	127	0.02	1.27
11.0	0.13	0.45	2	0.54	9	3.19	127	0.01	1.26

Table S5.20. Parameters retrieved from the FBM analysis of the excimer fluorescence decays of the PyC8N(x)-PNb samples in DMSO.

f_{Py} (mol%)	f_{EK2}	τ_{E0} (ns ⁻¹)	f_{EdiffE0}	f_{EE0}	τ_{D} (ns ⁻¹)	f_{ED}	χ^2
0.9	0.17	55	0.74	0.00	124	0.08	1.15
2.0	0.18	53	0.78	0.01	125	0.03	1.16
2.7	0.18	50	0.80	0.00	120	0.02	1.10
3.3	0.20	50	0.77	0.01	129	0.02	1.10
5.0	0.27	49	0.70	0.02	111	0.01	1.14
8.6	0.44	46	0.51	0.00	88	0.05	1.27
11.0	0.43	47	0.52	0.00	79	0.05	1.26

Table S5.21. Molar fractions of the pyrene species obtained from the analysis of the monomer and excimer fluorescence decays of the PyC8N(x)-PNb samples in DMSO.

f_{Py} (mol%)	f_{k2}	f_{diff}	f_{E}	f_{D}	f_{agg}	f_{free}	χ^2
0.9	0.05	0.23	0.00	0.03	0.03	0.69	1.15
2.0	0.11	0.48	0.00	0.02	0.02	0.39	1.16
2.7	0.13	0.57	0.00	0.02	0.02	0.29	1.10
3.3	0.17	0.63	0.01	0.01	0.02	0.19	1.10
5.0	0.25	0.65	0.02	0.01	0.03	0.06	1.14
8.6	0.44	0.50	0.00	0.05	0.05	0.01	1.27
11.0	0.43	0.52	0.00	0.05	0.05	0.01	1.26

Table S5.22. Parameters retrieved from the FBM analysis of the monomer fluorescence decays of the PyC12N(x)-PNb samples in DMSO.

f_{py} mol%	k_2 (ns ⁻¹)	$f_{\text{M}k_2}$	$k_e[\text{blob}]$ (μs ⁻¹)	$f_{\text{M}diff}$	k_{blob} (μs ⁻¹)	$\langle n \rangle$	τ_{M} (ns)	$f_{\text{M}free}$	χ^2
2.3	0.1	0.25	5	0.52	10	1.40	128	0.23	1.12
2.9	0.1	0.30	3	0.58	8	1.64	128	0.13	1.07
3.4	0.1	0.32	3	0.57	9	1.65	128	0.12	1.14
3.5	0.1	0.33	4	0.56	10	1.51	128	0.11	1.13
4.5	0.1	0.42	3	0.54	8	2.24	128	0.05	1.21
4.6	0.1	0.45	2	0.53	8	2.38	128	0.02	1.20

Table S5.23. Parameters retrieved from the FBM analysis of the excimer fluorescence decays of the PyC12N(x)-PNb samples in DMSO.

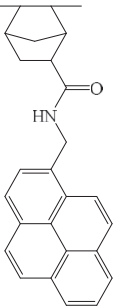
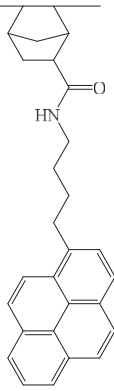
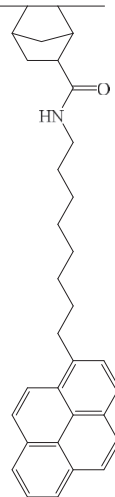
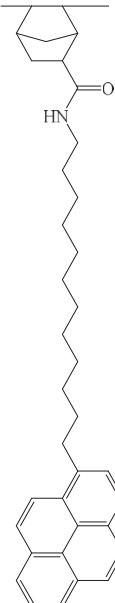
f_{Py} (mol%)	$f_{\text{E}k_2}$	$\tau_{\text{E}0}$ (ns ⁻¹)	$f_{\text{E}diff\text{E}0}$	$f_{\text{E}E0}$	τ_{D} (ns ⁻¹)	$f_{\text{E}D}$	χ^2
2.3	0.29	46	0.60	0.04	91	0.07	1.12
2.9	0.30	44	0.59	0.01	84	0.10	1.07
3.4	0.32	46	0.57	0.03	84	0.08	1.14
3.5	0.33	45	0.56	0.00	78	0.11	1.13
4.5	0.38	47	0.49	0.00	72	0.13	1.21
4.6	0.40	46	0.47	0.04	78	0.09	1.20

Table S5.24. Molar fractions of the pyrene species obtained from the analysis of the monomer and excimer fluorescence decays of the PyC12N(x)-PNb samples in DMSO.

f_{Py} (mol%)	f_{k_2}	f_{diff}	f_{E}	f_{D}	f_{agg}	f_{free}	χ^2
2.3	0.24	0.51	0.04	0.06	0.10	0.15	1.12
2.9	0.28	0.54	0.01	0.09	0.10	0.08	1.07
3.4	0.30	0.53	0.03	0.07	0.10	0.07	1.14
3.5	0.31	0.53	0.00	0.10	0.10	0.07	1.13
4.5	0.37	0.48	0.00	0.12	0.12	0.02	1.21
4.6	0.40	0.47	0.04	0.08	0.13	0.01	1.20

D] Molecular Mechanic Optimizations of PyCX(x)N-PNb-Ac

Table S5.25. Coordinates used to calculate the distance corresponding to the maximum reach of a pyrenyl label covalently attached onto a norbornene acid residue.

				
P15 (x,y,z)	(-18.02, -12.12, -4.10)	(-17.69, -14.23, -4.04)	(-17.25, -16.65, -5.47)	(-17.34, -19.49, -5.06)
P16 (x,y,z)	(-17.24, -10.92, -3.78)	(-17.27, -12.96, -4.65)	(-17.60, -15.23, -5.30)	(-17.71, -18.08, -5.02)
CoM (x,y,z)	(-17.63, -11.52, -3.94)	(-17.48, -13.60, -4.35)	(-17.42, -15.94, -5.39)	(-17.53, -18.79, -5.04)
α -C (x,y,z)	(-15.21, -1.67, -1.92)	(-14.24, 0.032, -2.08)	(-12.37, 2.74, -2.62)	(-12.29, 5.11, -1.99)
L _{PEF} (nm)	4.1	5.8	7.8	9.9

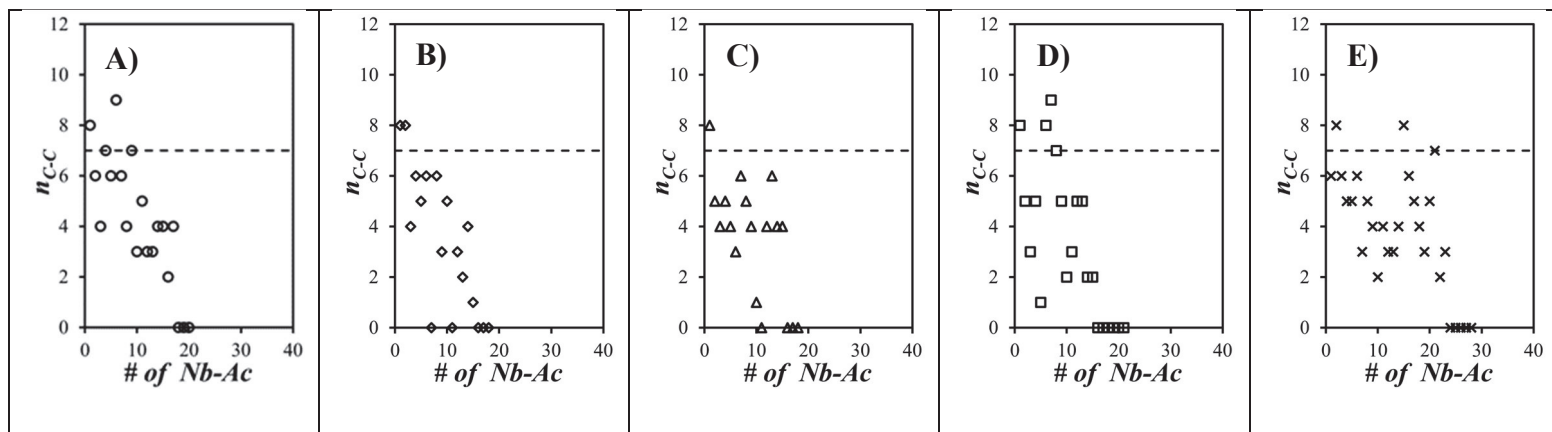


Figure S5.4. Plot of the number of carbon-carbon overlaps (n_{C-C}) between the reference and secondary pyrenyl labels for a 32-residue randomly coiled PNb-Ac construct labeled with 1-pyrene methylamine at the reference positions A) 1 (\bullet), B) 2 (\blacklozenge), C) 3 (\blacktriangle), D) 10 (\blacksquare), and E) 32 (\blacktimes).

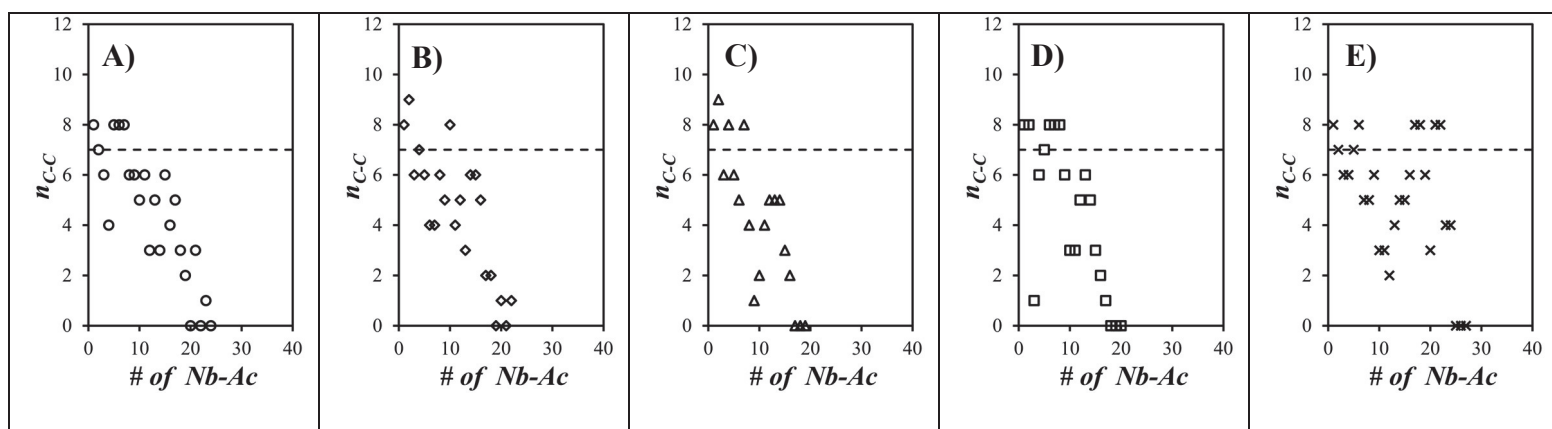


Figure S5.5. Plot of the number of carbon-carbon overlaps (n_{C-C}) between a reference and secondary pyrenyl moieties for a 32-residue randomly coiled PNb-Ac construct labeled with 1-pyreneethylamine at the reference positions A) 1 (\bullet), B) 2 (\blacklozenge), C) 3 (\blacktriangle), D) 10 (\blacksquare), and E) 32 (\blacktimes).

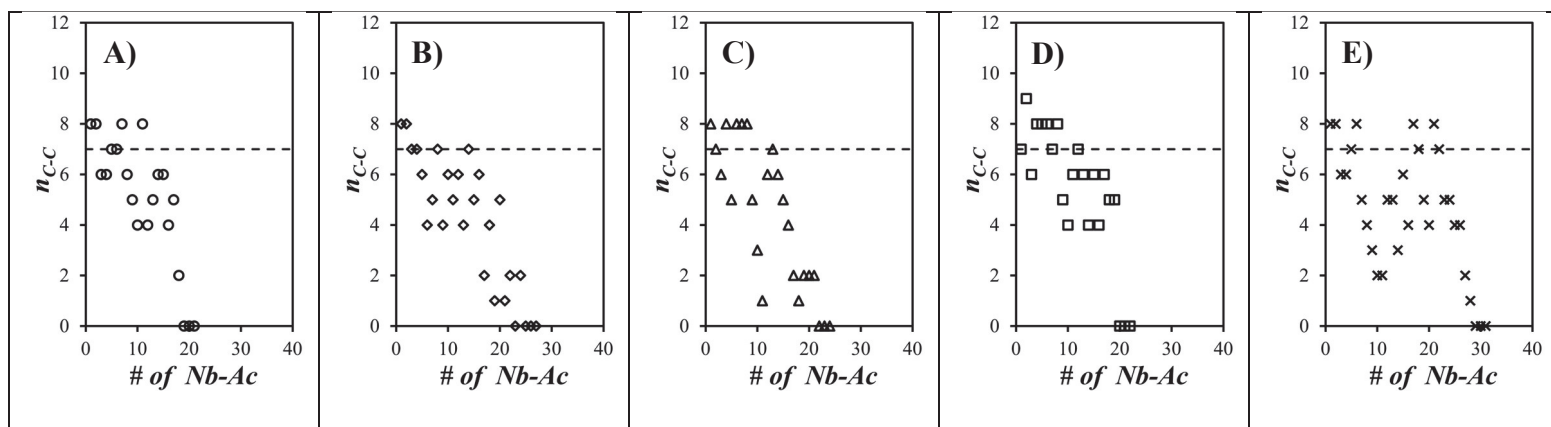


Figure S5.6. Plot of the number of the number of carbon-carbon overlaps (n_{C-C}) for a 32-residue PNb-Ac random coil construct labeled with 1-pyrenepropylamine at the reference positions A) 1 (○), B) 2 (◇), C) 3 (▲), D) 10 (◻) and E) 32 (✕).